LA-11842-P
Proposal

UC-410
Issued: August 1990

LA--11842-P

DE90 014841

A Proposal to Search for Neutrino Oscillations with High Sensitivity in the Appearance Channels $\nu_\mu \rightarrow \nu_e$ *and* $\bar{\nu}_\mu \rightarrow \bar{\nu}_e$

X-Q. Lu, G. Yodh
University of California, Irvine

S. Y. Fung, J. H. Kang, B. C. Shen, G. J. VanDalen
University of California, Riverside

R. C. Carlini, J. J. Napolitano
CEBAF

J. Amann, H. Baer, R. Burman, J. Donahue, W. Foreman, G. T. Garvey, M. Hoehn, T. Kozlowski, D. M. Lee, W. C. Louis, J. McClelland, E. C. Milner, M. Oothoudt, V. Sandberg, M. Schiliaci, N. Tanaka, R. Werbeck, D. H. White, D. Whitehouse
Los Alamos National Laboratory

A. Fazely
Louisiana State University

M. Brooks, B. B. Dieterle, C. P. Leavitt, R. Reeder
University of New Mexico

A. K. Mann
University of Pennsylvania

L. B. Auerbach, S. Kettell, W. K. McFarlane
Temple University

Los Alamos National Laboratory
Los Alamos, New Mexico 87545

TABLE OF CONTENTS

A Proposal to Search for Neutrino Oscillations with High Sensitivity in the Appearance Channels $\nu_\mu \rightarrow \nu_e$ and $\bar{\nu}_\mu \rightarrow \bar{\nu}_e$

X-Q. Lu, G. Yodh, S. Y. Fung, J. H. Kang, B. C. Shen, G. J. VanDalen, R. C. Carlini, J. J. Napolitano, J. Amann, H. Baer, R. Burman, J. Donahue, W. Foreman, G. T. Garvey, M. Hoehn, T. Kozlowski, D. M. Lee, W. C. Louis, J. McClelland, E. C. Milner, M. Oothoudt, V. Sandberg, M. Schillaci, N. Tanaka, R. Werbeck, D. H. White, D. Whitehouse, A. Fazely, M. Brooks, B. B. Dieterle, C. P. Leavitt, R. Reeder, A. K. Mann, L. B. Auerbach, S. Kettell, W. K. McFarlane

ABSTRACT

An experiment is proposed to search concurrently for $\nu_\mu \rightarrow \nu_e$ and $\bar{\nu}_\mu \rightarrow \bar{\nu}_e$ oscillations with high sensitivity at LAMPF. The detector consists of a tank with 200 tons of dilute liquid scintillator with 850 10-in. photomultiplier tubes mounted on the inside tank covering 28% of the surface. Both Čerenkov light and scintillation light will be detected. The tank will reside inside the existing E645 veto shield and the experiment will make use of the present A6 beam-stop neutrino source. After two years of data collection, 90% confidence level limits on $\bar{\nu}_\mu(\nu_\mu) \rightarrow \bar{\nu}_e(\nu_e)$ mixing strengths of $2.7(2.7) \times 10^{-4}$ can be obtained for all $\Delta m^2 > 1$ eV^2. Similarly, for maximal mixing the 90% C.L. limits on Δm^2 are $1.7(4.0) \times 10^{-2}$. This experiment will, therefore, provide the world's best terrestrial limits on $\nu_\mu \rightarrow \nu_e$ oscillations.

Other physics to be obtained includes measurements of the charged current reactions $\nu_e\mathrm{C} \rightarrow e^-\mathrm{N}$ and $\nu_\mu\mathrm{C} \rightarrow \mu^-\mathrm{N}$, of the inelastic neutral current reaction $\nu\mathrm{C} \rightarrow \nu\mathrm{C}^*$ (15.11-MeV γ), and a search for the rare decays $\pi^0 \rightarrow \nu\bar{\nu}$ and $\eta \rightarrow \nu\bar{\nu}$.

---

1. INTRODUCTION

In the last ten years, a series of experiments has been conducted at LAMPF to delineate fundamental properties of the neutrino. Low-energy neutrinos, such as those available at LAMPF, offer significant advantages in testing fundamental properties of the neutrino, and these advantages are exploited in the neutrino program at LAMPF. The first neutrino experiment at LAMPF (E31) established strong limits on the number of $\bar{\nu}_e$ emitted in μ^+ decay, implying additive lepton conservation, and measured the matrix element for the primary source of energy in the sun; the second experiment (E225) made the first observation of $\nu_e e \rightarrow \nu_e e$ elastic scattering and verified the destructive interference of the weak charged and neutral currents as predicted by the Standard Electroweak Theory (EWT). Recent experiments, E645 and E764, concentrated on the search for neutrino oscillations, and obtained significant limits on the magnitudes of the oscillation parameters.

It is proposed here to extend the search for neutrino oscillations of the type $\nu_\mu \rightarrow \nu_e$ by replacing the central detector in the most recent neutrino experiment at LAMPF (E645) with a more massive and appreciably more sensitive device. This detector (LSND) is based on an extension of a technique that has been used in large water Čerenkov devices such as Kamioka and IMB. These detectors are capable of reconstructing the energy and direction of low-energy electrons through the Čerenkov light emitted in the liquid. Kamioka, in particular, has observed recoil electrons from solar neutrinos below 10 MeV. We view the technique of imaging Čerenkov detectors for observing low-energy, simple-topology events as being well established. In this document, we propose an extension of this technique. Instead of using water as the target medium, it is proposed to use mineral oil with a refractive index of 1.47. This medium is composed approximately of CH_2 which is superior for detection of low-energy electrons by virtue of its lower density, higher refractive index, and lower radiation length. The addition of small quantities of scintillator to the mineral oil gives the additional benefit that the energy resolution is substantially improved and offers the possibility of detecting muons below Čerenkov threshold and low-energy neutrons—a crucial element in lowering the background to one of the oscillation signals in the detector. The performance that is expected in this experiment is dependent on the use of large-area, precise-timing phototubes that have been developed recently. All of these improvements in the imaging technique make it feasible to search for neutrino oscillations with high sensitivity at LAMPF.

It was earlier proposed to extend the LAMPF neutrino program with a high-precision measurement of low-energy neutrino (ν_e and ν_μ)—electron scattering, from which would be obtained a value of the fundamental EWT parameter $\sin^2\theta_W$ with an error of $< 1\%$. This measurement would utilize a large, imaging water Čerenkov detector (LCD) which would, with its attendant proton storage ring (PSR) pulsed proton beam and new beam line, constitute an ambitious new facility at LAMPF for neutrino physics.

The motivation for LCD is established in the proposal (Los Alamos National Laboratory report LA-11300-P) and is well recognized. Briefly, apart from precision measurements of the asymmetries of the products of e^+e^- collisions, precision νe scattering is the only purely leptonic process to test the EWT at the level of radiative corrections. Taken in conjunction with certain other precise measurements that are likely to be done in the coming decade, viz., Z and W masses, parity violation in atoms, possibly deep inelastic neutrino-nucleus and electron-nucleus scattering, and the aforementioned e^+e^- asymmetries, each

of which will yield a precise ($\sim 1\%$) value of $\sin^2\theta_W$, neutrino-electron scattering will be a fundamental part of a concentrated test of the EWT at the most precise level to be obtained from the multiplicity of phenomena that it governs.

While LCD is a large and expensive project by the standards of usual LAMPF detectors, it is not out of line with detectors with similar particle physics goals at other, mostly higher energy accelerators. We wish to affirm that LCD and the physics to be accomplished with it remain the primary goals of the LAMPF neutrino program, and we are encouraged toward that end by the R&D funds allocated in FY 1990 for that purpose.

LCD requires extrapolation of the techniques employed at present in large, imaging water Čerenkov detectors. The experiment proposed here (LSND) has the dual advantage of excellent physics together with development and testing of the techniques that will be required for exploitation of the Čerenkov-imaging detector method. LSND offers a search for neutrino oscillations that will be superior in sensitivity by an order of magnitude to any yet carried out with a terrestrial neutrino source. Furthermore, two appearance channels of neutrino oscillations, $\nu_\mu \rightarrow \nu_e$ and $\bar{\nu}_\mu \rightarrow \bar{\nu}_e$, with similar sensitivities but dissimilar event signatures, backgrounds, and systematic errors, can simultaneously be carried out. These would provide a degree of redundancy necessary to reach the lowest oscillation parameter limits, and, more important, the redundancy necessary for conviction should a positive oscillation signal be obtained.

Accordingly, we have assessed the value of an oscillation detector for the oscillation physics that it will yield and, independently, as a testing ground for LCD. We are convinced that a detector can be built and operated successfully to accomplish both purposes. We emphasize that, in our opinion, the quality of the neutrino oscillation physics alone justifies this venture. But the value of testing the methods and components intended for LCD in an actual experiment is an important consideration in our thinking.

In what follows, we discuss briefly the present status of neutrino oscillation data and the goals of this proposal. Then comes a short section on the detector. The next section treats the channel $\nu_\mu \rightarrow \nu_e$ in detail, and the following two sections discuss the channel $\bar{\nu}_\mu \rightarrow \bar{\nu}_e$ in the same manner. Section 7 describes the advantages of searching for neutrino oscillations in more than one channel, while Section 8 mentions some additional physics areas of interest that will necessarily be explored with the data taken in the oscillation search. The last section gives more details of the apparatus, costs, and schedule.

2. PRESENT STATUS OF NEUTRINO OSCILLATION RESULTS AND THE GOAL OF THIS EXPERIMENT

We show in Fig. 1 the two-parameter space, $\Delta m^2 \equiv m_1^2 - m_2^2$ (eV^2) and $\sin^2 2\theta$, that customarily describes the neutrino oscillation parameters, in which are plotted (i) the resulting limiting curve from the reactor (Gosgen)[1] disappearance ($\bar{\nu}_e \rightarrow \bar{\nu}_x$) experiments, (ii) the BNL (E734)[2] limiting curve for $\nu_\mu \rightarrow \nu_e$, (iii) the LAMPF (E645)[3] limit for $\bar{\nu}_\mu \rightarrow \bar{\nu}_e$, and (iv) the LAMPF (E764)[4] limiting curve for $\nu_\mu \rightarrow \nu_e$. Other experimental results might also be plotted, but for our purpose the four results shown adequately define the limits obtained so far from accelerator or reactor neutrino sources. Over the next several years new results are expected from the KARMEN experiment at Rutherford, and there are plans by F. Boehm and collaborators to build a larger reactor oscillation detector. In addition, there are various solar neutrino experiments, planned or in construction, that are possibly sensitive to neutrino oscillations at $\Delta m^2 < 10^{-2}$ eV^2.

Also indicated in Fig. 1 is the limiting curve expected from the $\bar{\nu}_\mu \rightarrow \bar{\nu}_e$ measurement of this proposal. If the experiment can be carried out as proposed here, the limit on $\sin^2 2\theta$ of approximately 3×10^{-4} for all $\Delta m^2 > 1$ eV^2 can be achieved, and the limit on Δm^2 of approximately 1.7×10^{-2} eV^2 will be obtained for $\sin^2 2\theta = 1$. The relative value of this proposal is partly summarized in the comparison of the outer curve in Fig. 1 with the cross-hatched area.

But of comparable importance is the redundancy in the experiment if a positive signal were to be observed. Figure 2 shows the limiting curve expected from the $\nu_\mu \rightarrow \nu_e$ measurement of this proposal, as well as that from the $\bar{\nu}_\mu \rightarrow \bar{\nu}_e$ measurement. Within the uncertainties of the calculations that yield Figs. 1 and 2, the sensitivities of the two proposed measurements are the same. Consequently, the two measurements, carried out at the same time, in the same beam(s), and with the same detector will provide independent checks on the validity of the final result on neutrino oscillations not available from previous measurements.

An additional search for $\bar{\nu}_\mu \rightarrow \bar{\nu}_e$ oscillations can be made with neutrinos from the PSR. Again, it will be done concurrently with the measurements above, and distinguished by timing alone. The sensitivity of this measurement is principally in the region of large $\sin^2 2\theta$, as shown in Fig. 2. Apart from the intrinsic interest in the measurement limit on Δm^2 ($< 3 \times 10^{-2}$ eV^2 at 90% C.L.), there is value in gaining experience with the PSR beam.

3. DETECTOR AND BEAM, EVENT SIMULATION, EVENT TRIGGER, AND RATES

3.1 Detector & Beam

The proposed detector is shown in Fig. 3 and consists of a cylindrical tank of dilute mineral-oil-based liquid scintillator approximately 6 m in diameter by 9 m long with an active mass of 200 tons. The tank will reside inside the existing E645 veto shield, which is located 27 m downstream of the proton beam stop and is at an angle of approximately 17° to the beam direction. The tank will be made of 1 cm thick steel and have 850 10-in. diameter, very low time jitter ($\sigma \sim 1$ ns) photomultiplier tubes (PMTs) mounted uniformly over the inside surface.

A layout of the A line beam stop, which we plan to use, and detector area are given in Fig. 4. The proton beam first passes through a water dump, then through an array of isotope stringers before striking a Cu beam dump. The proton kinetic energy entering the beam line is 780 MeV and the typical proton current is 800 μA. There exists about 8.5 m of Fe-equivalent between the Cu beam dump and the detector. In fact, there is sufficient shielding that beam-related neutrons have not been identified in the E645 experiment.

We propose 850 10-in. photomultiplier tubes covering 28% of the surface area of the tank. These tubes, shown in Fig. 5, are manufactured by Burle Corporation (C83061E photomultiplier tube) and have excellent timing resolution, 2.3-ns FWHM for single photons and full-face illumination. They also have single photoelectron separation and typical noise rates < 10 kHz. Fig. 6a shows the dark pulse plateau curve, while Figs. 6 b,c show the setup and results of tests performed on these tubes at LAMPF. The tubes will be encapsulated in a container as shown in Fig. 7. The container is impervious to both scintillator and water, and attention has been paid to the container tube seal and the single cable penetration.

The properties of the liquid scintillator are given in Table 1. We plan to use a dilute concentration of scintillator such that about 20% of the total light output will be Čerenkov light and 80% scintillation light. This concentration may vary after we perform further tests and optimizations. The liquid scintillator consists mostly of mineral oil ($> 99\%$) with the addition of psuedocumene, PPO, and BIS-MSB. Mineral oil has advantages relative to water for the detection of Čerenkov light as it has a higher index of refraction, a lower density so that electrons travel farther before stopping, and a sharper Čerenkov ring due to the longer radiation length. The absorption and emission spectra of the scintillator are

given in Fig. 8. Note that the absorption becomes small at a wavelength of $\sim$ 400 nm, and we are, therefore, sensitive to direct Čerenkov light above 400 nm. Furthermore, the 4 ns decay time of the liquid scintillator will be shown to be helpful for differentiating the prompt Čerenkov light.

Figure 9 is a layout of the E645 veto shield, which is described in detail elsewhere.[3] Briefly, the shield provides 4π coverage for the detection of cosmic-ray muons, which have been rejected on-line with an inefficiency of $\sim 10^{-4}$ and off-line with an inefficiency of $< 3 \times 10^{-6}$ by the E645 group. The shield has an overburden of about 2000 g/cm^2 of steel and earth, and the resulting cosmic muon rate is $<$ 10 kHz. We shall move the present water plug closer to the veto shield and add another 1000 g/cm^2 of overburden to eliminate any direct cosmic-ray hadrons and decrease the incident muon flux by a factor of two ($<$ 5 kHz). We also shall place more anti-muon counters around the perimeter of the downstream veto wall, as it has been determined that much cosmic-ray background comes from this region. Hardware dead-time losses are approximately 5% due to the $\sim$ 5 kHz veto rate and the $\sim$10 μs veto length.

3.2 Event Simulation

A Monte Carlo was written at the University of California at Irvine and has been used for event simulation in both the LCD[5] and SNO[6] water Čerenkov proposals. For simplicity, the Monte Carlo assumes the tank to be a right cylinder of 6.05 m diameter and height. This geometry has almost exactly the same area and volume as the detector we envisage. Each PMT has a 10-kHz noise rate, and the PMT area coverage is 28%. The Monte Carlo generates and reconstructs events in three steps. First, electrons (or photons) are generated with specific energy, position, and angular distributions (these distributions can be either fixed, random, or from a definite process such as neutrino-electron scattering arising from stopped π^+ decay), and the electron is then propagated through the liquid scintillator using the EGS4 electromagnetic showering code. Second, for our purpose, the photons produced by both Čerenkov and scintillation light are propagated to the photomultiplier tubes, taking into account Rayleigh scattering, absorption (L$\sim$ 10 m), and reflection off the PMT surfaces. The PMT quantum efficiency varies as a function of wavelength in accord with the properties of the Burle 10-in. tubes, and the tank surface between PMTs is assumed to be perfectly absorbing. Čerenkov light is generated according to its $1/\lambda$ distribution. The scintillation light yield is assumed to be 1 photon per 2000 eV

of deposited ionization energy, and the frequency spectrum is parameterized to reproduce the emission spectrum[7] of Fig. 8 above $\lambda = 400$ nm. Finally, making use of the time and number of photoelectrons associated with each hit tube, an event is reconstructed according to the algorithm described below.

An event is first reconstructed using the Irvine reconstruction algorithm, which uses only PMT timing and is fully described elsewhere.[5,6] The Irvine algorithm determines the event time and vertex by minimizing the function $\chi^2 = \Sigma(t_i - t_o - r_i/v)^2$, where the sum is over all hit tubes, t_i is the time of tube i, t_o is the fitted time, r_i is the distance from the fitted vertex to tube i, and $v = c/n$ is the velocity of light in liquid scintillator. Hit tubes that are too far off in time (or angle) are not used in the reconstruction. The electron angle with the initial neutrino direction is then determined by calculating the weighted average of the unit vectors from the fitted vertex to the hit PMTs used in the reconstruction, where the weight factor for each PMT is the number of photoelectrons.

The result of the Irvine fit is then used as the input to an improved reconstruction algorithm, which is similar to one developed by W. Frati[8] for the Kamioka experiment and which determines the electron direction by fitting the hit PMTs to a fixed angle (47° for liquid scintillator) Čerenkov cone. Specifically, the function $\chi^2 = \Sigma(f_{\theta i} + f_{ti}) * \text{wgt}$ is minimized, where the sum is over all hit tubes, weighted by time and the number of photoelectrons corrected for absorption length, $f_{\theta i} = (\theta_i - 47.14)^2/(2 * 15.81^2)$, $f_{ti} = (t_i - t_o - r_i/v)^2$, and $\text{wgt} = N_{pe} * e^{r_i/L} * (t_i - t_o - 10 - r_i/v)^2$, where θ_i is the angle in degrees between the fitted direction and tube i, t_i is the time in ns of tube i, t_o is the fitted time, r_i is the distance from the fitted vertex to tube i, $v = c/n$ is the velocity of light in liquid scintillator, and L is the attenuation length.

Figure 10a shows a typical 45-MeV electron event generated by the Monte Carlo. Each number corresponds to a hit photomultiplier tube and equals the number of photoelectrons. The detector cylinder has been unrolled to clearly show the phototube hit pattern. Figure 10b is the same as Fig. 10a but requires PMTs to have at least five photoelectrons and reconstructed times that are prompt. Note that the location of the Čerenkov ring can be seen by eye. Figures 11–13 give the energy resolution and the average error in position and angle as a function of electron energy. As seen in Table 2, the resolutions are $< 5\%$, < 10 cm, and $< 15°$, respectively, for 45-MeV electrons. Figures 14 a–d show the resolution functions of time, position, energy, and angle for a sample of 45-MeV electrons.

The energy is obtained from the number of photoelectrons, the position from the phototube timing, and the angle from the Čerenkov light emitted by the electron. Note that the average angular error due to multiple scattering for 45-MeV electrons in liquid scintillator is $\sim 10°$. Table 3 is the same as Table 2 for the case of 425 tubes (14% coverage) instead of 850 tubes, and Table 4 is for 850 tubes but with pure mineral oil instead of liquid scintillator, such that all of the emitted light is Čerenkov light. Finally, Figs. 15 a,b show the confidence level that an event is an electron for samples of 45-MeV electron and proton events. The confidence level is obtained from a fit to the Čerenkov cone. The probability that a proton is mistaken for an electron is $\sim 10^{-3}$ for the scintillation to Čerenkov light ratio of 4:1.

3.3 Event Trigger and Rates

The event trigger will simply require that there be > 10 MeV (> 200 photoelectrons or > 200 hit tubes) in a 100-ns interval with no cosmic muon in the preceding 20 μs. As the cosmic muon rate through the detector will be < 5 kHz, we expect the hardware trigger dead time to be $< 5\%$. There are a few contributions to the trigger rate, all of which are fortunately small. The rate due to genuine neutrino events is ~ 0.01 Hz. The on-line inefficiency of the active veto, $\sim 10^{-4}$,[3] gives a trigger rate due to cosmic muons of < 0.5 Hz. In addition, cosmic-ray neutrons contribute a rate of ~ 0.5 Hz. As the PMT noise rate is < 10 kHz per tube and the thermal neutron rate is < 0.8 kHz[9] (thermal neutrons absorbed on free protons emit a 2.2 MeV γ), the trigger rate due to accidentals is completely negligible. We, therefore, estimate a total trigger rate ~ 1 Hz for LSND.

Figure 16 shows the E645 total singles rate, with no veto signal in the previous 15 μs from the veto shield, in all of the liquid scintillator modules, where we define a single hit to be one or more liquid scintillator modules with both phototubes firing in a 1-μs interval. The singles rate above 10 MeV is ~ 1 Hz for E645, which is in agreement with our estimates. Note that we shall take data continuously, both during and between spills so that we can perform an accurate beam-off subtraction. There will also be a second trigger following the main trigger, which will record non-cosmic-ray events with > 1 MeV of deposited energy (> 20 phototubes) up to 1 ms after the original event. This second trigger will be described in detail later.

We can easily estimate the data flow rates by assuming 10 bytes per hit tube, a 1 ms time window for second triggers, and 20 hit tubes (up to 850) per MeV of deposited

energy. For a 1 Hz trigger rate we expect < 10 kB/s from triggered events and < 1 kB/s from thermal neutrons. The total data flow rate is, thus, < 11 kB/s or < 1.0 GB/day, corresponding to a few 6250-BPI magnetic tapes per day.

The front-end electronics and data acquisition system to handle the event triggers and above rates are designed to record and selectively process the pulse histories (charge and time) of each of the 850 photomultiplier tubes with minimal dead time and very high system reliability. They present no significant new problems and are discussed in Appendix F.

4. SEARCH FOR $\nu_\mu \rightarrow \nu_e$ OSCILLATIONS

4.1 Event Signature

A high-sensitivity search for $\nu_\mu \rightarrow \nu_e$ oscillations can be performed by using neutrinos with energies greater than $\sim$ 80 MeV from pion decay in flight in the beam dump. If oscillations occur, then ν_μ neutrinos oscillate into ν_e neutrinos, which would be detected via the reaction $\nu_e C \rightarrow e^- N$. The event signature for these oscillations is a single high-energy electron with energy in the approximate range $60 < E_e < 180$ MeV. The lower-energy events in this range will be most useful for establishing an oscillation limit at low Δm^2, while the higher-energy events will be most important at high Δm^2. This oscillation search can be performed equally well with either dilute liquid scintillator or pure mineral oil, but we assume dilute liquid scintillator, which is necessary for the $\bar{\nu}_\mu \rightarrow \bar{\nu}_e$ search discussed in the next section.

Although only about 2.5% of the pions decay in flight before stopping in the A6 beam dump, the cross section for the charged-current reaction $\nu_e C \rightarrow e^- N$, as shown in Fig. 17, is large,[10] and the electron energy is only about 17 MeV less than the ν_e energy. Figures 18 a,b give the ν_μ energy distribution that we expect from pion decay-in-flight and the resulting electron energy distribution ($\overline{E}_e \sim 100$ MeV) from $\nu_e C \rightarrow e^- N$.[11] Figures 19 a–d show the reconstructed time, position, energy, and angle resolution functions, respectively, for a sample of 100-MeV electron events generated by the Monte Carlo. The energy and time resolutions are approximately 2.8% and 0.24 ns, and the average errors in position and angle are 8.4 cm and 10.2°, respectively.

4.2 Event Rate

A simulation of the A6 beam line has determined[11] the π^+ decay-in-flight neutrino flux at a distance of $\sim$ 27 m from the beam stop to be $2.0 \times 10^{12} \nu_\mu/\text{cm}^2$ ($3.9 \times 10^{11} \bar{\nu}_\mu/\text{cm}^2$ from π^- decay in flight) for $E_\nu > 80$ MeV after 130 days of running at LAMPF ($\sim$ 3000 actual hours) or 8678 Coulombs. Using 5.9×10^{30} C nuclei, a $\nu_e C \rightarrow e^- N$ cross section[12] of 2.8×10^{-39} cm^2, and an acceptance of 0.513, we estimate the number of $\nu_e C \rightarrow e^- N$ events per 130 days for maximal neutrino mixing to be

$$(2.0 \times 10^{12})(2.8 \times 10^{-39})(0.513)(5.9 \times 10^{30}) = 16,950.$$

The $\nu_e C \rightarrow e^- N$ acceptance (0.513) is the product of the shield live time (86.0%), the 25-cm fiducial volume cut (66.3%), and the electron identification efficiency (90%), which results from rejecting possible proton events. The shield live time is the total live time and includes dead-time losses from the hardware trigger and the off-line analysis.

4.3 Backgrounds

There are three important backgrounds to consider: cosmic-ray background, μ^+ decay in flight, and the in-flight decay $\pi^+ \rightarrow e^+ \nu_e$. A detailed analysis[13] of high-energy events in E645 reveals 7 electron-like events with $E_e > 60$ MeV (3 events from beam-on and 4 events from beam-off) in cycles 2 and 3 of 1987, corresponding to 3800 C. (Note that cycle 1 of 1987 is not included because there was only 1000 g/cm^2 of overburden instead of 2000 g/cm^2.) From a Monte Carlo simulation, the total efficiency of the high-energy analysis in the energy interval $60 < E_e < 180$ MeV is 0.28. Taking into account the ratio of beam-on to beam-off data, 1:3.5, we estimate the acceptance-corrected number of beam-on background events in E645 after 8678 C to be

$$(7/4.5) \times (8678/3800)/0.28 = 12.7.$$

Extrapolating to LSND, we expect

$$12.7 \times 2.5 \times 0.2 \times 0.5 \times 0.37 \times 0.513 = 0.60$$

events per 130 days, corresponding to a background level of 3.5×10^{-5}. The factor 2.5 is the scale-up factor in extrapolating from E645 to LSND and was determined from a Monte Carlo simulation by assuming cosmic-ray neutrons were the source of the background. (This factor is 1.3 if the background is proportional to the detector area, which is expected for backgrounds with large cross sections.) The factor 0.2 accounts for the 200-MHz structure of the beam, since we can determine the time of an event, including the spread of the neutrino arrival time, to an accuracy of about 0.5 ns. Table 5 lists effects that can smear the determination of the proton spill time. If the various contributions are added in quadrature, a total time resolution of < 0.5 ns is obtained, which allows us to distinguish decay-in-flight events and reject background by a factor of ~ 5. We plan to add an additional 1000 g/cm^2 of overburden to the shielding, which reduces the rate by 0.5 (the reduction is much greater if the cosmic-ray background is due to a direct neutron component). The 1-cm steel tank wall and the 75-cm liquid scintillator buffer around the

surface (one interaction length) should further reduce the rate by 0.37 (or more reduction if the background is due to direct cosmic-ray muons that are missed by the veto). Finally, 0.513 is the LSND acceptance for high-energy electrons. Therefore, we expect about two background cosmic-ray events with $60 < E_e < 180$ MeV after two years or 260 days of data taking.

As shown in Figs. 20 a,b the expected neutrino and electron energy distributions for the backgrounds due to μ^+ decay in flight and $\pi^+ \rightarrow e^+\nu_e$ are much different from the signal at a level of 5×10^{-4}. The ratio of μ^+ to π^+ decay-in-flight events in the $60 < E_e < 180$ MeV electron energy range is about 2.6×10^{-4}, and we estimate nine background events from μ^+ decay in flight after two years. Finally, the ratio of $\pi^+ \rightarrow e^+\nu_e$ to $\pi^+ \rightarrow \mu^+\nu_\mu$ events with $60 < E_e < 180$ MeV is 6×10^{-5}, and this semi-rare decay contributes about two events per year. Therefore, we estimate a total of 13 background events after two years of data taking, corresponding to a background level of 3.8×10^{-4}. This estimate agrees with the results of Appendix B, where an independent background calculation is made.

4.4 Sensitivity

As discussed above, our per-event sensitivity after two years of data collection is 2.9×10^{-5}, which is based on a total of 33,900 $\nu_e \mathrm{C} \rightarrow e^- \mathrm{N}$ events for maximal mixing. Using a background level of 3.8×10^{-4}, or 13 events, a 90% confidence level limit of 2.7×10^{-4} for $\nu_\mu \rightarrow \nu_e$ oscillations at $\Delta m^2 > 3$ eV^2 can then be obtained. Note that the cosmic-ray background level can be precisely determined from the beam-off data, while the μ^+ decay-in-flight and $\pi^+ \rightarrow e^+\nu_e$ background can be determined in two ways: from the Monte Carlo simulation and from fitting to the energy distribution, as the background energy distribution is different from the energy distribution of the oscillation signal. Figure 2 shows the limiting oscillation curve in the Δm^2 vs $\sin^2 2\theta$ parameter space, which is seen to be comparable to the $\bar{\nu}_\mu \rightarrow \bar{\nu}_e$ limiting oscillation curve discussed in the next section.

5. SEARCH FOR $\bar{\nu}_\mu \rightarrow \bar{\nu}_e$ OSCILLATIONS

5.1 Event Signature

A high-sensitivity search for $\bar{\nu}_\mu \rightarrow \bar{\nu}_e$ oscillations can be performed with neutrinos from muon decay at rest with energies greater than ~ 40 MeV. If oscillations occur, then $\bar{\nu}_\mu$ neutrinos oscillate into $\bar{\nu}_e$ neutrinos, which are detected via the charged-current reaction on a free proton, $\bar{\nu}_e p \rightarrow e^+ n$, followed by the capture of the recoil neutron on hydrogen. The event signature is an electron in the energy range $37 < E_e < 50$ MeV in coincidence with a 2.2 MeV γ from neutron absorption on a free proton within 1 m and 0.5 ms of the electron event. These position and time requirements may vary somewhat after data are obtained and a further optimization is performed.

The reaction $\bar{\nu}_e p \rightarrow e^+ n$ has a relatively large cross section,[12] as shown in Fig. 21, and produces a characteristic high-energy positron, as the positron energy is between 1.3 to 6.0 MeV less than the $\bar{\nu}_e$ energy, depending on the angle of the recoil neutron. Figures 22 a–e compare the expected positron energy from neutrino oscillations with the electron energies from the reactions $\nu e \rightarrow \nu e$ and $\nu_e \mathrm{C} \rightarrow e^- \mathrm{N}$; as can be seen, there is little background above 35 MeV. Figures 14 a–d show the reconstructed time, position, energy, and angle resolution functions, respectively, for a sample of 45-MeV electron events generated by the Monte Carlo. The energy and time resolutions are approximately 3.9% and 0.21 ns, and the average errors in position and angle are 9.3 cm and 14.2°, respectively.

The recoil-neutron capture on hydrogen and the subsequent detection of the 2.2 MeV photon by scintillation light have been simulated extensively by Monte Carlo techniques. Figures 23 a,b show the capture time and straight-line distance traveled for a large sample of recoil neutrons from $\bar{\nu}_e p \rightarrow e^+ n$ interactions. The mean neutron capture time is 203 μs, and the average straight-line distance traveled by the neutron before capture is about 10 cm. Figures 24 a,b give the reconstructed energy and position resolution functions for a sample of 2.2 MeV γ events. The energy resolution is 20%, and the average position error is 44 cm. On average, a 2.2 MeV γ results in 34 hit photomultiplier tubes and 35 photoelectrons, given the dilute liquid scintillator to be employed. The average observed γ energy is 1.7 MeV, which is less than the 2.2 MeV photon energy due to low-energy photon absorption in the scintillator. Approximately 85% of the neutron-capture photons exhibit energies in the range $1 < E_\gamma < 2.5$ MeV (97.4%) and are reconstructed within 1 m (95.0%) and 0.5 ms (91.6%) of the e^+ (from $\bar{\nu}_e p \rightarrow e^+ n$) vertex.

We estimate the accidental neutron rate in LSND by extrapolating from E645 random-trigger data. Figure 25a shows the total singles rate in all of the E645 liquid scintillator modules at the beginning of the 1989 run as a function of energy. We define a single hit to be one or more E645 liquid scintillator modules with both phototubes firing in a 1-μs interval. The resulting energy threshold is between 0.5 MeV (for hits near the center of the liquid scintillator module) and 1.0 MeV (for hits near one of the two photomultiplier tubes). In Fig. 25b is shown the total E645 singles rate in the energy range $1 < E < 2.5$ MeV as a function of time, extending from the start of the 1988 E645 run to the end of the 1989 run. The observed singles rate decreases from 4.4 KHz to 3.1 KHz during this time interval, corresponding to a half life of 2.4 ± 0.1 y. This observed decay time is consistent with a dominant radioactive background from ^{22}Na, which has a half life of 2.601 y and which is known to be present in the tunnel containing the E645 detector. There are other factors that lead us to believe that this singles rate is almost completely due to radioactivity. First, the rate barely changed from accelerator-on to accelerator-off ($< 5\%$ difference) and did not change from LAMPF cycle 1 to cycle 2 of 1987, between which an additional 1000 g/cm^2 of overburden was added. Furthermore, the singles rate is not entirely due to low-energy neutrons, because B. Fujikawa of E645 measured[9] in 1987 the upper limit of low-energy neutrons in E645 to be < 0.8 KHz, which is in agreement with test measurements made by one of us (GTG)[14] and R. McKeown.[15] Using a singles rate of 3.4 KHz and extrapolating to LSND, we estimate a singles rate of

$$3400 \times 2.5 \times 0.14 = 1.2 \text{ KHz}.$$

The factor 2.5 is a conservative scale-up factor in extrapolating from E645 to LSND and was determined from a Monte Carlo simulation. This scale-up factor is < 1 if the background is from radioactivity in the air or on the E645 detector itself and 1.3 if the background is proportional to the outside detector area. The scale-up factor cannot be proportional to mass as the radioactivity in liquid scintillator is known[16] to be $< 10^{-12}$ g of U or Th per g of mineral oil. The factor 0.14 is the reduction due to the 1 cm steel tank wall and 50-cm liquid scintillator buffer between the tank and PMT surface (two photon attenuation lengths). The number of accidental neutron counts in a 0.5 ms time interval and within a 1 m sphere of LSND around the event is then given by

$$(1.2 \times 10^3) \times (5 \times 10^{-4}) \times (4\pi/3 \times 150) = 0.017,$$

where the active volume of LSND is 150 m^3. Thus, about 1 out of every 50 events will have an accidental recoil-neutron signature. Note that the time dependence of the neutron relative to the triggered event will be approximately flat for accidental neutrons and exponential with a 203 μs decay time (see Fig. 23a) for genuine recoil neutrons.

5.2 Event Rate

A simulation of the A6 beam line has determined[11] the decay-at-rest neutrino flux at a distance of $\sim$ 27 m from the beam stop to be $5.4 \times 10^{13} \nu_\mu/cm^2$ from pion decay at rest and an equal number of ν_e and $\bar{\nu}_\mu$ from muon decay at rest, after 130 days of running at LAMPF ($\sim$ 3000 actual hours) or 8678 Coulombs. Using 11.8×10^{30} free protons, a $\bar{\nu}_e p \to e^+ n$ cross section[12] of 1.5×10^{-40} cm^2, and an acceptance of 0.173, we can estimate the number of $\bar{\nu}_e p \to e^+ n$ events per year for maximal neutrino mixing to be

$$(5.4 \times 10^{13})(1.5 \times 10^{-40})(0.173)(11.8 \times 10^{30}) = 16,540.$$

The 0.173 $\bar{\nu}_e p \to e^+ n$ acceptance is the product of the shield live time (74.3%), the 25-cm fiducial volume cut (66.3%), the electron identification efficiency (90%), the fraction of events with $E_e > 37$ MeV (45.9%), and the recoil neutron detection efficiency (85.0%). The shield live time is the total live time and includes dead-time losses from the hardware trigger and the off-line analysis.

5.3 Backgrounds

The main background with a recoil neutron is π^- decay in flight in the beam dump followed by μ^- decay at rest, which produces a $\bar{\nu}_e$. The estimated background for this is

$$(0.2) \times (0.025) \times (0.10) \times (0.50) = 2.5 \times 10^{-4},$$

where 0.2 is the π^-/π^+ ratio, 0.025 is the probability that the π^- decays-in-flight, 0.10 is the probability that the μ^- decays before capture, and 0.50 reflects the better acceptance above $\sim$ 37 MeV for $\bar{\nu}_e$ from $\bar{\nu}_\mu \to \bar{\nu}_e$ oscillations compared to $\bar{\nu}_e$ from μ^- decay (see Fig. 26). The decay $\mu^+ \to e^+ \nu \bar{\nu}$ following $\bar{\nu}_\mu p \to \mu^+ n$ is also a background if the produced μ^+ has such little energy (< 1 MeV) that it is not observed and the recoil neutron is detected. We estimate that this process contributes at the level of $\sim 3.5 \times 10^{-5}$.

Other backgrounds, which do not have a recoil neutron and are suppressed by the neutron accidental relative rate of 0.017, are ν_e $^{13}C \to e^- N$, which contributes at a level of

about 4.3×10^{-5}, and the cosmic-ray background, which is < 1 event per 130 days. These backgrounds have much different energy distributions above 37 MeV than the oscillation signal.

The total estimated background is, therefore, at the level of 3.9×10^{-4}, which corresponds to 12.8 backgrounds after two years or 260 days and agrees with the results of Appendix B, where an independent background calculation is made.

5.4 Sensitivity

As discussed above, our per-event sensitivity after two years of data collection is 3.0×10^{-5}, which is based on a total of 33,080 $\bar{\nu}_e p \rightarrow e^+ n$ events for maximal mixing. Using a background level of 3.9×10^{-4}, or 12.8 events in two years, a 90% confidence level limit of 2.7×10^{-4} for all $\bar{\nu}_\mu \rightarrow \bar{\nu}_e$ oscillations with $\Delta m^2 > 1$ eV^2 can be obtained. For $\sin^2 2\theta = 1$, the 90% confidence level limit on Δm^2 is 1.7×10^{-2} eV^2.

Note that the sensitivity estimates are reasonable because the cosmic-ray background level can be precisely determined from the beam-off data, while the μ^- decay-at-rest background can be determined from fitting to the combined energy distribution. Figures 1 and 2 show the limiting oscillation curve in the Δm^2 vs $\sin^2 2\theta$ two-parameter space.

6. SEARCH FOR $\bar{\nu}_\mu \rightarrow \bar{\nu}_e$ OSCILLATIONS WITH PSR NEUTRINOS

A search for $\bar{\nu}_\mu \rightarrow \bar{\nu}_e$ oscillations at low Δm^2 can also be performed with neutrinos from the PSR. The event signature, an electron from the reaction $\bar{\nu}_e p \rightarrow e^+ n$ followed by the capture of the recoil neutron on hydrogen, is the same as discussed in the previous section, except that there is the additional constraint that the event time must correspond to within a few muon lifetimes with one of the short (270 ns) PSR spills. There is essentially no cosmic-ray, beam-neutron, or beam-neutrino background because the duty factor is so low ($\sim 10^{-4}$). This measurement will be done with the detector in the same location and concurrently with the measurements described in Sections 4 and 5.

The event rate can be estimated by comparison with Section 5.2. As the PSR intensity is $\sim$ 100 μA, the neutrino flux at a distance of $\sim$ 209 m from the PSR beam stop is estimated to be $1.13 \times 10^{11} \nu_\mu/\text{cm}^2$ from pion decay at rest and an equal number of ν_e and $\bar{\nu}_\mu$ from muon decay at rest after 130 days of running at LAMPF ($\sim$ 3000 actual hours) or 8678 Coulombs. Using 11.8×10^{30} free protons, a $\bar{\nu}_e p \rightarrow e^+ n$ cross section[12] of 1.5×10^{-40} cm^2, and an acceptance of 0.233 we can estimate the number of $\bar{\nu}_e p \rightarrow e^+ n$ events per year for maximal neutrino mixing to be

$$(1.13 \times 10^{11})(1.5 \times 10^{-40})(0.233)(11.8 \times 10^{30}) = 46.$$

The 0.233 $\bar{\nu}_e p \rightarrow e^+ n$ acceptance is the product of the the 25-cm fiducial volume cut (66.3%), the electron identification efficiency (90%), the fraction of events with $E_e >$ 37 MeV (45.9%), and the recoil neutron detection efficiency (85.0%). The acceptance does not include the 0.743 veto shield efficiency due to the low PSR duty factor.

Our per-event sensitivity after two years of data collection is 1.1×10^{-2}, which is based on a total of 92 $\bar{\nu}_e p \rightarrow e^+ n$ events for maximal mixing. As there is essentially no background, a 90% confidence level limit of 2.5×10^{-2} for $\bar{\nu}_\mu \rightarrow \bar{\nu}_e$ oscillations can be obtained at the peak sensitivity of $\Delta m^2 = 0.2$ eV^2. For $\sin^2 2\theta = 1$, the 90% confidence level limit on Δm^2 is 3×10^{-2} eV^2. Figure 2 shows the oscillation limit in the Δm^2 vs $\sin^2 2\theta$ two-parameter space. This $\bar{\nu}_\mu \rightarrow \bar{\nu}_e$ oscillation limit would be comparable to the limit obtained in the previous section for low values of Δm^2.

7. SUMMARY OF NEUTRINO OSCILLATIONS WITH LSND

In Sections 4 and 5 we have described two largely independent neutrino oscillation experiments with similar sensitivities that can be performed concurrently. Simply stated, one experiment looks for high-energy ν_e ($80 < E_\nu < 200$ MeV) produced by conversion to ν_e of the ν_μ from the decay-in-flight component of the beam-dump neutrino beam. Simultaneously, another experiment looks for low-energy $\bar{\nu}_e$ produced by conversion of $\bar{\nu}_\mu$ ($40 < E_\nu < 53$ MeV) from the decay-at-rest component of the same beam. In each experiment the incident beam, the event signature, and the backgrounds are different. Consequently, with similar sensitivities as shown in Fig. 2, the two experiments (plus the PSR experiment) provide important redundancy in addition to significantly wider coverage of the $\Delta m^2 - \sin^2 2\theta$ space than all previous accelerator searches for $\nu_\mu \rightarrow \nu_e$ ($\bar{\nu}_\mu \rightarrow \bar{\nu}_e$) oscillations combined.

The experimental techniques involved in accomplishing these searches are not especially demanding. The use of dilute mineral-oil-based liquid scintillator to allow the energetic electrons (positrons) to be detected by Čerenkov radiation and the neutron capture 2.2 MeV gamma ray (from $\bar{\nu}_e p \rightarrow e^+ n$) to be identified by scintillation light is novel. That technique has been (see Appendices D and G) and continues to be explored in test set-ups. It is worth pursuing in its own right for other possible applications and can be empirically validated in a reasonable scale prototype well before large-scale construction begins.

From the experience gained by E645, several members of which are also members of the LSND collaboration, the backgrounds in the LAMPF neutrino area are well understood. It is unlikely that any appreciable surprise will come from that quarter (see Appendix E).

It is possible that appreciable running time with the pulsed proton beam from the PSR may be acquired by LSND, again at the same time as the data-taking described above. This additional attack on the neutrino oscillation problem, described in Section 6, is less sensitive to low mixing strength at large Δm^2 than the high beam intensity experiments in Sections 4 and 5, but it has good Δm^2 sensitivity in the region of large mixing.

In short, neutrino oscillation searches proposed for LSND constitute a powerful program aimed at physics of topical interest and with every likelihood of successful achievement of that aim. Furthermore, the program makes use of and builds on the investment in and the experience gained from the previous neutrino oscillation experiments at LAMPF.

8. OTHER PHYSICS

There are many other physics objectives that can be pursued with the liquid scintillator detector. Searching for $\bar{\nu}_\mu \rightarrow \bar{\nu}_e$ oscillations is equivalent to searching for the lepton number violating decay $\mu^+ \rightarrow e^+\nu_\mu\bar{\nu}_e$. Limits on this decay are directly comparable to limits on neutrino oscillations, so that we should be sensitive to branching ratios as low as 10^{-4}. A branching ratio limit this low would be very interesting theoretically,[17] and would complement present searches for muonium-antimuonium conversion.

The νC $\rightarrow$ ν C* (15.11 MeV γ) neutral-current reaction, one of the only neutrino-nuclear neutral-current reactions that can be easily observed, will be measured to approximately 10% accuracy and will be recognized by the detection of the 15.11 MeV γ emitted by the excited carbon nucleus when it decays to the ground state. Our energy resolution at 15 MeV is $< 10\%$, so that we should observe a peak in the 13.5–16.5 MeV range. A precision measurement of this process is especially important because it allows a calibration of the calculations used in current models of neutrino-nucleus interactions during supernova bursts.[18] The predicted cross section for this reaction[19] as a function of energy is given in Fig. 27. We are able to measure this reaction at two energies, at about 30 MeV using decay-at-rest neutrinos and at about 150 MeV using decay-in-flight neutrinos, and we are able to separate these two classes of events with the 200-MHz LAMPF beam structure as the decay-in-flight events will be synchronous with the proton spill RF structure.

The rare decays $\pi^0 \rightarrow \nu\bar{\nu}$ and $\eta \rightarrow \nu\bar{\nu}$, followed by ν_eC $\rightarrow e^-$N, can be searched to sensitivities of about 10^{-8} and 10^{-4}, respectively, with very little background because the neutrinos from these decays are extremely energetic. These decays are forbidden for massless Weyl neutrinos and can proceed only if neutrino states of both chiralities exist or if lepton number is not conserved.[20] The current best limits for these decays are $\Gamma(\pi^0 \rightarrow \nu_e\bar{\nu}_e)/\Gamma(\pi^0 \rightarrow \text{all}) < 5.0 \times 10^{-7}$ and $\Gamma(\eta \rightarrow \nu_e\bar{\nu}_e)/\Gamma(\eta \rightarrow \text{all}) < 1.0 \times 10^{-3}$ from the LAMPF E645 experiment.[21] The expected branching ratios of these decays in the standard model for reasonable neutrino masses are much lower than our sensitivities; however, branching ratios as large as the current limit are possible in various phenomenological models.[20]

We shall also measure the ν_eC and ν_μC charged-current scattering cross sections and the νe elastic scattering cross section to approximately 10–15% accuracy. These measurements would test present theories of neutrino-nucleus scattering and provide an estimate of $\sin^2\theta_W$, the fundamental parameter of the standard model of electroweak interactions. The electron angular distribution in the νe elastic scattering process is strongly peaked

in the neutrino direction, while it is slightly peaked in the backward direction for the charged-current reaction. The $\nu_e C \rightarrow e^- N$ charged-current interaction is dominated by ^{12}C, as the fraction of ^{13}C nuclei is only about 1.1% of the total. Nevertheless, we shall be able to measure the ^{13}C component separately due to the larger ν_e $^{13}C \rightarrow e^- N$ cross section and the higher electron energy.

Finally, we will obtain a large sample of neutrino-proton elastic-scattering events, where the neutrinos are from pion decay in flight. The cross section for $\nu p \rightarrow \nu p$ is proportional to $G_A^2 + F_1^2 + Q^2/4/m_p^2 F_2^2$ at low Q^2. The term involving G_A is dominant, and a measurement of the cross section at low Q^2 affords a method of measuring G_A directly. The principal component of G_A is isovector, which is known from neutron decay at low Q^2. Any additional contribution (an isoscalar term, for example) would affect the total cross section. We expect to make a preliminary search for recoil protons from neutrino-proton elastic scattering in the 20- to 60-MeV range. These protons will be coherent with the beam spill from LAMPF in contrast to proton recoil from cosmic-ray or beam neutrons. A preliminary estimate of this background gives a signal to noise as evidenced by the 200-MHz RF time structure of about one. The number of neutrino-proton events expected per year is given in Appendix A.

9. SCHEDULE AND COST

The schedule for the construction portion of the experiment is divided into two phases, a development phase and a construction phase proper. As is discussed in Section 1, this experimental design relies on techniques that were developed for the large Čerenkov detector (LCD) proposal and, hence, represents a direct continuation of the development of the neutrino physics program at LAMPF. Separate from the conceptual issues that are involved in developing detection techniques for low-energy neutrinos, there has been a development process in collaboration with Burle Industries for a state-of-the-art phototube that is important in the detection methods for this experiment as well as LCD. This tube has proceeded through a phase of prototype construction and is now in the process of limited production to establish performance criteria for use on specifications for quantities sufficient for the complete experiment (LSND) as well as LCD. In parallel with this effort, Philips Corporation (Amperex) has developed a similar tube, and evaluation of this tube will also occur. This evaluation process is expected to be complete by May 1, 1990. In this period (to May 1990), it is expected that the background evaluation for LSND will be complete, reviews by DOE will also be complete, and construction can begin.

In Fig. 28 is shown a work breakdown structure for the construction planning process. In Fig. 29 is shown a PERT chart for the construction process with a starting date of 5/11/90. Completion of the construction is expected by 5/14/92, when acquisition of beam data will begin. The critical path for the project is driven by the delivery of tubes from the vendor; this delivery schedule represents less than half of the capability in the early stages of production, and is deemed reasonable. The encapsulation and installation are expected to proceed in parallel with tube delivery, and the boxes labeled 'lag' represent the extra time needed to complete these operations after the preceding operation is complete.

The liquid and tubes are enclosed in a containment vessel shown in Fig. 3: this vessel represents a major activity in the work breakdown structure. It is not a critical path item provided that detailed design can start by 6/90. In tank construction, a hydraulic test is scheduled, as well as an engineering test of a portion of the system using 50 tubes acquired in the development process. After this system engineering test is complete, installation of the full complement of tubes can proceed. It is anticipated that it will prove cost effective to build custom electronics for data acquisition in the VME hardware format. The system for LSND is relatively small, but it is the goal of this activity to make the electronics

compatible with possible use in LCD and for other projects that may use large physical size and precise timing phototubes as detection elements.

In Tables 6 and 7 are shown the cost estimate and cost schedule for construction of LSND. They assume that all channels will be connected to similar electronic channels and the cost is estimated accordingly. The phototube cost is based on informal contacts with vendors and is believed to be appropriate; this single cost dominates the cost of the detector. The cost for the containment vessel is also derived from preliminary cost estimates from vendors; the amount included is in the center of the distribution of estimates. The cost of the electronics is based on actual costs for similar components constructed locally.

All of the institutions will share in the development and construction of LSND. The main areas of responsibility are given below:

UC Irvine: Data acquisition electronics, Monte Carlo.

UC Riverside: Data acquisition electronics, software.

CEBAF: Veto shield, software.

Los Alamos: Tank construction, front-end electronics, calibration, project coordination.

Louisiana State: Calibration, software.

New Mexico: Liquid scintillator R&D and plumbing, electronics.

Pennsylvania: Front-end electronics.

Temple: PMT procurement, testing, and encapsulation.

REFERENCES

1. V. Zacek et al., Phys. Lett. 164B, 193 (1985).
2. L. A. Ahrens et al., Phys. Rev. D31, 2732 (1985).
3. L. S. Durkin et al., Phys. Rev. Lett. 61, 1811 (1988); James J. Napolitano et al., NIM A274, 152 (1989).
4. T. Dombeck et al., Phys. Lett. B 194, 591 (1987).
5. LCD Proposal, Los Alamos National Laboratory report LA-11300-P (1988).
6. SNO Proposal, SNO-87-12 (1987).
7. I. B. Berlman, *Handbook of Fluorescence Spectra of Aromatic Molecules*, Academic Press (1971).
8. W. Frati, Using Minuit to Reconstruct Vertex and Direction of Low Q Events (1987).
9. B. Fujikawa, private communication.
10. T. W. Donnelly, Phys. Lett. 43B, 93 (1973).
11. R. L. Burman, M. E. Potter, and E. S. Smith, Los Alamos National Laboratory document LA-UR-89-3346 (1989).
12. P. Vogel, Phys. Rev. D29, 1918 (1984); T. K. Gaisser and J. S. O'Connell, Phys. Rev. D34, 822 (1986); Felix Boehm and Peter Vogel. *Physics of Massive Neutrinos*, Cambridge University Press (1987).
13. A. Fazely, private communication.
14. G. Garvey, E645 Technical Note (1982).
15. R. McKeown, E645 Technical Note (1982).
16. F. Boehm and R. Steinberg, private communication.
17. Peter Herczeg and Rabindra Mohapatra, to be published; reported in Peter Herczeg, Proceedings of the Vancouver Rare Decay Symposium (1988).
18. W. C. Haxton, private communication.
19. T. W. Donnelly and R. D. Peccei, Phys. Rep. 50, 1 (1979).
20. Cyrus M. Hoffman, Phys. Lett. 208B, 149 (1988); Peter Herczeg, Proceedings of the Paris Workshop on Production and Decay of Light Mesons, World Scientific, ed. Patrik Fleury, 16 (1988); P. Herczeg and C. M. Hoffman, Phys. Lett. 100B, 347 (1981); 102B, 445 (E) (1981).
21. A. Fazely, private communication.
22. J. S. O'Connell, Proceedings of the Los Alamos Neutrino Workshop, 37 (1981).

Table 1. Properties of Liquid Scintillator

n	ρ	Composition	Decay Time	L	Light Output
1.47	0.858 g/cm^3	CH_2	4 ns	10 m	4% of anthracene

Table 2. Resolutions as a function of energy for 28% PMT coverage (850 phototubes).

Energy and Particle Type	$\delta E/E$ ($\pm$1%)	δr ($\pm$1 cm)	$\delta\theta$ ($\pm$2°)
200 MeV e^-	2.1%	9.6	8.1
150 MeV e^-	2.1%	10.1	12.0
100 MeV e^-	2.8%	8.4	10.2
55 MeV e^-	3.5%	8.7	13.5
45 MeV e^-	3.9%	9.3	14.2
35 MeV e^-	4.2%	8.5	15.4
25 MeV e^-	5.2%	9.1	20.7
15 MeV e^-	6.8%	13.2	38.0

Table 3. Resolutions as a function of energy for 14% PMT coverage (425 phototubes).

Energy and Particle Type	$\delta E/E$ ($\pm$1%)	δr ($\pm$1 cm)	$\delta\theta$ ($\pm$2°)
55 MeV e^-	4.9%	21.3	21.5
45 MeV e^-	5.5%	20.7	25.2
35 MeV e^-	6.2%	18.1	26.8
25 MeV e^-	7.4%	17.3	36.2
15 MeV e^-	9.6%	16.5	43.9

Table 4. Resolutions as a function of energy for 28% PMT (850 phototubes) coverage and pure mineral oil.

Energy and Particle Type	$\delta E/E$ ($\pm 1\%$)	δr (± 1 cm)	$\delta\theta$ ($\pm 1°$)
55 MeV e^-	7.5%	28.8	11.4
45 MeV e^-	5.6%	23.0	11.4
35 MeV e^-	7.9%	20.5	12.1
25 MeV e^-	8.8%	17.6	11.8
15 MeV e^-	11.6%	13.8	13.9

Table 5. Contributions to the error in the determination of the proton spill time, as relates to the 200-MHz beam microstructure. The total time error is 0.43 ns.

Contribution (rms)	δt (ns)
Location of p Interaction	0.07
Location of π Decay	0.18
Event Position Error	0.28
Event PMT Time Error	0.25
Time Spread of Spill at A6	0.10
Total RMS Time Error	0.43

Table 6A. LSND Cost Estimate I

Photomultiplier Tubes
Assumes use of preproduction tubes (50) and a total of 884 spigots
Active veto external to tank also included with 200 tubes reused from E645
Number of 10-in.tubes in Production Mode 850

Title	Unit Cost	#	Total	Cntgcy	Total with cntgcy
Tube Acquisition					
Burle 10-in.PMT FOB Lancaster	$1,150.00				
Burle 10-in.PMT FOB Lancaster		850	$977,500.00	20%	$1,173,000.00
Shipping cost to Los Alamos	$15.00				
Shipping cost to Los Alamos		850	$12,750.00	20%	$15,300.00
Testing fixtures for production	$75.00				
Testing fixtures for production		10	$750.00	20%	$900.00
Testing labor (1 hours / tube)	$40.00				
Testing labor (1 hours / tube)		850	$34,000.00	20%	$40,800.00
Encapsulation					
Tooling for encapsulation vessel	$12,000.00				
Tooling for encapsulation vessel		1	$12,000.00	30%	$15,600.00
Encapsulation container	$50.00				
Encapsulation container		1000	$50,000.00	30%	$65,000.00
PMT base	$40.00				
PMT base		1000	$40,000.00	20%	$48,000.00
Encapsulation labor (one hour per tube)	$40.00				
Encapsulation labor (one hour per tube)		1000	$40,000.00	20%	$48,000.00
Potting material	$25.00				
Potting material		209	$5,225.00	30%	$6,792.50
Active veto tube system tube cost	$180.00				
Active veto tube system tube cost		209	$37,620.00	20%	$45,144.00
Active veto encapsulation vessel	$40.00				
Active veto encapsulation vessel		209	$8,360.00	30%	$10,868.00
Active veto base	$75.00				
Active veto base		209	$15,675.00	30%	$20,377.50
Light baffle	$25.00				
Light baffle		209	$5,225.00	30%	$6,792.50

Table 6B. LSND Cost Estimate II

Installation					
Installation labor	$40.00				
Installation labor		900	$36,000.00	20%	$43,200.00
Input crate hardware					
Input crate hardware	$2,257.60				
Input crate hardware		6	$13,545.60	5%	$14,222.88
CPU-30 monoboard processor/ ethernet	$3,000.00				
CPU-30 monoboard processor/ ethernet		6	$18,000.00	10%	$19,800.00
S pmt and trigger card	$2,000.00				
S pmt and trigger card		6	$12,000.00	20%	$14,400.00
Dual port memory/ crate link	$2,200.00				
Dual port memory/ crate link		6	$13,200.00	10%	$14,520.00
MSM-84 mass storage module	$2,500.00				
MSM-84 mass storage module		6	$15,000.00	10%	$16,500.00
Input cards	$4,789.00				
Input cards		96	$459,744.00	20%	$551,692.00
High voltage power supplies	$2,400.00				
High voltage power supplies		6	$14,400.00	20%	$17,280.00
Master crate hardware					
Master crate hardware	$2,257.60				
Master crate hardware		1	$2,257.60	10%	$2,483.36
CPU-30 monoboard processor/ ethernet	$3,000.00				
CPU-30 monoboard processor/ ethernet		1	$3,000.00	20%	$3,600.00
Dual ported memory / crate link	$2,200.00				
Dual ported memory / crate link		1	$2,200.00	20%	$2,640.00
MSM-84 mass storage module	$2,500.00				
MSM-84 mass storage module		1	$2,500.00	20%	$3,000.00
Calibration system	$10,000.00				
Calibration system		1	$10,000.00	30%	$13,000.00
Experiment control					
Diskless workstation	$10,100.00				
Diskless workstation		1	$10,100.00	10%	$11,110.00
Master collator	$33,160.00				
Master collator		1	$33,160.00	10%	$36,476.00
Host system	$131,500.00				
Host system		1	$131,500.00	10%	$144,650.00

Table 6C. LSND Cost Estimate III

Liquid containment vessel					
Steel tank	$240,000.00				
Steel tank		1	$240,000.00	20%	$288,000.00
Cable bulkheads on tank	$675.00				
Cable bulkheads on tank		20	$13,500.00	30%	$17,550.00
Cable bulkheads on tank ends	$1,000.00				
Cable bulkheads on tank ends		2	$2,000.00	30%	$2,600.00
Racks for local electronics	$860.00				
Racks for local electronics		3	$2,580.00	5%	$2,709.00
Local electronics support (blue plug)	$3,000.00				
Local electronics support (blue plug)		1	$3,000.00	20%	$3,600.00
Cable plant					
Ring to exterior	$4.50				
Ring to exterior		684	$3,078.00	20%	$3,693.60
End to exterior	$5.00				
End to exterior		200	$1,000.00	20%	$1,200.00
Veto to exterior	$9.00				
Veto to exterior		209	$1,881.00	20%	$2,257.20
Bulkhead to local electronics	$5.70				
Bulkhead to local electronics		2186	$12,460.20	20%	$14,952.24
Cable connection to counting house	$150.00				
Cable connection to counting house		1	$150.00	30%	$195.00
Liquid handling					
Hydraulic system	$10,000.00				
Hydraulic system		1	$10,000.00	30%	$13,000.00
Liquid	$750.00				
Liquid		200	$150,000.00	10%	$165,000.00
External veto refurbish					
Remove cart & reattach	$50,000.00				
Remove cart & reattach		1	$50,000.00	30%	$65,000.00
Replacement bases	$50.00				
Replacement bases		246	$12,300.00	30%	$15,990.00
			$2,517,661.40		$3,000,896.58

Table 7. LSND Cost Schedule

		Total		$2,517,661.40	$0.00	$3,000,896.58	$3,538,557.93
		Total FY90		$12,375.00		$16,050.00	$16,050.00
F Y	Date	Title	#	Total	Cntgcy	Total with cntgcy	0%
FY90	8/31/90	Testing Fixtures for Production	5	$375.00	20%	$450.00	$450.00
FY90	9/1/90	Tooling for Encapsulation Vessel	1	$12,000.00	30%	$15,600.00	$15,600.00
		Total FY91		$1,767,126.40		$2,128,520.58	$2,271,495.81
F Y	Date	Title	#	Total	Cntgcy	Total with cntgcy	6%
FY91	1/2/91	Burle 10" PMT FOB Lancaster	550	$632,500.00	20%	$759,000.00	$804,540.00
FY91	12/31/90	Shipping Cost to Los Alamos	550	$8,250.00	20%	$9,900.00	$10,494.00
FY91	12/31/90	Testing Fixtures for Production	5	$375.00	20%	$450.00	$477.00
FY91	12/31/90	Testing labor (1 hours / tube)	550	$22,000.00	20%	$26,400.00	$27,984.00
FY91	12/31/90	Encapsulation Container	1000	$50,000.00	30%	$65,000.00	$68,900.00
FY91	12/31/90	PMT Base	1000	$40,000.00	20%	$48,000.00	$50,880.00
FY91	12/31/90	Encapsulation labor (one hour per tube)	550	$22,000.00	20%	$26,400.00	$27,984.00
FY91	3/31/91	Potting Material	209	$5,225.00	30%	$6,792.50	$7,200.05
FY91	3/31/91	Active veto tube system tube cost	209	$37,620.00	20%	$45,144.00	$47,852.64
FY91	3/31/91	Active veto encapsulation vessel	209	$8,360.00	30%	$10,868.00	$11,520.08
FY91	3/31/91	Active veto base	209	$15,675.00	30%	$20,377.50	$21,600.15
FY91	3/31/91	Light Baffle	209	$5,225.00	30%	$6,792.50	$7,200.05
FY91	6/30/91	Installation Labor	300	$12,000.00	20%	$14,400.00	$15,264.00
FY91	12/31/90	Input crate hardware	6	$13,545.60	5%	$14,222.88	$15,076.25
FY91	12/31/90	CPU-30 Monoboard Processor/ Etherne	6	$18,000.00	10%	$19,800.00	$20,988.00
FY91	12/31/90	S pmt and trigger Card	6	$12,000.00	20%	$14,400.00	$15,264.00
FY91	12/31/90	Dual port memory/ Crate link	6	$13,200.00	10%	$14,520.00	$15,391.20
FY91	12/31/90	MSM-84 Mass Storage Module	6	$15,000.00	10%	$16,500.00	$17,490.00
FY91	12/31/90	Input Cards	96	$459,744.00	20%	$551,692.80	$584,794.37
FY91	12/31/90	High Voltage Power Supplies	6	$14,400.00	20%	$17,280.00	$33,580.80
FY91	6/30/91	Master crate hardware	1	$2,257.60	10%	$2,483.36	$2,632.36
FY91	6/30/91	CPU-30 Monoboard Processor/ Etherne	1	$3,000.00	20%	$3,600.00	$3,816.00
FY91	6/30/91	Dual ported memory / Crate link	1	$2,200.00	20%	$2,640.00	$2,798.40
FY91	6/30/91	MSM-84 Mass Storage Module	1	$2,500.00	20%	$3,000.00	$3,180.00
FY91	12/31/90	Diskless Workstation	1	$10,100.00	10%	$11,110.00	$11,776.60
FY91	12/1/90	Steel Tank	1	$240,000.00	20%	$288,000.00	$305,280.00
FY91	3/1/91	Cable bulkheads on Tank	20	$13,500.00	30%	$17,550.00	$18,603.00
FY91	3/1/91	Cable bulkheads on tank ends	2	$2,000.00	30%	$2,600.00	$2,756.00
FY91	3/1/91	Racks for local electronics	3	$2,580.00	5%	$2,709.00	$2,871.54
FY91	3/1/91	Local electronics support (Blue Plug)	1	$3,000.00	20%	$3,600.00	$3,816.00
FY91	6/30/91	Ring to exterior	684	$3,078.00	20%	$3,693.60	$3,915.22
FY91	6/30/91	End to Exterior	200	$1,000.00	20%	$1,200.00	$1,272.00
FY91	6/30/91	Veto to exterior	209	$1,881.00	20%	$2,257.20	$2,392.63
FY91	6/30/91	Bulkhead to local electronics	2186	$12,460.20	20%	$14,952.24	$15,849.37
FY91	6/30/91	Cable connection to Counting House	1	$150.00	30%	$195.00	$206.70
FY91	12/1/90	Remove Cart & reattach	1	$50,000.00	30%	$65,000.00	$68,900.00
FY91	12/1/90	Replacement bases	246	$12,300.00	30%	$15,990.00	$16,949.40
		Total FY92		$606,660.00		$711,676.00	$1,080,325.12
F Y	Date	Title	#	Total	Cntgcy	Total with cntgcy	12%
FY92	12/31/91	Burle 10" PMT FOB Lancaster	300	$345,000.00	20%	$414,000.00	$695,520.00
FY92	12/31/91	Shipping Cost to Los Alamos	300	$4,500.00	20%	$5,400.00	$9,072.00
FY92	12/31/91	Testing labor (1 hours / tube)	300	$12,000.00	20%	$14,400.00	$24,192.00
FY92	12/31/91	Encapsulation labor (one hour per tube)	450	$18,000.00	20%	$21,600.00	$40,320.00
FY92	12/31/91	Installation Labor	600	$24,000.00	20%	$28,800.00	$56,448.00
FY92	2/1/92	Calibration System	1	$10,000.00	30%	$13,000.00	$14,560.00
FY92	12/31/91	Master Collator	1	$33,160.00	10%	$36,476.00	$40,853.12
FY92	12/1/91	Hydraulic System	1	$10,000.00	30%	$13,000.00	$14,560.00
FY92	12/1/91	Liquid	200	$150,000.00	10%	$165,000.00	$184,800.00
		Total FY93		$131,500.00		$144,650.00	$170,687.00
F Y	Date	Title	#	Total	Cntgcy	Total with cntgcy	18%
FY93	12/31/92	Host System	1	$131,500.00	10%	$144,650.00	$170,687.00

Fig. 1. The present $\bar{\nu}_\mu \rightarrow \bar{\nu}_e$ oscillation limits from reactor (Gosgen), BNL (E734), and LAMPF (E645,E764) experiments expressed in terms of the Δm^2 vs $\sin^2 2\theta$ two-parameter space. The oscillation probability is expressed as $P_{\bar{\nu}_\mu \rightarrow \bar{\nu}_e} = \sin^2 2\theta \sin^2[1.27\Delta m^2 L/E_\nu]$, where θ is the mixing angle, $\Delta m^2 = m^2_{\bar{\nu}_\mu} - m^2_{\bar{\nu}_e}$ in eV^2, L is the neutrino propagation distance in m, and E_ν is the neutrino energy in MeV. Also shown is the limiting curve expected from this proposal with neutrinos from μ^+ decay.

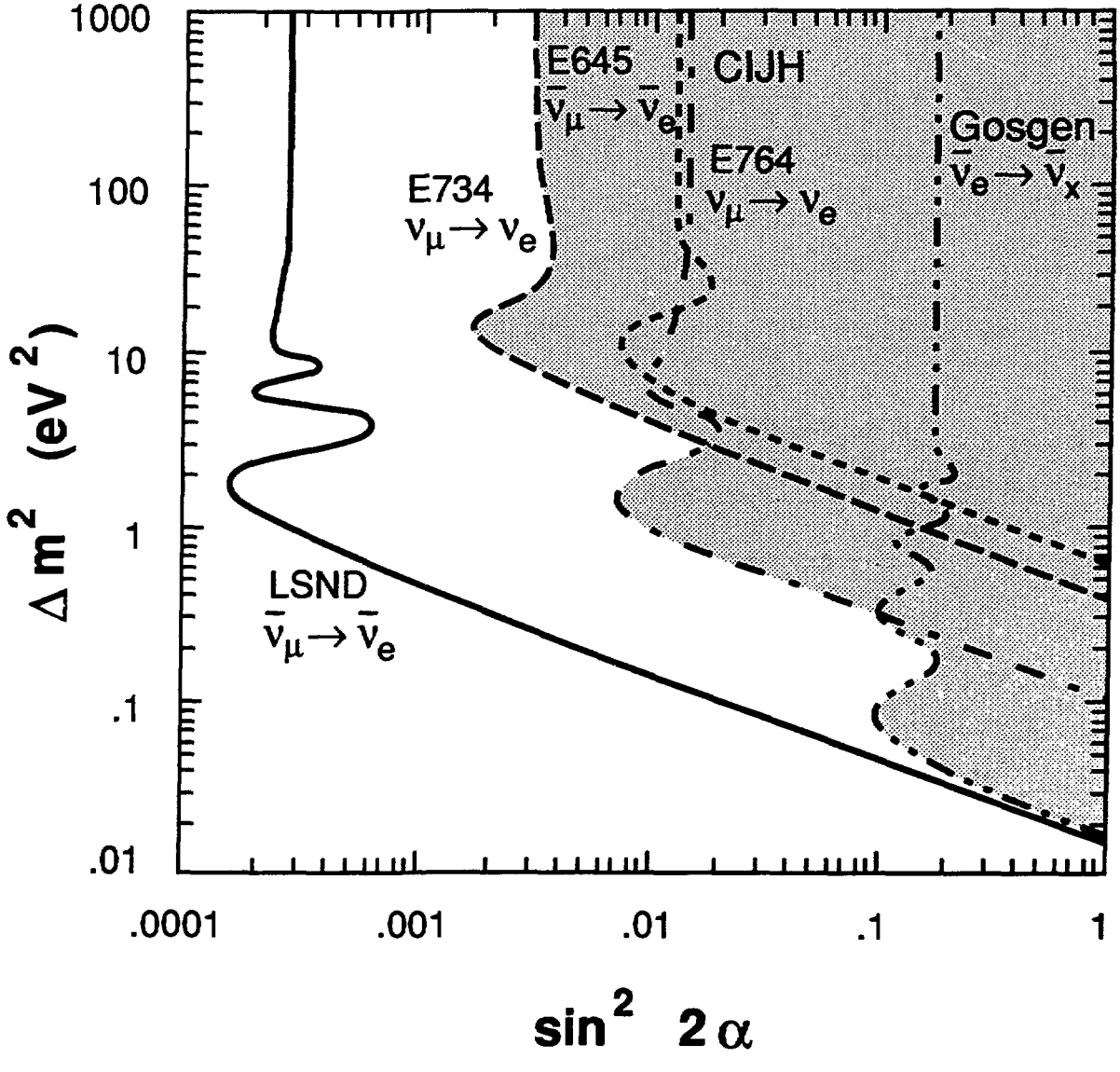

Fig. 2. The expected $\nu_\mu \rightarrow \nu_e$ and $\bar{\nu}_\mu \rightarrow \bar{\nu}_e$ oscillation limits from this proposal, expressed in terms of the Δm^2 vs $\sin^2 2\theta$ two-parameter space.

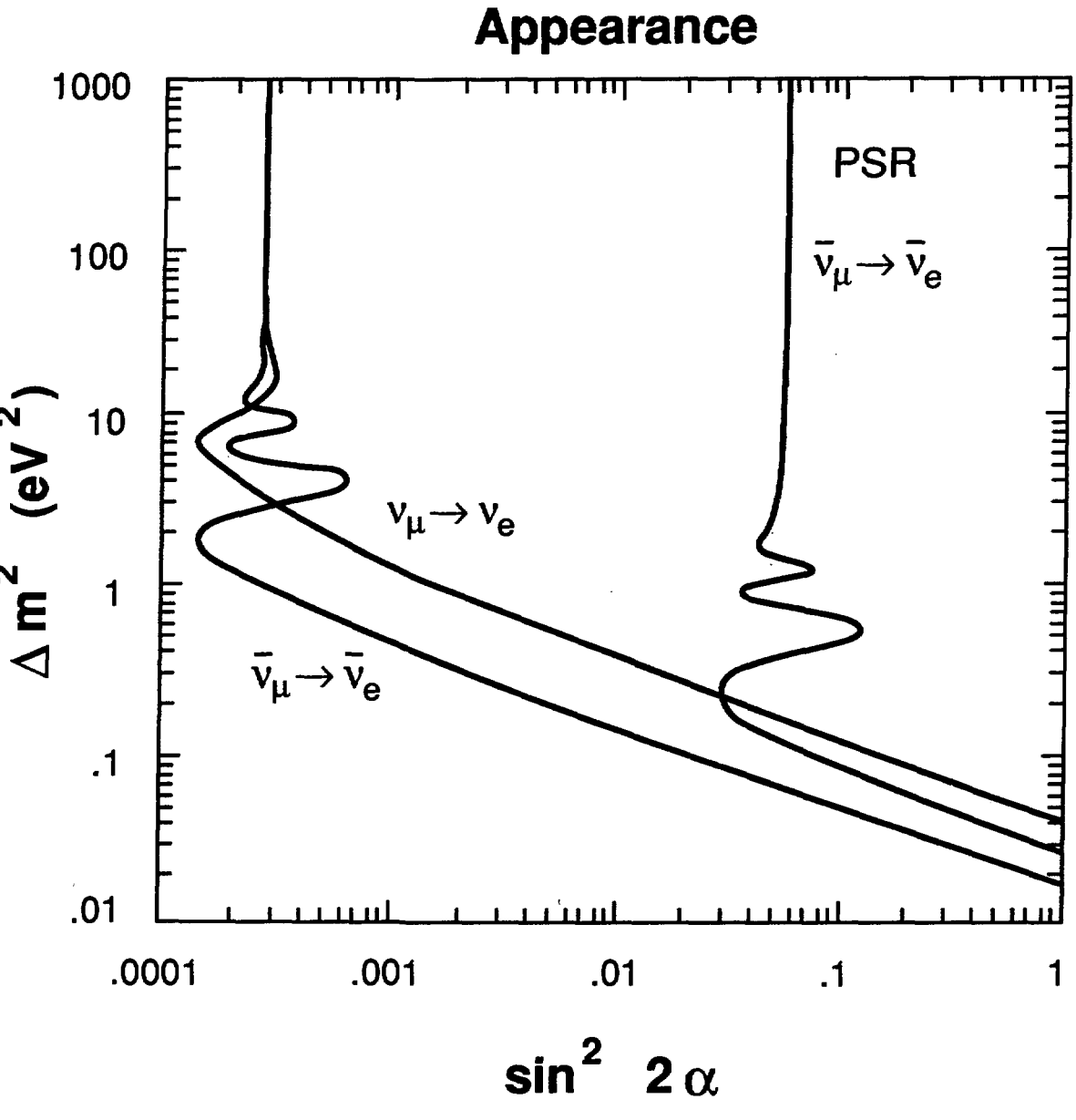

Fig. 3. A schematic view of the detector, consisting of a 6 m diameter by 9 m long cylindrical tank of dilute liquid scintillator with 850 10-in. photomultiplier tubes covering about 28% of the surface area of the tank.

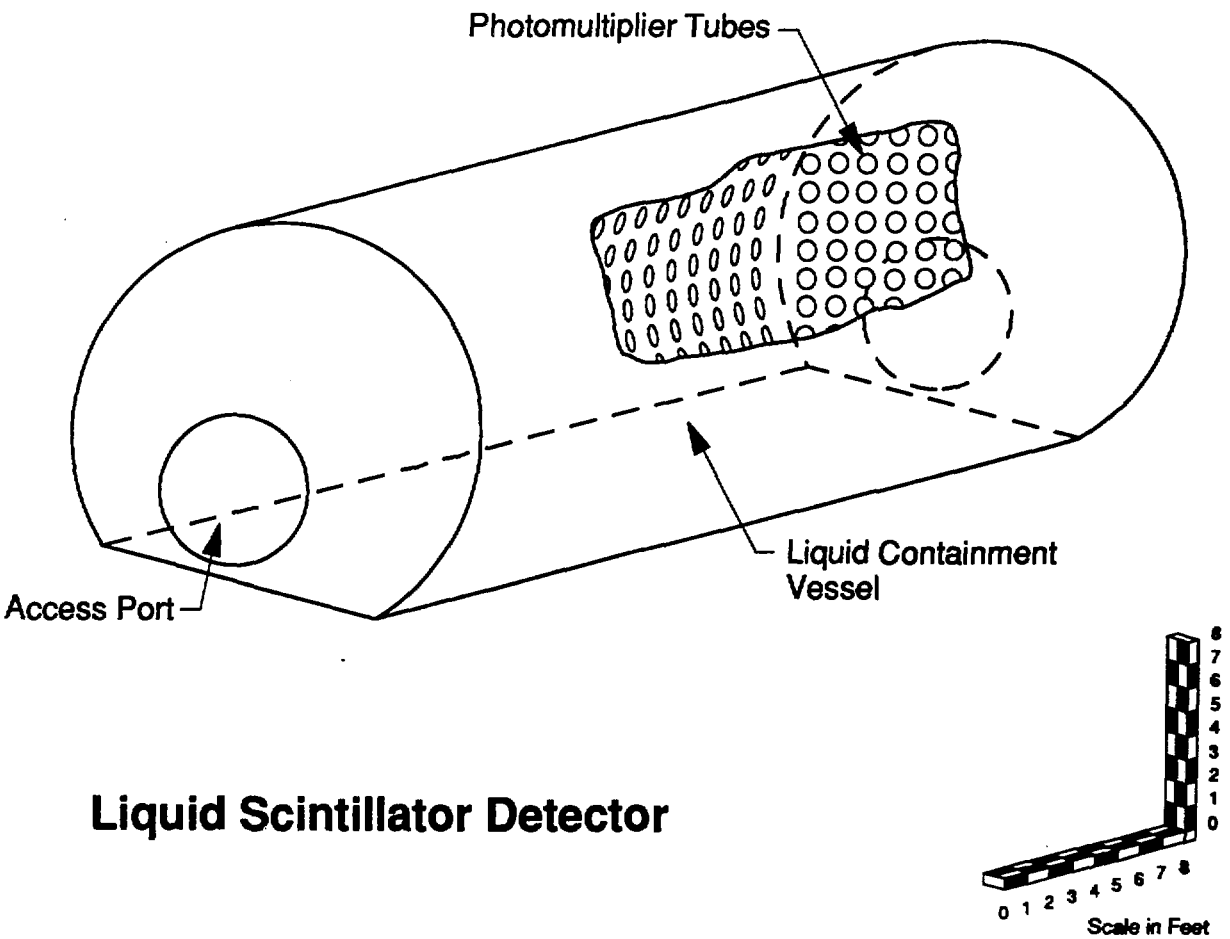

Fig. 4. A layout of the A6 beam line and detector area. The detector is approximately 27 m from the beam dump and at an angle of 17° to the proton beam direction.

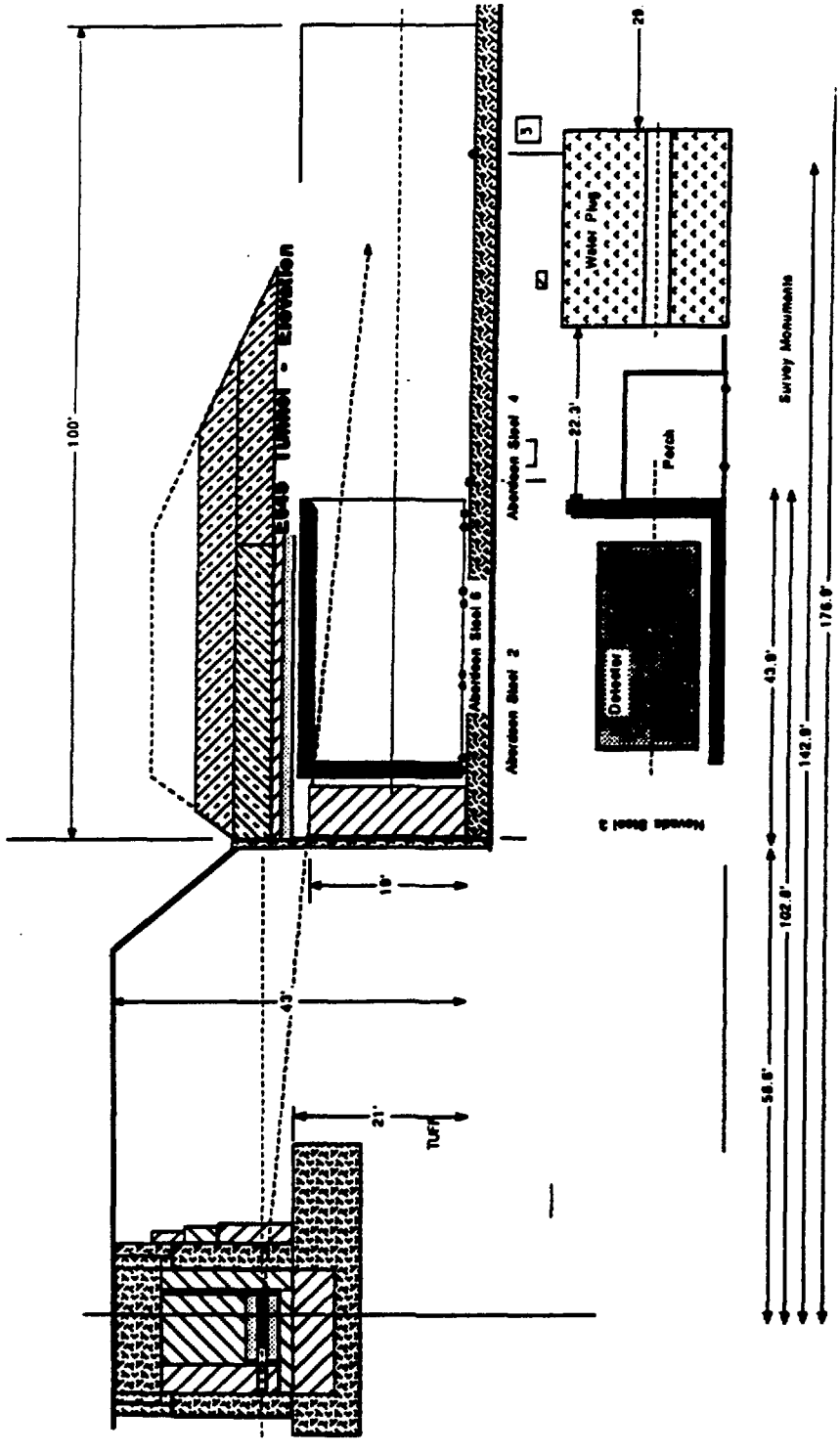

Fig. 5. Cross-sectional drawing of the 10-in. Burle C83061E photomultiplier tube that we plan to use in the experiment. The tube has excellent timing resolution, 2.3-ns FWHM for single photons and full face illumination, single photoelectron separation, and noise rates < 10 kHz.

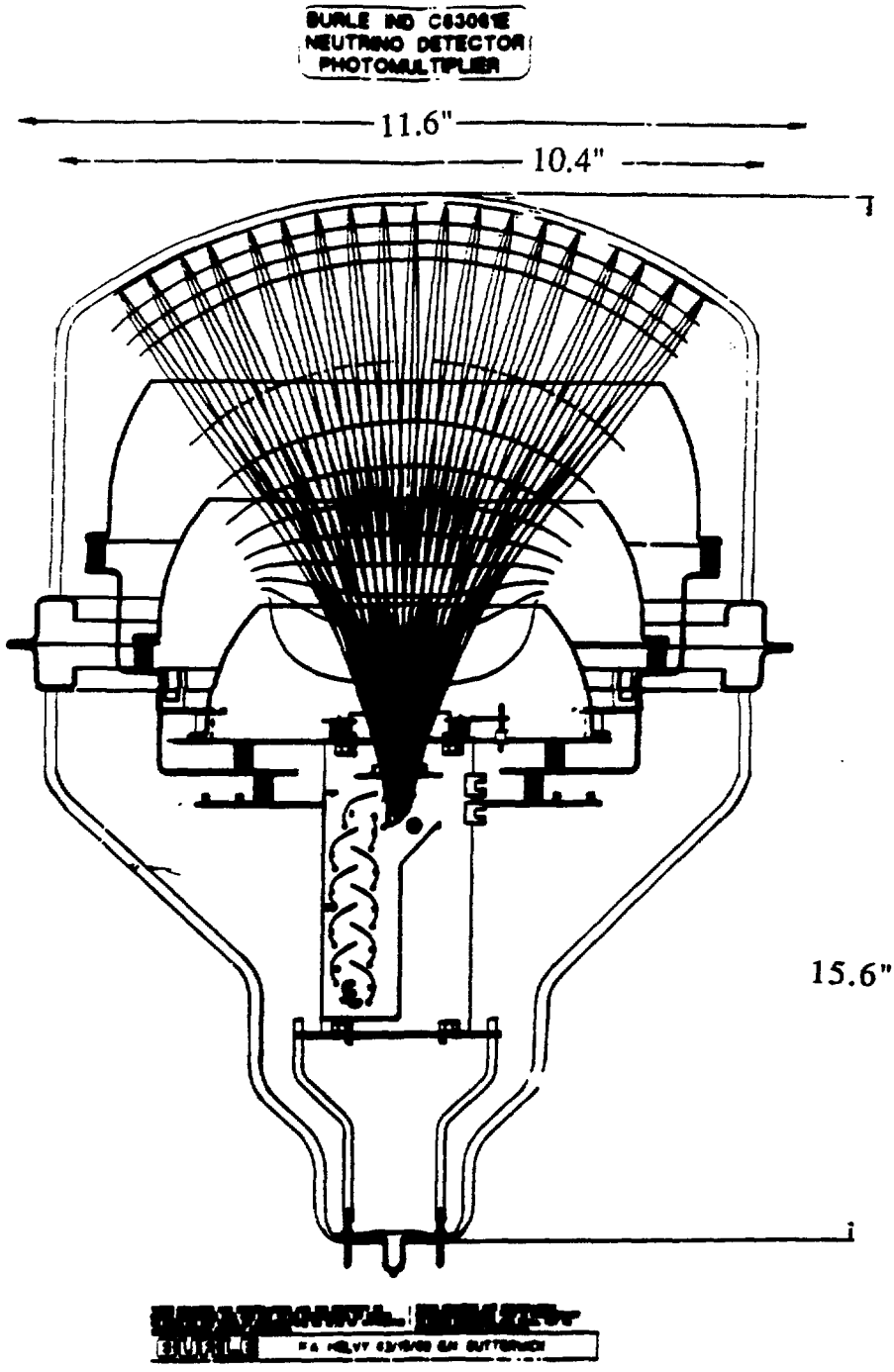

Fig. 6a. Dark pulse plateau curves for the Burle C83061E photomultiplier tube. The noise rate is < 10 kHz.

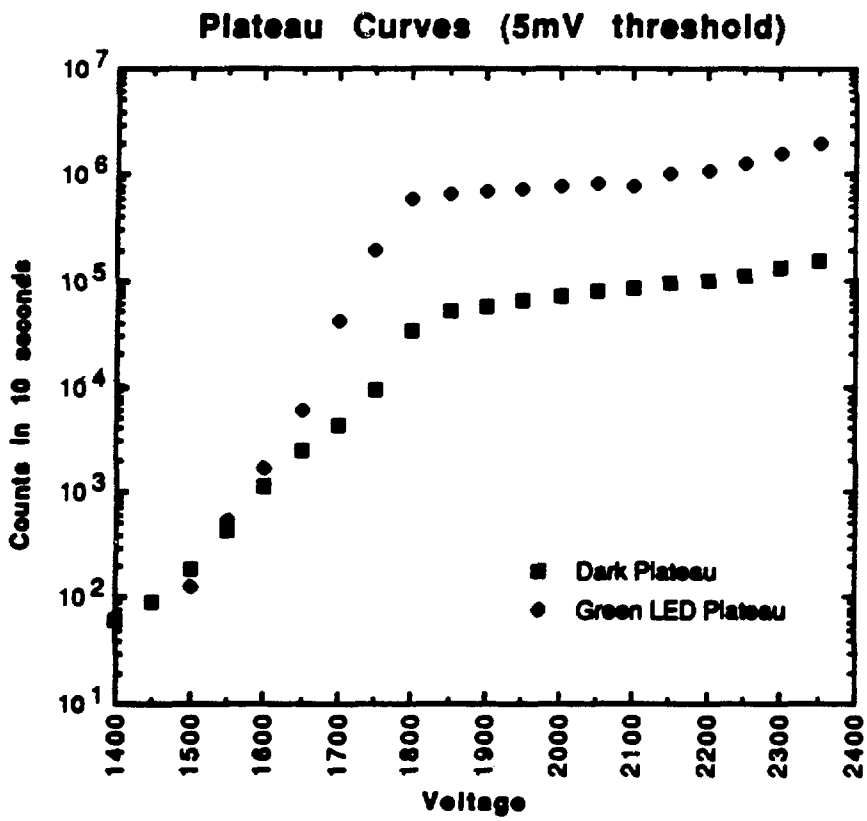

Fig. 6b. The ADC test setup, and the charge spectrum for full photocathode illumination at the single photoelectron level by a green light emitting diode. The single photoelectron peak is clearly separated from the double and triple photoelectron peaks.

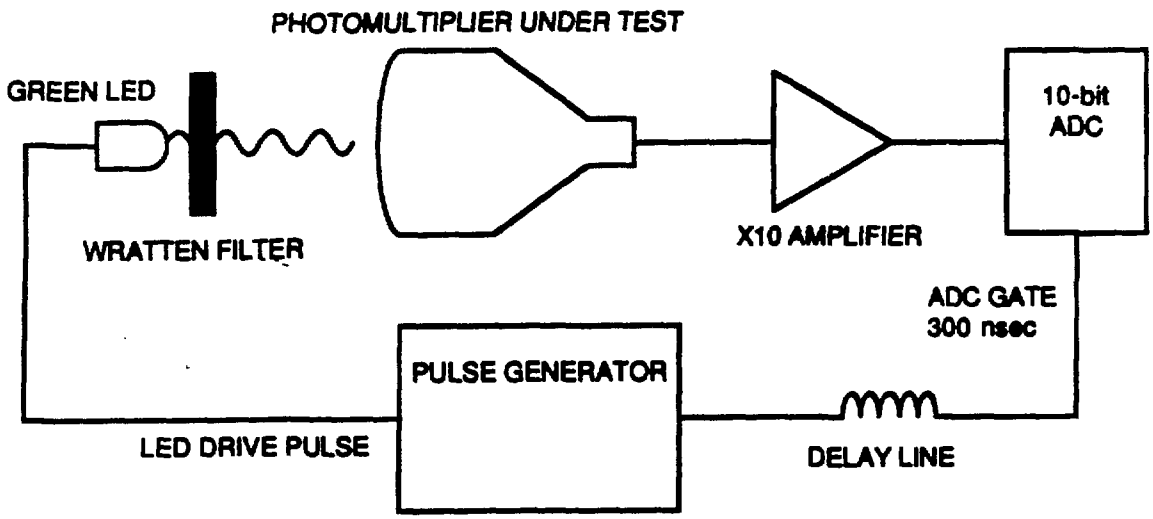

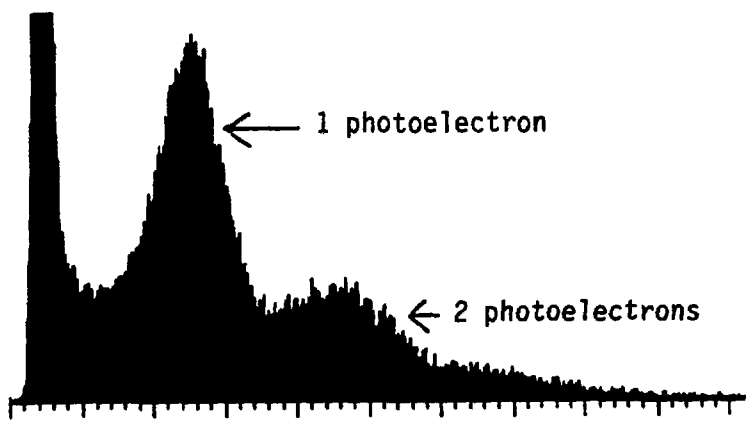

Fig. 6c. The Čerenkov light source and TDC test setup, and the time spectrum with starts and stops provided by two C83061E photomultiplier tubes. The FWHM time resolution corresponds to 2.3 ns per photomultiplier tube.

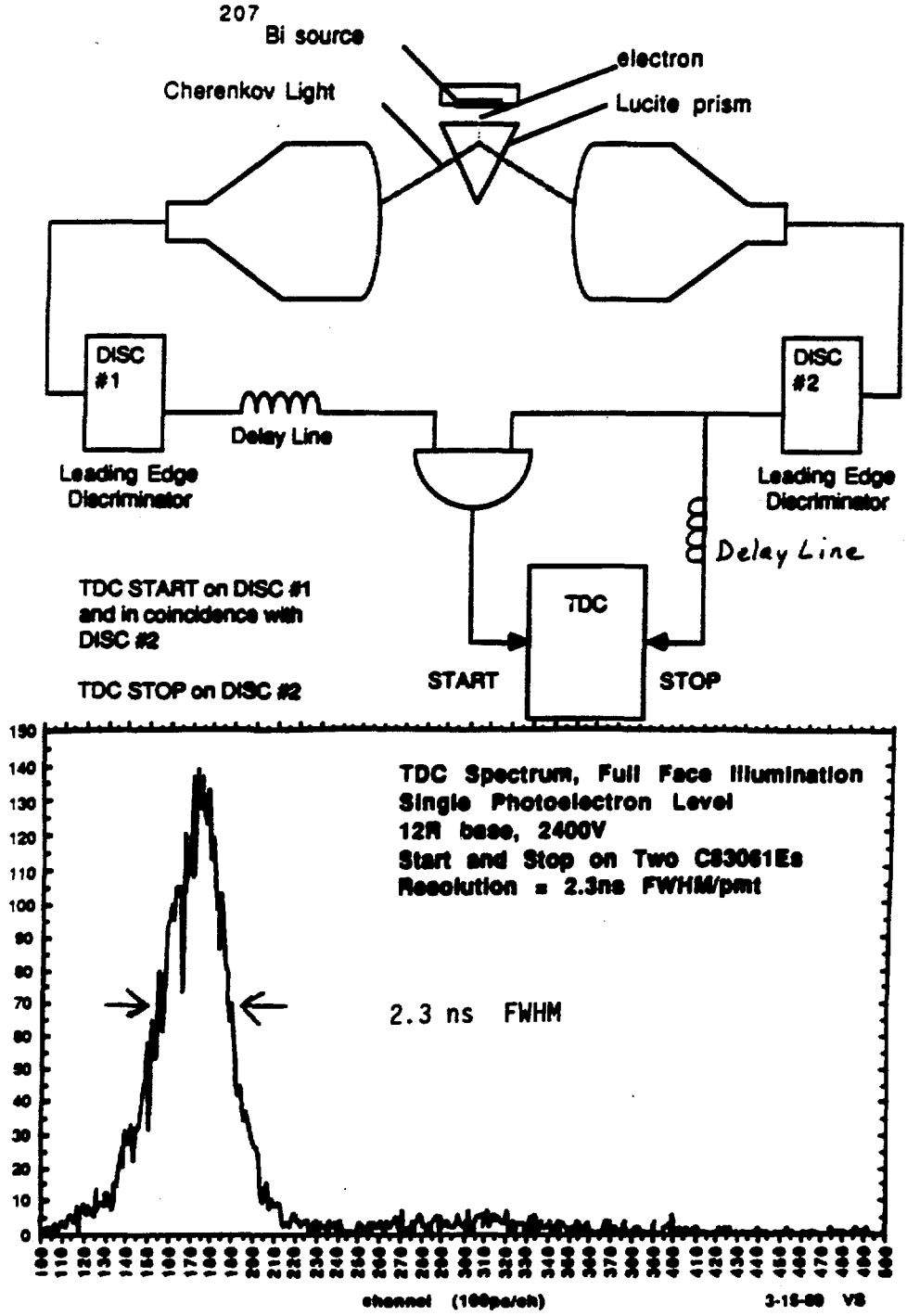

Fig. 7. A schematic drawing of the phototube encapsulation in a container. The container is impervious to both liquid scintillator and water.

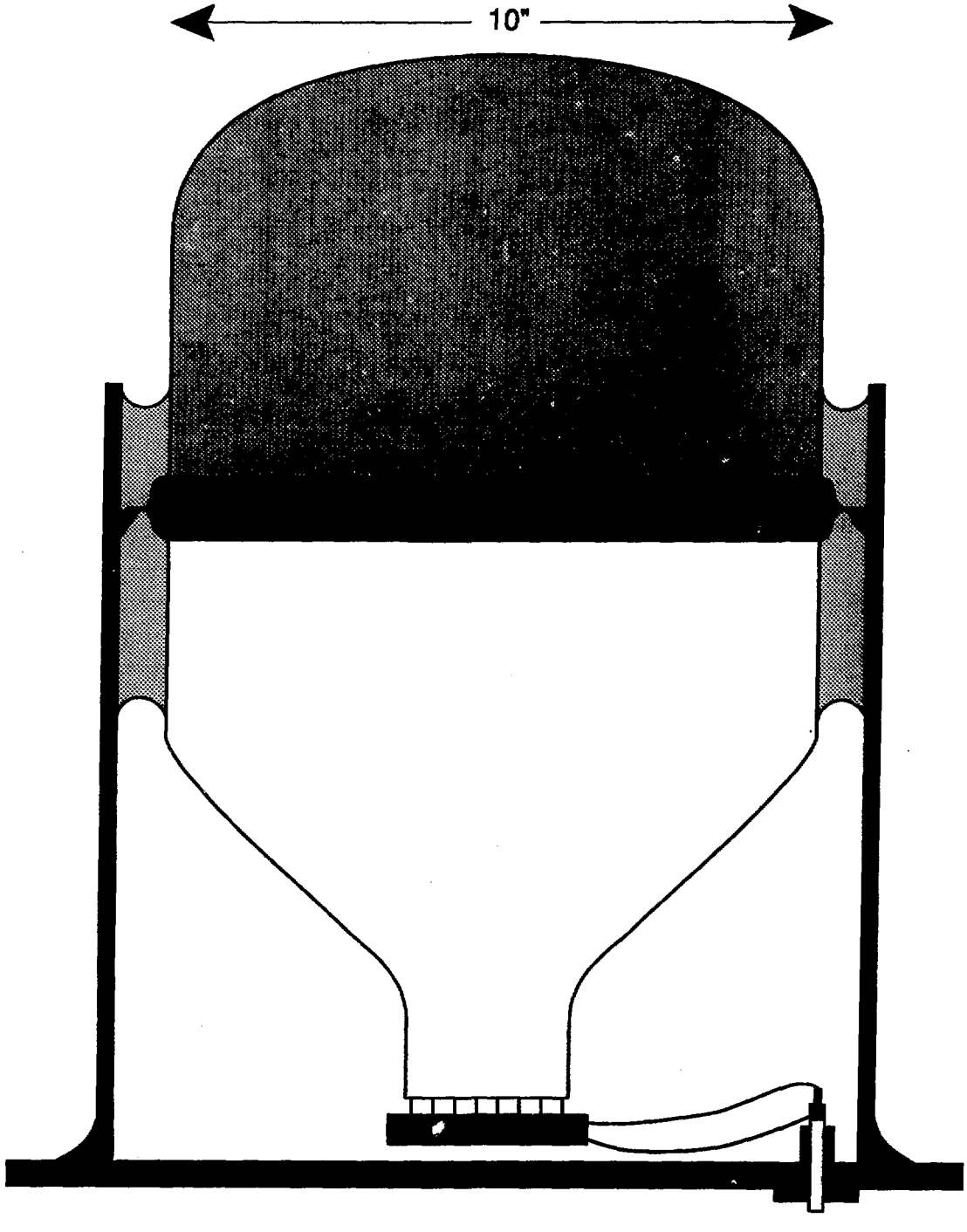

Fig. 9. Layout of the E645 veto shield.

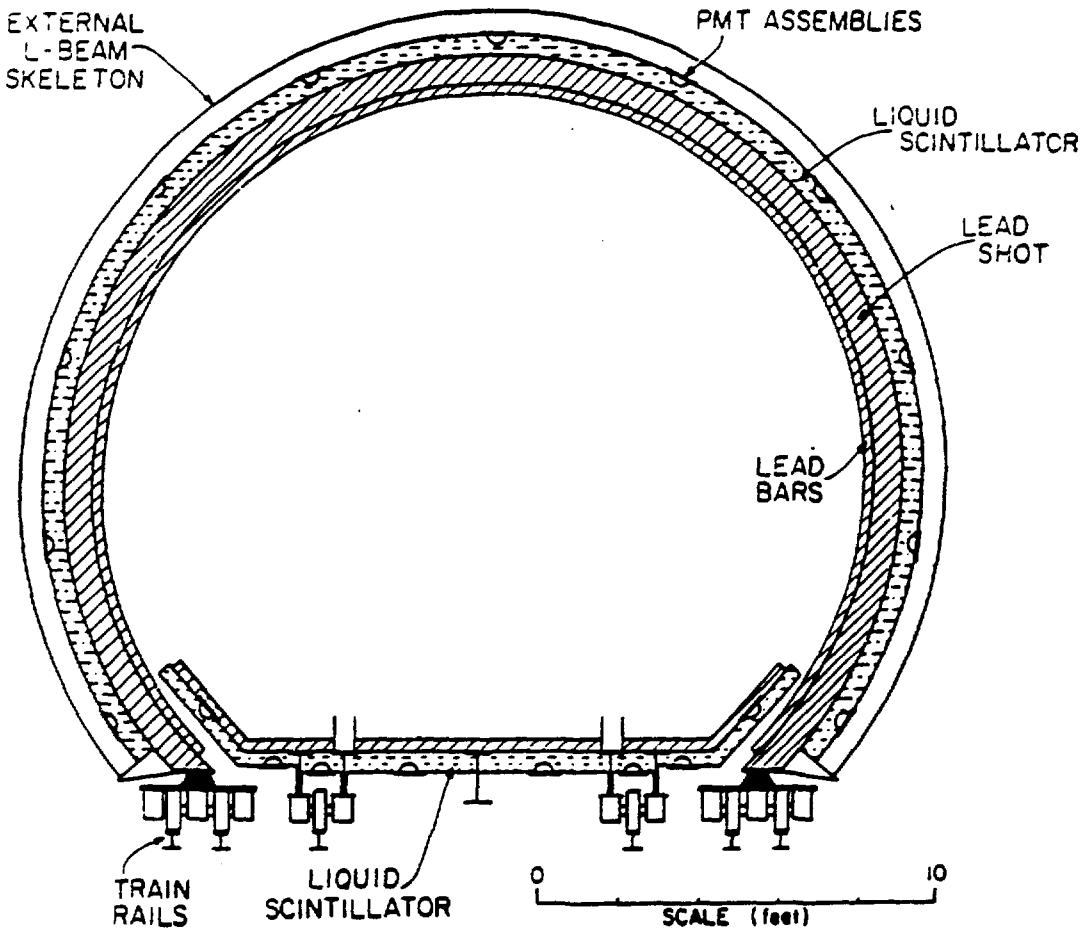

Fig. 8. The absorption and emission spectra of the liquid scintillator as a function of wavelength for (a) PPO only and (b) BIS-MSB waveshifter. (From Ref. 7.) The absorption is negligible for $\lambda > 400$ nm.

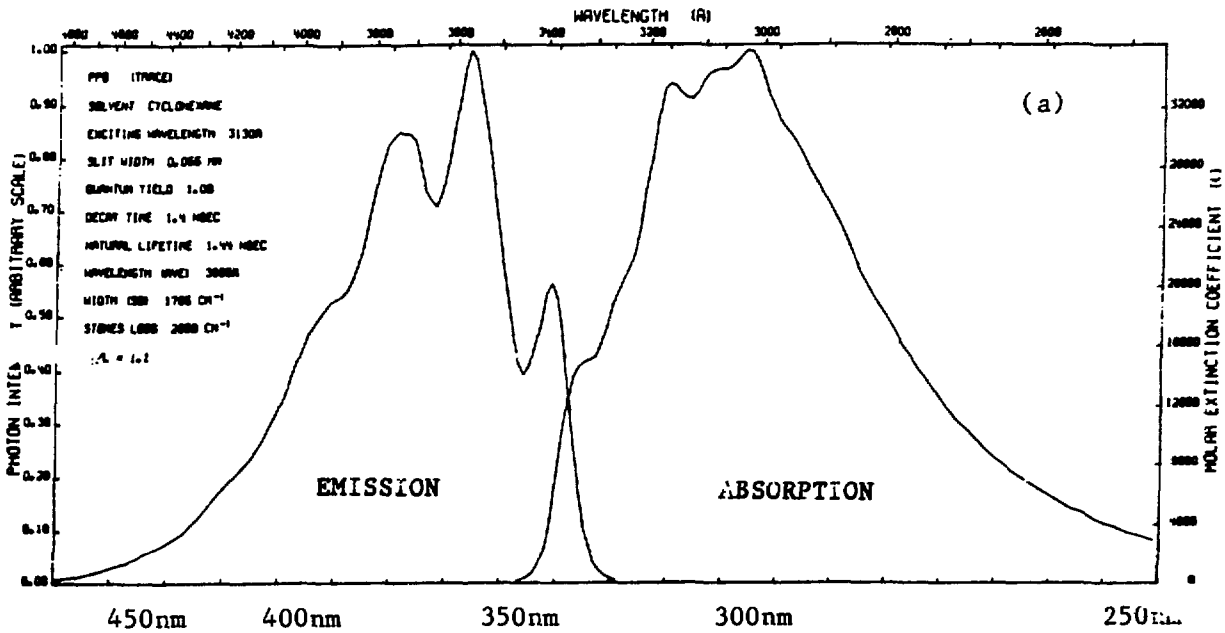

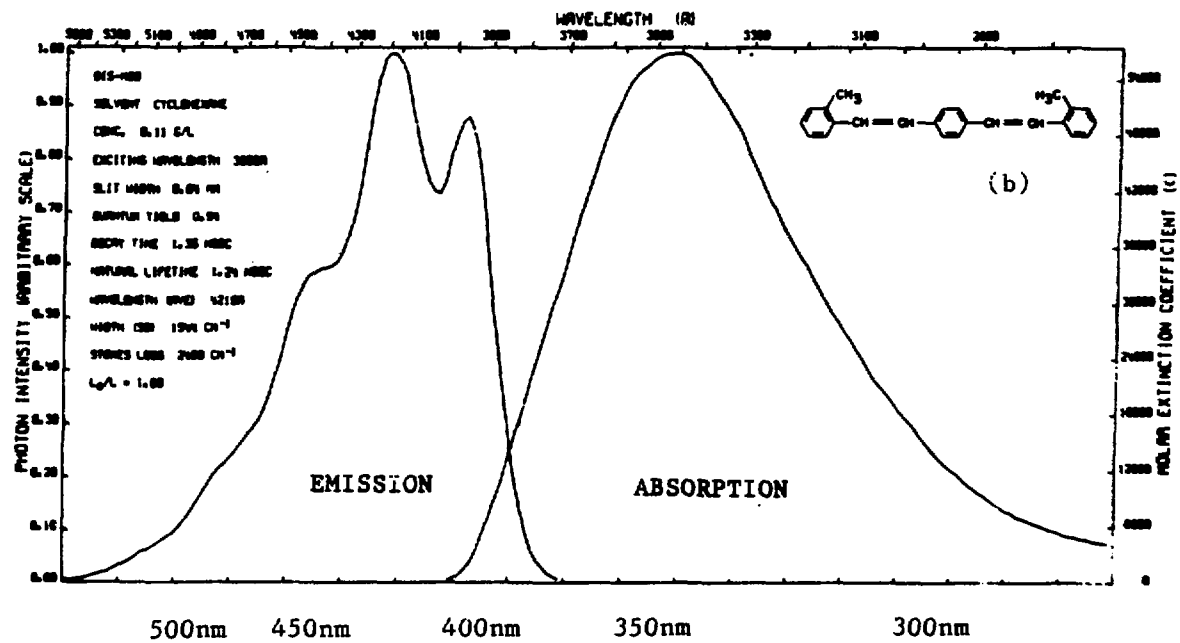

Fig. 10. (a) A typical 45-MeV electron event generated by the Monte Carlo simulation. Each number corresponds to a hit photomultiplier tube and equals the number of photoelectrons. The detector cylinder has been unrolled to clearly show the phototube hit pattern. (b) The same as Fig. 10a but with the requirement that PMTs have at least five photoelectrons and reconstructed times that are prompt. The location of the generated Čerenkov ring is shown in (b).

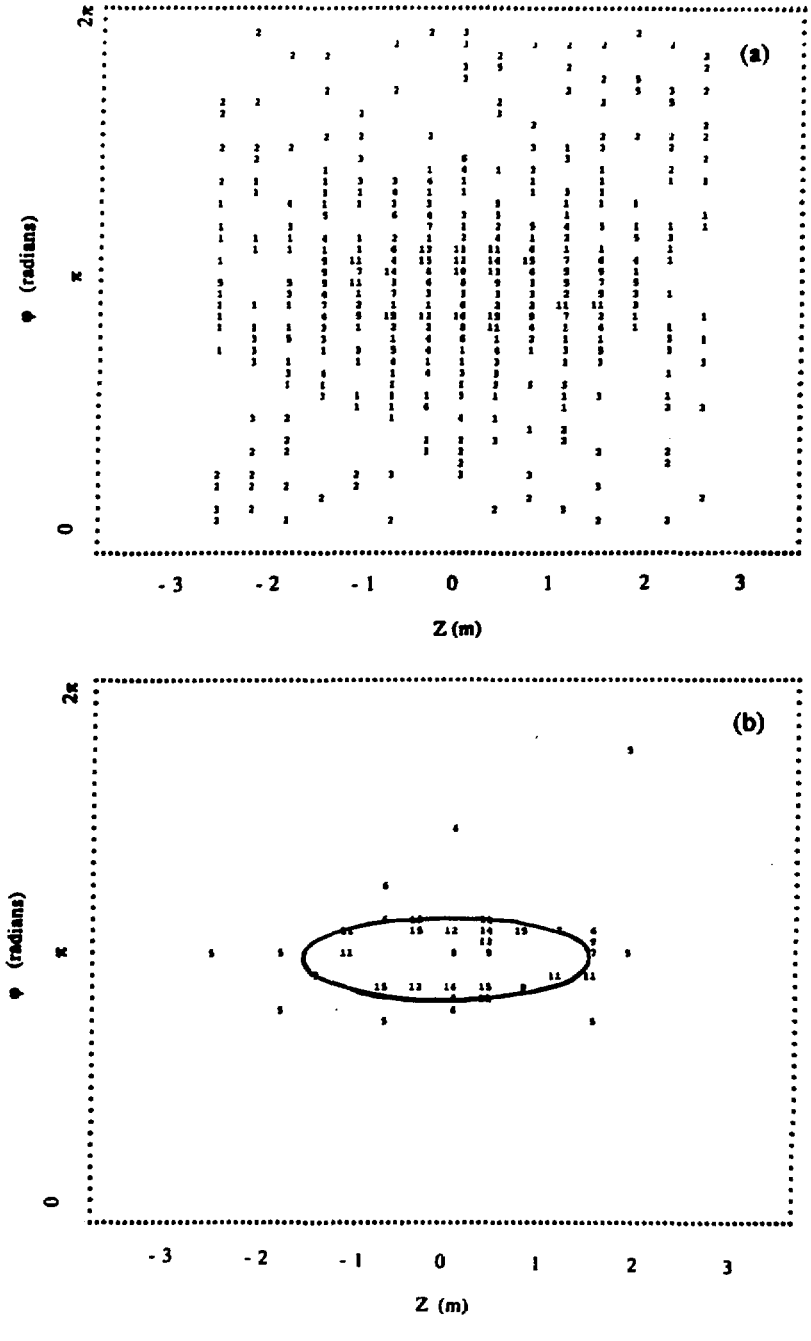

Fig. 11. The electron energy resolution as a function of the electron energy. The energy is determined from the number of photoelectrons.

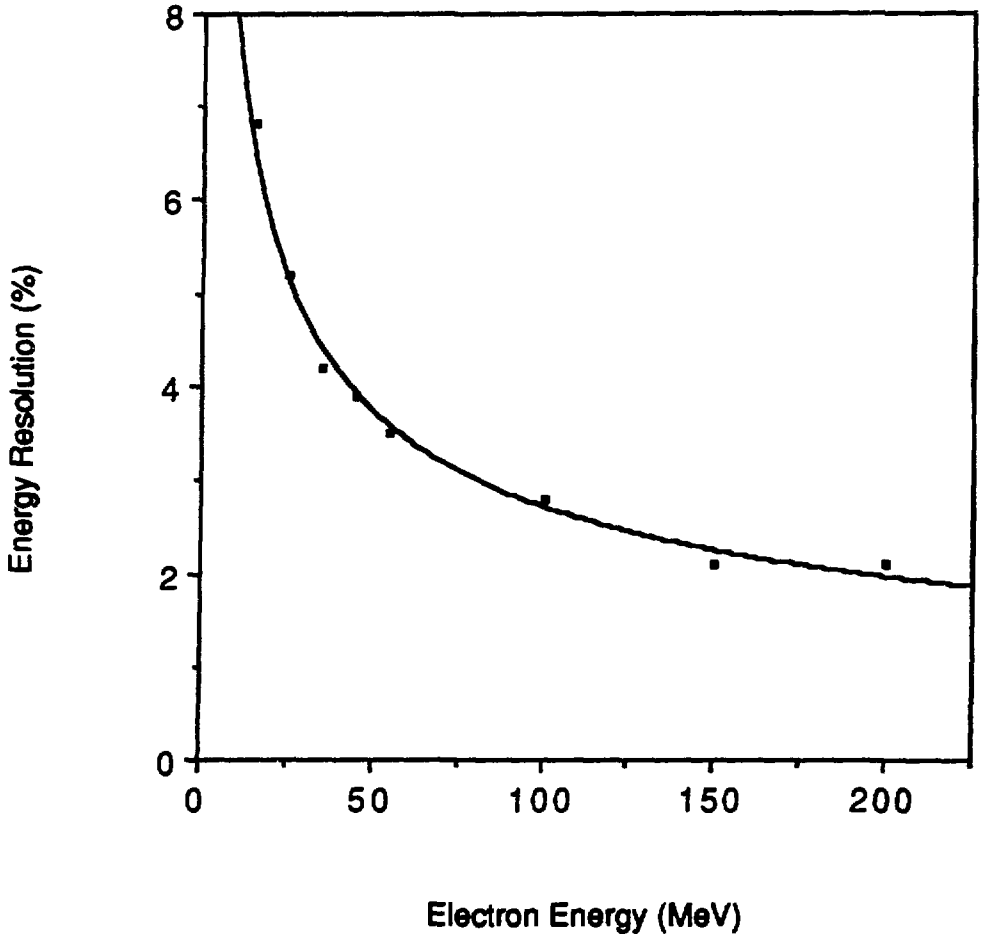

Fig. 12. The electron position resolution as a function of the electron energy. The position is determined from the phototube timing.

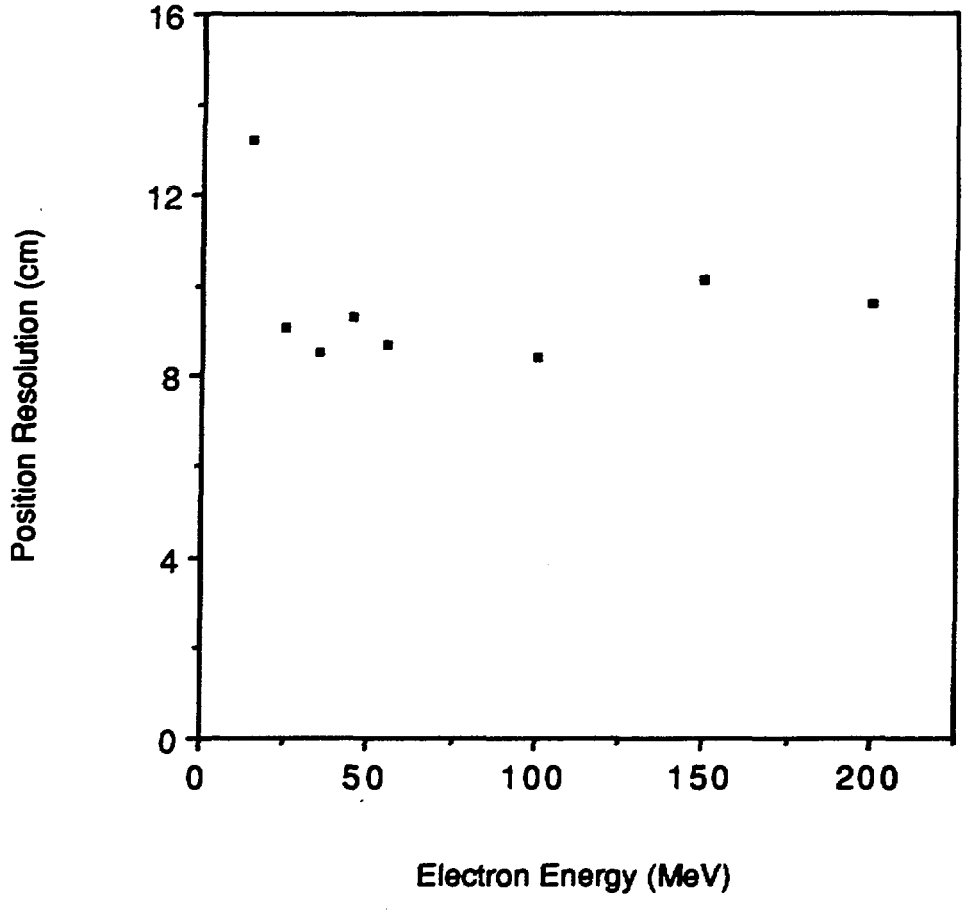

Fig. 13. The electron angular resolution as a function of the electron energy. The angle is determined from the Čerenkov light emitted by the electron. At high energies the dominant angular error is from electron multiple scattering in liquid scintillator.

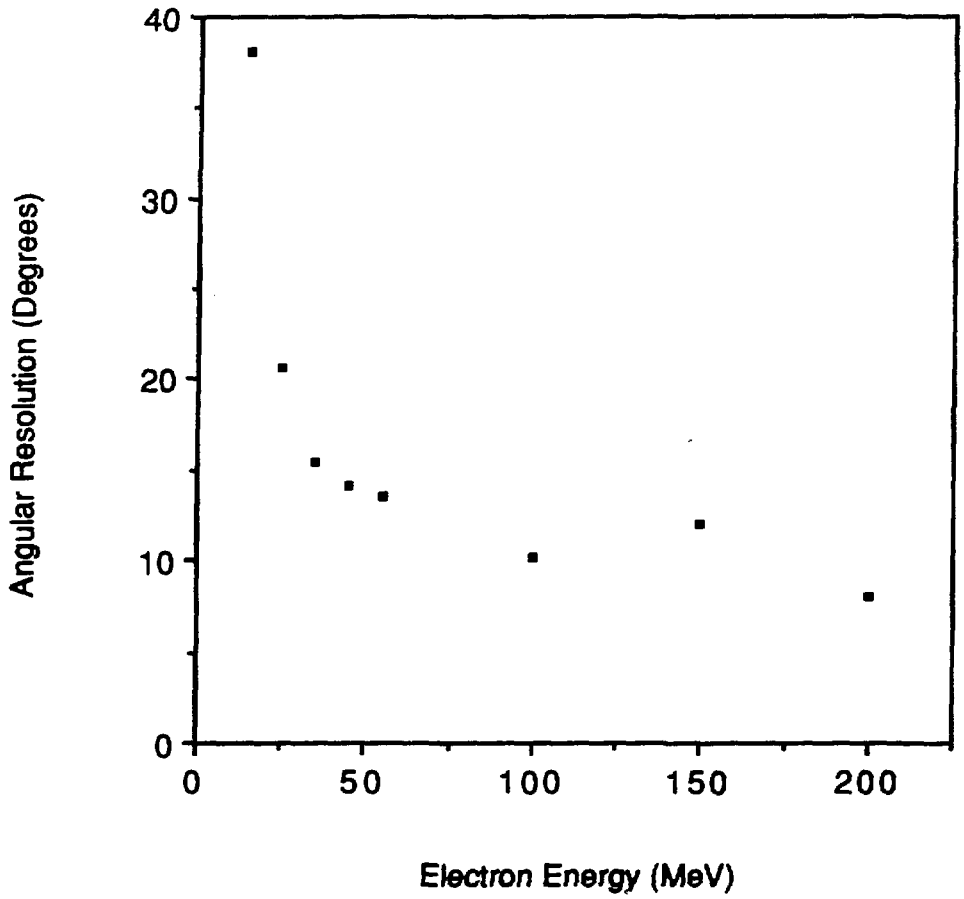

Figs. 14 a,b. The (a) time and (b) position electron resolution functions for a sample of 45-MeV electrons. The time resolution is approximately 0.21 ns, and the average error in position is 9.3 cm.

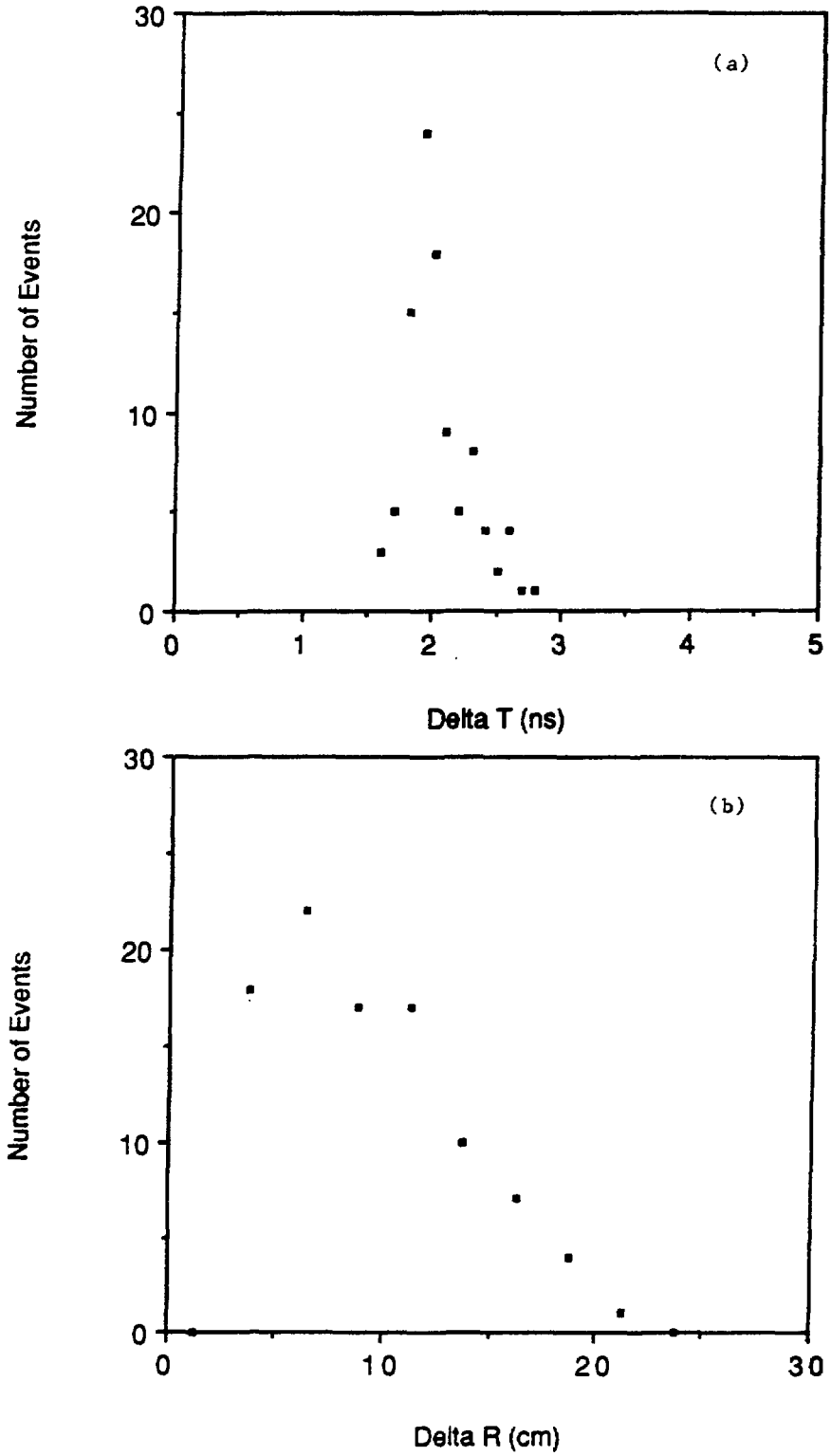

Figs. 14 c,d. The (c) energy and (d) angular electron resolution functions for a sample of 45-MeV electrons. The energy resolution is approximately 3.9%, and the average error in angle is 14.2°.

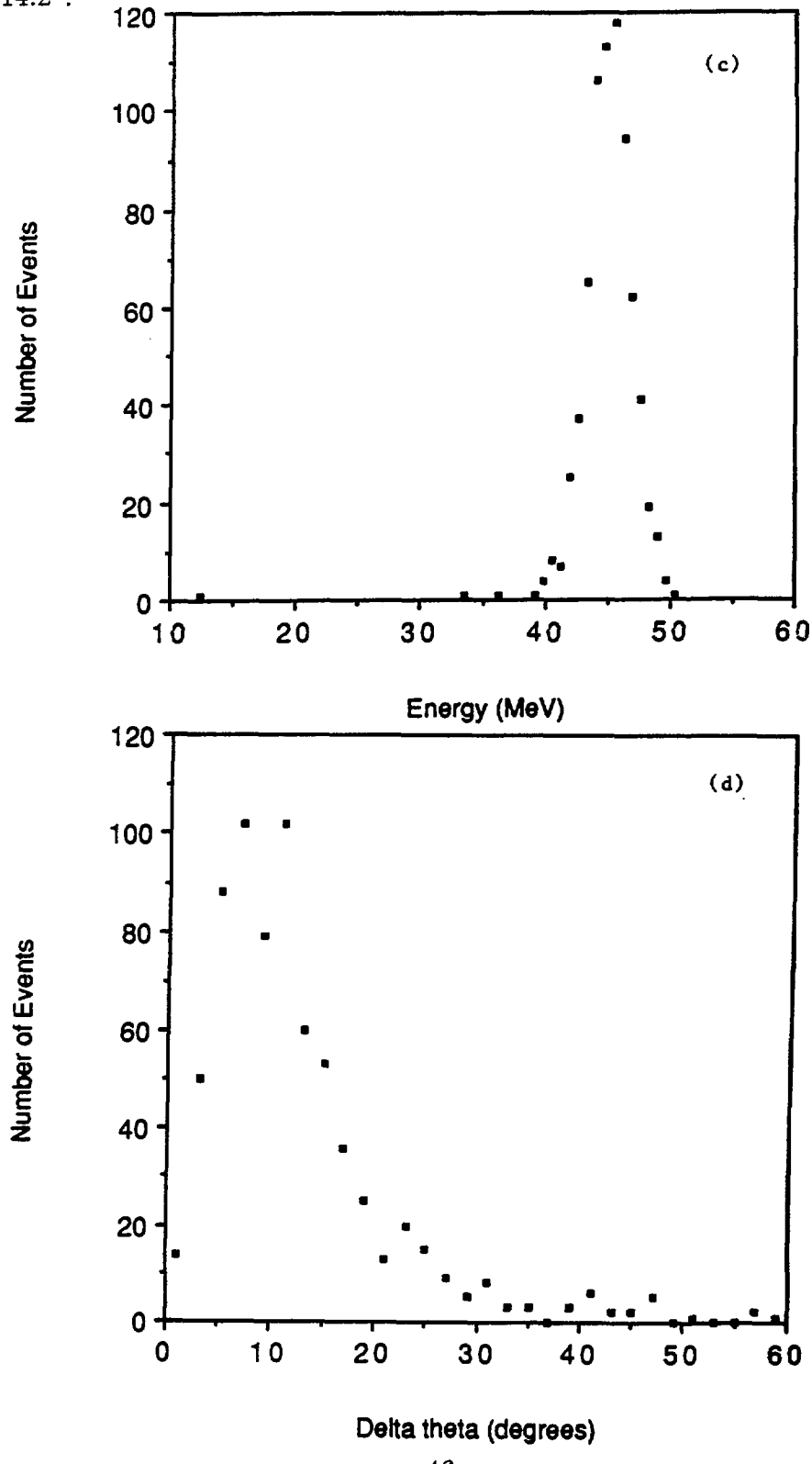

Fig. 15. The confidence level (C.L.) that an event is an electron for (a) electron events and (b) proton events with 45 MeV deposited energy. Approximately 90% of the electron events have C.L. $> 10\%$, while the background due to protons is $\sim 10^{-3}$

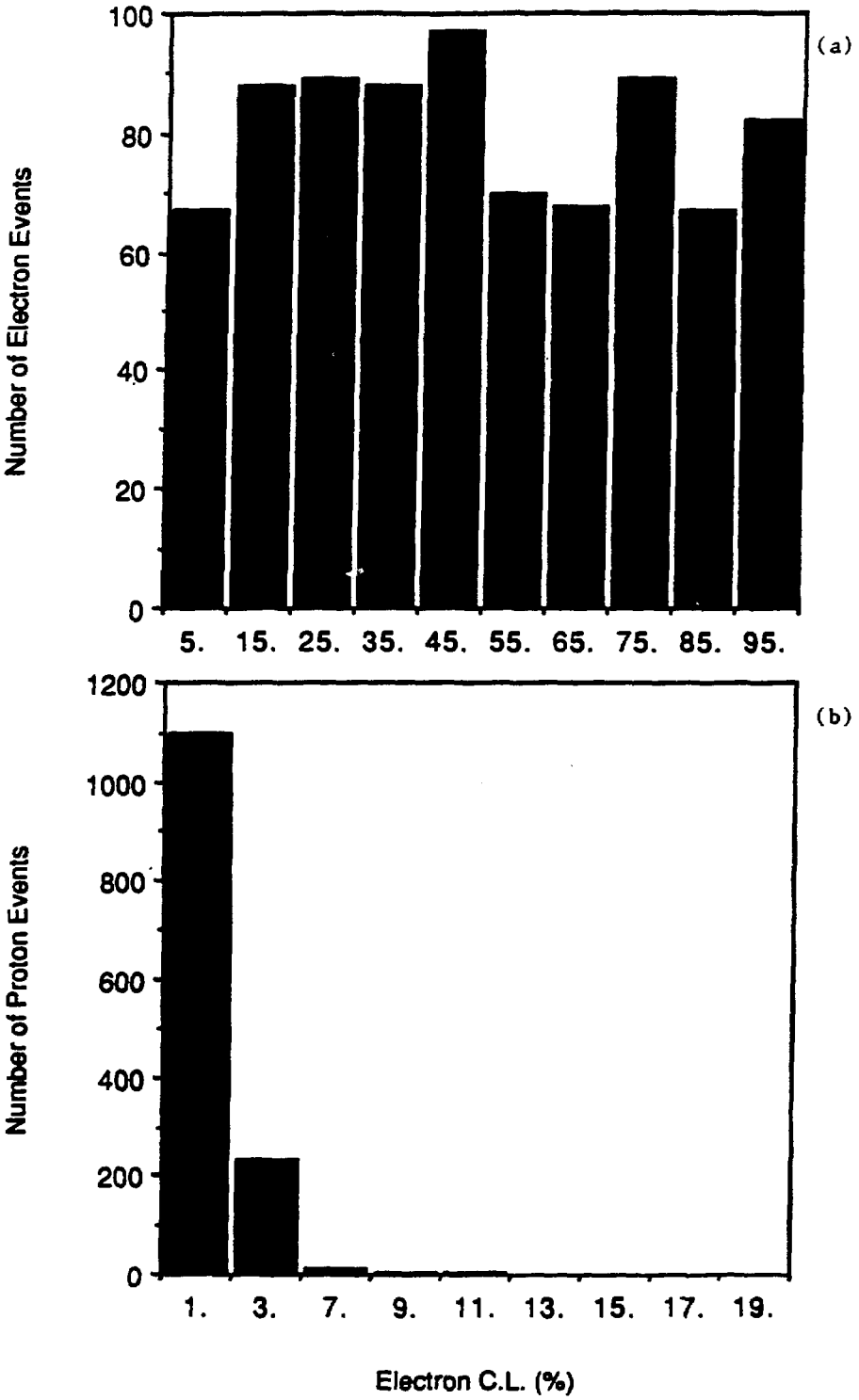

Fig. 16. E645 total singles rate in all of the liquid scintillator modules with no veto signal in the previous 15 μs from the veto shield, where we define a single hit to be one or more liquid scintillator modules with both phototubes firing in a 1-μs interval. The singles rate above 10 MeV is $\sim$ 1 Hz, which is in agreement with the estimates discussed in the text. The horizontal error bars denote the energy bin width.

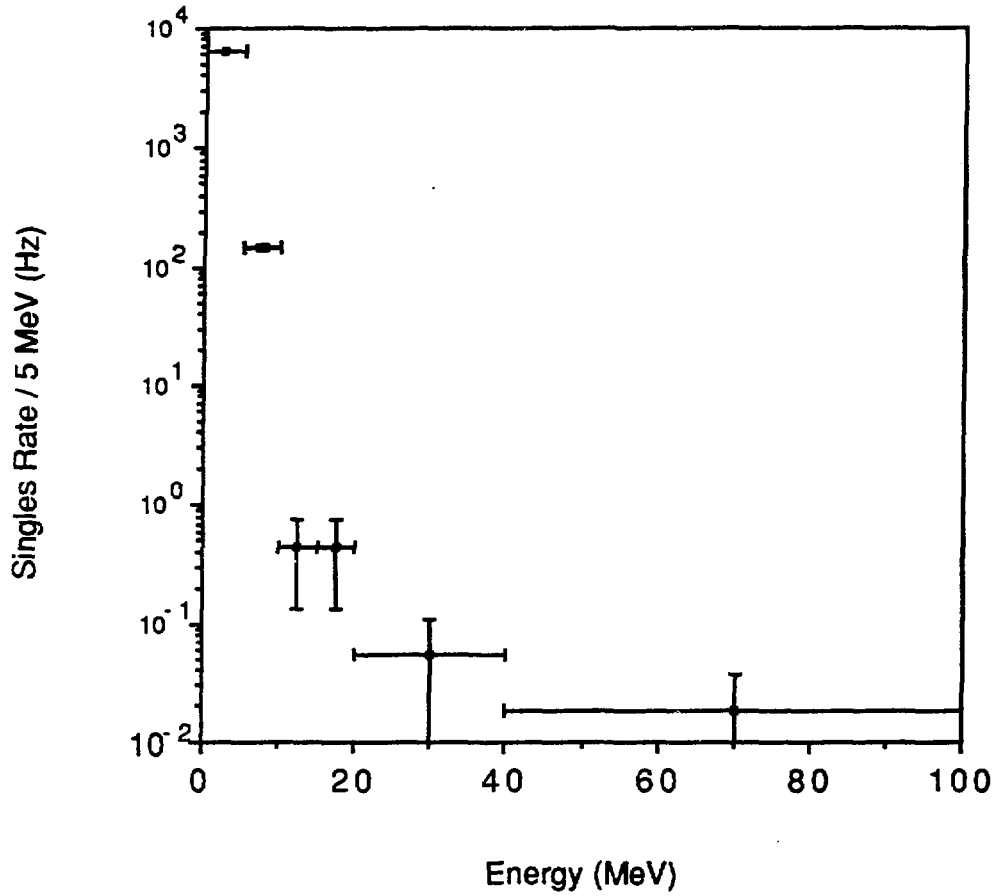

Fig. 17. (a) The total cross sections for electron neutrinos on free neutrons ($\nu_e n$) and bound neutrons ($\nu_e A$) and antineutrinos on free protons ($\bar{\nu}_e p$) and bound protons ($\bar{\nu}_e A$). (b) The same as (a) for muon neutrinos. (From Ref. 22.)

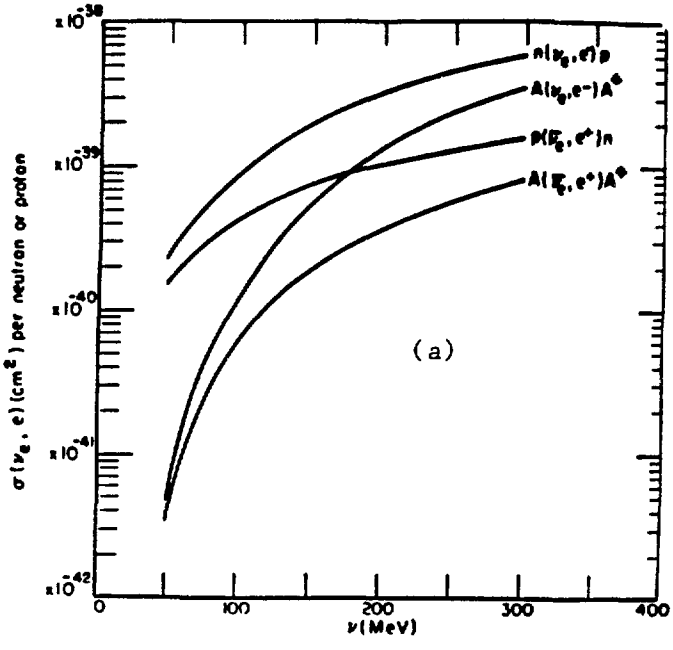

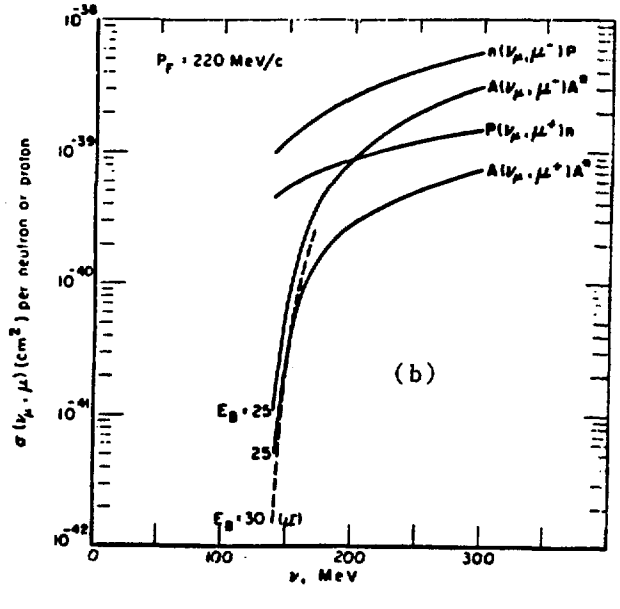

Fig. 18. (a) ν_μ energy distribution expected from pion decay in flight. (b) Electron energy distribution expected from the reaction $\nu_e C \rightarrow e^- N$, where the electron-neutrinos come from $\nu_\mu \rightarrow \nu_e$ oscillations.

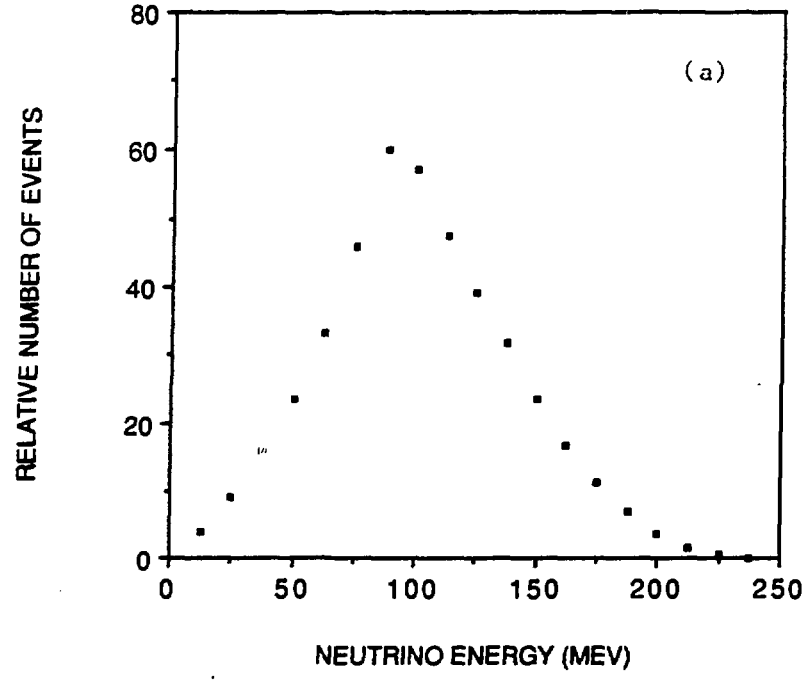

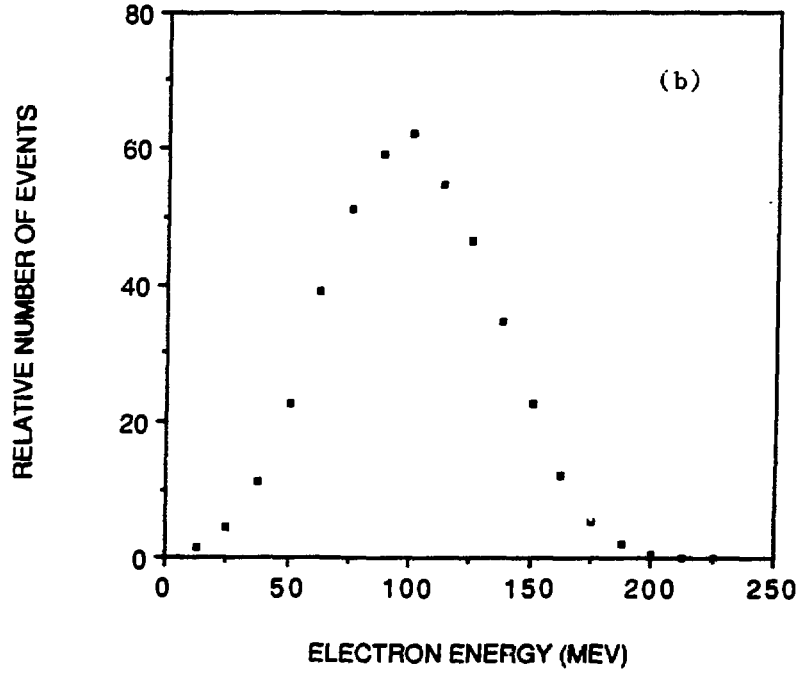

Figs. 19 a,b. The (a) time and (b) position electron resolution functions for a sample of 100-MeV electrons. The average time resolution is 0.24 ns, and the average error in position is 8.4 cm.

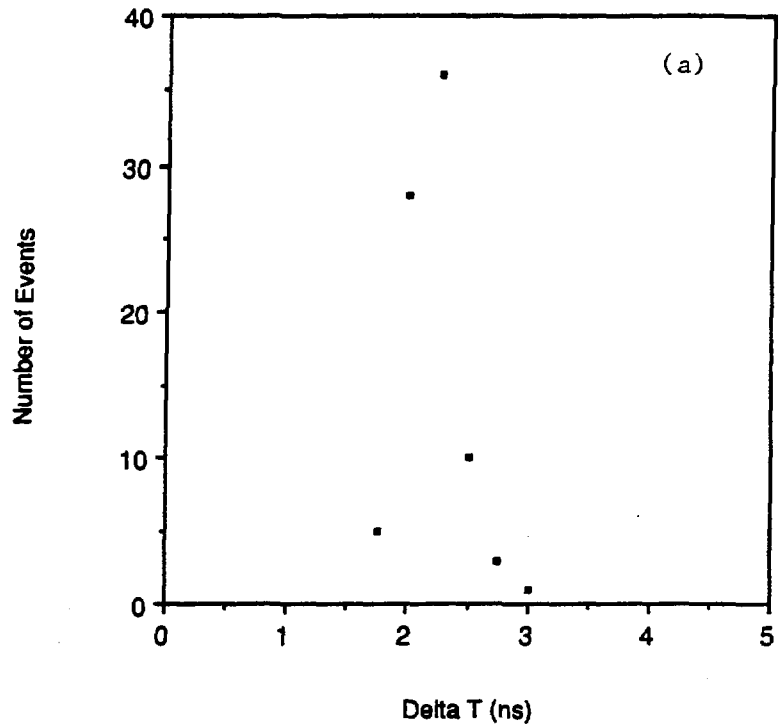

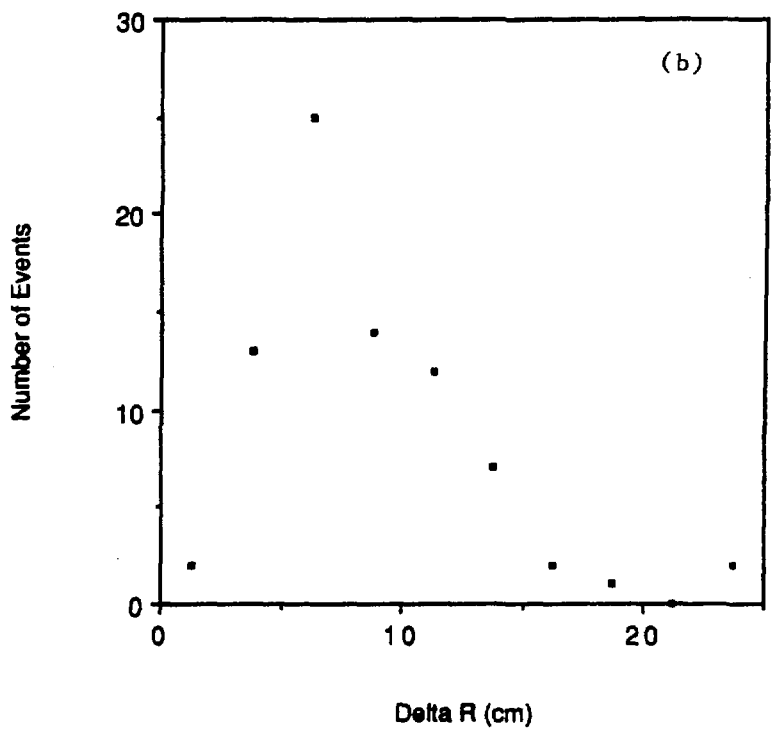

Figs. 19 c,d. The (c) energy and (d) angle electron resolution functions for a sample of 100-MeV electrons. The energy resolution is approximately 2.8%, and the average error in angle is 10.2°. The angular error is dominated by electron multiple scattering in liquid scintillator.

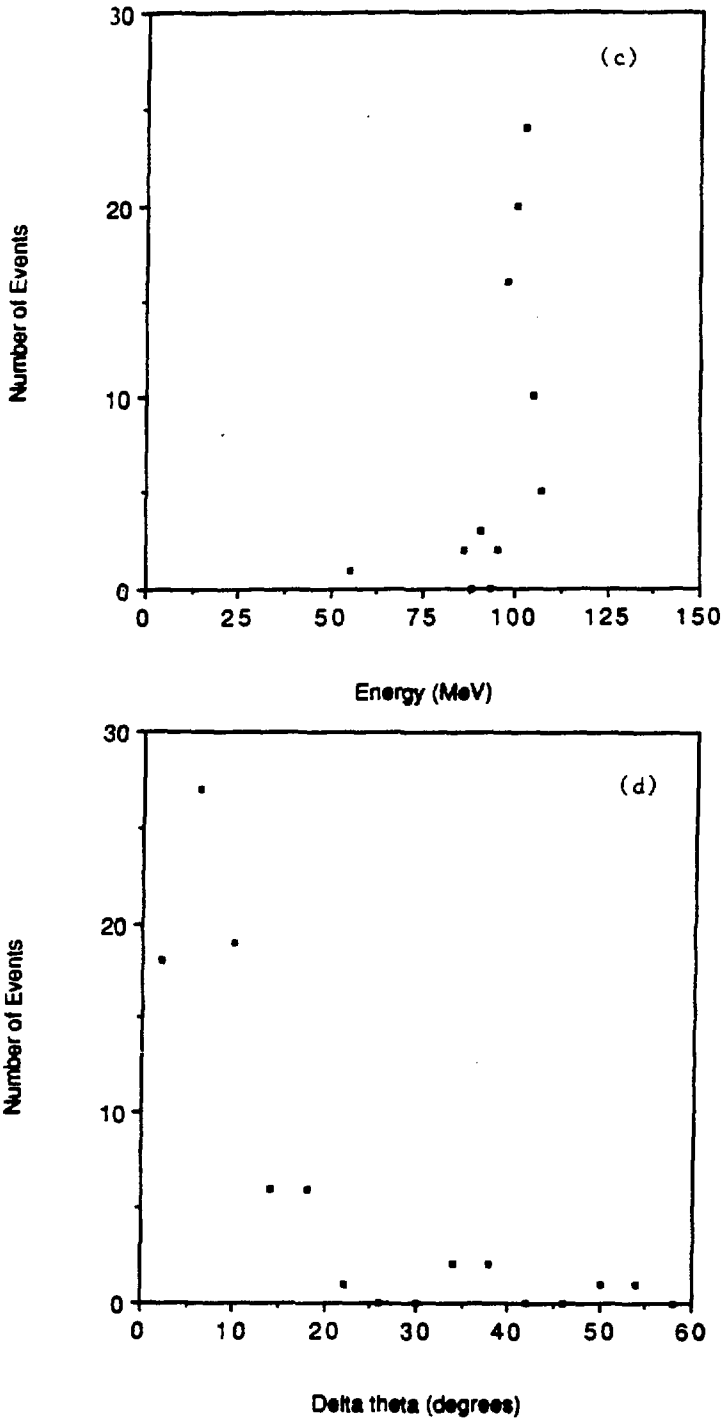

Fig. 20. (a) The expected neutrino energy distributions for $\nu_\mu \rightarrow \nu_e$ oscillations at a level of 5×10^{-4}, μ^+ decay-in-flight background, and $\pi^+ \rightarrow e^+\nu_e$ background. (b) Same as (a) for the expected electron energy distributions.

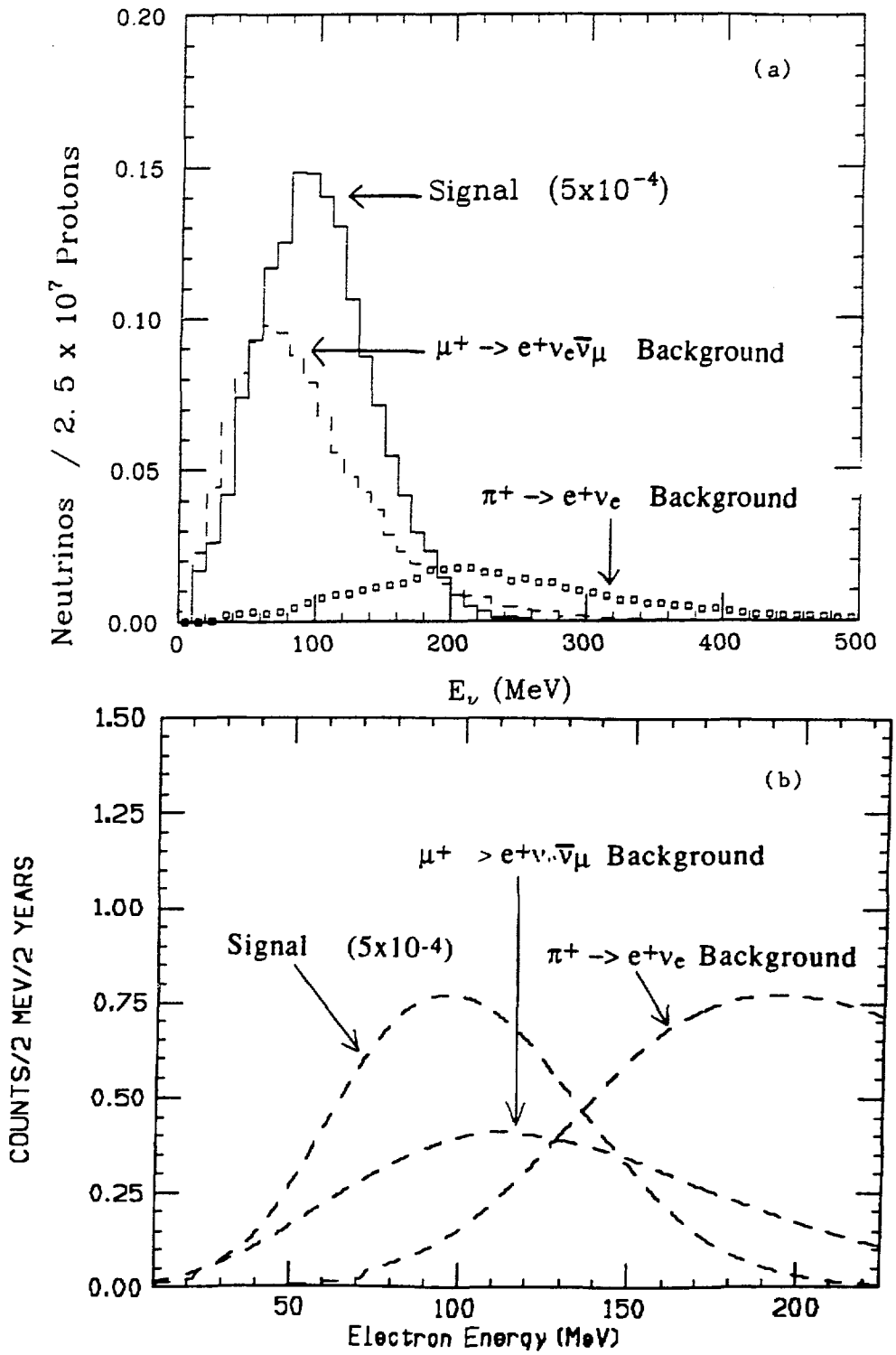

Fig. 21. The total low energy cross sections for electron neutrinos on neutrons ($\nu_e n$) and antineutrinos on protons ($\bar{\nu}_e p$). The dashed curves are for free nucleons and the solid curves are for bound nucleons. (From reference 13.)

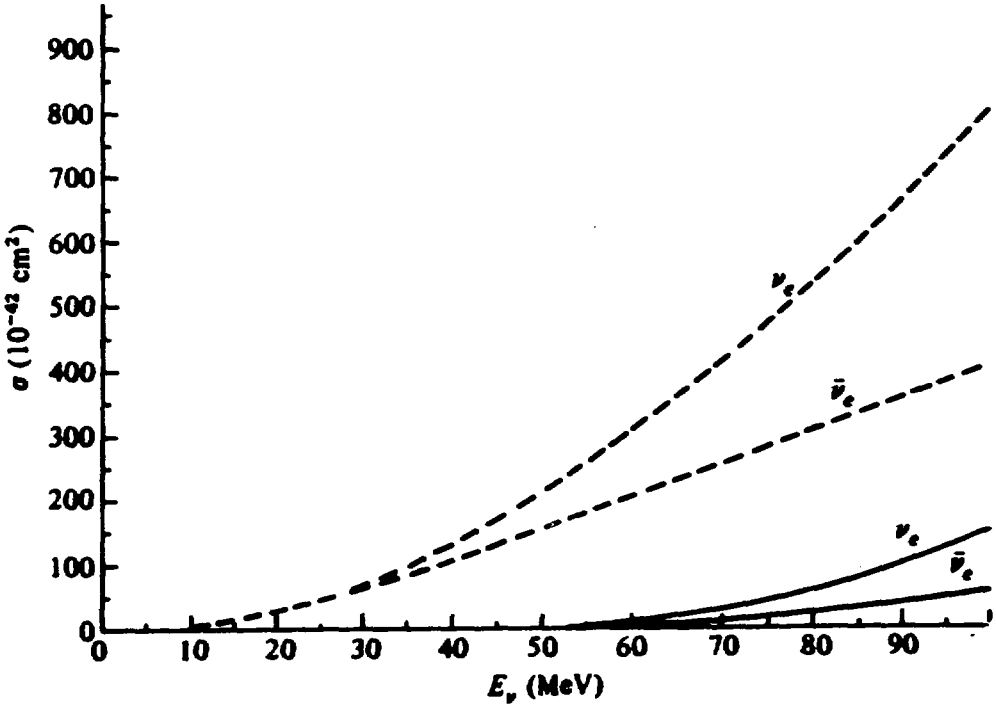

Figs. 22a-c. Expected electron energy distributions for the reactions $\nu_e e \rightarrow \nu_e e$, $\nu_\mu e \rightarrow \nu_\mu e$, and $\bar{\nu}_\mu e \rightarrow \bar{\nu}_\mu e$. The neutrinos are from pion and muon decay-at-rest.

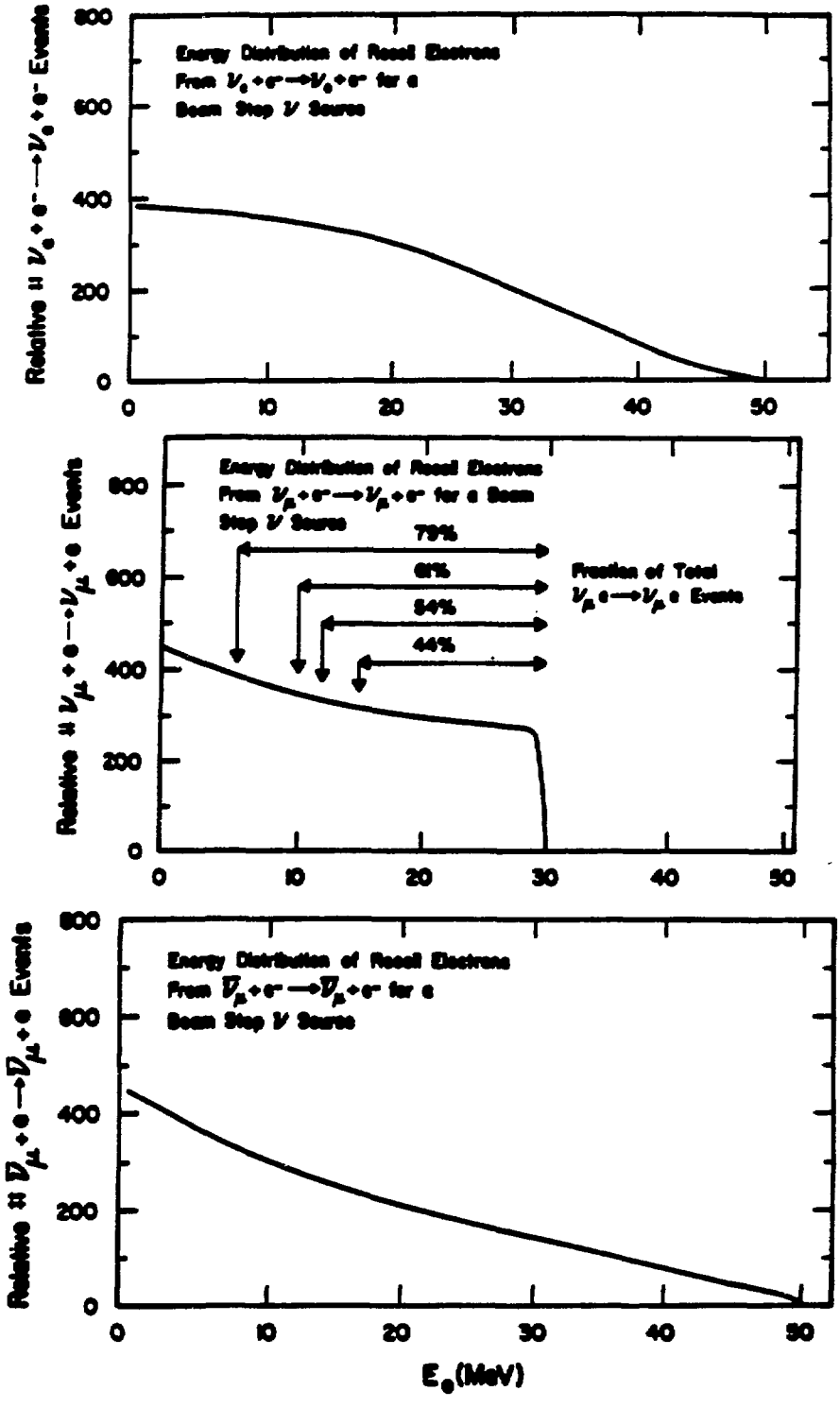

Figs. 22d,e. Expected electron energy distributions for the reactions (d) $\nu_e C \rightarrow e^- N$ and (e) $\bar{\nu}_e p \rightarrow e^+ n$. The shape of the energy distribution for $\bar{\nu}_e p \rightarrow e^+ n$ is much different from the other energy distributions. The neutrinos are from muon decay-at-rest.

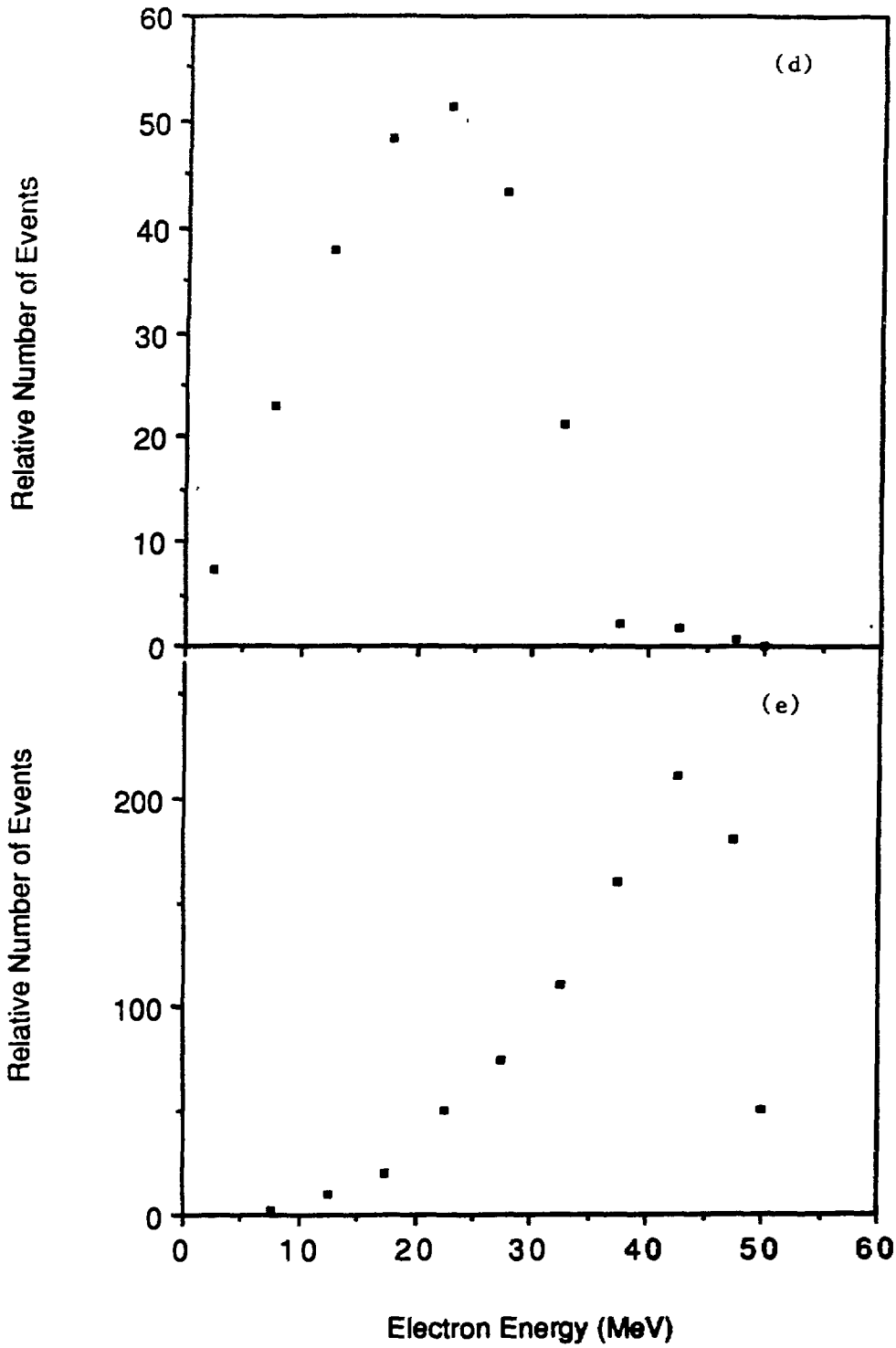

Fig. 23. The (a) capture time and (b) straight-line distance traveled for a large sample of recoil neutrons from $\bar{\nu}_e p \rightarrow e^+ n$ interactions. The mean neutron capture time is 203 μs and the average straight-line distance traveled by the neutron before capture is about 10 cm.

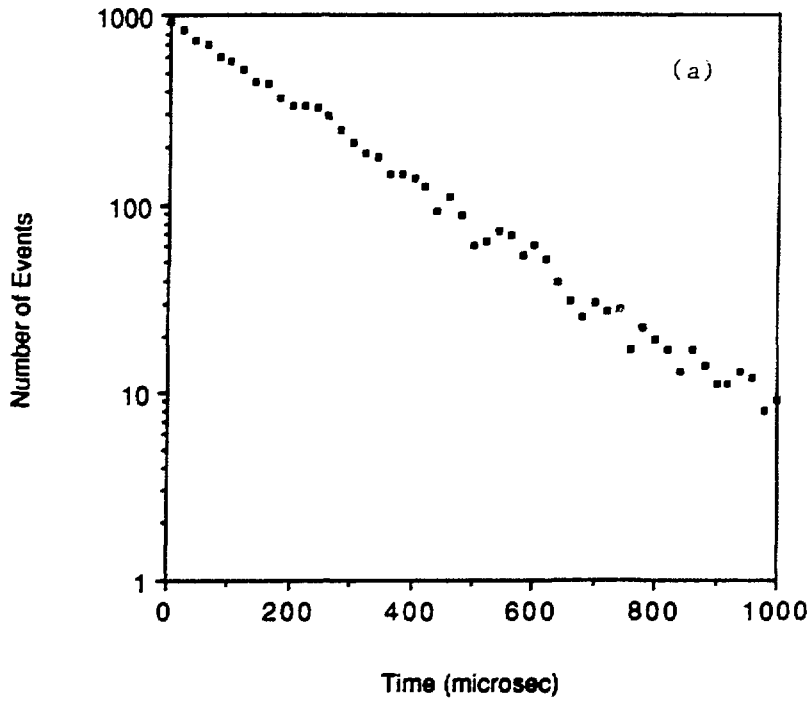

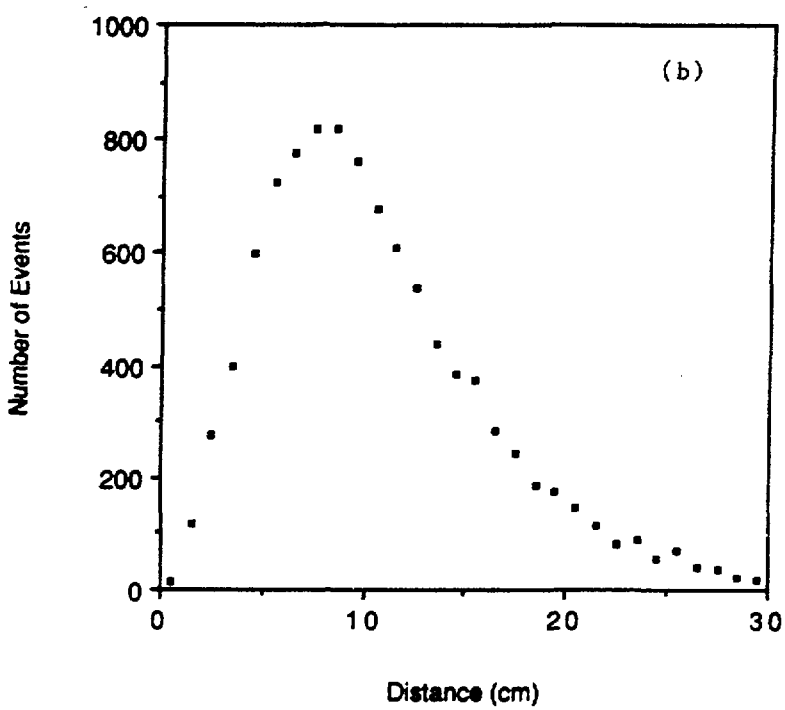

Fig. 24. The reconstructed energy and position resolution functions for a sample of 2.2 MeV γ events. The energy resolution is 20%, and the average position error is 44 cm.

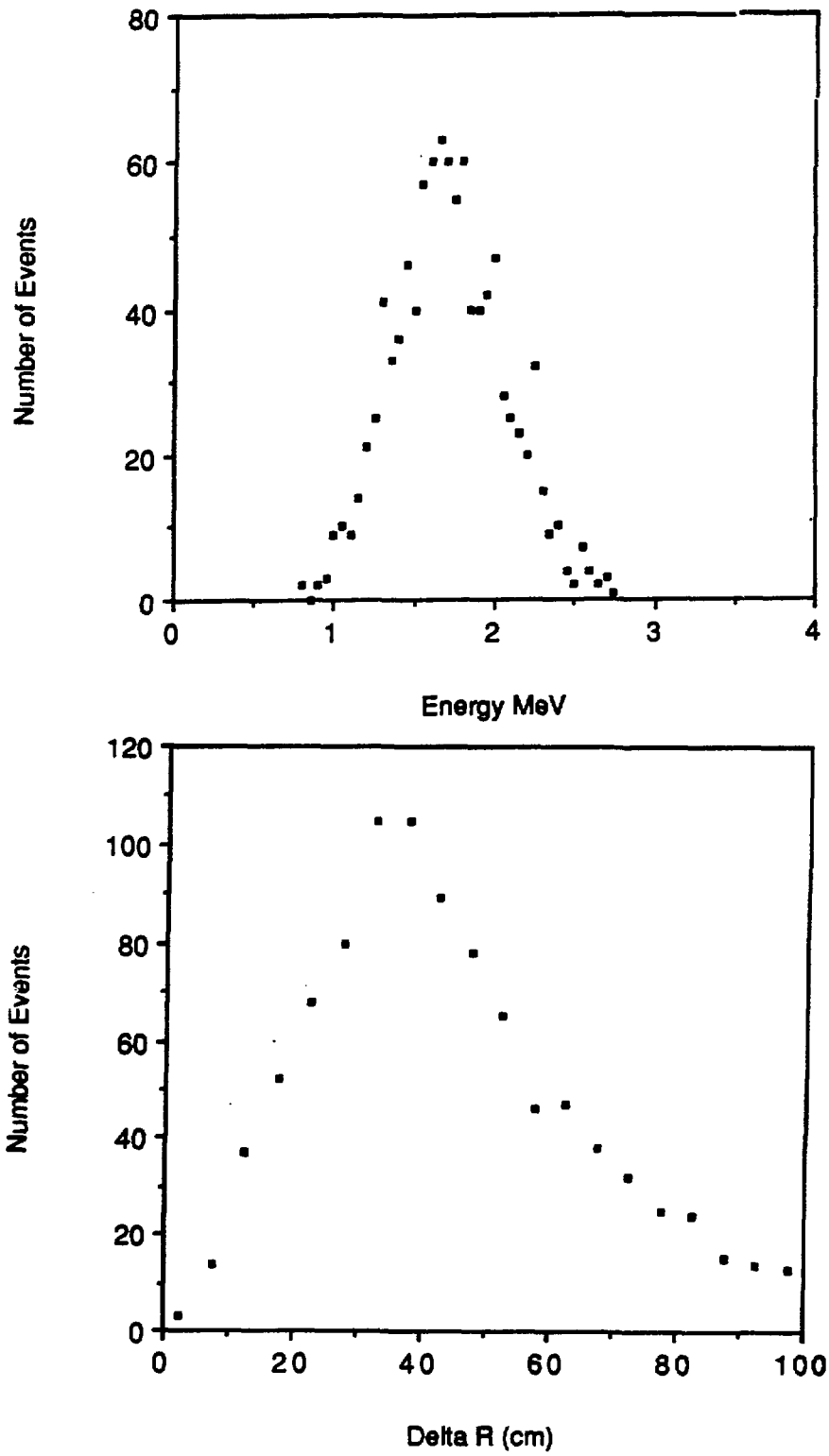

Fig. 25a. The total singles rate in all of the E645 liquid scintillator modules at the beginning of the 1989 run. We define a single hit to be one or more E645 liquid scintillator modules with both phototubes firing in a 1-μs interval. The resulting energy threshold is between 0.5 MeV (for hits near the center of the liquid scintillator module) and 1.0 MeV (for hits near one of the two photomultiplier tubes). In the energy range $1 < E < 2.5$ MeV the observed singles rate was 3.4 KHz.

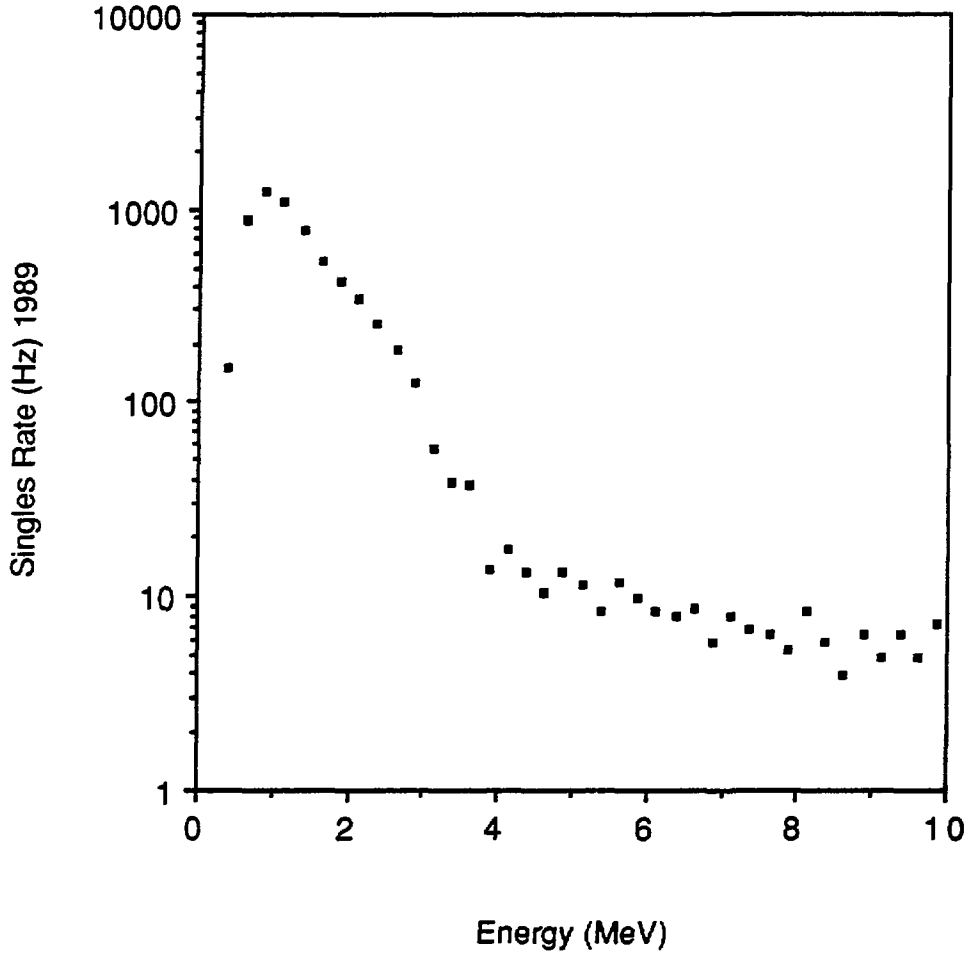

Fig. 25b. The total E645 singles rate in the energy range $1 < E < 2.5$ MeV as a function of time, extending from the start of the 1988 E645 run to the end of the 1989 run. The observed singles rate decreases from 4.4 KHz to 3.1 KHz during this time interval, corresponding to a half life of 2.4 ± 0.1 y. This observed decay time is consistent with a dominant radioactive background from ^{22}Na, which has a half life of 2.601 y.

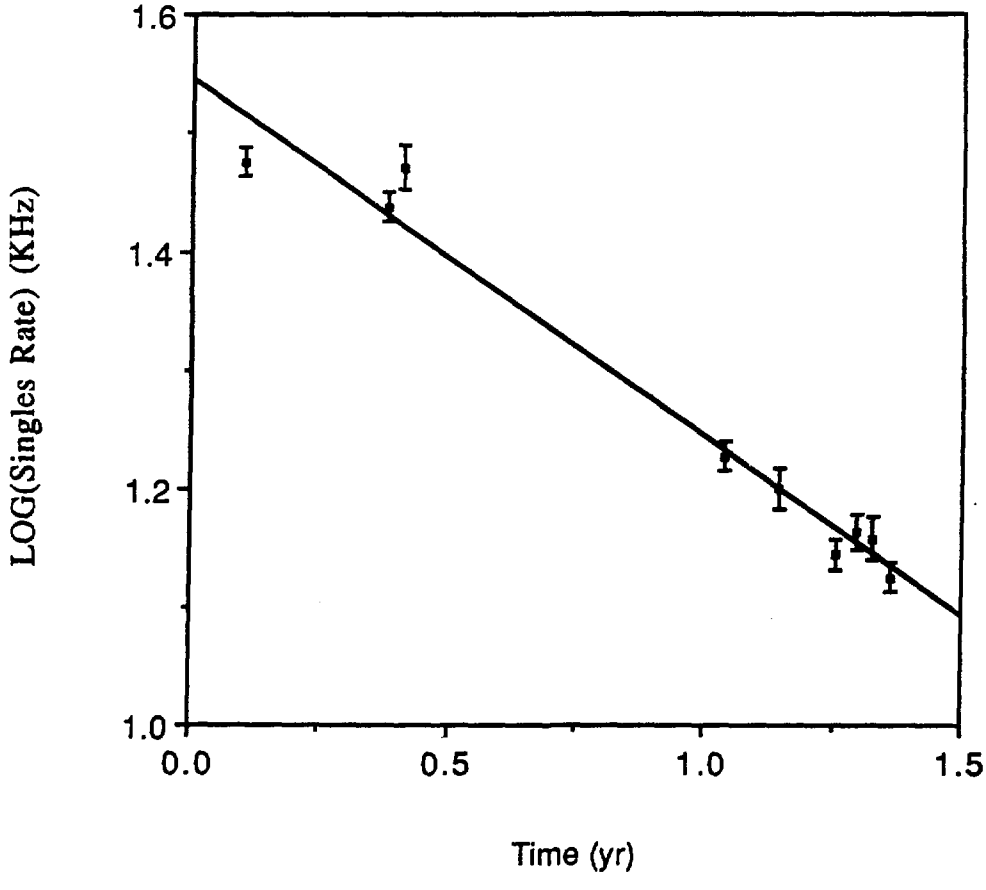

Fig. 26. The expected positron energy distributions from $\bar{\nu}_e p \rightarrow e^+ n$ events for $\bar{\nu}_e$ from $\bar{\nu}_\mu \rightarrow \bar{\nu}_e$ oscillations at a level of 5×10^{-4} and μ^- decay-at-rest background. Also shown are the expected electron energy distributions from the backgrounds $\nu_e\ ^{12}\mathrm{C} \rightarrow e^-\ ^{12}\mathrm{N}$ and $\nu_e\ ^{13}\mathrm{C} \rightarrow e^-\ ^{13}\mathrm{N}$.

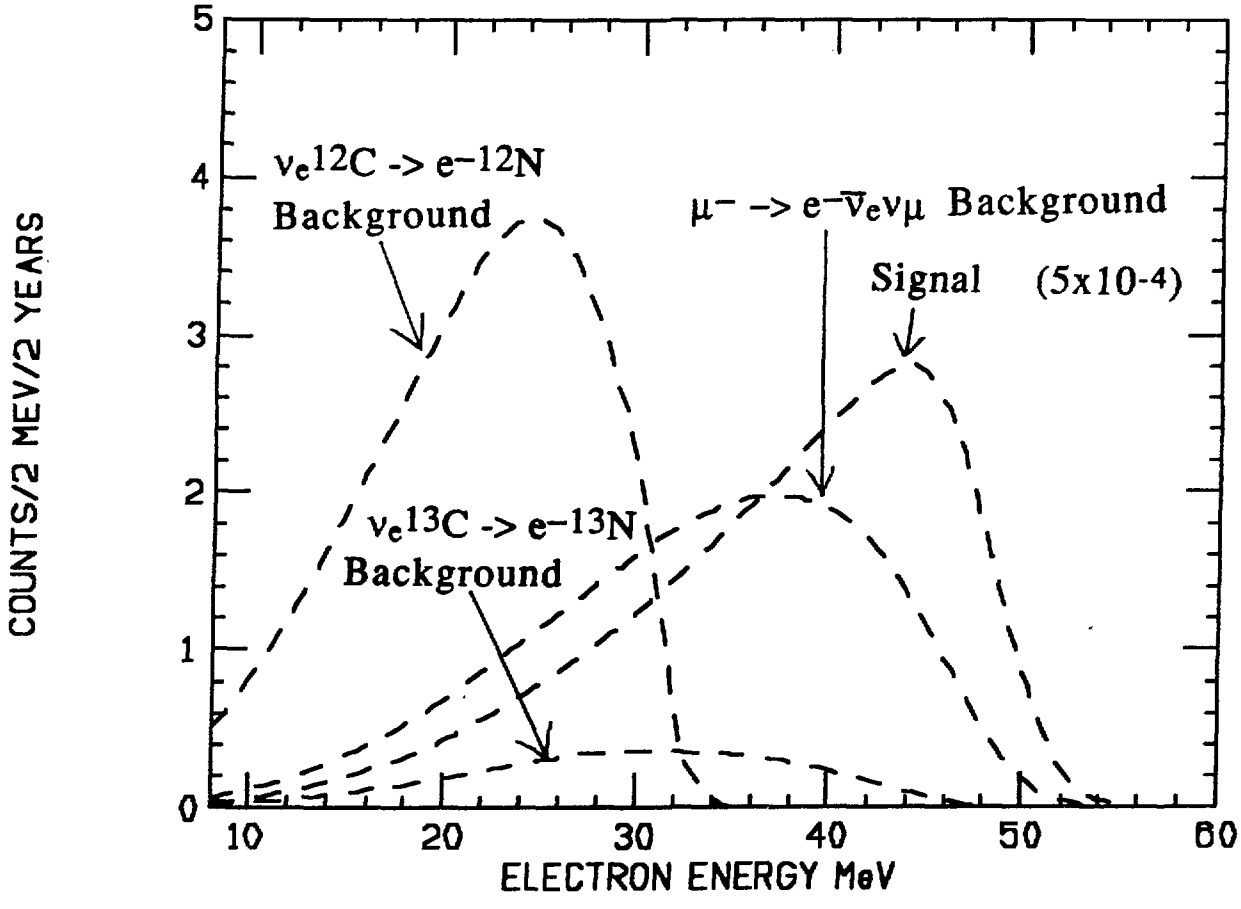

Fig. 27. The predicted cross section for the reaction $\nu C \rightarrow \nu C^*$ (15.11 MeV γ) as a function of neutrino energy. The solid and dashed lines correspond to incident neutrinos and antineutrinos, respectively. Curve 1 is the prediction for the Standard Model of electroweak interactions. Curves 2-5 are for various gauge theory models: (2) b-quark; (3) q-quark; (4) Vector; (5) SU(3)XU(1). (From Ref. 18.)

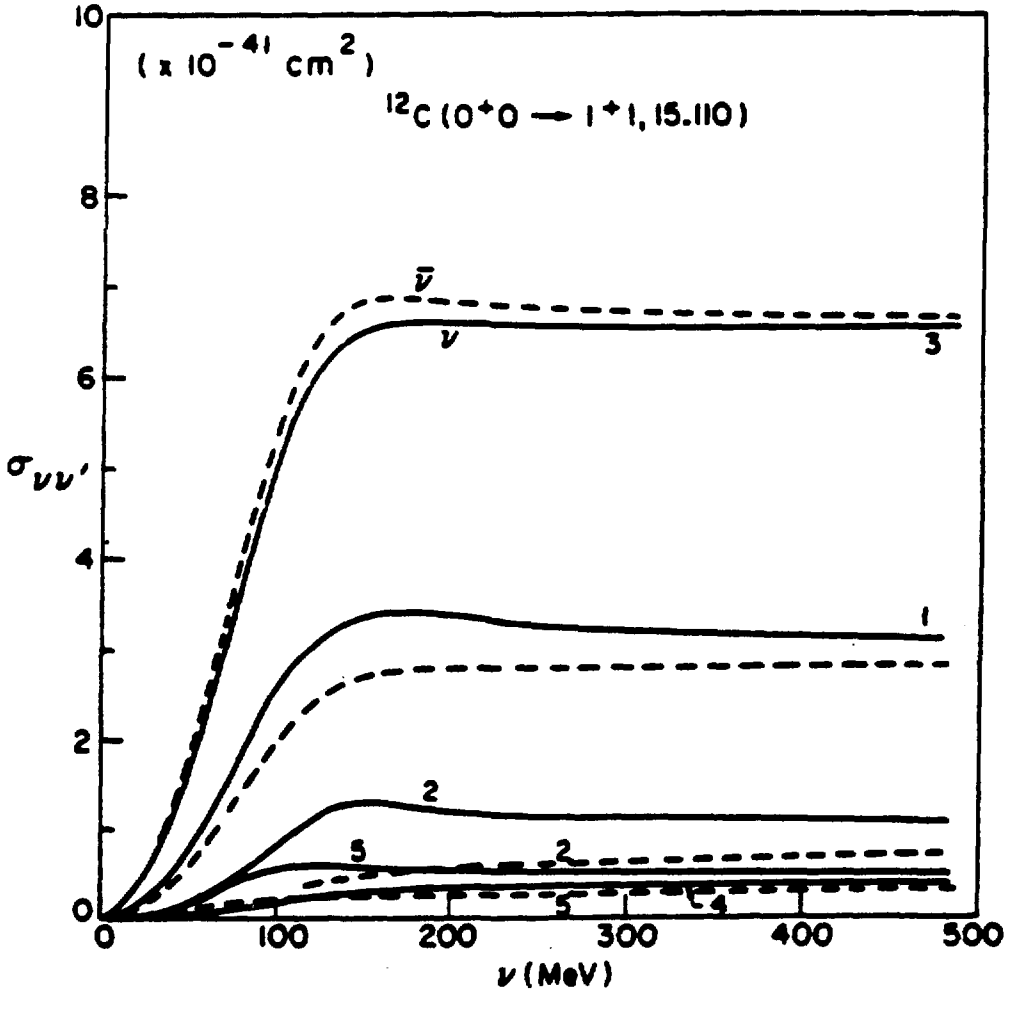

Fig. 28. A work breakdown structure for the construction planning process.

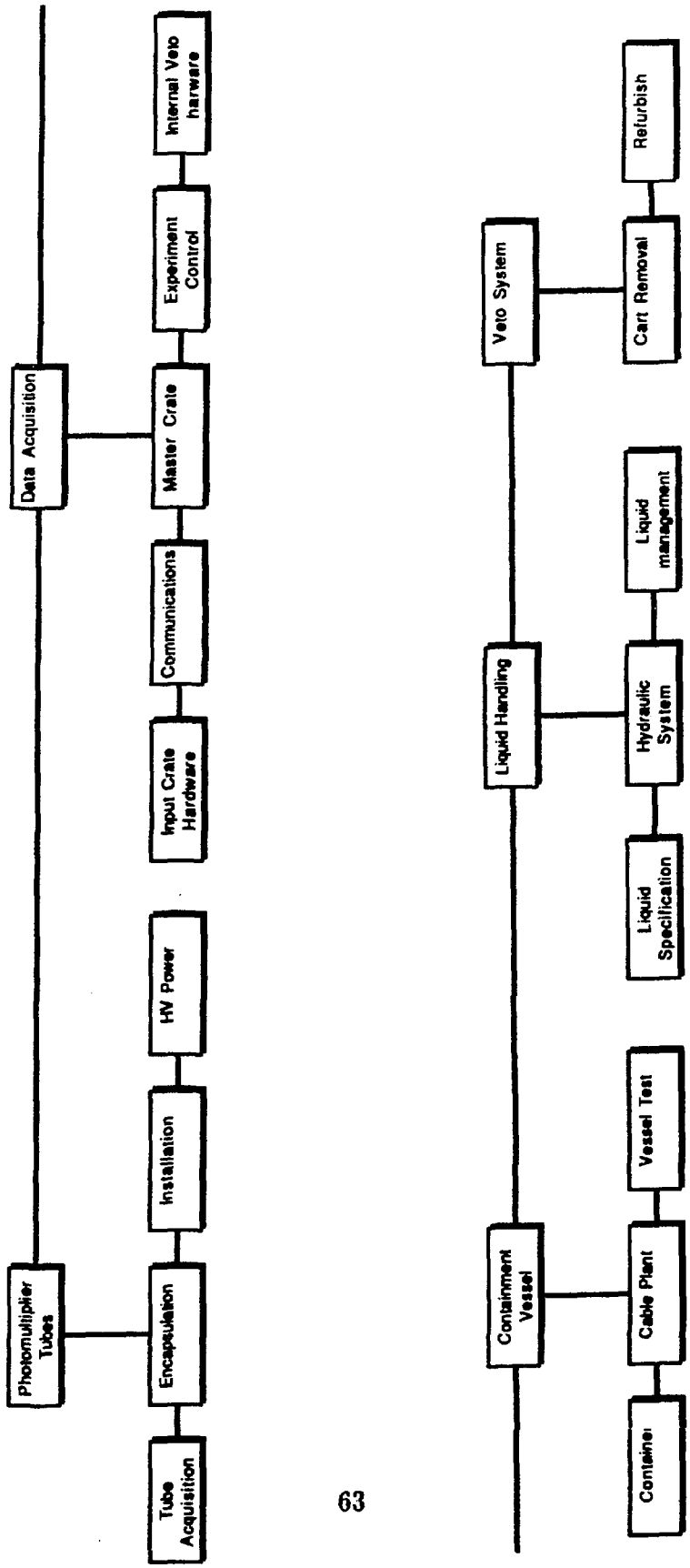

Fig. 29. A PERT chart for the construction process with a starting date of 5/11/90. Completion of the construction is expected by 5/14/92, when acquisition of beam data will begin.

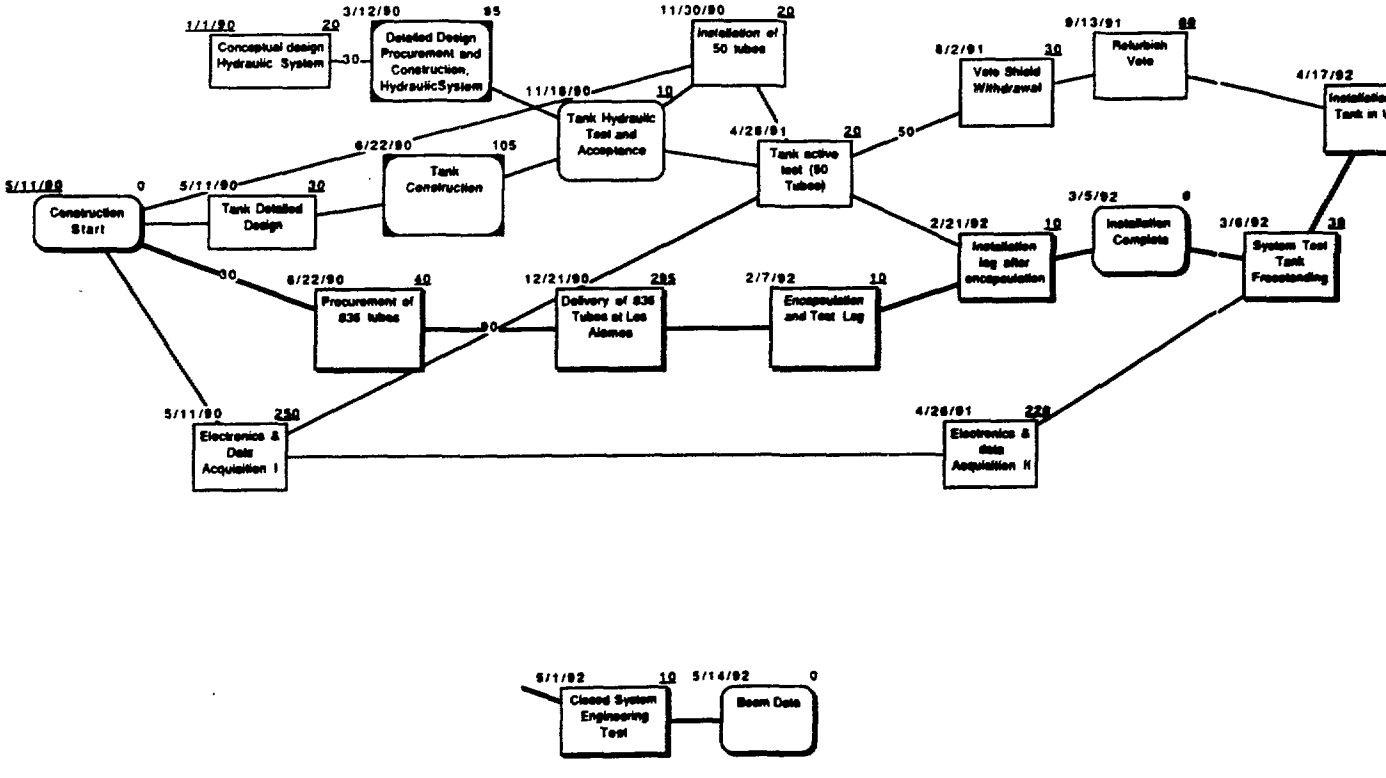

APPENDIX A. EVENT RATES

An estimate of our event rates is shown in Table A1 for neutrinos from pion decay at rest and Table A2 for neutrinos from pion decay in flight. A simulation[11] of the A6 beam line has determined the neutrino flux at a distance of $\sim$ 27 m from the beam stop to be $5.4 \times 10^{13} \nu_\mu/\mathrm{cm}^2$ from pion decay at rest and an equal number of ν_e and $\bar{\nu}_\mu$ from muon decay at rest after 130 days of running at LAMPF ($\sim$ 3000 actual hours) or 8678 Coulombs. Using 5.9×10^{30} C nuclei, a cross section[12] of 1.5×10^{-41} cm^2, and an acceptance of 0.298, we can estimate the number of $\nu_e \mathrm{C} \rightarrow e^- \mathrm{N}$ events to be

$$(5.4 \times 10^{13})(1.5 \times 10^{-41})(0.298)(5.9 \times 10^{30}) = 1380.$$

The 0.298 $\nu_e \mathrm{C} \rightarrow e^- \mathrm{N}$ acceptance is the product of the shield live time (74.3%), the 25-cm fiducial volume cut efficiency (66.3%), the electron identification efficiency (90%), and the fraction of events with $E_e > 10$ MeV (67%). Similarly, we estimate 295 $\nu e \rightarrow \nu e$ events and 1055 $\nu \mathrm{C} \rightarrow \nu \mathrm{C}^*$ events in one year from pion decay at rest. For maximal $\bar{\nu}_\mu \rightarrow \bar{\nu}_e$ mixing, we would obtain 16,540 $\bar{\nu}_e p$ events with $E_e > 37$ MeV, and we get several high-energy $\nu_e \mathrm{C} \rightarrow e^- \mathrm{N}$ scattering events for a 10^{-8} $\pi^0 \rightarrow \nu\bar{\nu}$ branching ratio.

For pion decay in flight, we estimate $2.0 \times 10^{12} \nu_\mu/\mathrm{cm}^2$ ($3.9 \times 10^{11} \bar{\nu}_\mu/\mathrm{cm}^2$) for $E_\nu > 80$ MeV after 130 days of running at LAMPF. With the present A6 beam stop configuration, we should detect 2110 νp elastic scattering events above a 10-MeV threshold (due to saturation effects in the scintillator, a 10-MeV threshold corresponds to $\sim$ 20-MeV proton energy), while many more events should be observed if a decay path is added to the beam stop. For νp elastic scattering, we use a tighter 50-cm fiducial volume cut in order to reduce neutron-induced background. In addition, we should observe about 3400 $\nu_\mu \mathrm{C} \rightarrow \mu^- \mathrm{N}$ charged-current events and 16,950 $\nu_e \mathrm{C} \rightarrow e^- \mathrm{N}$ events for maximal $\nu_\mu \rightarrow \nu_e$ mixing.

Table A1. Event rates per 130 days for neutrinos from pion decay at rest.

Process	Cross Section (cm^2)	Acceptance	Events	Comments
$\bar{\nu}_e p \rightarrow e^+ n$	1.5×10^{-40}	0.173	16,540	max-mix., $E_e > 37$ Me
$\nu_e\ ^{12}\mathrm{C} \rightarrow e\ ^{12}\mathrm{N}$	1.46×10^{-41}	0.298	1380	$E_e > 10$ MeV
$\nu_e\ ^{13}\mathrm{C} \rightarrow e^{13}\mathrm{N}$	1.09×10^{-40}	0.426	165	$E_e > 10$ MeV
$\nu e^- \rightarrow \nu e^-$	4.0×10^{-43}	0.288	295	$E_e > 10$ MeV
$\nu \mathrm{C} \rightarrow \nu \mathrm{C}^*$	7.5×10^{-42}	0.443	1055	C* emits 15.11 MeV γ

Table A2. Event rates per 130 days for neutrinos from pion decay in flight.

Process	Cross Section (cm^2)	Acceptance	Events	Comments
$\pi^0 \rightarrow \nu\bar{\nu}$		0.443	$\sim 10^8$	for B.R.=1
$\eta \rightarrow \nu\bar{\nu}$		0.443	$\sim 10^4$	for B.R.=1
$\nu_\mu p \rightarrow \nu_\mu p$	4.5×10^{-40}	0.203	2110	$E_p > 20$ MeV
$\nu_e \mathrm{C} \rightarrow e^- \mathrm{N}$	2.8×10^{-39}	0.513	16,950	max-mix., $E_e > 60$ MeV
$\nu_\mu \mathrm{C} \rightarrow \mu^- \mathrm{N}$	7.4×10^{-40}	0.395	3400	$E_\mu > 10$ MeV
$\bar{\nu}_\mu p \rightarrow \mu^+ n$	2.5×10^{-40}	0.395	450	$E_\mu > 10$ MeV
$\bar{\nu}_\mu \mathrm{C} \rightarrow \mu^+ B$	2.6×10^{-40}	0.389	240	$E_\mu > 10$ MeV
$\nu_\mu \mathrm{C} \rightarrow \nu_\mu \mathrm{C}^*$	3.3×10^{-41}	0.443	170	C* emits 15.11 MeV γ
$\nu_\mu e^- \rightarrow \nu_\mu e^-$	2.5×10^{-43}	0.443	10	$E_e > 10$ MeV

APPENDIX B. BACKGROUND LEVELS AND OSCILLATION FITS

The principal backgrounds contributing to $\nu_\mu \rightarrow \nu_e$ and $\bar{\nu}_\mu \rightarrow \bar{\nu}_e$ oscillations are discussed in Sections 4 and 5, respectively. Here we present the results of an alternate calculation of the expected event rates (assuming maximal mixing) using a Fermi-gas model[12] of lepton production by neutrinos on free and bound nucleons. We use this same model to calculate an independent estimate of the principal backgrounds (except cosmic-ray induced) described in Sections 4 and 5, as well as some of the other less significant backgrounds.

To obtain the relevant lepton yields, we fold the incident neutrino energy spectrum with the model differential cross section for lepton production. The decay-at-rest neutrino spectra are well known. The decay-in-flight spectra were obtained from a Monte Carlo simulation of the A6 beam line, as mentioned in Section 4.2.

The mathematical details of the Fermi-gas model are fully described in Ref. 22, so we shall omit them here. The total cross sections per nucleon obtained from the model are shown in Figs. B1 and B2 for electrons and muons, respectively. The Q values shown are appropriate for a ^{12}C target and no free nucleon in the final state; they are slightly greater if a free nucleon is in the final state. The differential cross section at $E_\nu = 200$ MeV and $\theta = 90°$ is illustrated in Fig. B3 for the electron from a ^{12}C target.

B.1 $\nu_\mu \rightarrow \nu_e$ Oscillations

The calculated decay-in-flight neutrino spectrum from $\pi^+ \rightarrow \mu^+\nu$ is shown in Fig. B4. Assuming maximal mixing, we then fold this spectrum (now ν_e) with the model differential cross section for $^{12}\mathrm{C}(\nu_e, e^-)\mathrm{X}$ ($Q = 16.8$ MeV) to obtain the electron spectrum shown in Fig. B5. If we choose the lower limit of electron energy to be 60 MeV, then the optimum choice of upper limit would be 140 MeV; this choice becomes apparent later when we analyze background events from $\pi^+ \rightarrow e^+\nu_e$. The number of events obtained for 130 days (8678 C of beam) in the energy range $60 < E_e < 140$ MeV is 25741. After applying cuts for shield live time (0.860), fiducial volume (0.663), and e^- detection efficiency (0.9) in order to reject protons, we obtain $0.513 \times 25741 = \underline{13205}$ net counts.

B.1.1 $\mu^+ \rightarrow e^+\nu_e\bar{\nu}_\mu$

The principal background for $\nu_\mu \rightarrow \nu_e$ arises from $\pi^+ \rightarrow \mu^+\nu_\mu$ (decay in flight), followed by $\mu^+ \rightarrow e^+\nu_e\bar{\nu}_\mu$ (decay in flight), then by $^{12}\mathrm{C}(\nu_e, e^-)\mathrm{X}$. The calculated ν_e spectrum

for μ^+ decay in flight is shown in Fig. B6. After folding with the model differential cross section, the electron spectrum shown in Fig. B7 is obtained. The net number of events with $60 < E_e < 140$ MeV is then $0.513 \times 7.13 = 3.66$ (8678 C of beam), which is $\underline{2.8 \times 10^{-4}}$ of the maximum signal.

B.1.2 $\pi^+ \rightarrow e^+\nu_e$

The second most important background for $\nu_\mu \rightarrow \nu_e$ is due to the less common decay $\pi^+ \rightarrow e^+\nu_e$. The calculated ν_e spectrum for this decay is shown in Fig. B8. The resulting electron spectrum is shown in Fig. B9. Because of the rising shape of this background a low cut-off at high energies is desirable. The net number of events in the range $60 < E_e < 140$ MeV is $0.513 \times 3.82 = 1.96$, which is $\underline{1.5 \times 10^{-4}}$ of the maximum signal.

B.1.3 $^{12}C(\nu_\mu, \mu^-)X$

A less important background comes about from misidentifying a μ^- as an e^- because of the number of photons produced, both Čerenkov and scintillation. The ν_μ spectrum is given in Fig. B4. The yield of Čerenkov photons versus energy is plotted in Fig. B10. Folding the ν_μ spectrum with the differential cross section for μ^- production off ^{12}C yields the μ^- spectrum shown in Fig. B11. Taking account of the fact that the scintillator produces one photon per 2000 eV deposited, together with the Čerenkov yield, we deduce that a 79 MeV μ^- is equivalent in light output to a 60 MeV electron. From Fig. B11, we obtain 527 events with $E_\mu > 79$ MeV. In addition to the usual cuts for shield live time (0.860) and fiducial volume (0.663), we must include the probability that the muon does not decay (~ 0.1) and the likelihood of identifying the μ^- Čerenkov cone as being due to an e^- (0.03). The net number of events is then $0.00171 \times 527 = 0.90$, which is $\underline{6.8 \times 10^{-5}}$ of the maximum signal.

B.1.4 $\nu_\mu e \rightarrow \nu_\mu e$

The number of events resulting from $\nu_\mu e^-$ elastic scattering can be estimated as follows:

2.5×10^{-43} cm$^2/e^- \times 8e^-/CH_2 \times 5.9 \times 10^{30} CH_2 \times 2 \times 10^{12} \nu/\text{cm}^2 = 23.6$ events.

In addition to the usual cuts (0.513), we include a cut for angles greater than 30° (0.0693) and a cut for e^- energies greater than 60 MeV (~ 0.5). The net number of events is then $0.0178 \times 23.6 = 0.42$, which is $\underline{3.2 \times 10^{-5}}$ of the maximal signal.

B.1.5 Cosmic Rays

We consider four types of background associated with cosmic rays: (1) atmospheric neutrons; (2) neutrons arising from muon deep inelastic scattering in the vertical annular region surrounding the shield; (3) neutrons from μ^- capture in the region adjacent to the shield; and (4) muons that stop and decay in the detector. The first three processes can give both proton and electron signals in the detector, the latter via (n,γ) reactions, while the last process yields only electron events.

The muonic component of cosmic rays has a flux of ~ 170 s^{-1}m^{-2} at sea level, and is $\sim 20\%$ greater at Los Alamos. The atmospheric neutron component has a flux of ~ 25 s^{-1}m^{-2} at sea level, and is a factor of ~ 7 greater at Los Alamos. The muons are attenuated in the steel overburden and surrounding tuff with an attenuation length of ~ 1300 g/cm^2 down to ~ 3000 g/cm^2 below the surface (at Los Alamos), after which the attenuation length is ~ 4300 g/cm^2. The neutrons attenuate in steel ($\rho = 7.87$ g/cm^3) with an attenuation length of 171 g/cm^2, and in tuff ($\rho = 1.6$ g/cm^3) an attenuation length of 150 g/cm^2 is assumed. The neutron yield per g/cm^2 increases with depth as the ~ 0.6 power, reflecting deep inelastic muon reactions and the increasing average muon energy with depth.

E645 reports 2.3×10^4 proton events per 130 days with energy greater than 160 MeV, and our calculations agree almost exactly with this figure. We estimate that ~ 0.2 of the neutrons penetrate the shield without being detected, and we used 50 mb for the np elastic cross section. About 95% of these events are due to neutrons arising from muon deep inelastic reactions.

E645 observes 13 high-energy ($E > 60$ MeV) electron events per 130 days (acceptance corrected), and our calculations give 26 events per 130 days. About 70% of these events are due to muons stopping and decaying in the detector and $\sim 30\%$ are due to (n,γ) reactions, with the neutron produced by muon deep inelastic scattering. For the low-energy ($37 < E < 50$ MeV) electron events, E645 reports 24 events per 130 days for the first three run cycles (25% with only 1000 g/cm^2 overburden), and we calculate 28 events. Clearly, our calculational techniques work very well in describing the E645 backgrounds. Thus, we have every reason to be confident in applying these methods to the present experiment.

For the low-energy electron events, we predict 16 events, all due to (n,γ) reactions with neutrons arising from muon deep inelastic scattering. After applying cuts for undetected

neutron penetration of 75 cm of scintillator (0.161), shield live time (0.743), 25-cm fiducial volume (0.663), electron identification efficiency (0.9), and probability of neutron capture within 1 m (0.2), we obtain 0.86 events, which yields a background level of $\underline{1.5 \times 10^{-5}}$.

For the high-energy electron events, we predict 28 events, 90% from muon deep inelastic neutron production and 10% from muons stopping and decaying in the detector. After applying cuts for shield live time (0.860), 25-cm fiducial volume (0.663), electron identification efficiency (0.9), 200-MHz beam structure (0.2), and undetected neutron penetration of 75 cm of scintillator (0.9×0.161), we obtain 1.6 events, which yields a background level of $\underline{3.7 \times 10^{-5}}$. The photon spectrum from (n, γ) events with cosmic-ray induced neutrons is shown in Fig. B12.

B.1.6 Beam Neutrons

The neutron spectrum emanating from the beam stop was determined using the Monte Carlo code HETC. This spectrum was then attenuated by 8.5 m of steel ($\lambda = 171$ g/cm^2). The detector events were assumed due to the following (n, γ) processes: (1) neutron-proton bremsstrahlung, (2) neutron-proton capture, and (3) giant-dipole resonance. Details of the calculation are found in the LCD proposal. The resulting photon spectrum is shown in Fig. B12. The number of events with $60 < E_\gamma < 140$ MeV is 0.719. After applying the usual cuts (0.513) plus a cut provided by the 200-MHz beam structure (0.20), the net number of events is $0.103 \times 0.719 = 0.0741$, which is $\underline{5.6 \times 10^{-6}}$ of the maximal signal.

B.2 $\bar{\nu}_\mu \rightarrow \bar{\nu}_e$ Oscillations

The decay-at-rest neutrino spectra for ν_e and $\bar{\nu}_\mu$ from $\mu^+ \rightarrow e^+ \nu_e \bar{\nu}_\mu$ is shown in Fig. B13. Assuming maximal mixing, we then fold the $\bar{\nu}_\mu$ spectrum (now $\bar{\nu}_e$) with the model differential cross section for $\bar{\nu}_e p \rightarrow e^+ n$ to obtain the positron spectrum shown in Fig. B14. The number of events obtained for 130 days in the energy range $37 < E_e < 50$ MeV is 40848. After applying the usual cuts (0.443) and the recoil neutron detection efficiency (0.85), the net number of counts is $\underline{15382}$.

B.2.1 $\mu^- \rightarrow e^- \bar{\nu}_e \nu_\mu$

The principal background for $\bar{\nu}_\mu \rightarrow \bar{\nu}_e$ arises from π^- decay in flight (2.5%) followed by μ^- decay at rest (10%), then $\bar{\nu}_e p \rightarrow e^+ n$. We assume the number of π^- to be one-fifth the number of π^+. The $\bar{\nu}_e$ spectral shape is the same as the ν_e shape in Fig. B13.

After folding with the model differential cross section, we obtain the positron spectrum shown in Fig. B15. The net number of events in the range $37 < E_e < 50$ MeV is then $0.443 \times 0.025 \times 0.10 \times 0.85 \times 3856 = 3.63$, which is $\underline{2.4 \times 10^{-4}}$ of the maximal signal.

B.2.2 $\bar{\nu}_\mu p \rightarrow \mu^+ n$ with μ^+ Decay

The only other significant background involving a detectable recoil neutron arises from the sequence: $\pi^- \rightarrow \mu^- \bar{\nu}_\mu$ (decay in flight); $\bar{\nu}_\mu p \rightarrow \mu^+ n$; $\mu^+ \rightarrow e^+ \nu_e \bar{\nu}_\mu$ (decay at rest). The e^+ produced by the μ^+ decay at rest has an almost identical spectrum to the signal e^+. The π^- decay-in-flight $\bar{\nu}_\mu$ spectrum is assumed to be one-fifth of the π^+ decay-in-flight ν_μ spectrum (Fig. B4). The μ^+ spectrum obtained by folding the $\bar{\nu}_\mu$ spectrum with the model differential cross section is shown in Fig. B16. Assuming that the μ^+ with $E_\mu > 1$ MeV can be detected (a 1-MeV muon causes about 10 PMTs to be hit), we need only count those events with $E_\mu < 1$ MeV (4.22 events). In addition to the usual cuts (0.443 and 0.85), we must include only that fraction of e^+ in the range $37 < E_e < 50$ MeV (0.48). The net number of events is then $0.443 \times 0.85 \times 0.48 \times 4.22 = 0.76$, which is $\underline{5.0 \times 10^{-5}}$ of the maximal signal.

B.2.3 Backgrounds Without a Recoil Neutron

The principal background not accompanied by a recoil neutron arises from μ^+ decay at rest followed by $^{13}\mathrm{C}(\nu_e, e^-)\mathrm{X}$. This reaction has a relatively large event rate, despite the 1.1% ^{13}C abundance, because of its low Q value (1.7 MeV). The e^- spectrum is shown in Fig. B17. After applying the usual cuts (0.443), the net number of events in the range $37 < E_e < 50$ MeV is $0.443 \times 71.7 = 31.8$.

Other, less important, contributions to this type of background, together with their corresponding events per 130 days, are:

(a) νe elastic (2.75 events);

(b) π^+ decay in flight followed by $^{12}\mathrm{C}(\nu_\mu, \mu^-)\mathrm{X}$ followed by μ^- decay at rest, producing an e^- with a similar spectrum to the signal e^+ (6.42 events);

(c) $\pi^+ \rightarrow e^+ \nu_e$ decay at rest followed by $^{12}C(\nu_e, e^-)\mathrm{X}$ (4.65 events).

The sum for all the backgrounds without a recoil neutron is 45.6 events, which taken with the 1.7% accidental neutron rate yields a background level of $45.6 \times 0.017/15382 = 5.0 \times 10^{-5}$.

B.3 Background Summary

In Table B1 we summarize the background levels for $\nu_\mu - \nu_e$ and $\bar{\nu}_\mu - \bar{\nu}_e$ oscillations per 130 days (8678 C of beam). The estimates made in Sections 4 and 5 are given in brackets, where applicable. Note that the levels for the worst background in each experiment are the same and the others are in substantial agreement.

B.4 Oscillation Fits

The sensitivity of this experiment to $\bar{\nu}_\mu \rightarrow \bar{\nu}_e$ and $\nu_\mu \rightarrow \nu_e$ oscillations was studied by generating data sets with the predicted backgrounds and then fitting for the oscillation signal. This allowed the expected oscillation limits to be studied as a function of energy resolution, absolute energy calibration and neutron tagging efficiency. Maximum likelihood fits to the data were done using the CERN Library program Minuit. For each set of conditions, 100 data sets were generated with statistical fluctuations; a fit was then done for each data set and the 90% confidence level for the upper limit on the oscillation signal was histogrammed.

For the $\bar{\nu}_\mu \rightarrow \bar{\nu}_e$ channel, only the backgrounds from $\mu^- \rightarrow e^- \bar{\nu}_e \nu_\mu$, $\nu_e\ ^{13}\mathrm{C} \rightarrow e^- \mathrm{X}$ and $\nu_e\ ^{12}\mathrm{C} \rightarrow e^- \mathrm{X}$ were included. Although the $\nu_e\ ^{13}\mathrm{C}$ background is negligible at the expected neutron tagging accidental rate of 1.7%, it was included in order to study the effects of higher accidental rates. Likewise, in the region over which the fits were done (35–52 MeV) there is no background from $\nu_e\ ^{12}\mathrm{C}$, but a shift in the energy calibration could push some counts into this region. The $\nu_e\ ^{12}\mathrm{C}$ was included in the data sets, but it was not a parameter in the fits. Figure B18 shows the predicted spectrum after 2 years of running assuming $\sin^2(2\theta) = 1 \times 10^{-3}$ and $\Delta m^2 = 100$ eV^2. In Fig. B19, the limits on $\sin^2(2\theta)$ are given for large Δm^2. The spread of the results is simply due to the difference in statistical fluctuations between the data sets. The median result of $\sin^2(2\theta) \leq 2.7 \times 10^{-4}$ is taken to be our experimental limit. In these fits the $\mu^- \rightarrow e^- \bar{\nu}_e \nu_\mu$ background was constrained to be within $\pm 10\%$ of the predicted level. If this constraint is loosened to $\pm 20\%$, the median result worsens to $\sin^2(2\theta) \leq 2.9 \times 10^{-4}$. Increasing the neutron tagging accidental rate from 1.7% to 10% increased the median limit to $\sin^2(2\theta) \leq 3.5 \times 10^{-4}$. The importance of energy resolution was studied by varying the gaussian response function from 9% to 12% FWHM and by shifting the data in energy relative to spectra used in the fitting. The results were not sensitive to the energy resolution, but the absolute energy calibration was found to be important. A shift of 1 MeV increased the median limit to 3.8×10^{-4} and

a shift of 2 MeV resulted in a limit of $\sin^2(2\theta) \leq 4.8 \times 10^{-4}$. It should be possible to calibrate the detector to better than 1 MeV in the region of the endpoint of the Michel spectrum.

The fits to the decay-in-flight data included the backgrounds from $\pi^+ \rightarrow e^+\nu_e$ and $\mu^+ \rightarrow e^+\nu_e\bar{\nu}_\mu$ decay in flight at the levels given in Sections B.1.1 and B.1.2. Figure B20 shows the predicted spectrum after two years of data collection, assuming Δm^2 is large and $\sin^2(2\theta) = 1 \times 10^{-3}$. The data was fit over the energy range from 60 MeV to 225 MeV with the backgrounds held to within $\pm 10\%$ of their predicted levels. Figure B21 gives the distribution of 90% confidence limits on $\sin^2(2\theta)$ for $\Delta m^2 = 100$ eV^2. The median of the distribution gives $\sin^2(2\theta) \leq 2.7 \times 10^{-4}$. If the constraints on the backgrounds are loosened to $\pm 20\%$ the median limit is $\sin^2(2\theta) \leq 3.4 \times 10^{-4}$.

Table B1. Summary of background levels. The numbers in brackets are from the independent estimates discussed in Sections 4 and 5.

$\nu_\mu \rightarrow \nu_e$: 13,205 events [16,950 (60-180 MeV)]
($60 < E_e < 140$ MeV, 8678 C of beam, maximal mixing)

$\mu^+ \rightarrow e^+\nu_e\bar{\nu}_\mu$	2.8×10^{-4}	$[2.6 \times 10^{-4}]$
$\pi^+ \rightarrow e^+\nu_e$	1.5×10^{-4}	$[6.0 \times 10^{-5}]$
$^{12}\mathrm{C}(\nu_\mu, \mu^-)\mathrm{X}$	6.8×10^{-5}	
$\nu e \rightarrow \nu e$	3.2×10^{-5}	
Cosmic rays	3.7×10^{-5}	$[3.5 \times 10^{-5}]$
Beam neutrons	5.6×10^{-6}	

$\bar{\nu}_\mu \rightarrow \bar{\nu}_e$: 15,382 events [16,540]
($37 < E_e < 50$ MeV, 8678 C of beam, maximal mixing)

$\mu^- \rightarrow e^-\bar{\nu}_e\nu_\mu$	2.4×10^{-4}	$[2.5 \times 10^{-4}]$
$\bar{\nu}_\mu p \rightarrow \mu^+ n, \mu^+$ decay	5.0×10^{-5}	$[3.5 \times 10^{-5}]$
Cosmic rays	1.5×10^{-5}	$[6.0 \times 10^{-5}]$
No neutron recoil	5.0×10^{-5}	$[5.7 \times 10^{-5}]$

Fig. B1. Total (ν, e) cross sections as a function of energy, using the Fermi-gas model of O'Connell.[22]

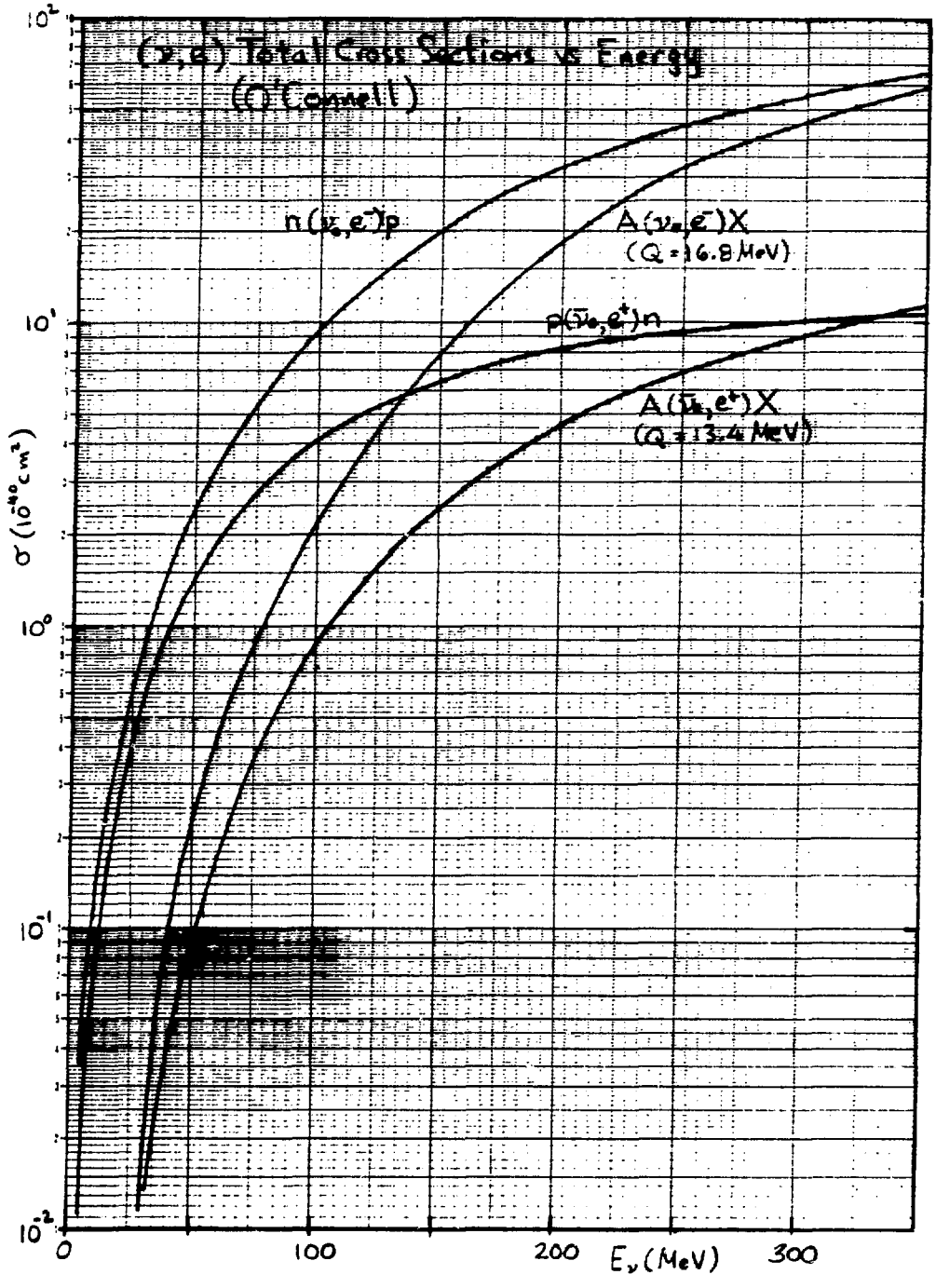

Fig. B2. Total (ν, μ) cross sections as a function of energy, using the Fermi-gas model of O'Connell.[22]

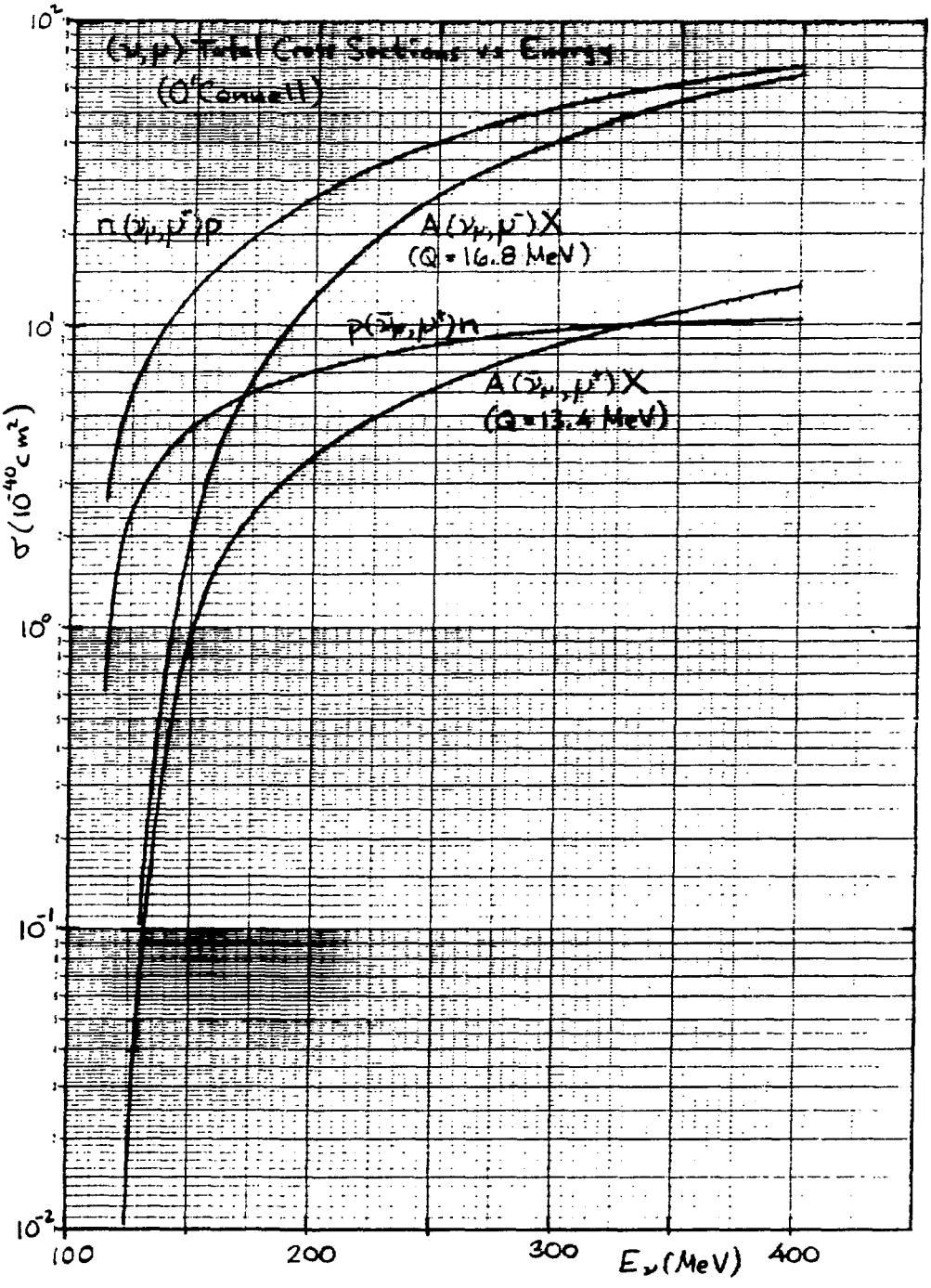

Fig. B3. The differential cross section at $E_\nu = 200$ MeV and $\theta = 90°$ for the electron from the reaction $\nu_e C \rightarrow e^- X$.

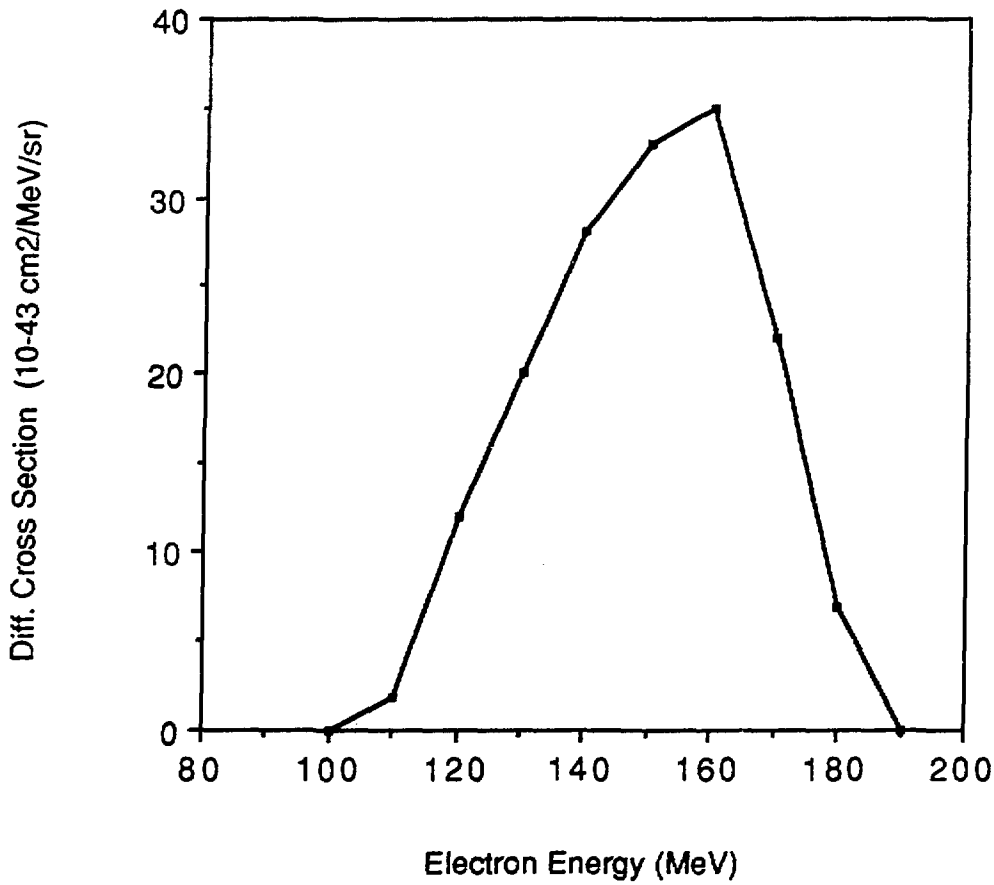

Fig. B4. The calculated decay-in-flight neutrino energy spectrum from $\pi^+ \rightarrow \mu^+ \nu_\mu$.

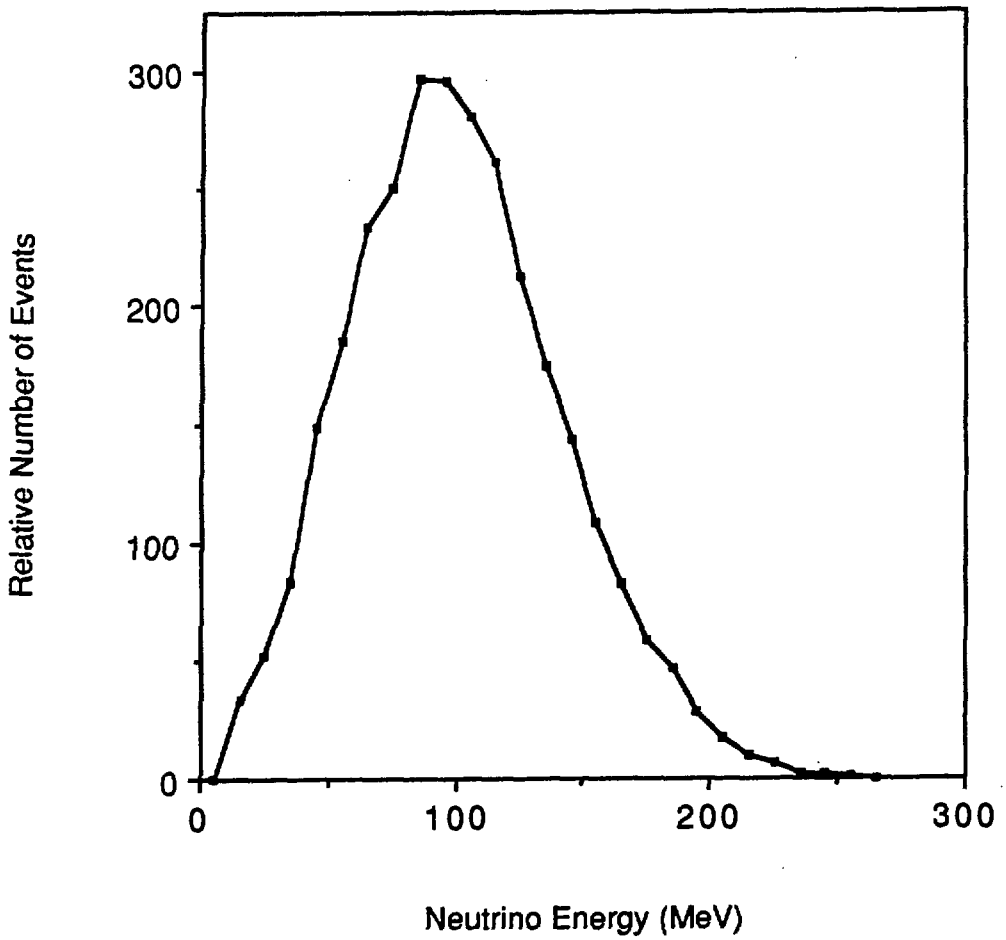

Fig. B5. The calculated electron energy spectrum from $\nu_\mu \rightarrow \nu_e$ oscillations, $^{12}C(\nu_e, e^-)X$.

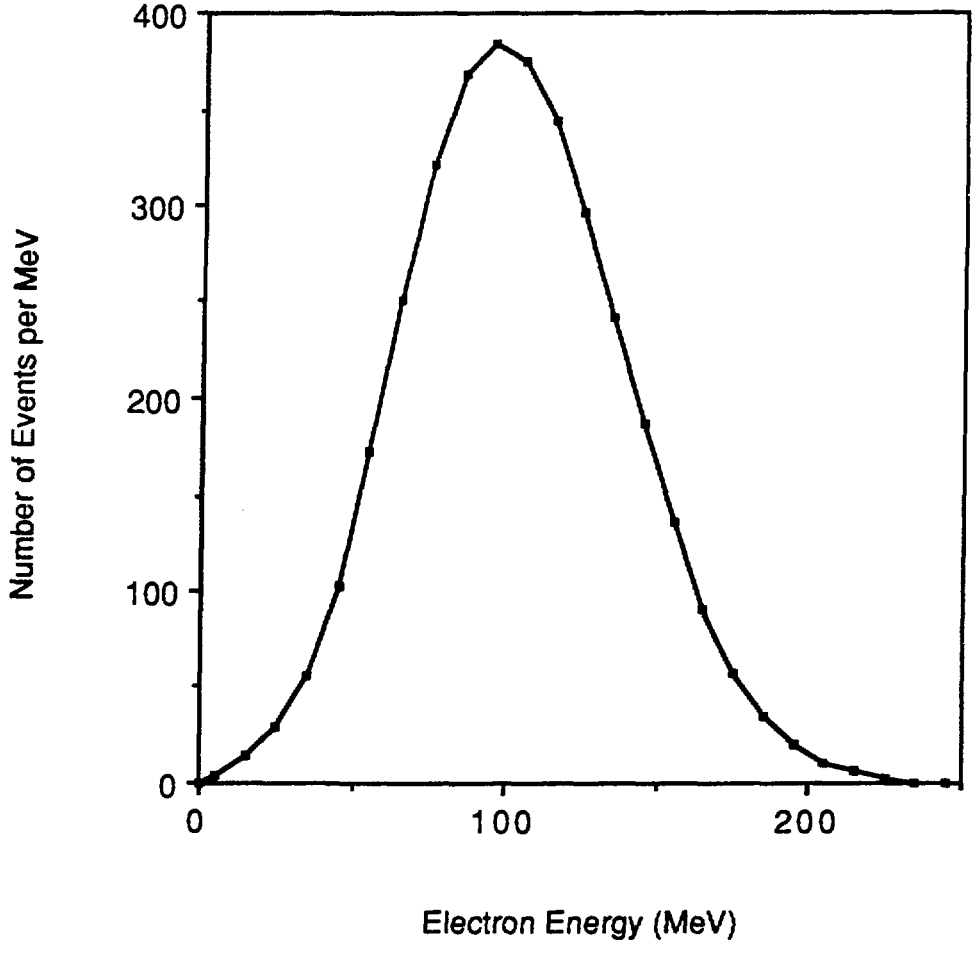

Fig. B6. The calculated ν_e energy spectrum from μ^+ decay in flight.

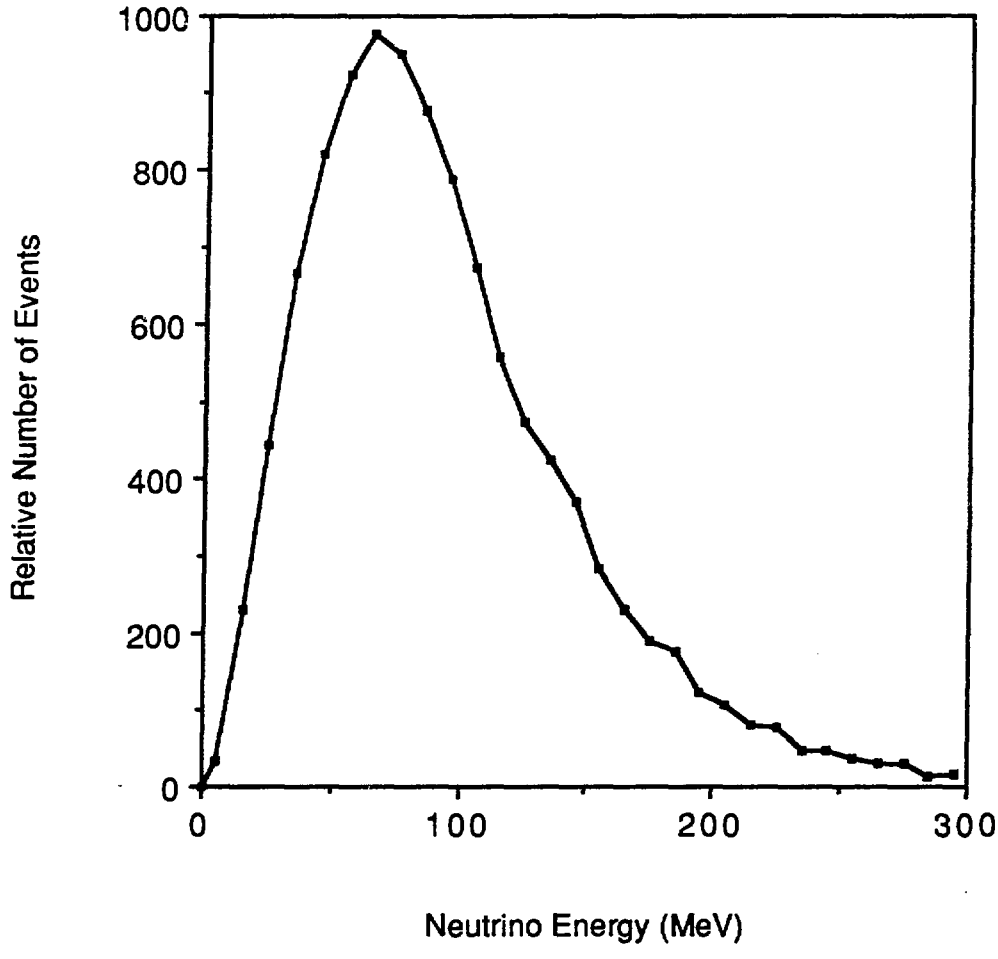

Fig. B7. The calculated electron energy spectrum from μ^+ decay-in-flight, $^{12}C(\nu_e, e^-)X$.

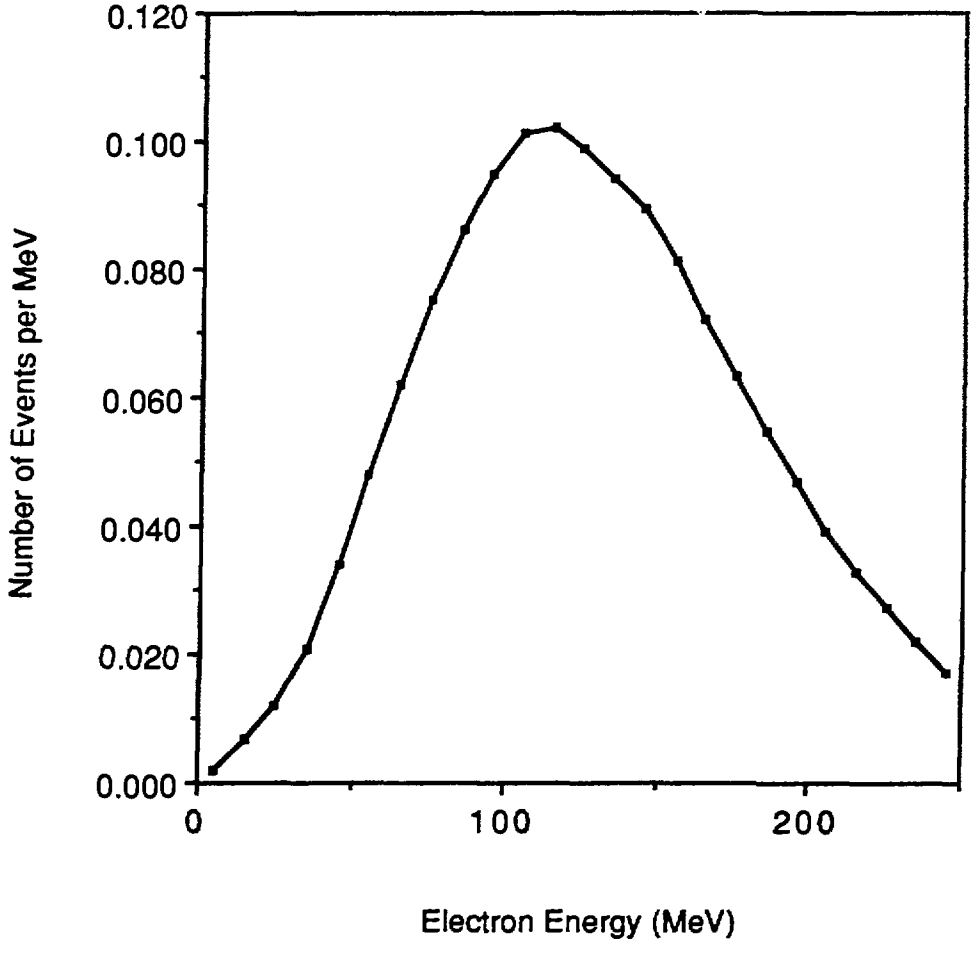

Fig. B8. The calculated ν_e energy spectrum from $\pi^+ \rightarrow e^+\nu_e$ decay in flight.

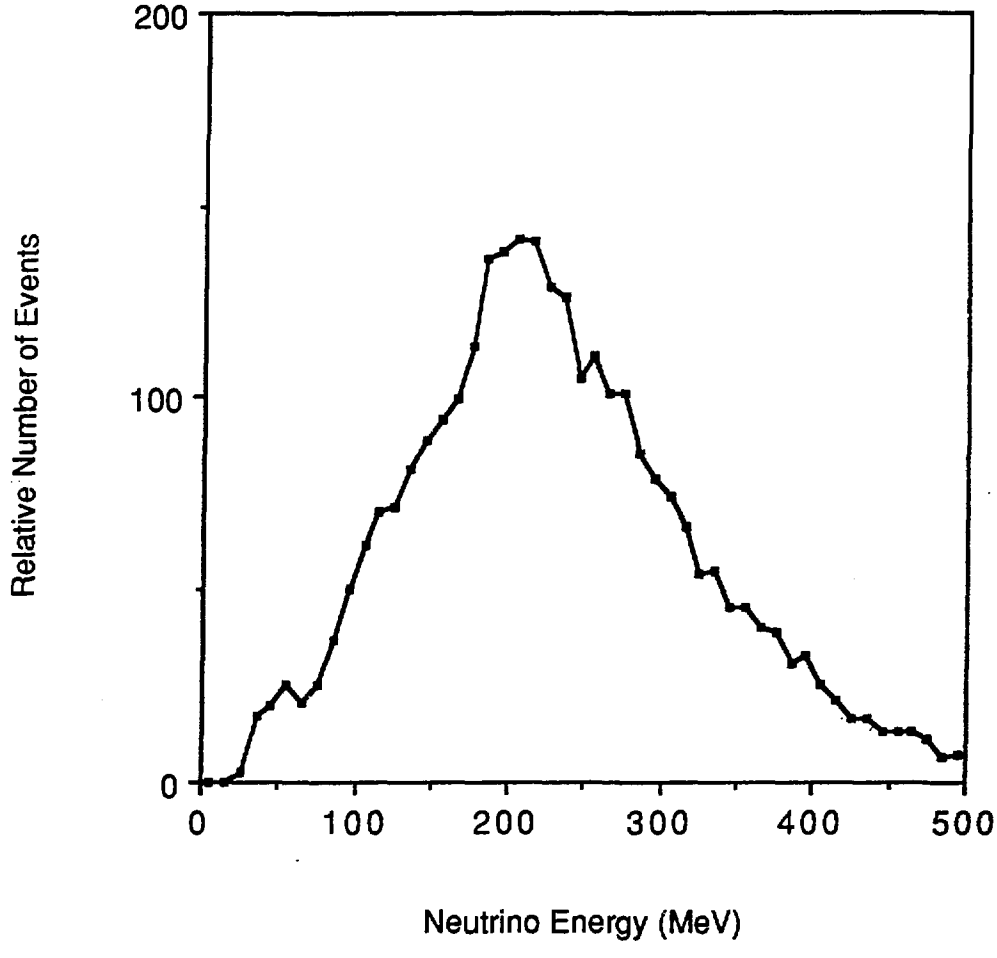

Fig. B9. The calculated electron energy spectrum from $\pi^+ \rightarrow e^+\nu_e$ decay-in-flight, $^{12}C(\nu_e, e^-)X$.

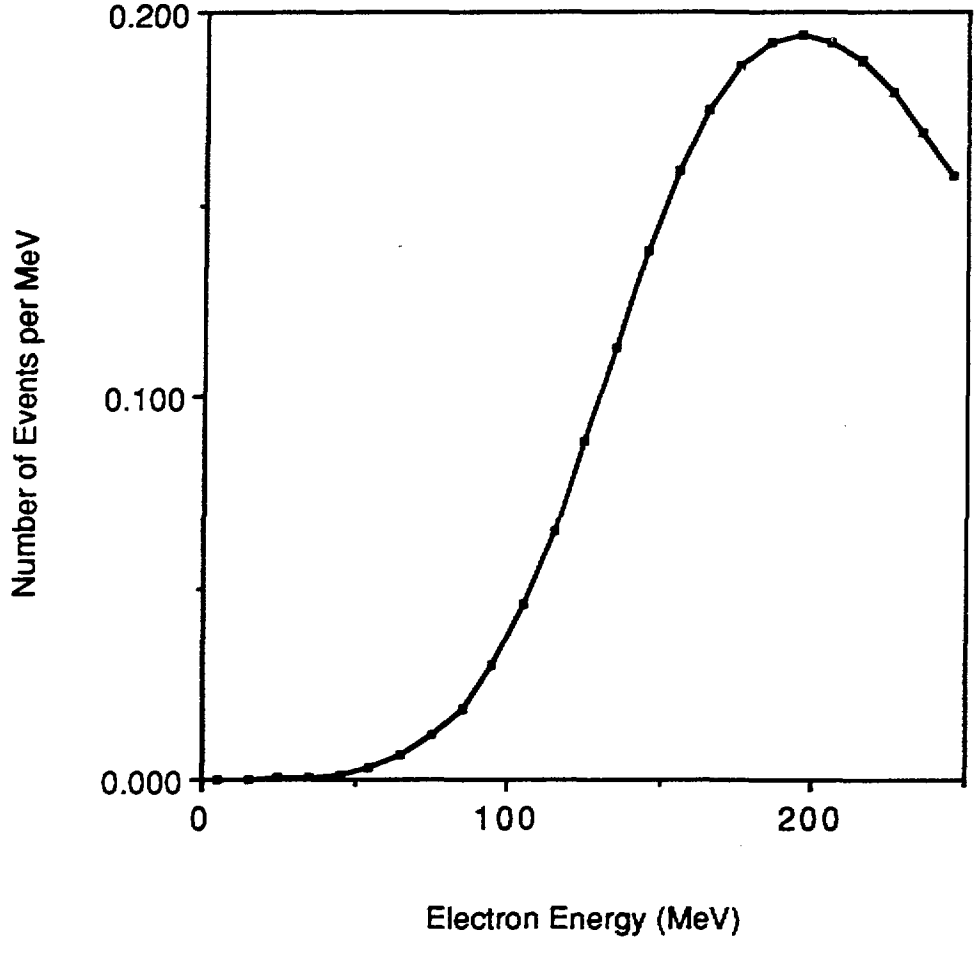

Fig. B10. The yield of Čerenkov photons versus energy for electrons, muons, pions, and protons.

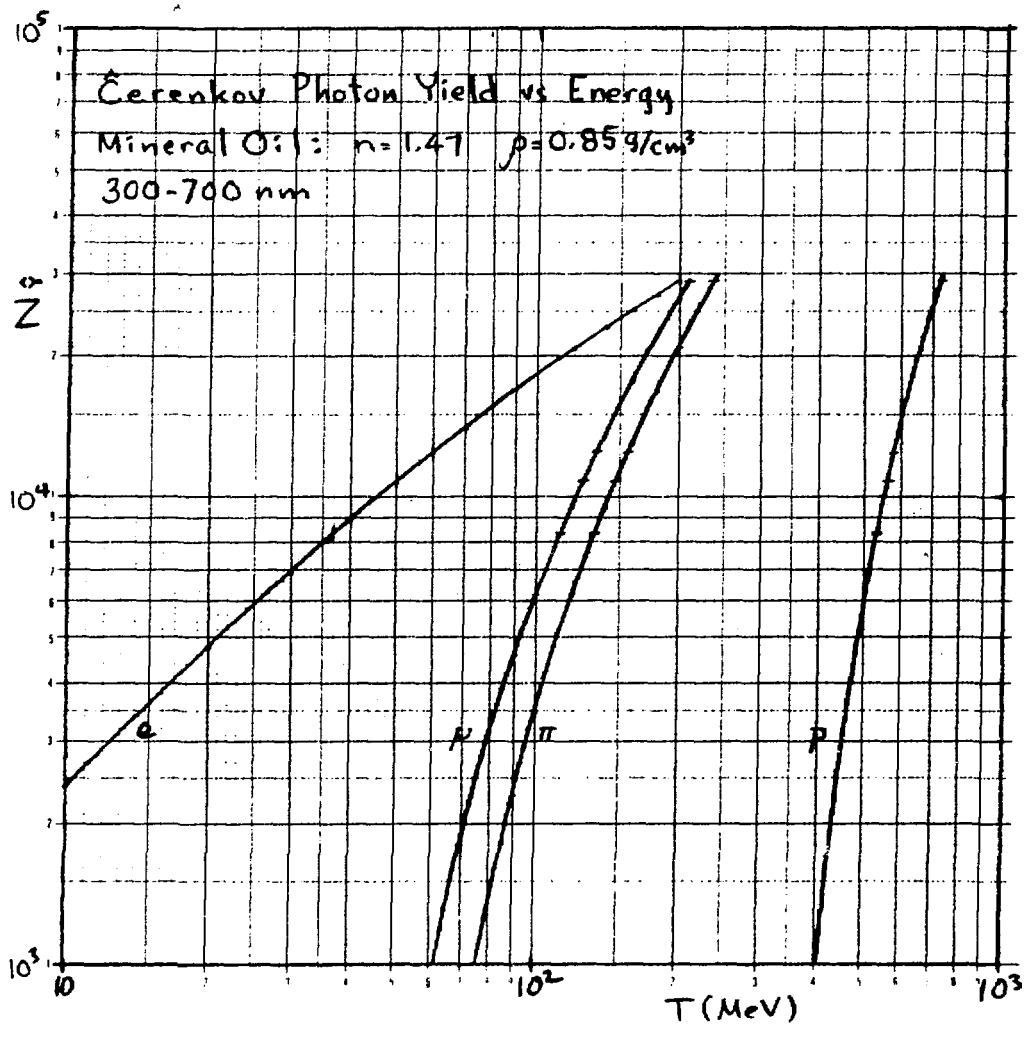

Fig. B11. The calculated muon energy spectrum from the reaction $\nu_\mu\ ^{12}C \rightarrow \mu^- X$.

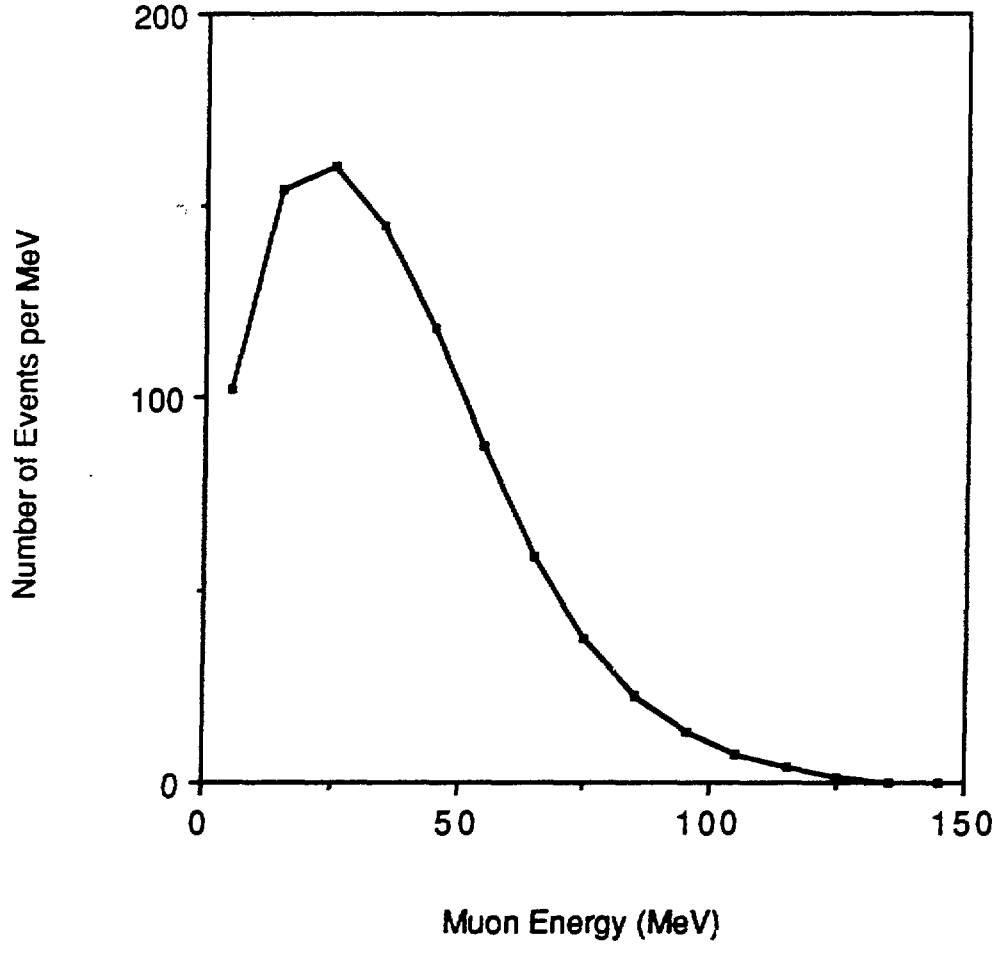

Fig. B12. The calculated photon energy spectrum from cosmic-ray and beam-neutron induced (n, γ) events.

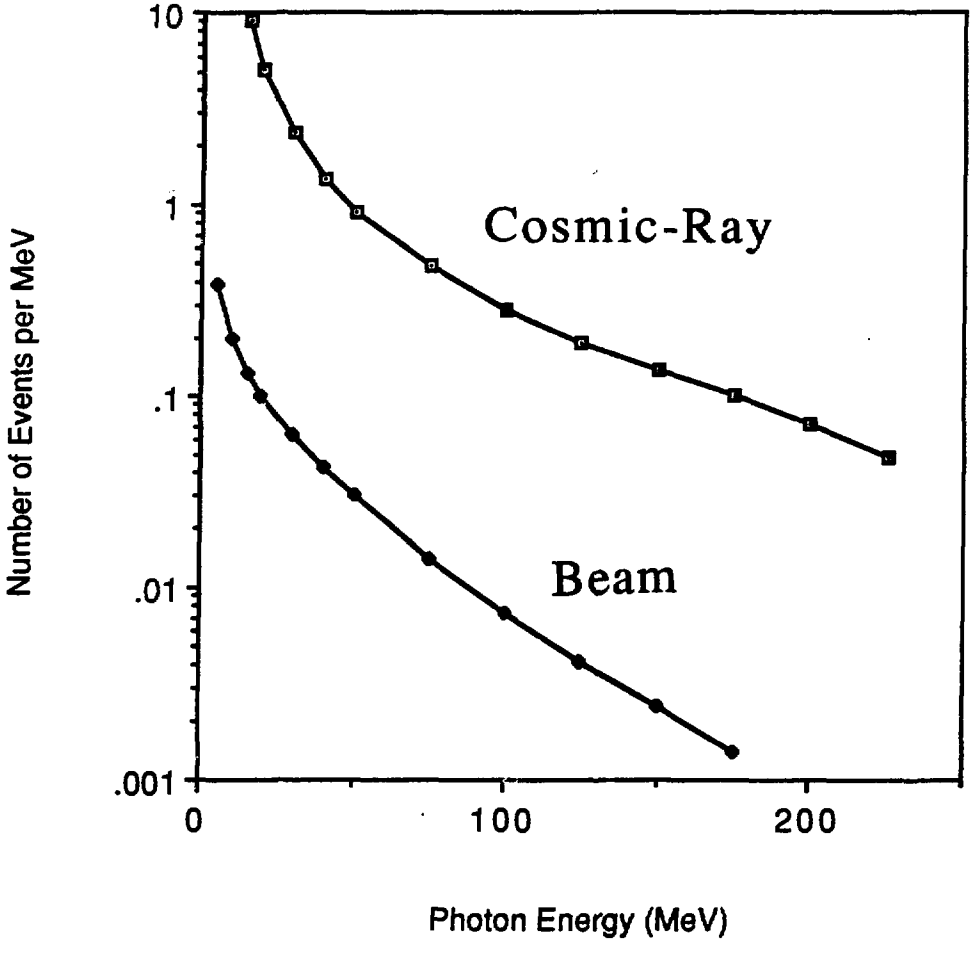

Fig. B13. The decay-at-rest neutrino energy spectra for ν_e and $\bar{\nu}_\mu$ from $\mu^+ \rightarrow e^+ \nu_e \bar{\nu}_\mu$.

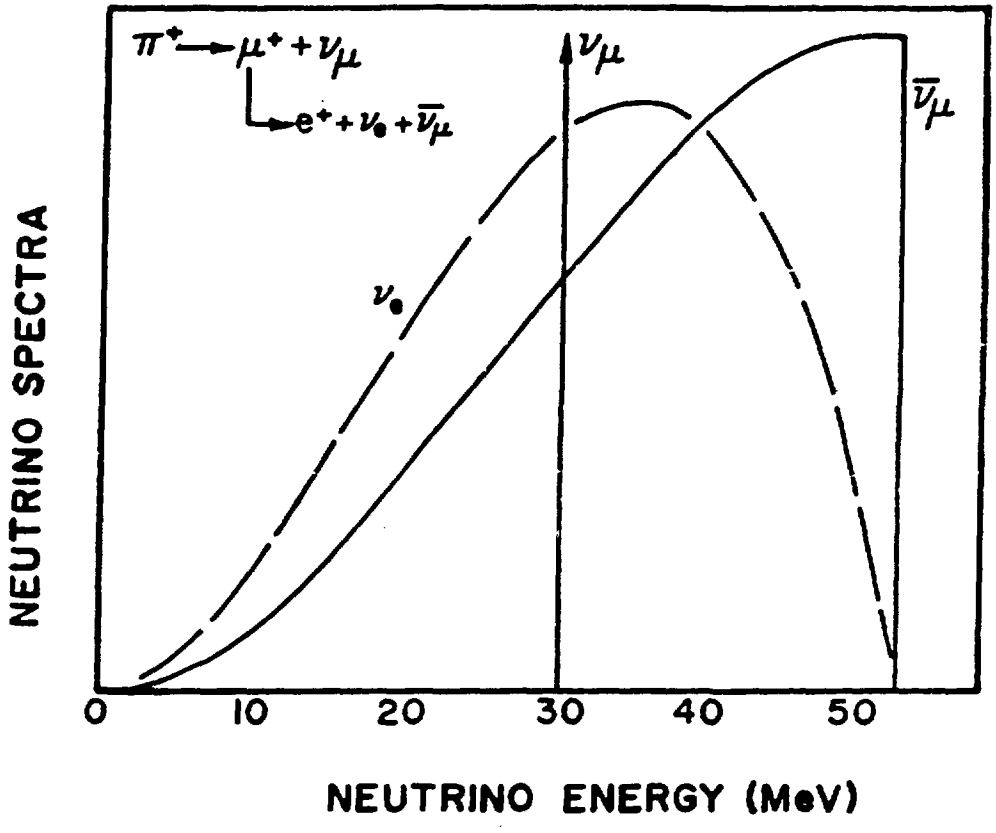

Fig. B14. The calculated positron energy spectrum from $\bar{\nu}_e p \rightarrow e^+ n$ for neutrinos from $\bar{\nu}_\mu \rightarrow \bar{\nu}_e$ oscillations.

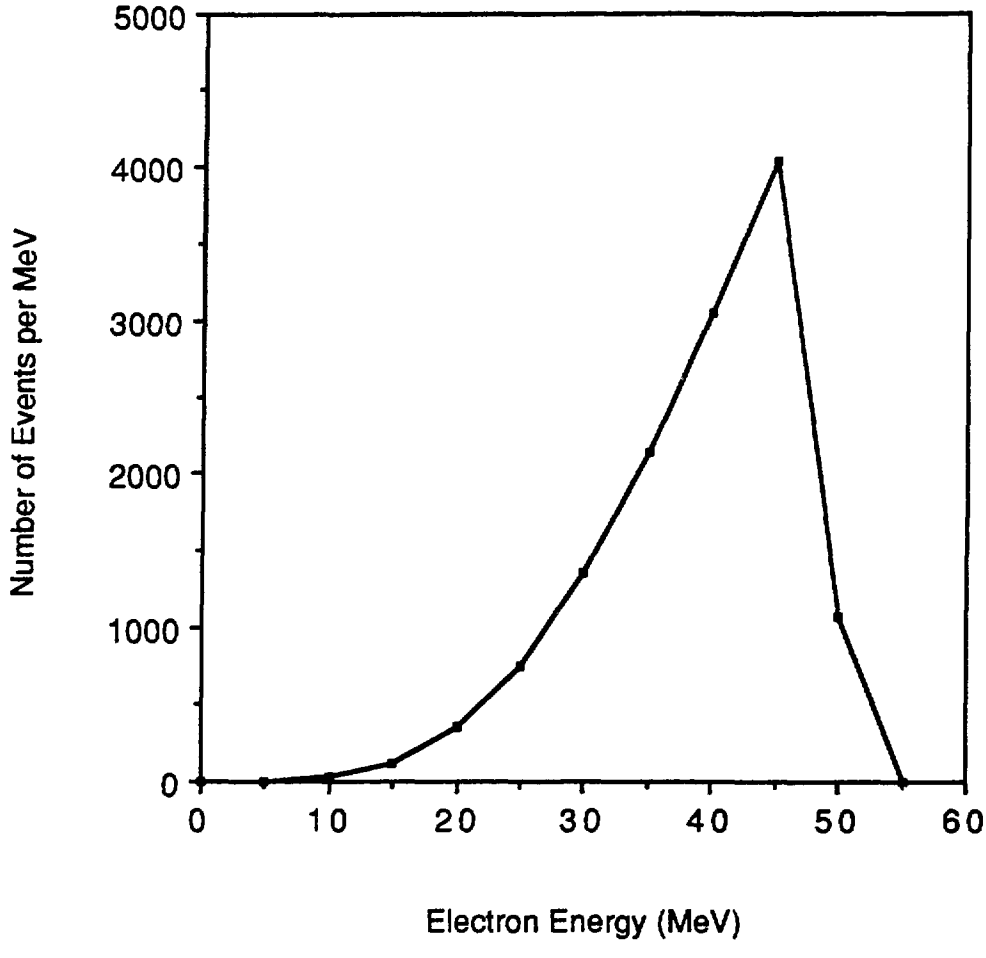

Fig. B15. The calculated positron energy spectrum from $\bar{\nu}_e p \rightarrow e^+ n$ for neutrinos from μ^- decay at rest.

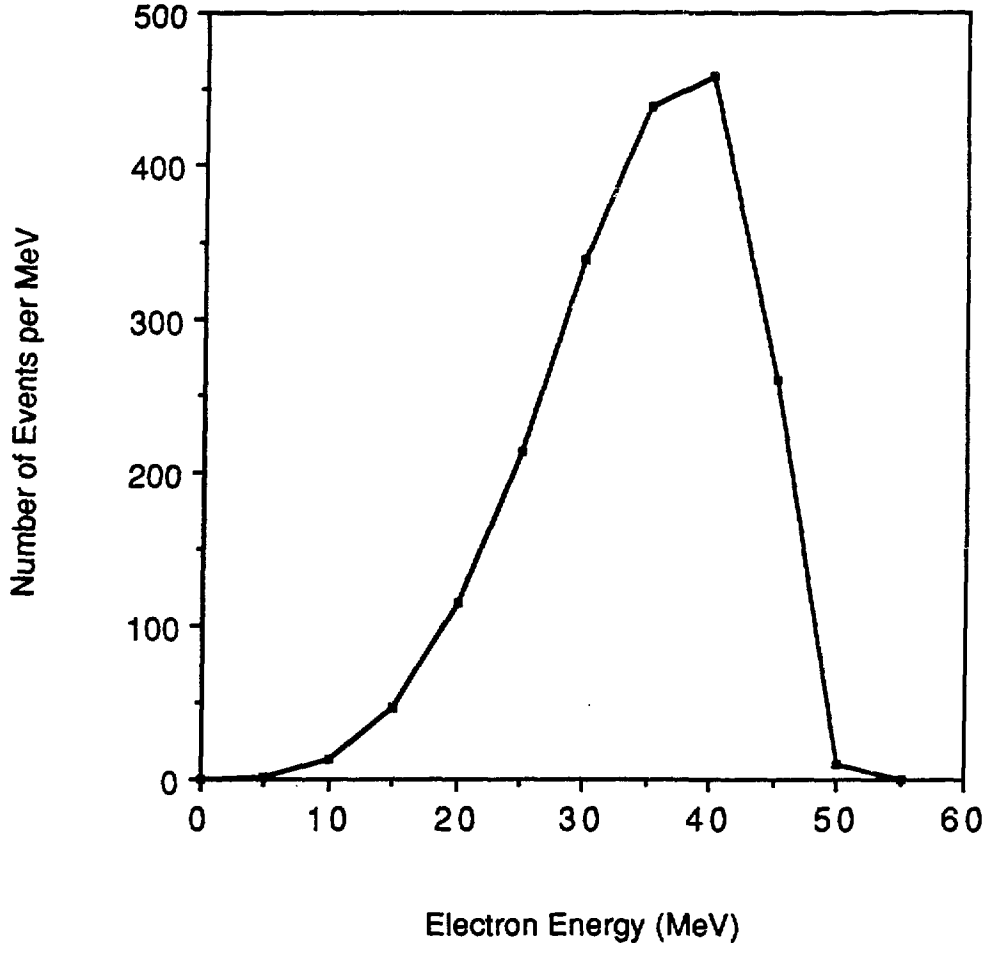

Fig. B16. The calculated muon energy spectrum from the reaction $\bar{\nu}_\mu p \rightarrow \mu^+ n$, $\bar{\nu}_\mu$ from π^- decay in flight.

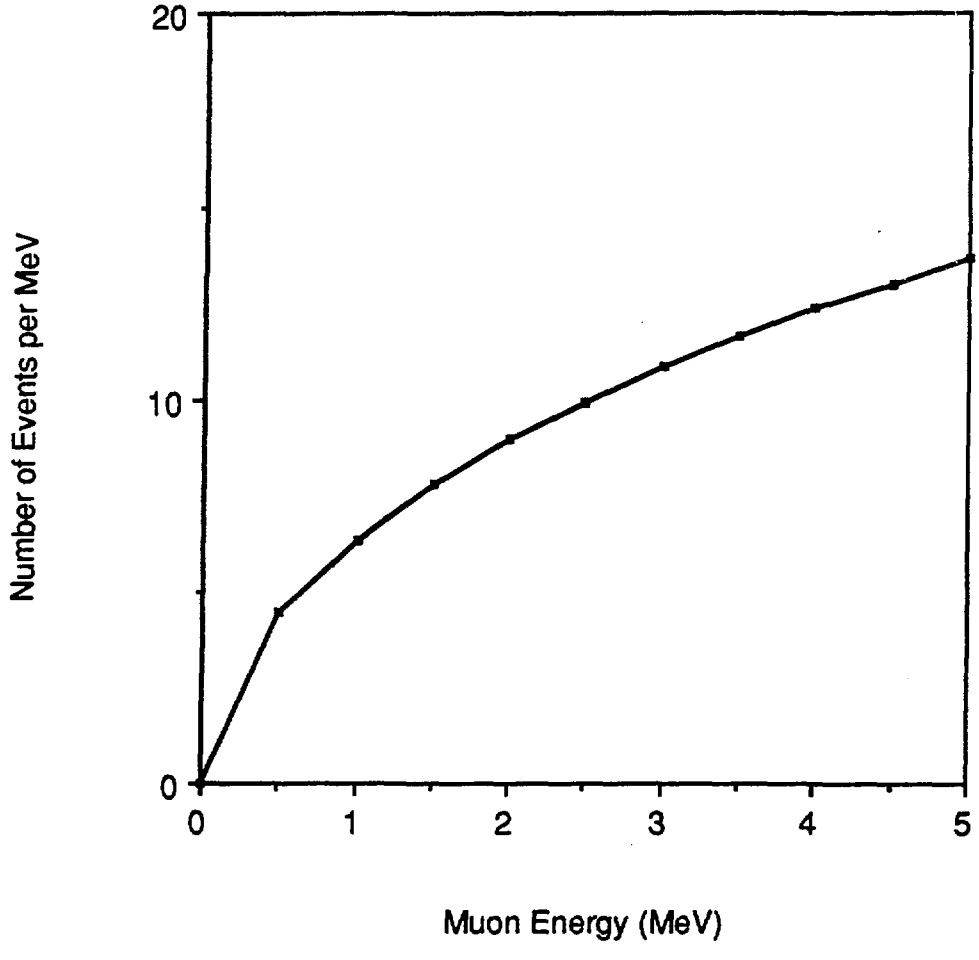

Fig. B17. The calculated electron energy spectrum from the reaction $\nu_e\ ^{13}C \rightarrow e^-X$, ν_e from μ^+ decay at rest.

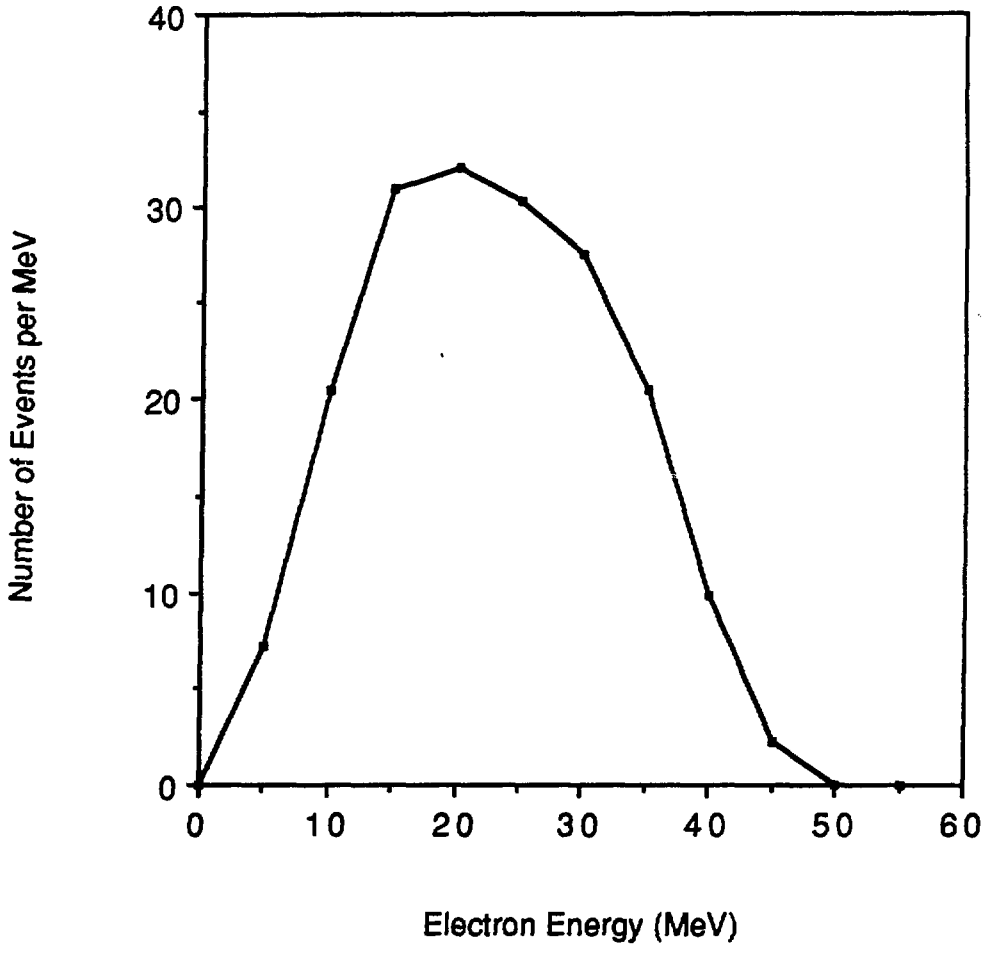

Fig. B18. The predicted electron energy spectra of the $\bar{\nu}_\mu \rightarrow \bar{\nu}_e$ oscillation signal and backgrounds after 2 years of data collection, assuming $\sin^2(2\theta) = 1 \times 10^{-3}$ and $\Delta m^2 = 100\ \mathrm{eV}^2$, which corresponds to a signal level of 5×10^{-4}.

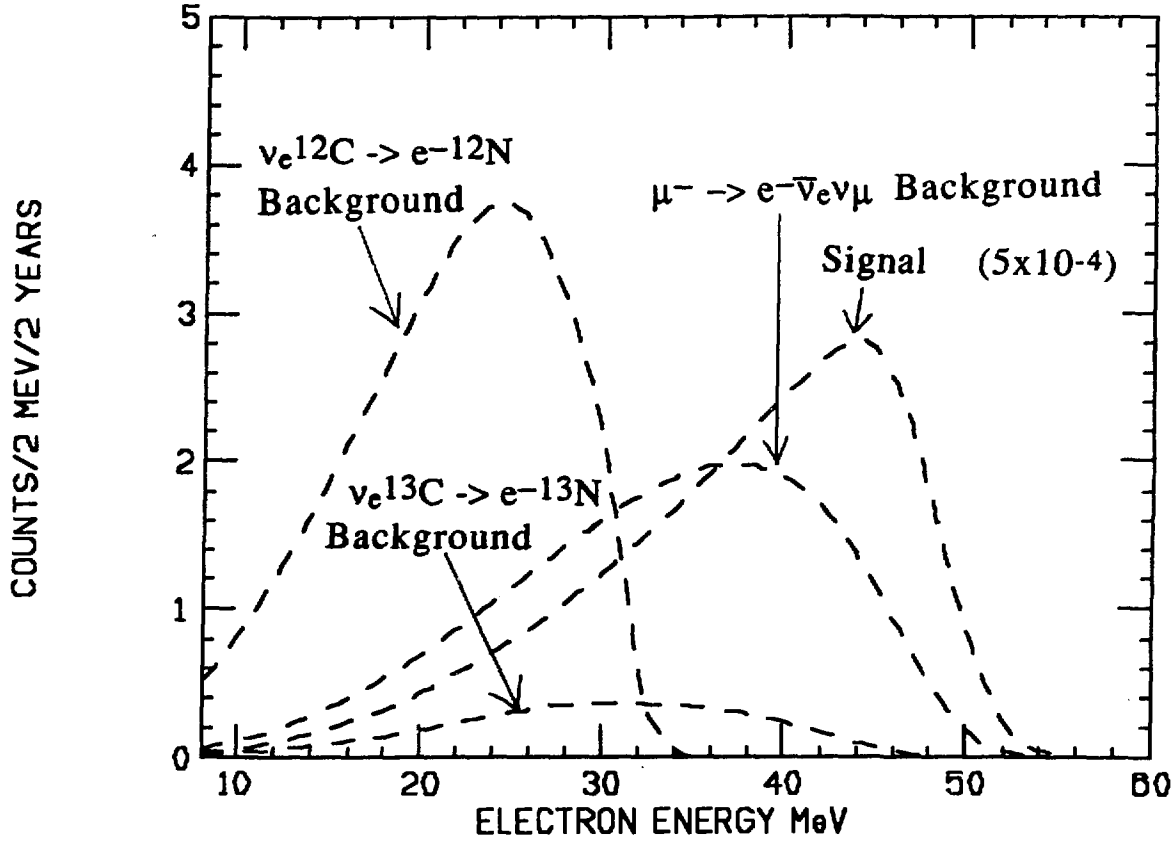

Fig. B19. The $\bar{\nu}_\mu \rightarrow \bar{\nu}_e$ oscillation limits on $\sin^2(2\theta)$ for large Δm^2. The spread of the results is simply due to the difference in statistical fluctuations between the data sets. The median result is $\sin^2(2\theta) \leq 2.7 \times 10^{-4}$.

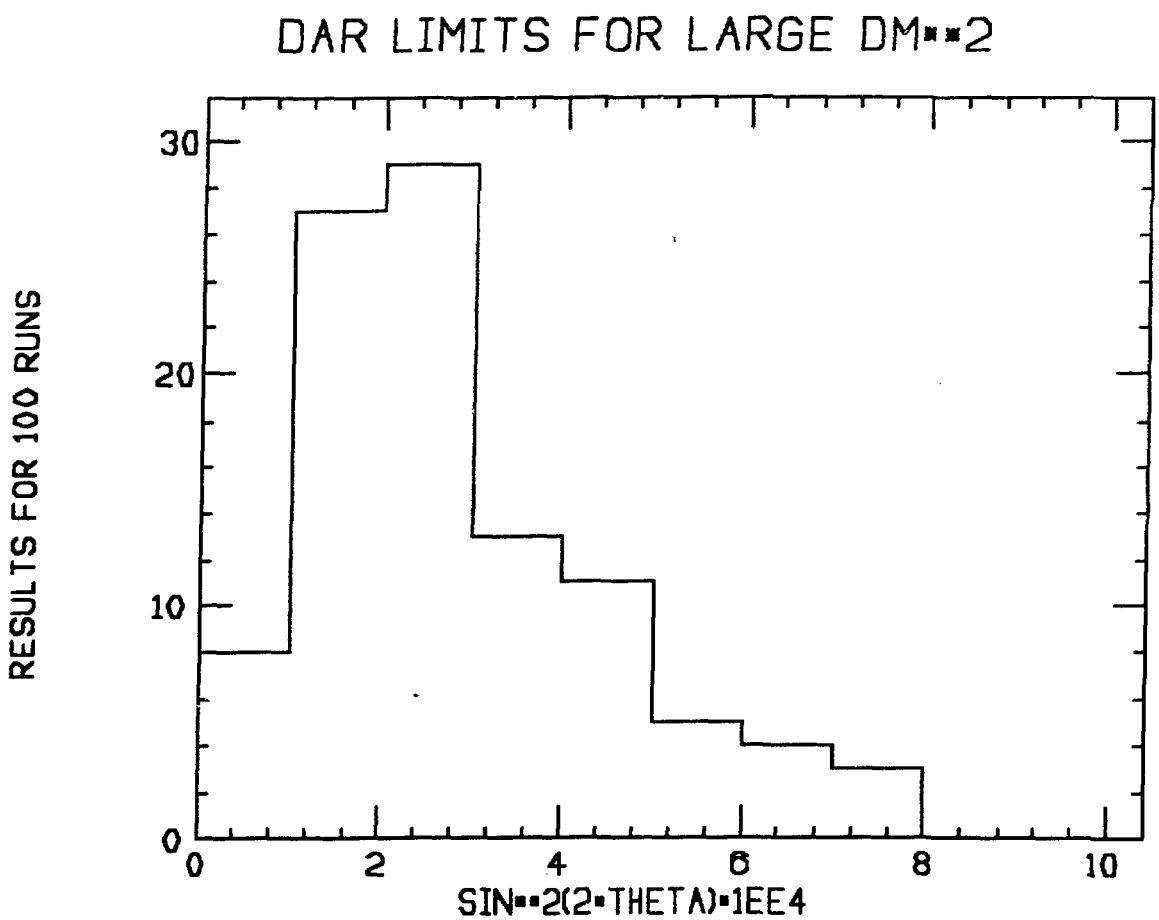

Fig. B20. The predicted electron energy spectra of the $\nu_\mu \rightarrow \nu_e$ oscillation signal and backgrounds after two years of data collection, assuming $\sin^2(2\theta) = 1 \times 10^{-3}$ and $\Delta m^2 = 100\ \mathrm{eV}^2$, which corresponds to a signal level of 5×10^{-4}.

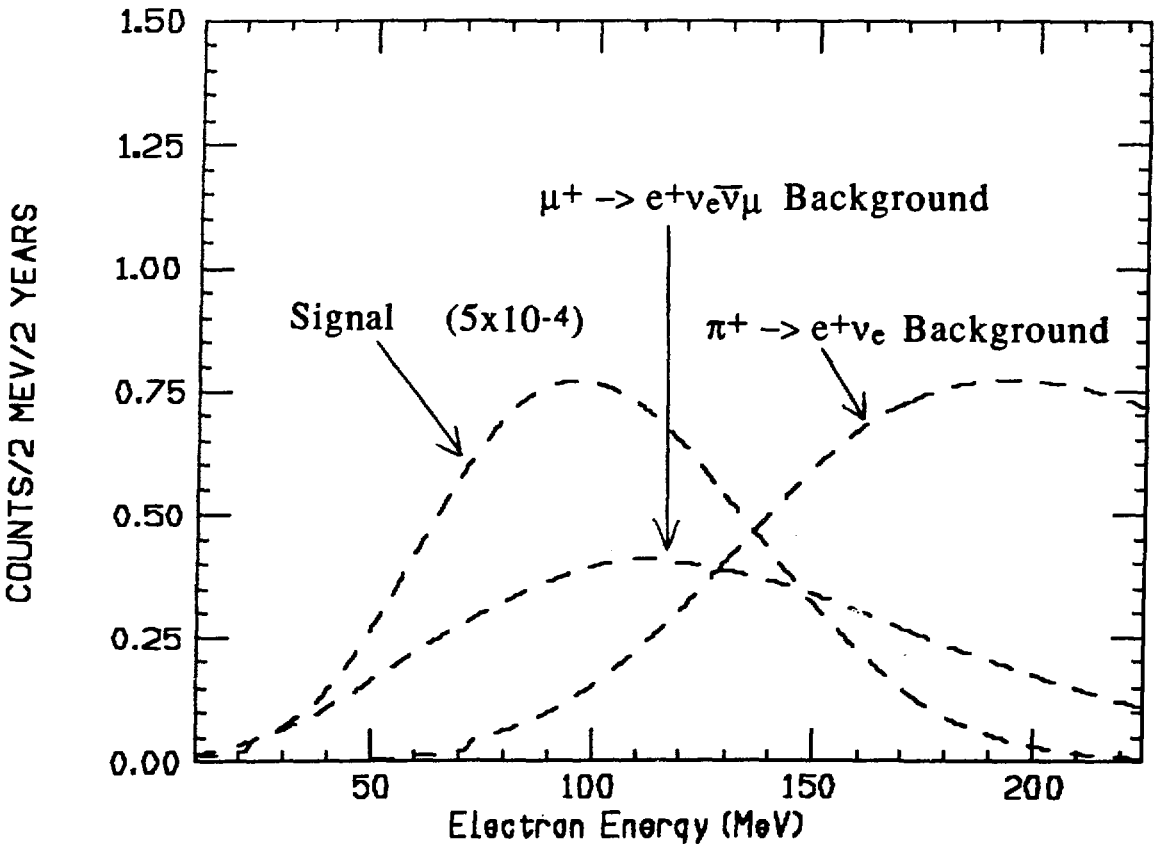

APPENDIX C.
FLUX NORMALIZATION AND ENERGY AND TIMING CALIBRATIONS

In order to both understand our sensitivity to neutrino oscillations and to measure cross sections to an accuracy of 10–20%, we must be able to determine the neutrino flux to better than 10%. This flux normalization can be achieved in two ways: from a Monte Carlo simulation and from normalization to νe elastic scattering events. At the low energies of the LAMPF proton beam, the proton, pion, and muon interactions are well understood and predictable. There exists a pion and muon transport Monte Carlo program at LAMPF [11] which has been used for both the E225 and E645 beam stop neutrino experiments and which has been judged to be accurate to 7.3%. We believe that with further measurements this program can be improved to give an uncertainty of $\sim 5\%$. An independent normalization comes from $\nu e \rightarrow \nu e$ interactions for neutrinos from both pion decay in flight and decay at rest. We expect to obtain several hundred neutrino-electron elastic scattering events per year, so that a 10–15% normalization can be achieved after two years. The $\nu e \rightarrow \nu e$ interactions from pion decay at rest will have background due to cosmic-ray interactions and to the $\nu_e C \rightarrow e^- N$ reaction, but these backgrounds can accurately be subtracted by applying an angular cut. The $\nu e \rightarrow \nu e$ interactions from pion decay in flight should have very little background. Note that the νe cross section is theoretically very clean and depends only on the parameter $\sin^2\theta_W$, which is known to sufficient accuracy for this purpose already.

In order to handle background subtraction for neutrino oscillations from pion decay at rest and to define measured cross sections, we must know the absolute energy scale to $\sim$ 1 MeV. The methods we describe are those successfully used in calibrating the KAMIOKANDE II (KII) detector; as participants in KAMIOKANDE are also working on LSND, we see no obstacle to transferring the technology. It has been demonstrated that a 3% energy-scale calibration can be achieved and maintained over long periods of time; this accuracy corresponds to about 1 MeV at the sensitive region (40 MeV) for background subtraction for oscillations from decay-at-rest neutrinos.

The method for establishing the energy scale is based on using Čerenkov or scintillator light from physical processes that deposit an appropriate range of energies in the mineral oil. These are the Michel spectrum from muon decay, the conversion of gammas (of about 6- to 9-MeV energy) from neutron capture in nickel, and possibly the 1-MeV beta line from the decay of ^{207}Bi. By comparing the pulse-height spectra obtained from these processes

Fig. B21. The $\nu_\mu \rightarrow \nu_e$ oscillation limits on $\sin^2(2\theta)$ for large Δm^2. The spread of the results is simply due to the difference in statistical fluctuations between the data sets. The median result is $\sin^2(2\theta) \leq 2.7 \times 10^{-4}$.

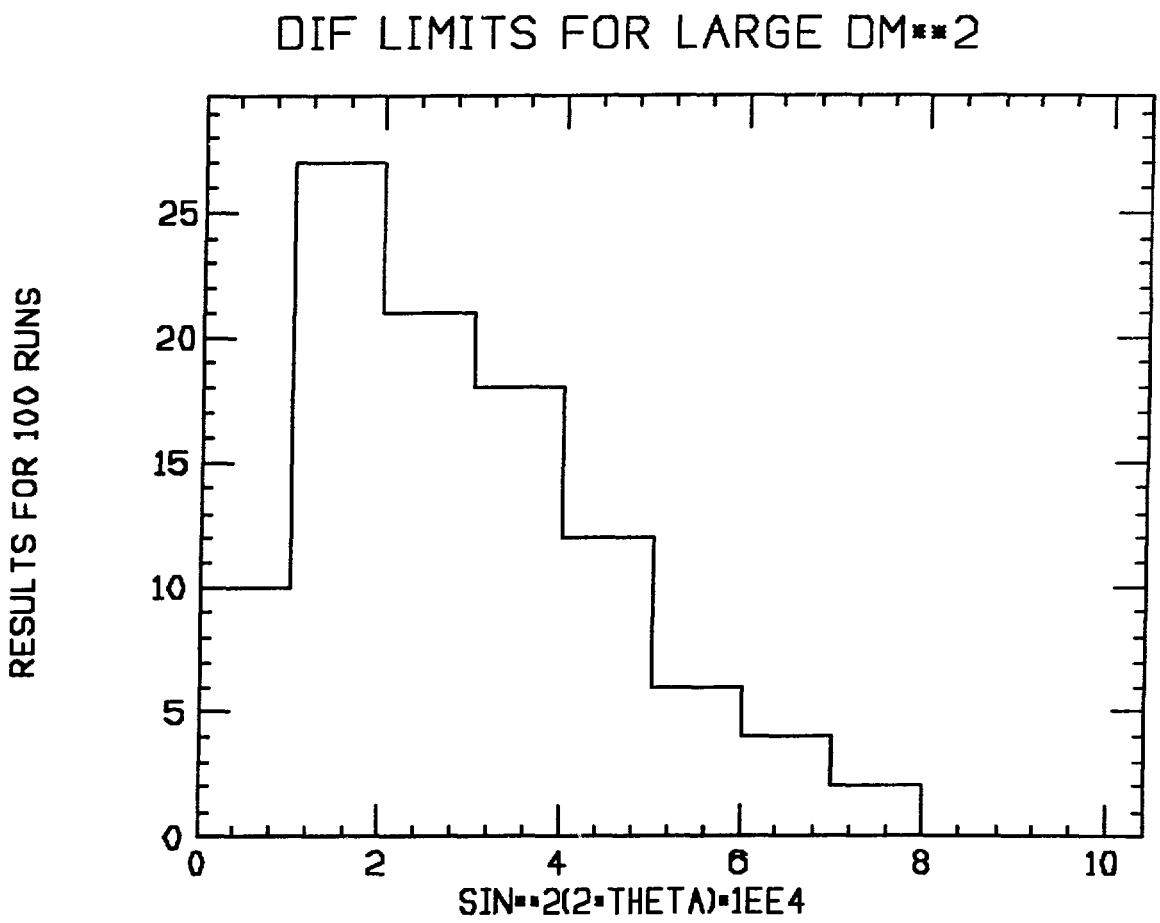

with the prediction of Monte Carlo simulations, we shall calibrate the detector over the range from 0 to 50 MeV, which is the critical range for us.

Figure C1 shows the results achieved in simulating the energy spectrum of electrons from events in which a muon stopped in KII and subsequently decayed. Events per bin of 1.8 N_{eff} are plotted versus N_{eff}, the corrected number of photoelectrons detected. The success in fitting the Monte Carlo simulation to the data is obvious. Parameters fitted include optical absorption in the water and the quantum efficiencies of individual photomultiplier tubes. It will be straightforward for us to trigger on stopped cosmic-ray muons between beam bursts, so a large sample of events covering the entire detector volume will be collected. The cylindrical geometry of LSND is similar to that of KII and will be straightforward to simulate.

Neutron capture on nickel produces a number of gamma rays, in the energy range 7–9 MeV, that provide a convenient calibration at a lower energy than the peak in the Michel spectrum. The neutrons will be produced by decay of ^{252}Cf, which undergoes spontaneous fission with a branching ratio of 3.1% and with a half-life of 2.65 y. Since the ^{252}Cf itself produces gamma rays and electrons in the 0- to 8-MeV energy range, a difference technique must be used. Figure C2 shows the difference spectrum as measured by the KII collaboration; a solid calibration point at 9 MeV is achieved.

We plan to calibrate the timing of the tubes by using the scintiball technique developed by the KII group. A pulsed UV laser will drive several quartz fibers, each of which will excite a scintillator radiator. The radiator will be in the shape of a ball and will contain diffusing pigment. The resulting emission of light is quite isotropic, and the spectrum is similar to that of Čerenkov light. This type of system is essential for testing and monitoring all channels independently of the detailed analysis necessary to establish the energy scale. The method can be automated, using a remote-positioning device. We see no difficulty in using this method to give us calibration of the timing channels to better than 0.5 ns.

Fig. C1. Spectrum of light collected from stopped muons in KII. Events/bin of 1.8 N_{eff} are plotted versus N_{eff}, the corrected number of photoelectrons detected. The points indicate the data; the histogram, the simulation.

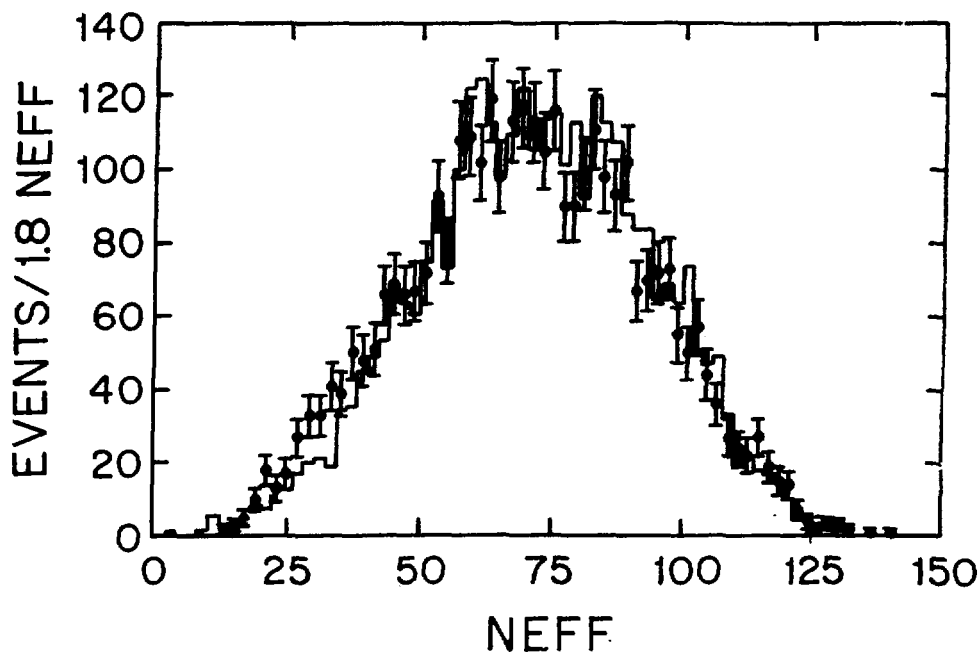

Fig. C2. Difference spectrum for a californium-nickel source. This is the spectrum of gammas from neutron capture in nickel. The points indicate the data; the line, the simulation.

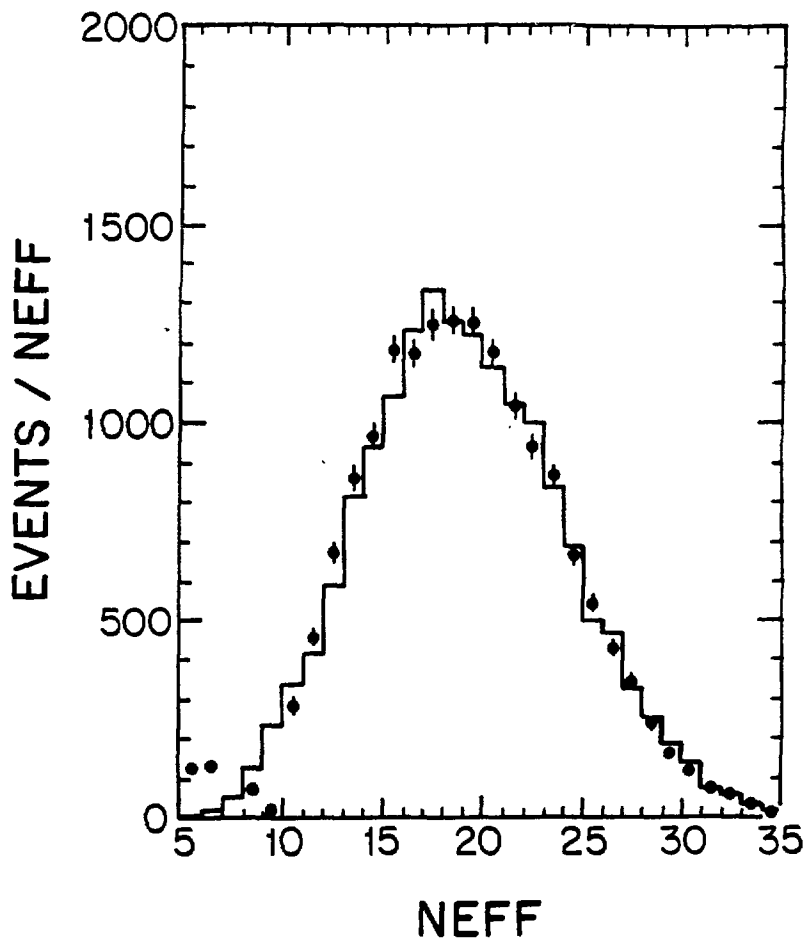

APPENDIX D. CHERENKOV LIGHT IN SCINTILLATOR

In our dilute scintillator we expect electrons to make a 47° cone of Čerenkov light and isotropic scintillation light. Protons should make only scintillation light. With the scintillator concentration adjusted to give a light output 4 times greater than the Čerenkov light output, a slow 1-MeV muon can be detected reliably. Also, a ring should be easily identifiable in the PMT hit patterns of a 40-MeV electron. This has already been demonstrated in Monte Carlo simulations in which the ring stands out due to the higher population of hits on PMTs in the Čerenkov cone. In addition, the average number of photoelectrons on a PMT in the ring is about 2.5 times greater than out of the ring.

Based on the absorption and emission spectra of mineral oil and the liquid scintillator, we expect the latter to have about two-thirds the Čerenkov emission of pure mineral oil. The lost portion consists of the light with wavelengths below 400 nm, which is absorbed and fluoresces isotropically. It is indistinguishable from scintillation light. However, the Čerenkov light above 400 nm is above the absorption band and has an attenuation length of about 10 m or more. Thus the Čerenkov light should form a ring on the detector wall consistent with the multiple scattering angle of about 10 degrees (for 40 MeV electrons).

In order to show that Čerenkov rings actually exist and have a usable intensity, we are conducting tests using cosmic rays defined in a narrow cone by a three-counter telescope. This beam passes through a long, 5-cm diameter tube with a PMT at one end. We are able to scan through the angle where Čerenkov light is expected (47°). In our first tests (see Fig. D1), we found that the count rate in the cone was significantly higher than out of the cone. This is in accord with the expected number of photoelectrons: 5 in the cone, and 0.2 when the tube was set at angles outside the Čerenkov cone. Outside the cone, Poisson statistics limit the counting efficiency to 20%.

Figure D2 shows the data, and an estimated resolution curve. The four-fold coincidences peak at the Čerenkov angle with a width consistent with the geometrical resolution. We have modified the scintillation counters to obtain better geometry and resolution, and have replaced the PMT on the long tube that views the fluid with one capable of single-photoelectron resolution. This will allow us to get the absolute and relative number of photoelectrons associated with Čerenkov light produced in mineral oil and scintillator.

In summary, we have observed a clean Čerenkov ring in dilute scintillator fluid. The intensity of the ring has not been measured. Further tests are underway that will measure

this quantity, which affects the ultimate choice of scintillator concentration by virtue of its impact on electron identification, angular resolution, and energy resolution.

Fig. D1. A schematic diagram of the liquid scintillator test setup. Downward-going cosmic muons are defined by the three scintillator paddles forming the cosmic ray telescope. The liquid scintillator is in the long 5-cm diameter tube, which is at an adjustable angle θ relative to the muon direction.

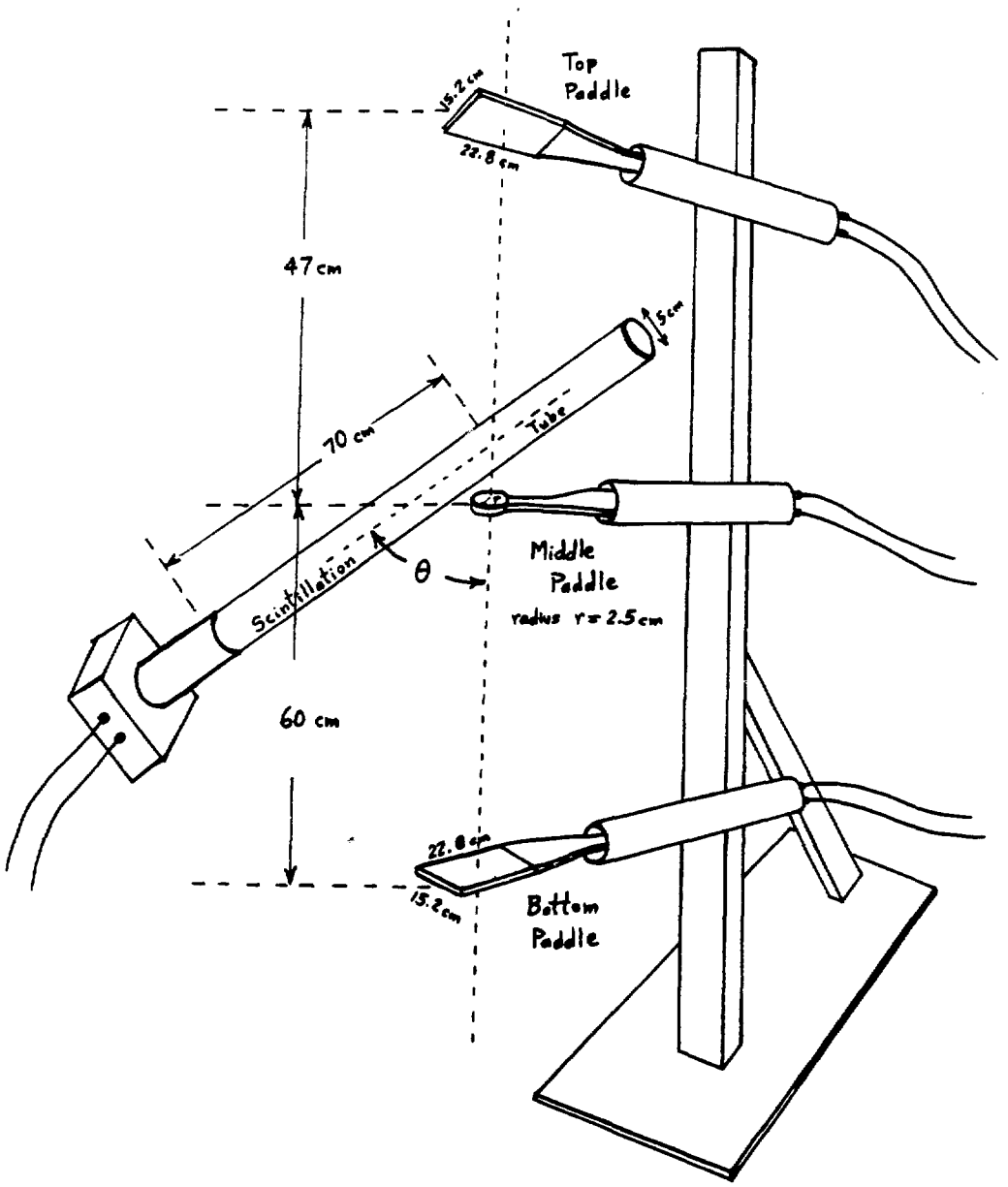

Fig. D2. The ratio of counts in the liquid scintillator tube to cosmic muon triggers as a function of the angle of the tube relative to the muon direction. The ratio is maximum at the 47° Čerenkov angle expected for liquid scintillator ($n = 1.47$). The dashed curve shows the estimated angular resolution of the cosmic ray telescope.

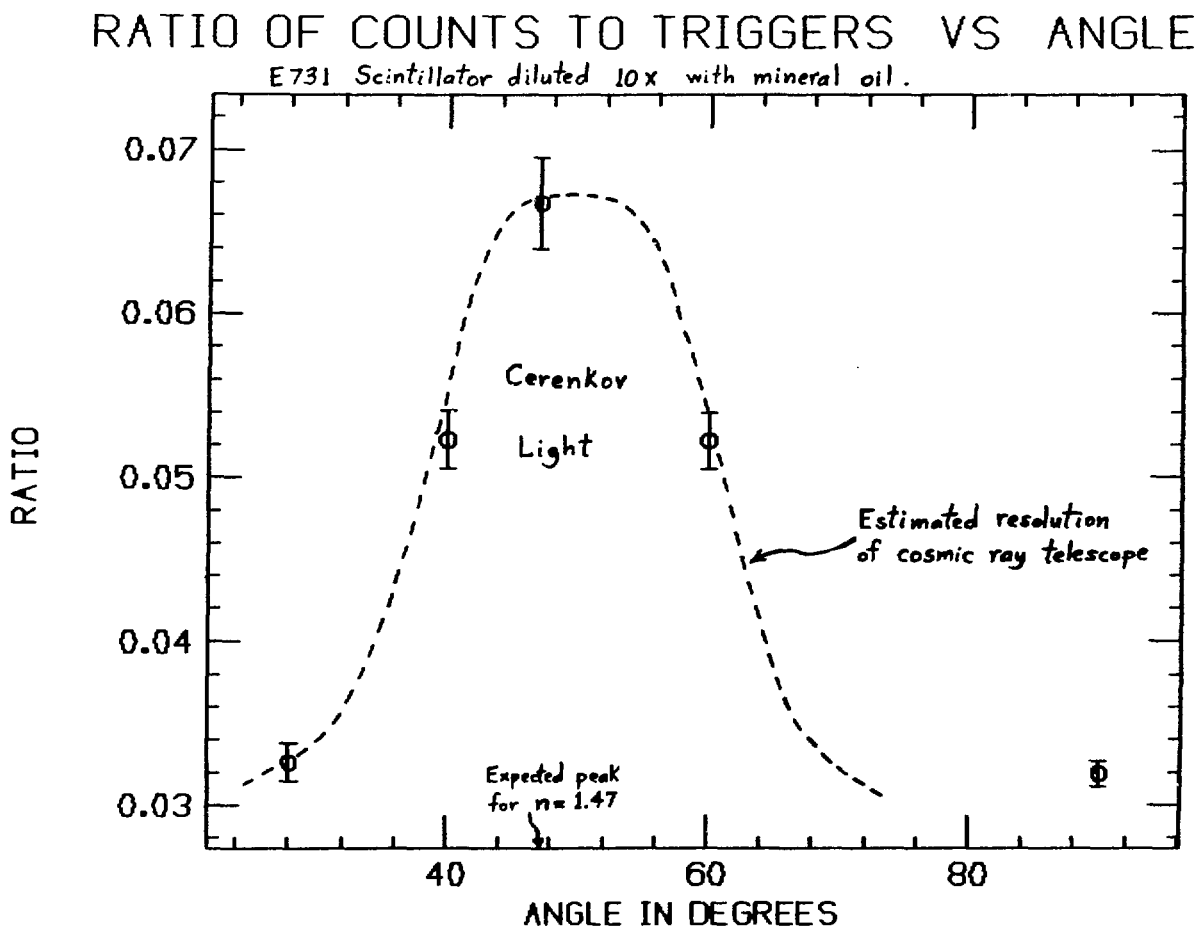

APPENDIX E. HIGH-ENERGY BACKGROUND FOR $\nu_\mu \rightarrow \nu_e$ OSCILLATION

The E645 detector, shown in Fig. E1, was located 26.8 m from the beam stop. It contained 15 tons of liquid scintillator, which served as the active target. The liquid scintillator was stored in 40 vertical planes sandwiched between vertical and horizontal proportional drift tubes (PDT) in order to provide tracking capability. A scintillator plane consisted of 12 modules, which were 30-cm high by 366-cm long by 3-cm deep. A Hammamatsu R878 photomultiplier tube (PMT) was attached to each end of a scintillator module. The detector was triggered by end-to-end coincidence of modules in three out of four contiguous scintillation planes. A 4π active shield with 360 12.7-cm diameter PMTs vetoed cosmic rays.[3] The electronics read-out and data acquisition system are described in more detail elsewhere.[3]

The results presented here were obtained during the 1987 LAMPF operation period. A total of 3800 Coulombs of protons were incident on the LAMPF beam stop. Note that the amount charge (3800 C) used for these analyses, does not include the first cycle of LAMPF operation in 1987. This is because the passive shielding during this cycle was only 1000 g/cm^2. At this level of overburden, the hadronic component of cosmic rays is not eliminated to an acceptable level, and the high-energy background was too high. Approximately, 8.47×10^5 triggers were written onto tapes. The overwhelming majority of these triggers was cosmic-ray induced and was classified as through-going muons, electrons from stopping muon decays and recoil protons from neutrons colliding with different nuclei.

In order to obtain a sample of events arising possibly from $\nu_\mu \rightarrow \nu_e$ oscillation, the data were subjected to a series of software cuts. Determination of efficiencies for a number of these cuts required a Monte Carlo simulation of the ν_eC charged-current reaction. A neutrino-flux-averaged[11] electron spectrum weighted with ν_eC cross section was generated using EGS4. A 3AND trigger-efficiency was determined from these MC data to be 67%. Furthermore, the data were subjected to the following requirements: (i) an internal consistency test to confirm existence of certain pulses, (ii) the random triggers generated by a pulse generator were written onto a separate file in order to be used to check the efficiency of the veto shield, (iii) the anticoincidence shield not have a cluster of two or more PMTs in-time (± 0.5 μs) with the trigger and with pulse heights (PH) above a specified magnitude, (iv) a track can be reconstructed using the PDT information, (v) the total volume of the detector constitutes the fiducial volume, (vi) stopping muons with constructible muon

and electron tracks and shield hits were removed. The efficiencies of these software cuts referred to as "first pass" are shown in Table E1.

The second pass of data reduction was designed to eliminate events that seemed to be entering the detector from an inefficient region of the active shield. Removal of these events was carried out by projecting their tracks back onto the shield and requiring that they pass through the inefficient region. The efficiency for this cut was determined from a MC to be 99.5%.

The third pass of software cuts starts with a very severe in-time shield cut. It requires a single hit in the shield below 0.1 minimum ionizing (M.I.) with a time gate of 1.75 μs. Second, a cut was applied to eliminate events that have scintillation counters with a PH more than four times M.I., either on or off-track. Third, a dE/dx cut was employed to remove heavily ionizing particles. Fourth, the tracking was reinforced by requiring at least 3 scintillators on a given track. Finally, a total energy cut of > 60 MeV was applied. The efficiencies of these cuts were determined from a MC calculation. The shield cut efficiency was obtained from a random data sample. These efficiencies are shown in Table E2. The overall efficiency is about 28%. The number of electron-like events passing all cuts is seven: three beam-on gate events and four beam-off gate events. Note that the beam-off gate for E645 was 3.5 times larger than the beam-on gate.

Table E1. First Pass Cut Efficiencies.

Cut	Efficiency (%)
3-AND Trigger	67.0
Consistency	99.9
Random removal	100.0
In-Time shield	98.0
Track found	97.3
Fiducial volume	97.0
Stopping muon	100.0

Table E2. Third Pass Cut Efficiencies.

Cut	Efficiency (%)
dE/dx	99.6
> 4 M.I.	93.2
3 Tanks on track	82.9
Total energy	67.4
In-Time shield	88.0

Fig. E1. Perspective view of the E645 detector and cosmic-ray anticoincidence shield.

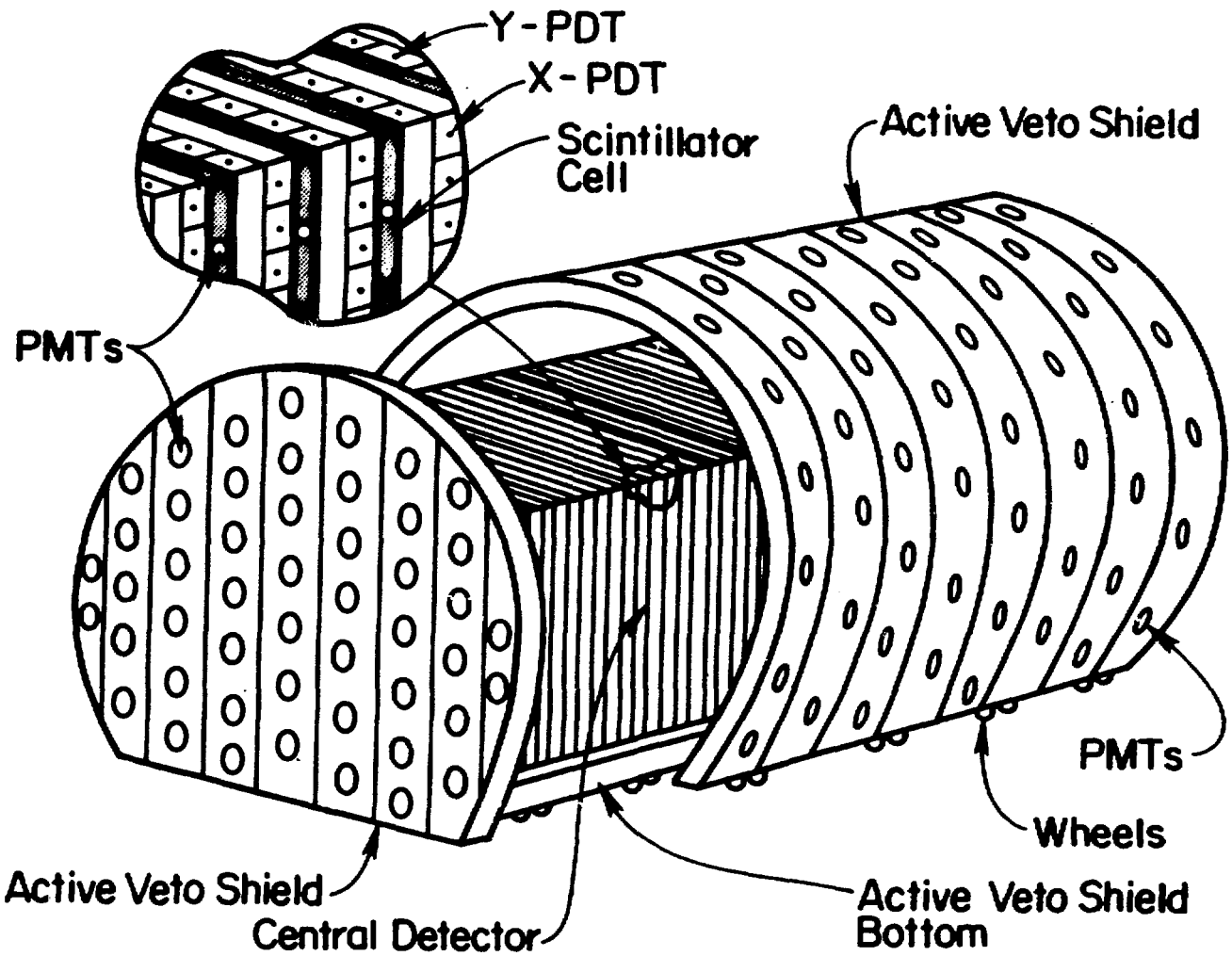

APPENDIX F. FRONT-END ELECTRONICS AND DATA ACQUISITION

The front-end electronics and data acquisition system are described in this appendix. The reader may wish to refer to the block diagram shown in Fig. F1 for the discussion that follows. The system is designed to record and selectively process the pulse histories (charge and time) of each of the approximately 1000 photomultiplier tubes with minimal deadtime and very high system reliability. Because of the front-end data buffering a major fraction of the detector is "on" all the time and is "gateless." The system runs in an "event driven" data acquisition mode where data is continuously collected and stored in circular buffer memories. An intelligent Event Builder (a dedicated monoboard microprocessor based computer) makes it possible to select useful data from the large data samples while providing time buffering. This time buffering makes it possible to delay a trigger decision until information from the entire detector is available and to reduce the deadtime in the detector to nearly zero. Separate event triggers for cosmic rays, electrons, neutrons, supernova, and calibrations are determined by a majority coincidence trigger generator.

Upon generation of a trigger signal, the following sequences take place: the Event Builder notes the time of occurrence of the trigger and type of trigger and begins a serial scan of each photomultiplier channel memory. In each photomultiplier memory it locates the pulses that occur near the trigger time, and sends them to an event data structure located on one of several memory cards. These memory cards are dual-ported with one port connected to the main data acquisition system bus (labeled "Extended VME bus" in Fig. F1), and with the other port connected to a microprocessor through a dedicated local bus. Upon completion of a scan, the Event Builder adds the time of the trigger, type of trigger, and other logging information (such as the status of the accelerator beam spill) to the data, passes an address pointer to this data structure to the associated microprocessor, and signals the microprocessor to begin the data analysis and reduction of the event. The Event Builder notes which processor-memory units are available (through a semaphore control), and upon receipt of the next trigger it begins an event build in the next available processor-memory unit. Upon completion of analysis and reduction of an event, the microprocessor writes the reduced event to a data-storage medium (for example, VHS tape) through a conventional SCSI bus and then signals the Event Builder that it is ready for another event.

Monitoring and control is done by a host computer (a micro-VAX) that allows multiple user access to the on-line data, but it is not in the data flow channel. The host may

sample the data stream as it flows to the recording media, but it cannot corrupt the data acquisition. The Extended VME bus is controlled by the Event Builder, which acts as the bus master. Bus arbitration is handled by the Event Builder.

This system exploits the advantage of commercially available hardware and software through extensive use of VME-bus and SCSI-bus formats. The only hardware that needs to be developed by the collaboration are the Input cards and the High Voltage Control cards. Intercrate communication is accomplished with simple dual-ported memory cards that allow for simple bus synchronization and buffering. (This method of extending the VME bus is similar to the successful design employed by the OPAL data acquisition system.) The microprocessors are based on available MC68xxx monoboard computers and use the OS-9 (commercial) real time operating system. The CERN Physics Analysis Workstation (PAW) analysis package and the ZEBRA data management structure are the software and database packages we plan to use. A similar data acquisition system has been used in the OPAL detector at LEP with excellent results.

The electronics are deployed in three subsystems: the High Voltage Control cards, the Input cards, and the Event Builder and microprocessor cards. All are in VME format with the following crate breakdown: The High Voltage Control cards and the Input cards are 9U × 320 mm (VXI bus size "D") and have three 96-pin rear connectors labeled P1, P2, and P3. The P1 and P2 connectors comprise the standard VME bus plus the clock-tick distribution bus (16 bits) (see below) and the PMT summation bus (10 bits). The P3 connectors are used exclusively for analog signals, namely the photomultiplier anode signals, and are physically and electrically isolated from the noisy, digital busses. The High Voltage cards and the Input cards reside in separate VME crates, there being four high-voltage crates and four input crates, as shown in Fig. F1. The photomultiplier high-voltage and anode signal share the same coaxial cable. The high voltage distribution and control circuit for a single channel is shown in Fig. F2, and the positive-high-voltage photomultiplier base is shown in Fig. F3. The anode signals are extracted by the High Voltage Control cards and routed via the P3 connectors to the Input cards. The input circuit for each channel is shown in Fig. F4. The Event Builder and microprocessor cards reside in one standard VME crate (6U × 160 mm) with the P1 and P2 VME bus connectors.

The front-end photomultiplier pulse processing and history recording buffers are based upon the flash digitization of stretched pulses with RC-exponential decays of a few clock intervals. A block diagram of the front-end electronics for each photomultiplier channel

is shown in Fig. F4. The anode signal for a single photoelectron from a C83061E photomultiplier with a gain of 1.0×10^7 is shown in Fig. 3 from Appendix I. (The C83061E photomultiplier is described in detail in appendix I.) The pulse at the anode is approximately 10 mV high, has a 3-ns rise time, and an exponential fall with a time constant of approximately 9 ns. The pulse will be reduced in height and lengthened in time to approximately 25 ns after traveling through the 150 feet of coaxial cable that connects the photomultiplier tube to the High Voltage Control card. The anode pulses are sent to the Input card, where the cable is terminated and the signal amplified and shaped by a conventional bipolar video shaping amplifier (for example, an NE 592 or equivalent). The amplified output goes to a leading-edge discriminator and an RC-stretcher. The discriminator output goes to latch a global clock signal, to a PMT summation bus for the majority coincidence logic, to the local control logic, and to another RC-stretcher. The stretched discriminator pulse provides the 0.3 ns vernier time resolution information between clock ticks (one tick every 50 ns). The stretched anode pulse provides the charge information.

The stretched pulses are digitized by (Motorola MC10310) 8-bit 25-MHz flash analog-to-digital converters (FADCs). The FADCs are clocked continuously from a common 20-MHz clock that is synchronized with the global system clock. On each clock cycle their data are written as the upper and lower bytes of a word into a local static random-access memory (sRAM). The RAM is partitioned into pulse record structures, which consist of a set of 10 contiguous words that are addressed with a circular topology. The RAM address within a pulse record is incremented on each clock cycle, recording in memory the FADC value taken during that clock cycle, until an anode pulse of sufficient magnitude fires the discriminator. The FADC-RAM writing cycle is then repeated for 8 more cycles to collect the charge and time information in the pulse. Note that there are two measurements of the charge-stretcher state prior to the pulse. The ability to determine the state of the charge stretcher prior to the pulse allows for a pedestal or residual correction (for example, from pile up on the tail of a large pulse). This is a "gateless" front end. A pulse record consists of the initial state plus the exponential decaying waveform. Finally, the value of the clock-tick latch is written into the memory location next to the 10-word pulse record, and a new pulse record is begun after the clock-tick word. Each pulse record is identified and distinguished from other pulse records by the clock-tick word. This process is repeated until the RAM is filled. The earlier pulse records are then overwritten. In terms of buffer capacity, a pair of 8-bit $\times$ 2 KByte sRAMs have a capacity for 166 pulses, or a time record

of 16.6 msec, before overwriting. (These numbers are based on a 100 microsec per pulse time interval, which corresponds to a pulse rate of 10 kHz, between noise and cosmic-ray pulses from a C83061E photomultiplier.) When being read by the Event Builder, the transfer of words between FADCs and RAM is suspended and the RAM is connected to the system VME bus. This is the only time a channel is not collecting pulse data.

The use of the 8-bit 25-MHz FADC is a compromise that balances speed against cost and power dissipation. There are faster FADCs available that can sample analog signals at rates of 200 MHz or greater, but to be used effectively they must be followed by very high speed buffer memory and a suitable acquisition system to take advantage of the tremendous volume of data. The system outlined here could be extended to handle such a front-end design if cost were not a concern. Instead, we have adopted the technique of stretching the anode pulse with a (relatively) long time constant RC-integrator and sampling the integrator voltage with the "slower" FADC and its associated RAM. The time constant is then chosen to allow the FADC to capture an anode pulse no matter when it may occur within a clock-tick interval. This condition argues for a long time constant. The desire to have the best pulse-pair resolution time argues for a small time constant. The optimal value seems to be within a few clock intervals. It is then necessary to correct for the exponential "droop" of the integration voltage, and this may be accomplished by multiplying the FADC value by a correction factor that is equal to $\exp(T/R1C)$, where T is the time from the beginning of the pulse to the clock tick, which will be measured by the time vernier to be described below, and $R1C$ is the charge integrator's time constant. This is illustrated in Fig. F5. The time vernier measurement of T is carried out with the aid of a similar RC-integrator, but driven by a standardized pulse of known pulse height Vo. The time T is then computed from the FADC value VFADC by the relation

$$T = R2C \ln(Vo/V\mathrm{FADC}),$$

where $R2C$ is the time-vernier's time constant. The time of a pulse relative to a clock tick is determined by the exponential fall of a signal that began with a known pulse height. The charge (or initial pulse height) in that pulse is determined by the exponential fall of a signal during a known amount of time. In this way a rough measure of the charge and time of a pulse is recorded as the simple numerical value of the two 8-bit integers stored in the RAM word, and the whole pulse record contains the information to provide precise time and charge values.

The system timing is provided by a 20-MHz clock that is synchronized with a global positioning system (GPS) satellite time base. The GPS system is based on the Navistar system and a receiver manufactured by Kinemetrics—True Time. It provides geodetic position information and a universal time coordinate (UTC) accurate to better than 1 microsec. The GPS clock provides our coarse time for event labeling and correlation with astronomical events. The 20-MHz clock provides the intermediate time base for the digitizers, and the vernier time algorithms operating on the FADC data provide the fine time resolution (to 0.3 ns) for the track reconstruction. The 20-MHz clock is scaled and distributed to all the input channels over a 16-bit wide clock-tick bus, where it is used to label the individual pulses in the input buffers.

The nature of the data sent to the microprocessors by the Event Builder depends upon the particular trigger. In general, pulses with clock-tick labels within an interval of a few hundred nanoseconds are used to delimit an event. Pulses with later clock-tick labels may signal muon decays, radioactive processes, or other long-timescale but correlated events. The Event Builder (also a commercial monoboard computer) is the VME-bus master and directs and controls all data flow over this bus. The nature of the data acquired in response to a trigger is determined by the software in the Event Builder and may be as involved as is deemed necessary. The pulse data is buffered in the input RAMs, so as long as the Event Builder does not dwell too long in real time on a decision, the problem of event building delays does not affect the front-end data collection.

The data acquisition system processes the data only to the precision that it needs for a particular decision. The high precision but calculation intensive processes are put off until further down the data collection stream. For example, the timing to within a 50-ns clock tick is available as a simple integer word, the charge is roughly known to within a few percent in a single byte. These numbers are adequate for rapid on-line decision making regarding the keeping or disposing of the pulse. High resolution time and charge values require more detailed processing, which may be carried out when the information is needed, for example, for a precision track reconstruction.

The development of prototype input cards and simulation studies of the data flow are being carried out now. As the design matures, a number of schemes are being tested to further enhance operation. For example, we consider the addition of a 1-bit register to a cluster of adjacent channels to flag if any of the channels have recorded data since the last event-build operation. This flag could then be scanned by the Event Builder to determine

if interesting data were present. The presence of an intelligence in the event building offers a wide range of possibilities early on in the data-acquisition stream.

Fig. F1. Block diagram of the LSND data-acquisition system. Additional channels may be included by adding extra high voltage and input crate pairs and modifying the code in the event builder to include the new addresses.

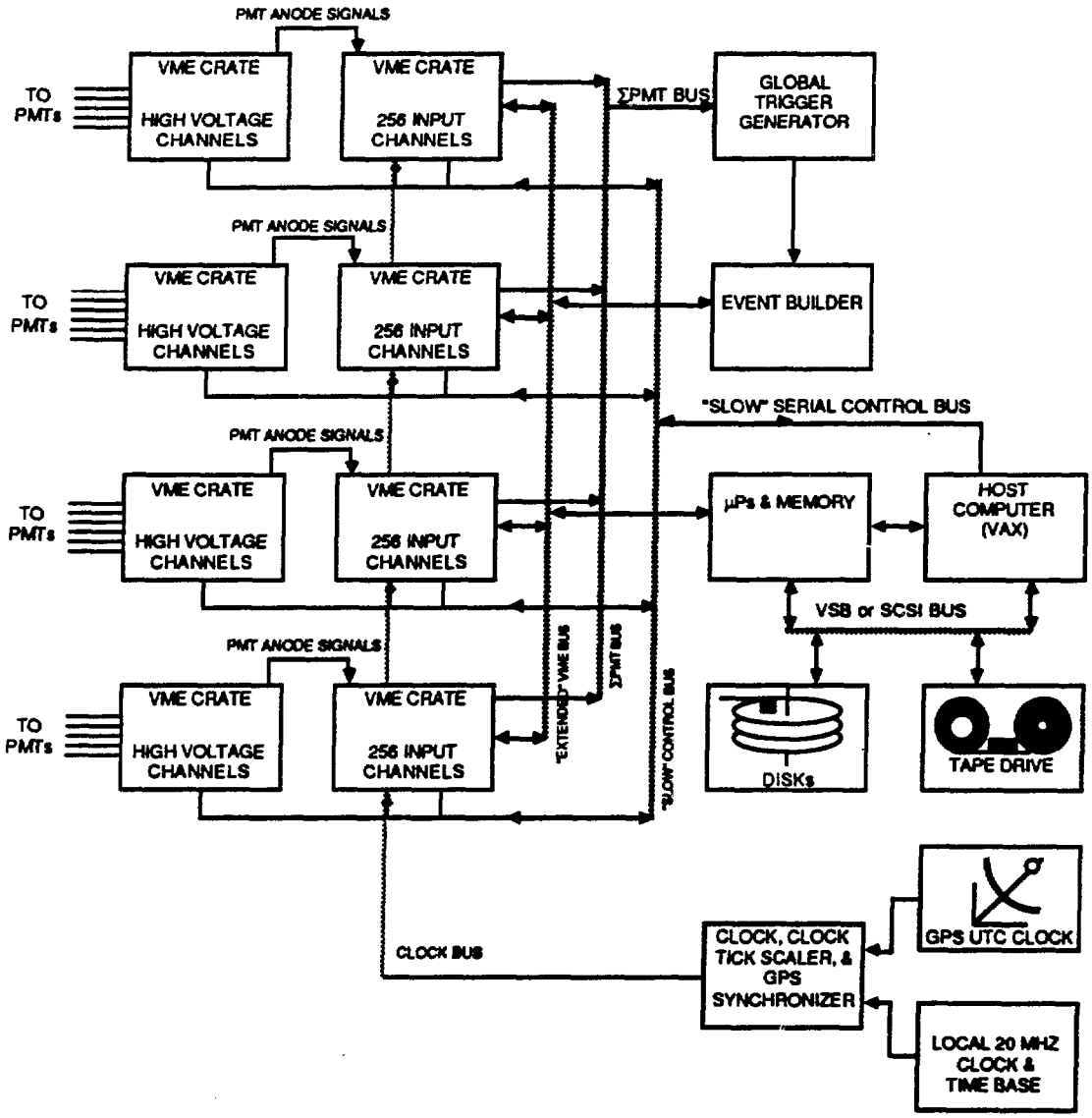

Fig. F2. Photomultiplier high voltage distribution and control. Illustrated is a single channel, one of 16 per card. The resistor Rtrim is selected to set the operating voltage for the tube. The tube voltage is measured and the value made available to the host computer through the multiplexing and ADC system shown. The host computer may also disable the high voltage to a channel through a shunt switch, which may also be used to deliver test pulses to the input electronics for diagnostic and calibration purposes.

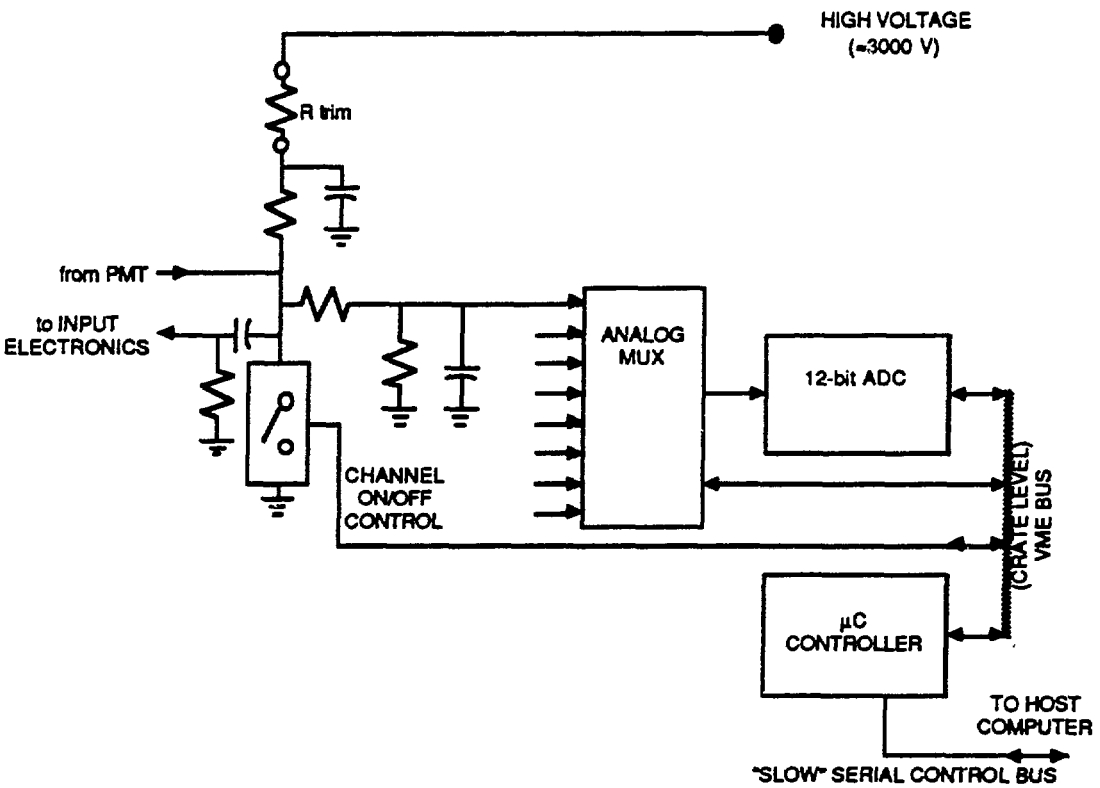

Fig. F3. Photomultiplier tube base design for the Burle C83061E. The design shown uses positive high voltage to keep the cathode at ground potential. The anode signal and tube high voltage share the same cable, with the anode signal split off at the high-voltage supply end of the cable.

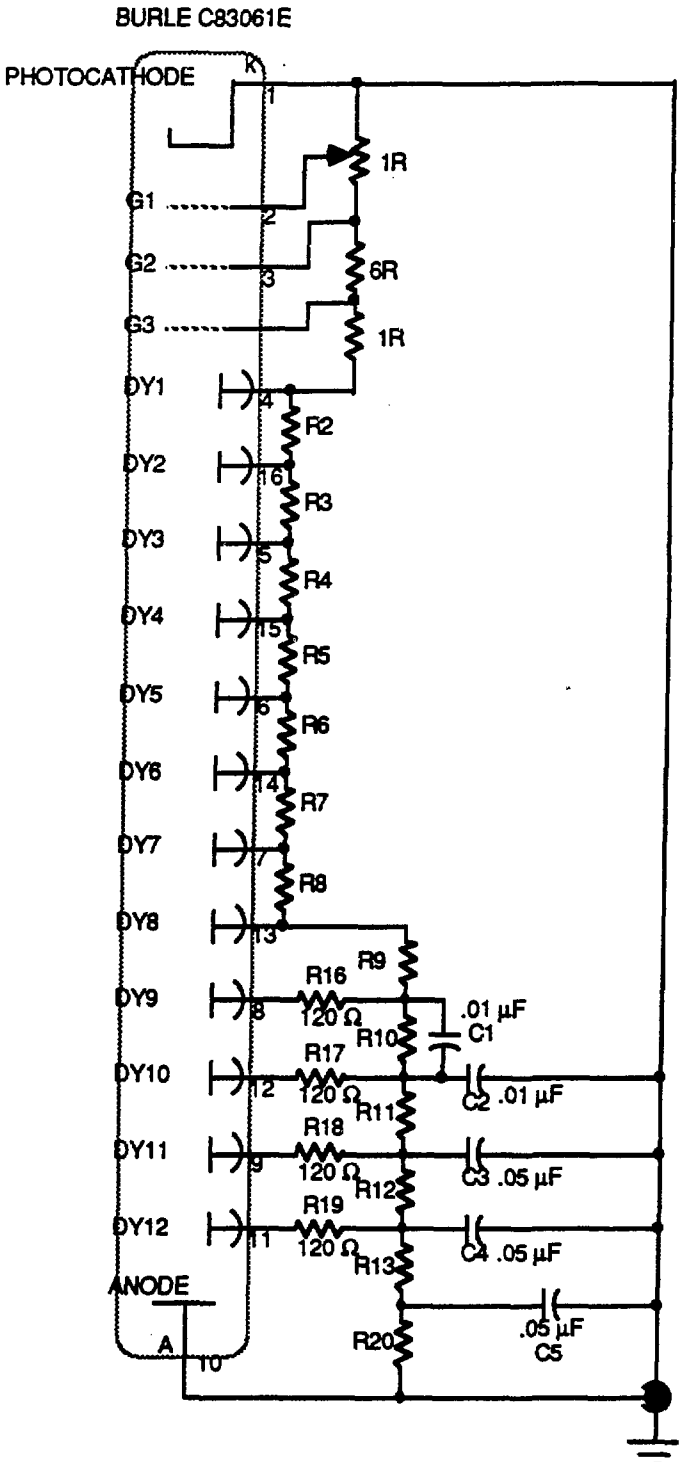

Fig. F4. The front-end electronics for each photomultiplier tube channel.

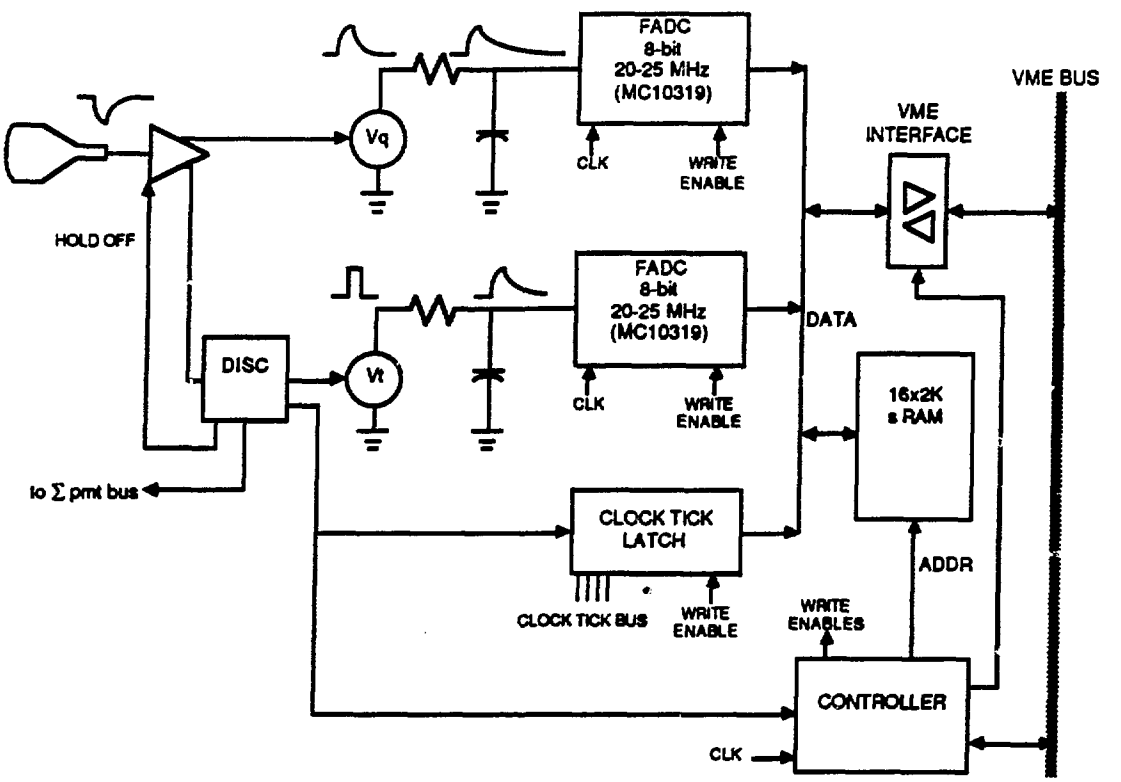

Fig. F5. The recovery of precision time or pulse height information from the exponential decay of a stretched pulse.

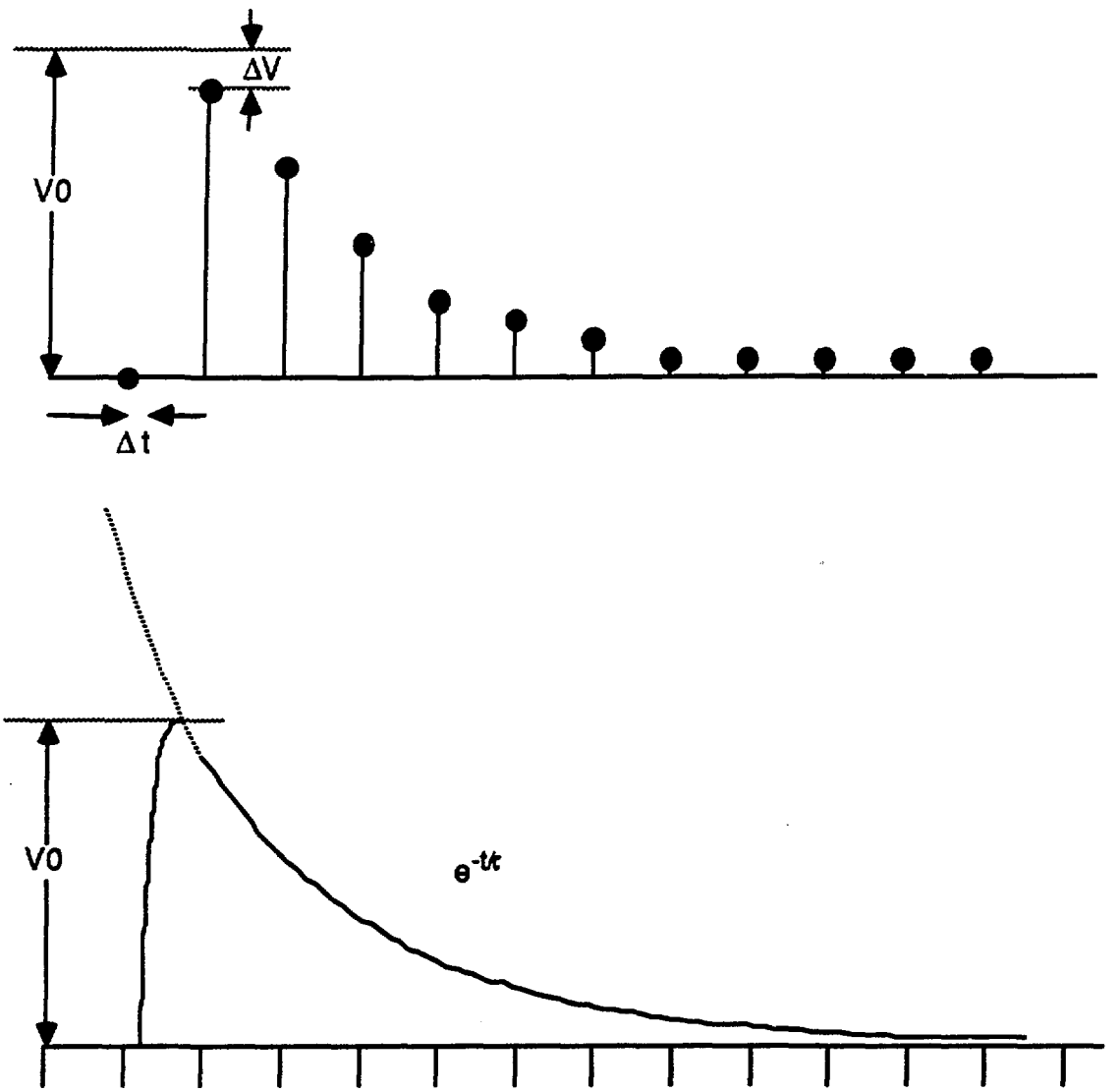

APPENDIX G. DILUTE LIQUID SCINTILLATOR TIMING TESTS

In this appendix we report upon ongoing tests of timing from Čerenkov light and scintillation light from 1-MeV electrons in very dilute solutions of liquid scintillator in mineral oil. The purpose of these tests is to determine the confidence we can place on the detection of first arrival photoelectrons as being due to Čerenkov light. This is a report on work in progress, with results that should be regarded as preliminary and encouraging.

The tests were/are carried out in a 25 liter (ℓ) rectangular tank that is filled with 20 ℓ of mineral oil plus scintillator added in 100-mℓ increments. The setup is illustrated in Fig. G1. Two 5-inch diameter Burle 8854 Quantacon photomultiplier tubes are positioned at the top of the liquid level and separated 5 inches apart. At the bottom of the tank we place a ^{207}Bi radioactive source of electrons, arranged so that the electrons are either directed up towards the photomultipliers (we call this the Čerenkov mode, or "C-mode") or down away from the photomultipliers (we call this the scintillation mode, or "S-mode"). The photomultipliers are connected to a data acquisition system as shown in Fig. G2, which collects charge and time difference information when triggered by a coincidence between the two tubes.

Three types of configurations are used for each increment of scintillator: A background run is made with no source in the tank. This measures the noise and cosmic ray rates. An S-mode run is made to measure the timing from scintillation light only. Finally, a C-mode run is made to measure the timing from the combined Čerenkov light and scintillation light. These measurements are made at the single photoelectron level, as confirmed by the charge spectra taken by the ADCs.

The ^{207}Bi source has a 99% branching ratio to monoenergetic electrons from internal-conversion transitions. Its principal emissions have energies of 482, 976, and 1048 keV. The ^{207}Bi is enclosed in an aluminum disk 5 mm thick with a thin foil window on one side. When placed in the mineral oil plus scintillator, the radiated electrons produce both Čerenkov light and scintillation light.

The scintillator used in the tests was from the Brookhaven experiment E734 and was a 50% dilution of Bicron 517L with mineral oil. The Bicron 517L scintillator had the following recipe:

85% mineral oil

15% pseudocumene (1,2,4-trimethylbenzene)

1 gm/ℓ PPO

0.001 gm/ℓ Bis-MSB.

When diluted to 50% it had a 92.5% mineral oil and 7.5% pseudocumene mixture. For our tests we added 100-mℓ increments of the BNL scintillator to the 20 ℓ of mineral oil. This produced the concentrations shown in Table G1.

In the process of converting the energy loss by the electrons into scintillation light, the pseudocumene transfers its energy to the PPO, which produces light in the 350–400-nm range. The Bis-MSB is a waveshifter that shifts the PPO light into the range 400-450 nm, which matches the bialkali response of the photocathode. Scintillation mixes with a relatively large fraction of pseudocumene transfer their energy by collisions between the pseudocumene and the PPO and this occurs on a rapid time scale. However, in dilute solutions radiative energy transfer becomes the dominant transfer mechanism with the result of a longer time interval between the initial excitation of the scintillator and the production of 450-nm light. We are studying the concentration dependence of this transition. As a preliminary indication, we show in Fig. G3 the coincidence rate for S-mode and C-mode configurations.

In Figs. G4 and G5 we show the results of our tests for selected concentrations of the time interval of light arrival between the two photomultipliers. Further tests are in progress, including a careful study of pure mineral oil, and will be available in the near future. In all the case a clear central peak can be distinguished in the C-mode, which is significantly more pronounced than the central peak in the S-mode.

Table G1. Pseudocumene Concentrations in Mineral Oil

Test	Fluid in Tank (ℓ)	Scintillator (mℓ)	Pseudocumene (mℓ)	Pseudocumene Fraction
1	20.0	0	0.0	0.0
2	20.1	100	7.5	3.7×10^{-4}
3	20.2	200	15.0	7.4×10^{-4}
4	20.3	300	22.5	11.1×10^{-4}
5	20.4	400	30.0	14.7×10^{-4}
6	20.5	500	37.5	18.3×10^{-4}

Fig. G1. Test setup for scintillation light and Čerenkov-scintillation light time resolution studies.

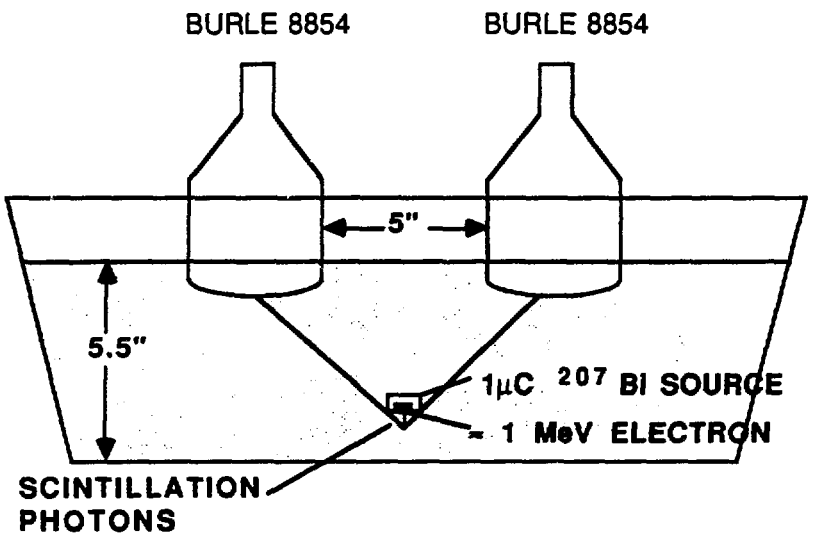

Scintillation or S-mode arrangement

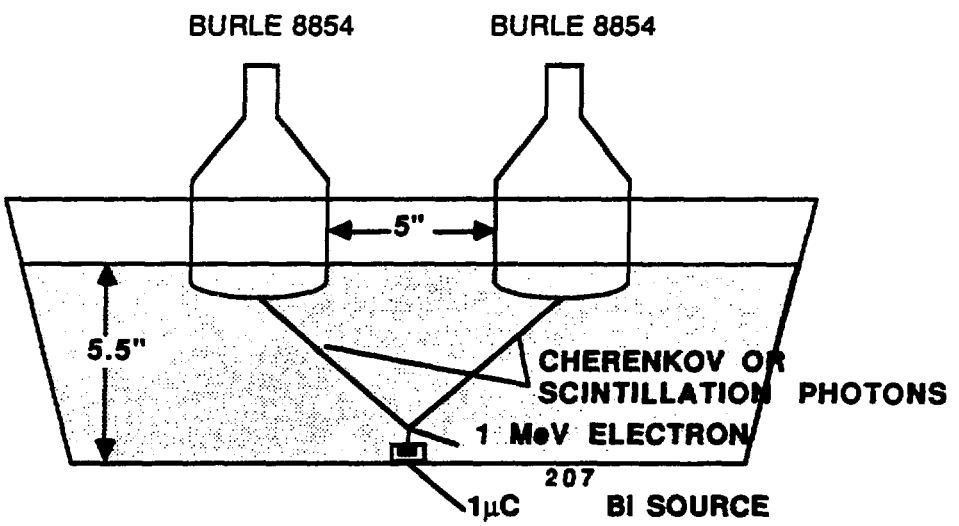

Cherenkov or C-mode arrangement

Fig. G2. Electronics and data acquisition system for the time resolution studies.

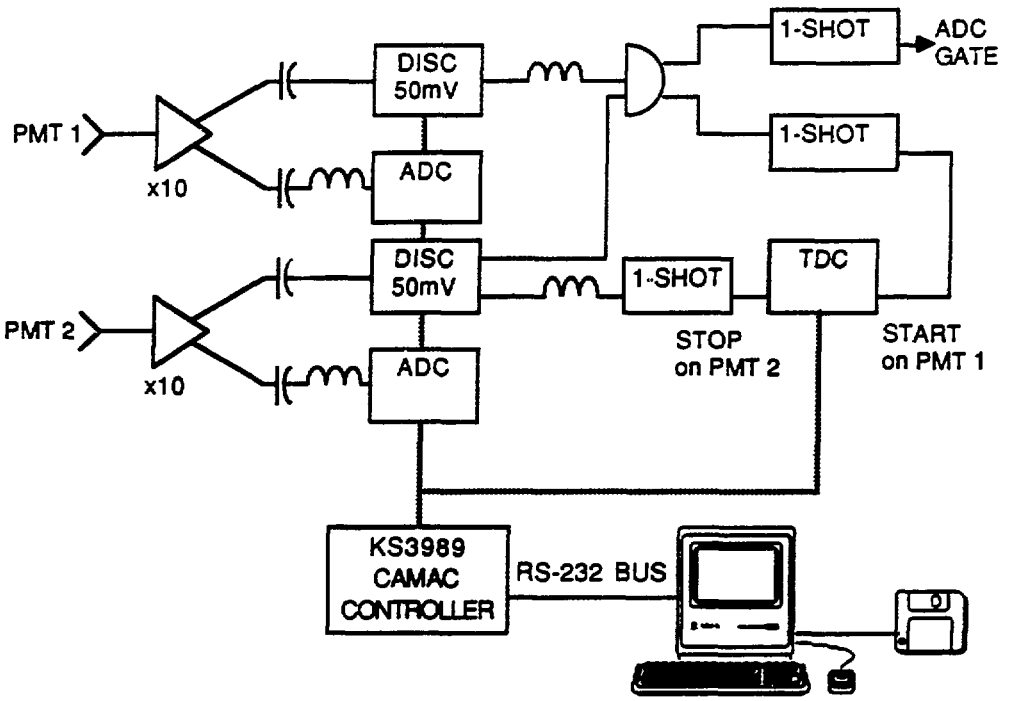

Fig. G3. Coincidence rate as a function of the concentration of scintillator. Note the suggestion of a knee in the S-mode configuration.

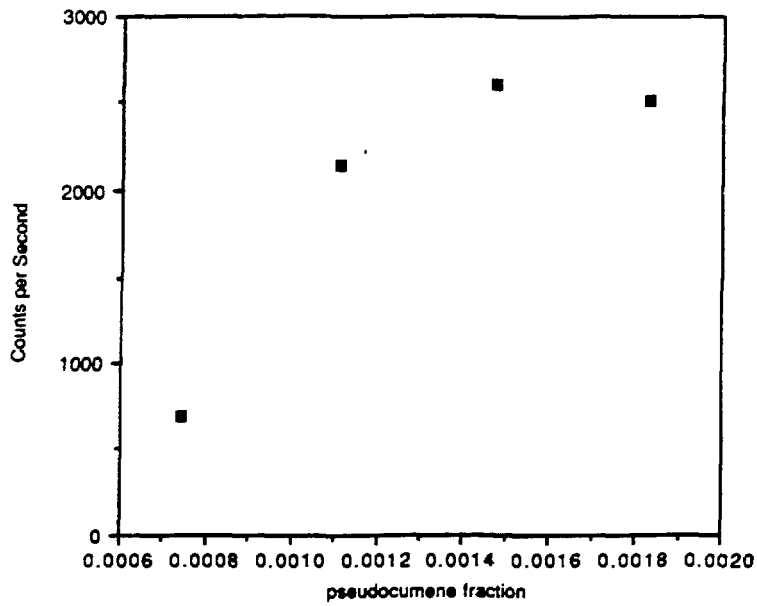

S-mode CONFIGURATION

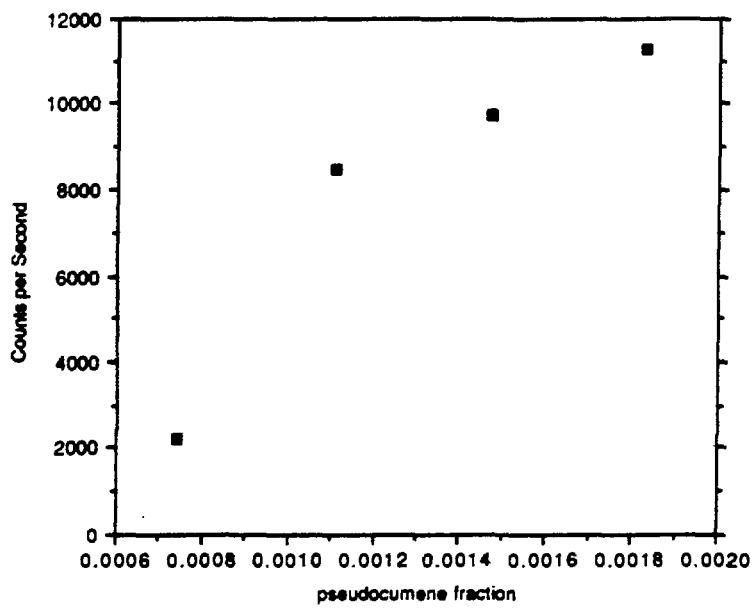

C-mode Configuration

Fig. G4. Time spectra histograms for selected concentrations of scintillator. The horizontal axis is in 0.1 ns per channel and each histogram bin is 8 channels wide. Note the narrow central peak in the C-mode data.

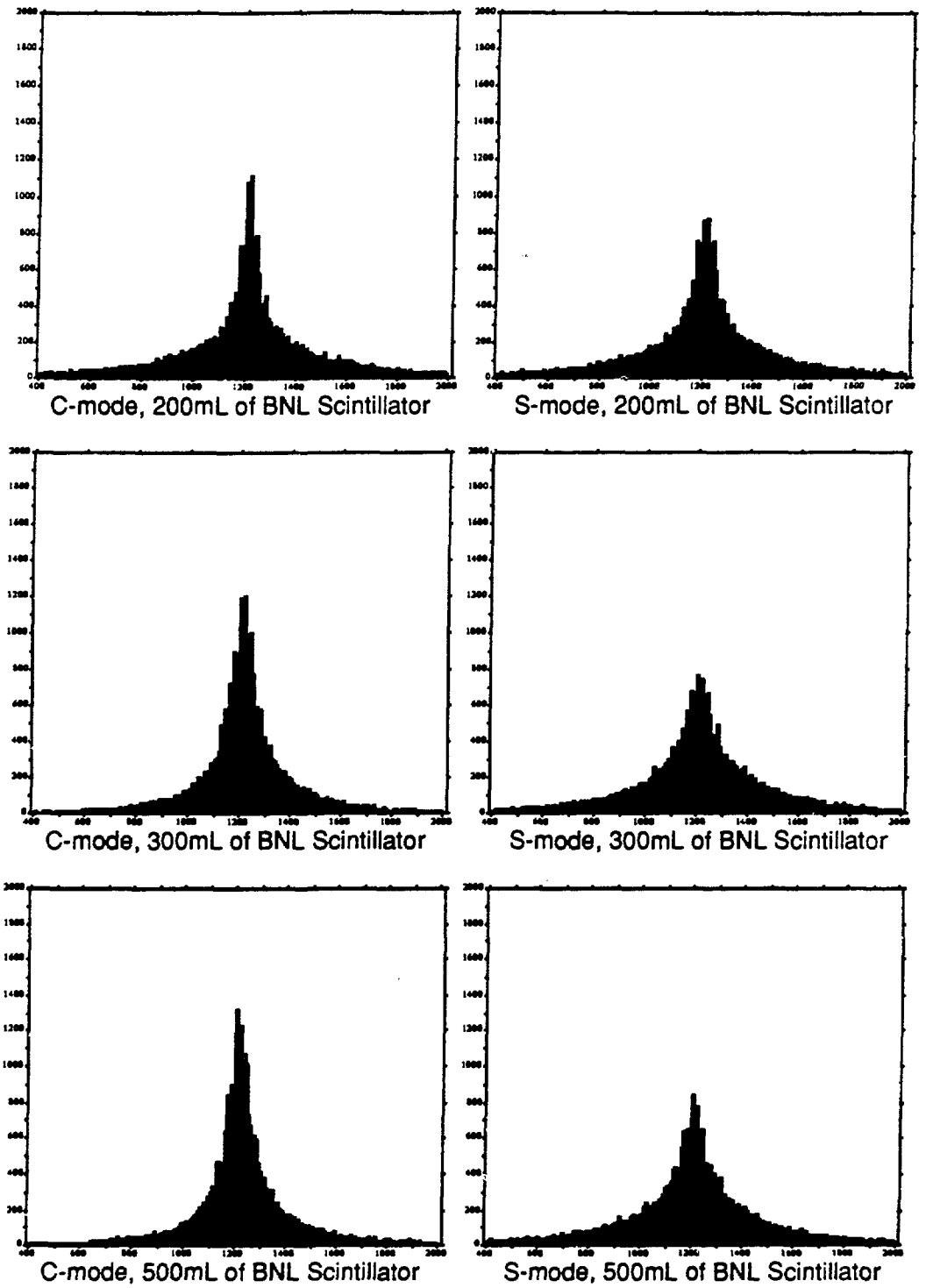

Fig. G5. Time spectra histograms for selected concentrations of scintillator. The horizontal axis is in 0.1 ns per channel and each histogram bin is eight channels wide. The logarithmic ordinate illustrates the exponential character of the tails, particularly in the S-mode data.

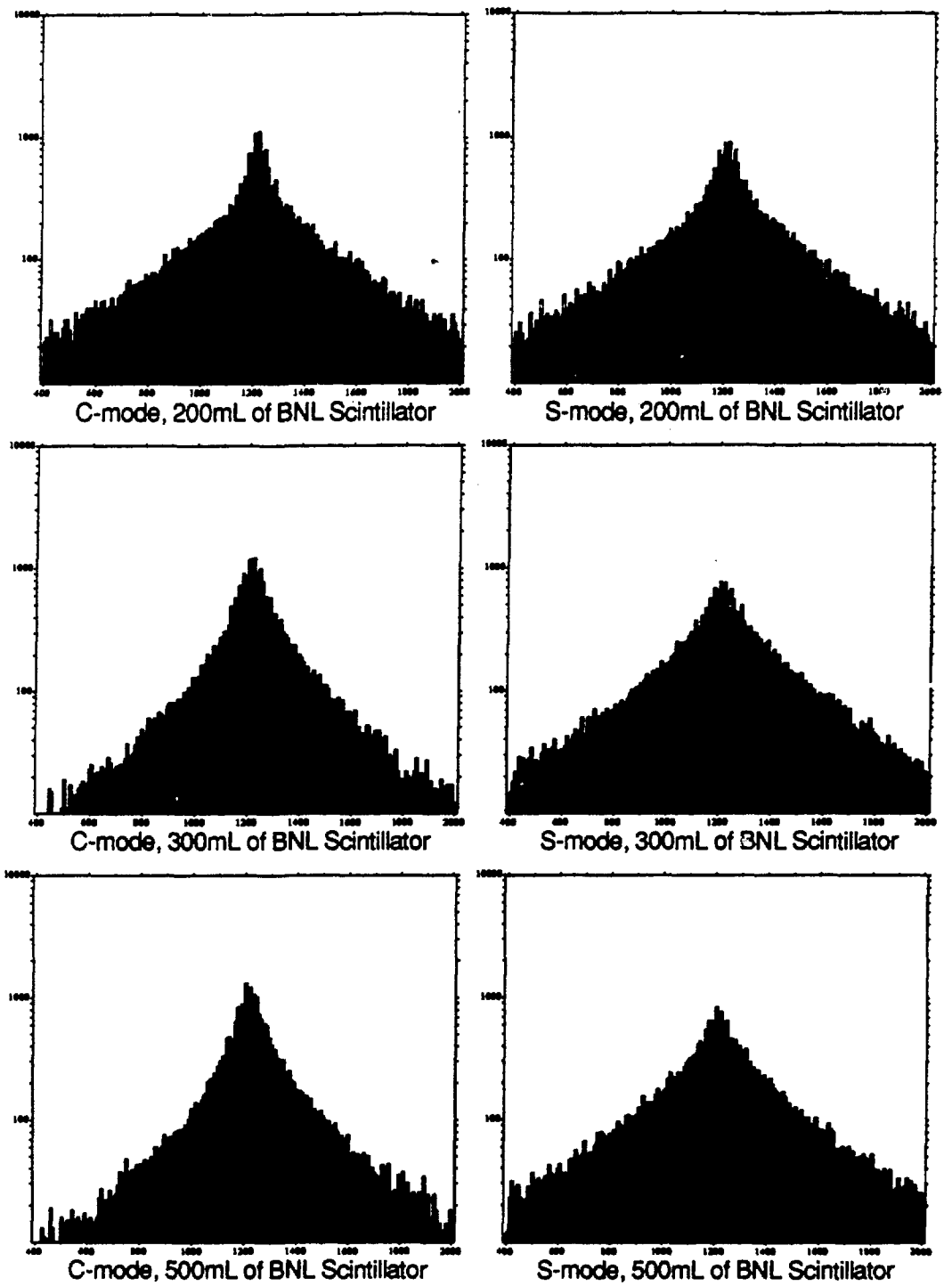

APPENDIX H

Monte Carlo Simulation of Neutrino Production by Medium-Energy Protons in a Beam-Stop

R. L. Burman and M .E. Potter
Los Alamos National Laboratory, Los Alamos, NM 87545, USA

E.S. Smith*
Ohio State University, Columbus, OH 43210, USA.

14 September 1989

Abstract

We describe a Monte Carlo program which generates the distribution of stopped pions produced by medium-energy protons in a beam stop. This distribution can be used to predict the absolute neutrino flux from this source to 7.3%. The same Monte Carlo program also produces neutrinos from the in-flight decay of pions and muons in the beam stop environment.

*Now at CEBAF, Newport News, VA 23606, USA.

1 Introduction

Several neutrino-physics experiments are either proposed or under way at medium-energy accelerators [1,2,3,4]. The need for reliable simulation of neutrino production by protons in a thick target is therefore becoming essential to the development of these programs.

The dominant source of neutrinos from the beam stop comes from the production and subsequent decay of single positive pions. The decay sequence $\pi^+ \rightarrow \mu^+ \nu_\mu$ is followed by $\mu^+ \rightarrow e^+ \bar{\nu}_\mu \nu_e$ which produces equal numbers of ν_μ, $\bar{\nu}_\mu$ and ν_e's. The spectra of these neutrinos have the characteristic energies of pions and muons decaying in their rest frame. Negative pions are strongly absorbed when they come to rest, and therefore the decay chain beginning with π^- is practically absent. The deviations of the neutrino spectra from this decay scheme are due to pions decaying in flight, accounting for about 2% of the total. These decay-in-flight neutrinos have a wide range of energies, and can represent an important source of useful interactions as well as backgrounds. The goal of the present Monte Carlo is then two-fold: (a) to reproduce the spatial distribution of stopped π^+'s decaying within a beam stop, and (b) to generate neutrinos from the decay in flight of $\pi^+$and μ^+.

LAMPF experiment E866 [5] has measured the distribution of pions stopping inside a mockup beam stop. The Monte Carlo program described in this paper has been used to reproduce these data by adjusting the overall normalization of measured proton and pion cross sections within the experimental uncertainties ($\sim$ 10%). The Monte Carlo uses smooth parameterizations of pion production and reactions cross sections for proton energies up to 800 MeV and can be used to predict the neutrino production by medium energy protons in beam stop with arbitrary compositon and shape.

2 Monte Carlo Code and Inputs

The Monte Carlo must model the following processes in the beam stop: proton transport; pion production, transport, interactions and decay; muon transport and decay. Our goal is to model all these processes in enough

detail so that uncertainties in the predictive power of the program are well understood and adequate simulations can be performed on a mini- computer. The basic procedure is to model pion production and reaction cross sections in such a way that the dependence on material and proton and pion kinetic energies (T_p and T_π) is smooth and is well-behaved outside the regions where it is constrained by data. We then compare the predictions of the program with data from the E866 experiment and adjust a few parameters to fit the measurements within the expected experimental uncertainties. Details of the parameterization of the cross sections can be found in Ref. [6]. The adjustment factors are overall multiplicative factors that are specified separately. This enables us to use our original parameterization, simply scaled by these multiplicative factors, to best reproduce the E866 data.

The geometrical configuration of the target is handled by the versatile and convenient external geometry package of MCNP [7], where it is specified by an input file. This allows flexibility in changing the composition and shape of the target while leaving the Monte Carlo code intact. The FORTRAN code used to predict the distribution of stopping pions in the mockup beam stop for E866 is then identical to the one used for a more realistic and complicated geometry relevant to the calculation of neutrino fluxes for an experiment.

The neutrino production from a thin target is determined by the pion production cross sections and decay kinematics. However, there are several aspects which affect neutrino production in a thick-target geometry in addition which must be included in our simulation. These include

- Proton beam degradation
- Proton energy loss
- Pion absorption
- Pion scattering
- Pion energy loss
- Pion decay
- Muon decay

The interrelationship of these physical processes within the Monte Carlo program is exhibited by the flow chart in Figure 1. The program begins with a definition of the beam stop geometry and a Monte Carlo choice of initial proton coordinates from the beam phase space. A proton is then tracked through the beam stop, until the energy is less then T_{MIN}, with a test for a nuclear reaction at each step; if a reaction occurs, a pion is produced weighted by the ratio of the pion production cross section σ_π to the proton reaction cross section σ_I, in order to improve the Monte Carlo efficiency. The energy and angle of the pion are chosen from an integral probability table based upon the parameterized pion production cross sections. Sequential production of pions by an individual proton is included in the code, but it is not shown in Figure 1 in order that the flow chart be relatively simple. The pion is then tracked through the geometry with tests for decay-in-flight, inelastic reactions, and absorption. If the π^+ survives to the end of its range, it is tallied as a π^+ and μ^+ decay-at-rest.

Pion decay-in-flight, however, leads to another sequence of events. Energies and angles are chosen for the μ^+ and ν_μ, and the μ^+ is tracked until the end of its range. Differential decay probabilities for the μ^+ are calculated along its track and stored with the associated position and momentum. Since the muon decay probability is small, the total decay probability for the track is used to weight a forced decay. At the chosen point of the μ^+ decay, energies and angles are calculated for the resultant ν_e and $\bar{\nu}_\mu$, taking in account the muon polarization [8]. The entire sequence for pion decay-in-flight is repeated, typically 100 times, in order to improve the program efficiency.

We next review, in detail, the inputs to the Monte Carlo program with emphasis on the global features.

2.1 Pion Production Cross Sections

There exist two sets of measurements of pion production cross sections, at proton kinetic energies of T_p=585 and 730MeV [9,10], that have covered a wide variety of nuclei as well as a broad range of produced pion energies (T_π) and angles (θ). We therefore use their data as a basis for our parameterization and use other measurements [11,12,13] only for a check of consistency. The doubly-differential π^+ cross section for a given atomic

number Z and fixed proton kinetic energy T_p is written in the following form:

$$\frac{d^2\sigma}{d\Omega_\pi dT_\pi} = Amp(\theta)\ e^{-\left(\frac{\overline{T}-T_\pi}{\sqrt{2}\sigma(\theta)}\right)^2} \times \left(1+e^{\frac{T_\pi-T_F}{B}}\right)^{-1} \quad (\mu b/MeV/sr)$$

$$\sigma_\pi = \int\int \frac{d^2\sigma}{d\Omega_\pi dT_\pi} dT_\pi d\Omega_\pi \qquad (1)$$

Functional forms for the parameters $Amp(\theta)$, $\overline{T}$ and σ have been expressed in simple and flexible forms (see Ref. [6]) in order to cover the entire range of variables in the problem. The high-energy cut-off function is intended to take account of kinematical factors. In general, the cut-off is used to insure energy conservation ($T_F = T_p$ - 140 MeV - 2B, where B is set equal to 25 MeV.)

The energy dependence of the total pion production cross sections are assumed to be a piecewise linear function of T_p, as shown in Figure 2. The total cross sections obtained by integration of the parameterization of the differential cross section reproduce the published cross sections to within 10%, but the normalisation is handled separately as an overall scale factor. We have adjusted this normalization by a factor of 1.11 to come into agreement with the E866 data. Typical relative uncertainties in the cross sections are of order 10%, with an additional 10% uncertainty in overall normalization, so this correction is quite reasonable. The effect of this normalisation will be illustrated in Section 3.

In Figures 3-6, we compare our parameterization of the differential pion production cross section with measurements [9,10,11]. Production on hydrogen, carbon and copper at several energies of interest for pion production are shown; the agreement is quite good over the entire data set. The data on carbon at 800 MeV (Fig. 5) were not used to determine any parameters, so the comparison is a valid check of our parameterized extrapolation. The curves in the figures do not include the factor of 1.11 which renormalizes the total cross sections. A more detailed discussion of the parameterization of pion production is given in Ref. [6].

2.2 Thick Target Production

The program must handle the transport of protons and pions in a realistic way. The energy loss by ionization is calculated with the parameterization of Barkas and Berger [15], which is a fit to proton range measurements as a function of ionization potential (I_{adj}) and kinetic energy. The energy loss is obtained from a difference of ranges so that the computed accuracy is independent of the Monte Carlo step size. Multiple scattering is included for pions, using formulas for the multiple-Coulomb-scattering angle, θ_{MCS}, suggested by the Particle Data Group [16]; the principal effect of multiple scattering is to decrease the observed range. This corresponds to about 5 g cm^{-2}, or 2% of the range of a 500 MeV pion. The effects of multiple scattering for protons are not included, since they are masked by the wide-range in pion production angles.

The proton beam degradation within the target is described by the inelastic proton cross section, which we take to be the energy-independent cross section measured in neutron-nucleus collisions [17], for a nucleus of atomic number A.

$$\begin{aligned} \sigma_I &= 1.12 \times \sigma_{0I} A^{\beta_I} \\ \sigma_{0I} &= 43.2 \pm 2.3\ mb \\ \beta_I &= .719 \pm .012 \end{aligned} \tag{2}$$

These measurements are consistent with the measured proton-nucleus cross section at 800 MeV. The factor of 1.12 was added in order to reproduce the data from E866. Each inelastic proton collision is assumed to reduce the energy of the proton by an amount appropriate for pion production,as the quasi-free pion production in proton-nucleus scattering accounts for 40-50% of the reaction cross section [18]. Protons are followed, losing energy either through collisional or ionisation energy loss, until reaching the minimum energy for pion production, T_{MIN} . Pion production through secondary proton interactions accounts for approximately 10% of the total.

The locations in the stack of each proton interaction are recorded and a pion with the appropriate energy and direction is traced beginning at that location. Each pion is weighted by the ratio of σ_π/σ_I. As the pions are tracked through the target, they are allowed to scatter inelastically or be absorbed. Elastic scattering is ignored, since the effects are generally small

compared to uncertainties in the initial production angles. The sum of the first two processes is controlled by the reaction cross section

$$\sigma_{reac} = \sigma_{abs} + \sigma_{inelastic} \tag{3}$$

We have parameterized the reaction cross section [19] and the ratio of absorption to reaction cross sections [20] to specify the interactions of pions in the beam stop:

$$\sigma_{reac} = \sigma_0(T_\pi)A^{\alpha(T_\pi)} \tag{4}$$

$$Frac(A) = \frac{\sigma_{abs}}{\sigma_{reac}} \tag{5}$$

In the above equations A is the atomic weight and the parameters σ_0 and α are both functions of the pion energy T_π. For maximum flexibility we use a parameterization for σ_0 and α based on B-splines (see [6] for details). The decomposition into absorption and inelastic channels is assumed to be energy independent; as shown in Figure 7, a reasonable agreement with the available data is obtained.

The kinematical features of inelastic pion scattering from nuclei are consistent with quasi-free scattering [22,23,24]. The peak in the energy spectrum of the scattered pion follows the kinematics of free π^+p kinematics and its width is consistent with Fermi broadening. Since we integrate over both angle and energy, we assume a simple angular distribution (80% p-wave and 20% s-wave) and then impose the kinematics of free-nucleon scattering.

3 Simulation of an Instrumented Beam Stop

The E866 experiment [5] measured the distribution of stopped pions inside several configurations of an instrumented beam stop, each of which consisted of a series of $25.4 \times 25.4\ cm^2$ slabs of water, copper or lead. Interspersed between the slabs, in various positions, were eight plastic scintillation counters of 0.64 cm thickness. Each counter registered, in coincidence, pulses from a stopping pion, the decay muon, and the decay positron. Data were acquired with the External Proton Beam (EPB) at LAMPF incident

upon a copper stack at beam energies of T_p=797 [1], 766 and 716 MeV, a "Full" stack (20 cm of water followed by copper) at T_p=797 and 766 MeV and a lead stack at T_p=797 MeV. Measurements were also made of pions exiting the front and sides of the beam stop in some of the above configurations. We have compared the Monte Carlo output with these data and have adjusted parameters to best fit the data.

The experiment measured the number of pions which decayed inside the mockup beam stop by tagging the decay sequence $\pi^+ \rightarrow \mu^+\nu_\mu$, $\mu^+ \rightarrow e^+\bar{\nu}_\mu\nu_e$. The positions of the pions which decayed were recorded and, after corrections, gave directly the spacial distribution of the neutrino source inside the beam stop. These distributions have been reproduced with the Monte Carlo program by adjusting the two overall normalisation factors previously mentioned. The distribution of pions decaying within the mockup beam stop are shown in comparison with the Monte Carlo prediction in Figures 8-11; the Monte Carlo simulation reproduces the measured data quite well. The increase in the inelastic proton cross section(σ_I) by the multiplicative factor of 1.12 in eqn (2) enables the Monte Carlo to follow the decrease in stopped-pion decay with increasing depth in the stack. An enhanced pion production in the 20 cm of water, shown in the data of Figure 8, is well represented in the simulation, as is the energy dependence illustrated in Figure 9 and the atomic-number dependence in Figure 10.

A comparison of the stopped-pion rate given by the Monte Carlo code to the measured rate in experiment E866 [5] is shown in Table 1 for various target configurations and beam energies. The ratios of the Monte Carlo calculation, with the two adjusted cross section factors described in Sections 2.1 and 2.2, to the E866 data are listed in the third column. These ratios, along with the uncorrelated errors from the E866 data shown in the fourth column, lead to an average fit of the Monte Carlo code compared to the data

$$< Monte\ Carlo\ /\ E866\ Data >= 1.001 \pm .024 \qquad (6)$$

The shapes of the front and side leakage from the Full stack are reasonably handled by the Monte Carlo simulation as shown in Fig. 11. However, the side leakage is somewhat overestimated; the ratio of the Monte Carlo

[1]The beam energies at LAMPF are known to 1.5 MeV

prediction to the data is $1.38 \pm .22$, where the error is dominated by systematics in the measurement. We were unable to reduce the predicted leakage out the side without making unacceptable changes to the pion decay rate inside the stack.

A correction was applied to the E866 data to compare with the Monte Carlo predictions due to the difference in production in scintillator and the material comprising the target. The correction was .99, .97 and .92 for the Full, copper and lead targets, respectively.

4 Realistic Simulation of Neutrino Production

The Monte Carlo can be used to predict the absolute neutrino flux from a beam stop at a medium-energy proton accelerator by simply changing the input file that specifies the geometry of the stop. In general, the beam stop geometries are quite complicated due to the need for cooling, and their composition might even change as a function of time depending on various programs at the accelerator; for example, the proton beam at LAMPF is used to produce radioisotopes for commercial applications [25]. Thus the integrated average neutrino flux for a given experiment must be appropriately computed.

To illustrate the effects of beam stop composition, we use the Monte Carlo code to calculate neutrino production as a function of atomic number. A "generic" beam stop configuration, a cylinder 30 cm in diameter and 200 cm long surrounded by steel shielding, is used to represent a standard geometry. Results, for the primary dump consisting of water, aluminum, copper or uranium, are given in Table 2. It can be seen that neutrino production from stopped π^+ decay is appreciably smaller for materials of higher atomic number. This results from the increasing neutron to proton ratio for higher-Z elements and the much smaller cross section for proton-neutron production of π^+ compared to that for proton-proton production.

The comparison in Table 2 of neutrino production from stopped versus decay-in-flight π^+ illustrates a possible complication in beam stop design. An experiment to search for neutrino oscillations in the channel $\overline{\nu}_\mu \rightarrow \overline{\nu}_e$ would be subject to a background from $\overline{\nu}_e$ arising from π^- to

μ^- decay-in-flight and subsequent μ^- decay. This background is roughly proportional to the rate for π^+ decay-in-flight, and as seen from Table 2 it decreases faster as a function of atomic number than the rate for stopped π^+ decay. Therefore, an optimal experiment design might well call for a high-Z beam dump.

Next, we compute the average neutrino flux from the actual LAMPF beam stop. We do the calculation for the 1984-1986 running period of E225, an experiment that measured the absolute ν_ee elastic scattering cross section. A schematic version of the LAMPF beam stop is shown in the upper part of Figure 12 and includes a 20 cm water degrader, nine insertable isotope production stringers with aluminum housings, and a water-cooled copper stop. The cavity is surrounded by steel which stops any pions and muons which exit the beam stop proper. The purpose of the water degrader is to increase the neutrino flux, for the reasons demonstrated above; the calculated increase is 24%. Substantial pion production at the water degrader and at the isotope stringers is clearly apparent in the middle figure. The position of π^+ decay-in-flight within the beam stop for LAMPF cycles 42-47 is shown in the lower part of Figure 12. As expected, this distribution is spread out compared to the production distribution. Table 3 shows the calculated number of pions which are produced and decay for each proton incident on the LAMPF beam stop. During 1984-1986, conditions at the LAMPF beam stop changed: differing upstream target thicknesses produced different proton beam energies at the beam stop; the water degrader was removed in cycle 41; and different numbers of isotope production stringers were used in the various cycles. As shown in Table 3, these variations resulted in significant changes in neutrino production.

From the reults sumarized in Table 3, the time-integrated neutrino flux into the E225 detector was calulated. The estimated errors in the neutrino flux in the detector come from six sources:

1. Fit of all E866 data points to the Monte Carlo (2.4%)
2. Simulation of actual beam stop configuration (3%)
3. Systematic effects in the E866 measurement (5.9%)
4. Energy of proton beam (0.3%)

5. Number of protons on target (2%)

6. Distance between source and detector (0.5%)

The quadrature sum of the above contributions yields a 7.3% total error for the neutrino flux normalization of the elastic scattering experiment E225.

The provisions in the Monte Carlo code for recording π^+ and μ^+ decay-in-flight have been used for preparation of a recent LAMPF reseach proposal [26] for a neutrino oscillation search. In Figure 13, the calculated neutrino flux for a possible signal at the 5×10^{-4} level from $\nu_\mu \rightarrow \nu_e$ oscillation is shown along with the calculated ν_e background fluxes from decay-in-flight of μ^+ and the π_{e2} decay-in-flight of π^+ . It is clearly important in the design of such experiments that the decay-in-flight neutrino fluxes be calculable.

5 Summary

The prediction of the neutrino flux from the decay of stopping pions produced from proton interactions in a beam-stop requires extensive knowledge of pion production and pion reaction cross sections. Theoretical models do not predict these cross sections in enough detail to be used for the flux calculation. We have therefore turned to representations of the data which are well-behaved and can be extrapolated smoothly to regions where there are no measurements. These calculations have in turn been normalized to the experiment E866 which directly measured the ratio of stopped pions to incident protons in an instrumented beam stop. The Monte Carlo program has then been used to predict the absolute neutrino flux from the LAMPF beam stop to an accuracy of 7.3%. Neutrino fluxes from decay-in-flight at the same LAMPF beam stop have been calculated for both the signal and backgrounds to be expected for a proposed neutrino oscillation search.

The complexity of the stopping or decay distributions, and the significant effects due to different materials, illustrate the need for the detailed Monte Carlo code.

6 Acknowledgements

We wish to acknowledge helpful conversations with J. B. Donahue and with D. A. Krakauer. We are grateful to H. Lichtenstein for supplying the MCNP geometry package and for helping mesh this code with our Monte Carlo code, and to M. Wexler for his initial aid in using this package. This work was supported in part by the U. S. Department of Energy, Office of Energy Research, and by the U. S. National Science Foundation under Grant No. HY-8501559.

References

[1] R.C. Allen *et.al.*, Phys. Rev. Lett. **55**, 2401 (1985).

[2] L.S. Durkin *et.al.* Phys. Rev. Lett. **61**, 1811 (1988).

[3] Large Cerenkov Detector Project, "A Proposal for a Precision Test of the Standard Model by Neutrino-Electron Scattering," Los Alamos National Laboratory report LA-11300-P (1988).

[4] "Search for Neutrino Oscillations with KARMEN," presented by R. Maschuw in **Proceedings of the Sixth Moriond Workshop on Massive Neutrinos in Astrophysics and in Particle Physics**, 1986, edited by O. Fackler and J. Trân Thanh Vân (Editions Frontières), p. 293 (1986).

[5] R.C. Allen *et.al.* "A Measurement of the Neutrino Flux from a Stopped Pion Source," to be published in Nucl. Instr. and Meth.

[6] R.L. Burman and E.S. Smith, "Parameterization of Pion Production and Reaction Cross Sections at LAMPF Energies," Los Alamos National Laboratory Report LA-1502-MS (1988).

[7] Judith F. Briesmeister, editor, "MCNP–A General Monte Carlo Code for Neutron and Photon Transport," Los Alamos National Laboratory Manual LA-7396-M, Rev. 2 (1986).

[8] Giles Barr,T.K. Gaisser and Todor Stanev, Phys. Rev. **D39**, 3532 (1989).

[9] J.F. Crawford *et al.*, Phys. Rev. **C22**, 1184 (1980).

[10] D.R.F. Cochran *et al.*, Phys. Rev. **D6**, 3085 (1972).

[11] Peter Denes *et al.*, Phys. Rev. **C27**, 1339 (1983).

[12] F.H. Cverna *et al.*, Phys. Rev. **C23**, 1698 (1981).

[13] See references in [9].

[14] N.J. DiGiacomo *et al.*, Phys. Rev. **C31**, 292 (1985).

[15] W.H Barkas and M.J. Berger, "Tables of Energy Losses and Ranges of heavy Charged Particles," NASA Special Publication SP-3013 (1964).

[16] Particle Data Group, Phys. Lett. **170B**, 45 (1986).

[17] W. Schimmerling *et al.*, Phys. Rev. **C7**, 248 (1973).

[18] J.A. McGill "Inclusive Proton Spectra and Total Reaction Cross Sections for Proton-Nucleus Scattering at 800 MeV," Los Alamos National Laboratory Thesis LA-8937-T (1981).

[19] Daniel Ashery and John P. Schiffer, Ann. Rev. Nucl. Part. Sci. **36**, 207 (1986).

[20] J.P. Schiffer, Nucl. Phys. **A335**, 339 (1980).

[21] D. Ashery *et al.*, Phys. Rev. **C23**, 2173 (1981).

[22] C.H.Q. Ingram, Nucl. Phys. **A374**, 319 (1982).

[23] S.M. Levenson *et al.*, Phys. Rev. Lett. **47**, 479 (1981).

[24] S.M. Levenson *et al.*, Phys. Rev. **C28**, 326 (1983).

[25] *Newsline*, The Journal of Nuclear Medicine **28**, 1371 (1987).

[26] "A Proposal to Search for $\bar{\nu}_\mu \rightarrow \bar{\nu}_e$ Oscillations with High Sensitivity at LAMPF" LAMPF proposal P1173 (1989)

Table 1: Normalization of the Monte Carlo code to the E866 data for different stack configurations and proton beam energies. A systematic error of 5.9% that contributes equally to all measurements is not included in the last column.

Target Configuration	T_p *(MeV)*	*Monte Carlo/ Data*	*Uncorrelated Error*
Full	797	1.007	.047
Full	766	1.048	.076
Copper	797	0.978	.051
Copper	766	1.024	.055
Copper	716	0.998	.066
Lead	797	0.969	.064

Table 2: Neutrino production as a function of atomic number. The primary beam dump is a cylinder 30 cm dia. and 200 cm long.

Beam Dump Material	*Stopped* π^+ *per Proton*	*Decay-in-Flight* π^+ *per Proton*
Water	.106	.0018
Aluminum	.091	.0017
Copper	.065	.00043
Uranium	.034	.00021

Table 3: Neutrino production for LAMPF cycles 38-47. For every stopped pion the source produces a ν_μ, $\overline{\nu}_\mu$ and ν_e.

LAMPF Cycle	T_p *(MeV)*	*Target Configuration*	π^+/p
38-40	751	Full	.082
41	768	No Water	.068
42-47	772	Full	.089

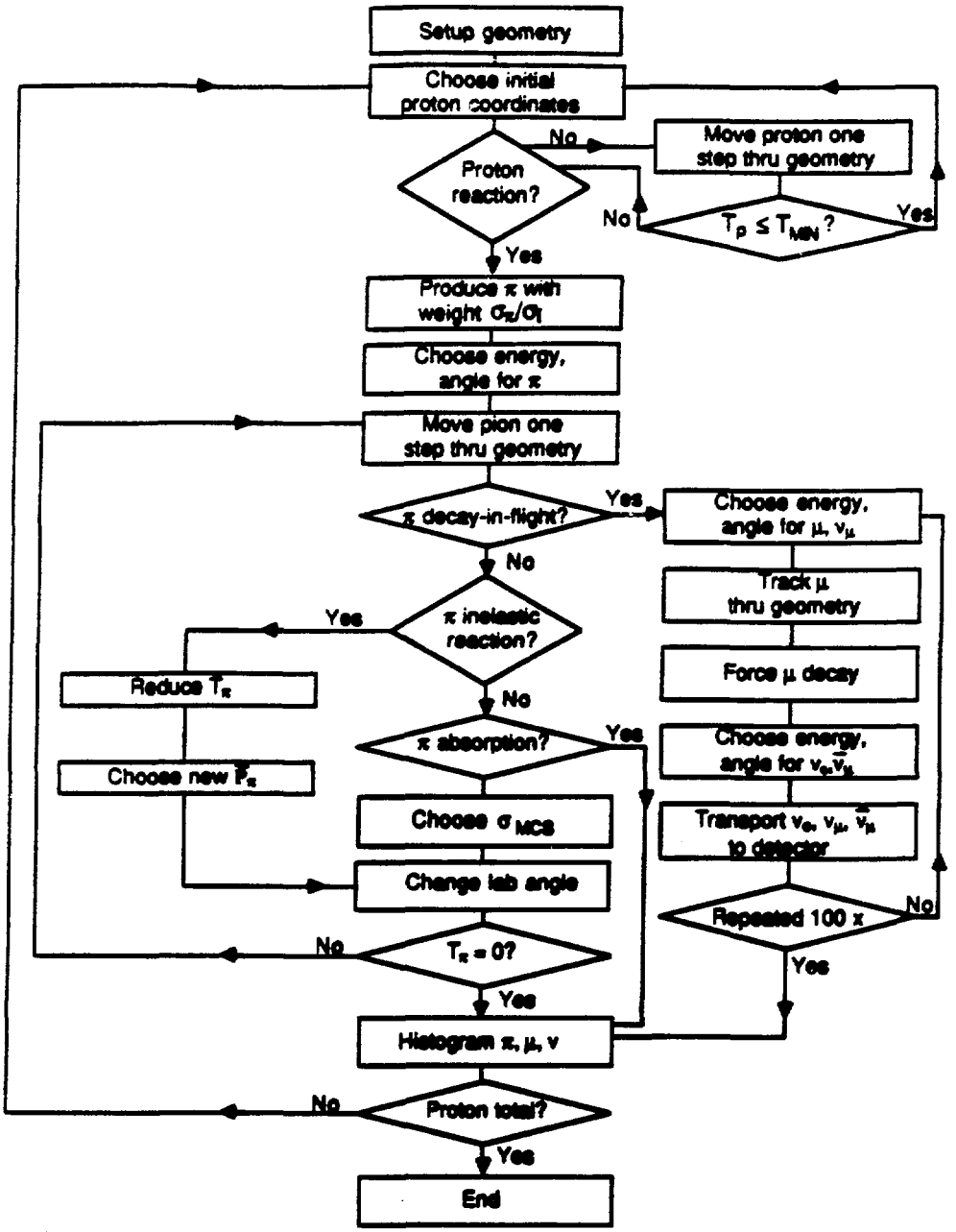

Figure 1: A schematic flow chart of the Monte Carlo code.

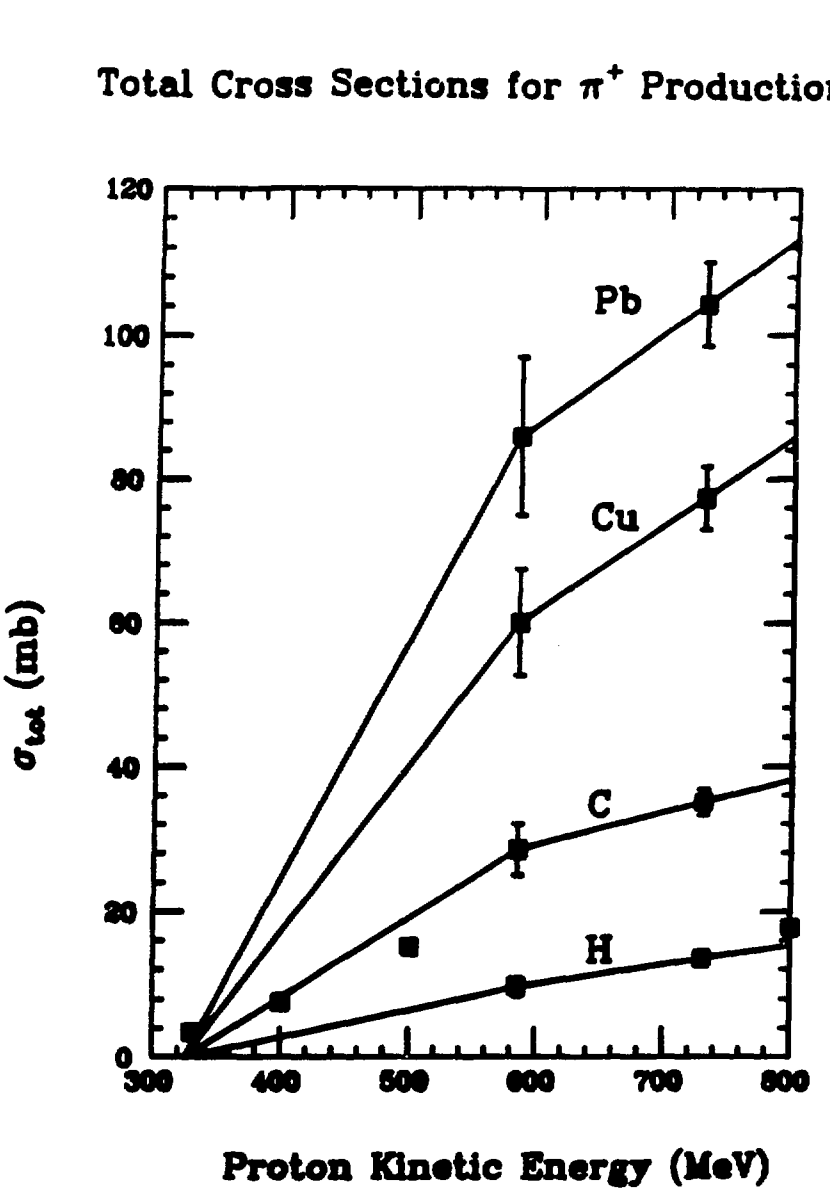

Figure 2: We show the assumed dependence of the total pion production cross section on proton energy T_p. Note that the pion production cross section is assumed to go to zero at T_{MIN}= 325 MeV. The data points are from references [9,10,14]. Overall normalization uncertainties are not included in the errors. In the Monte Carlo these cross sections are increased by a factor of 1.11 to reproduce the E866 data.

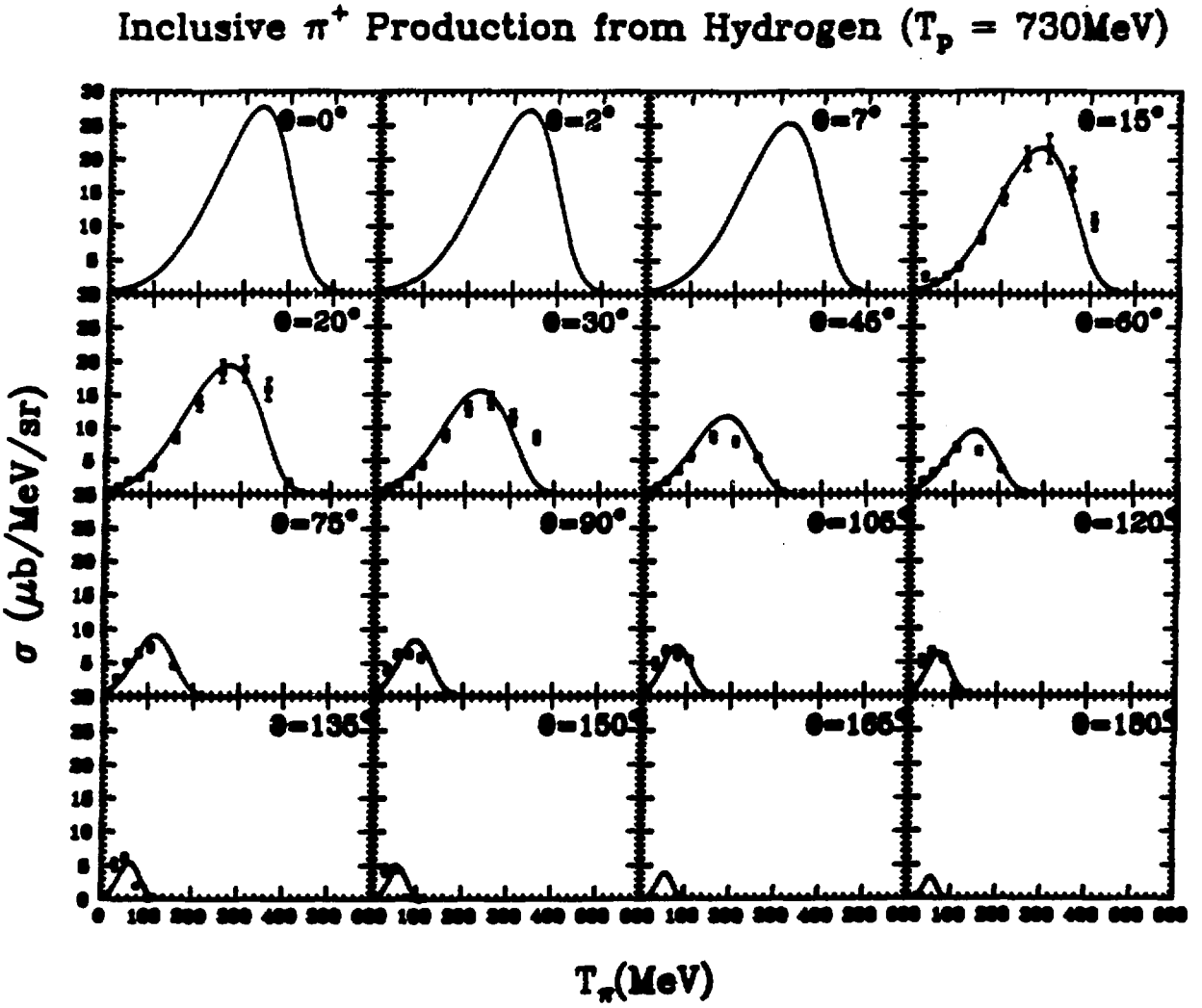

Figure 3: The parameterisation for π^+ production from hydrogen at 730 MeV is compared with the data from reference [10].

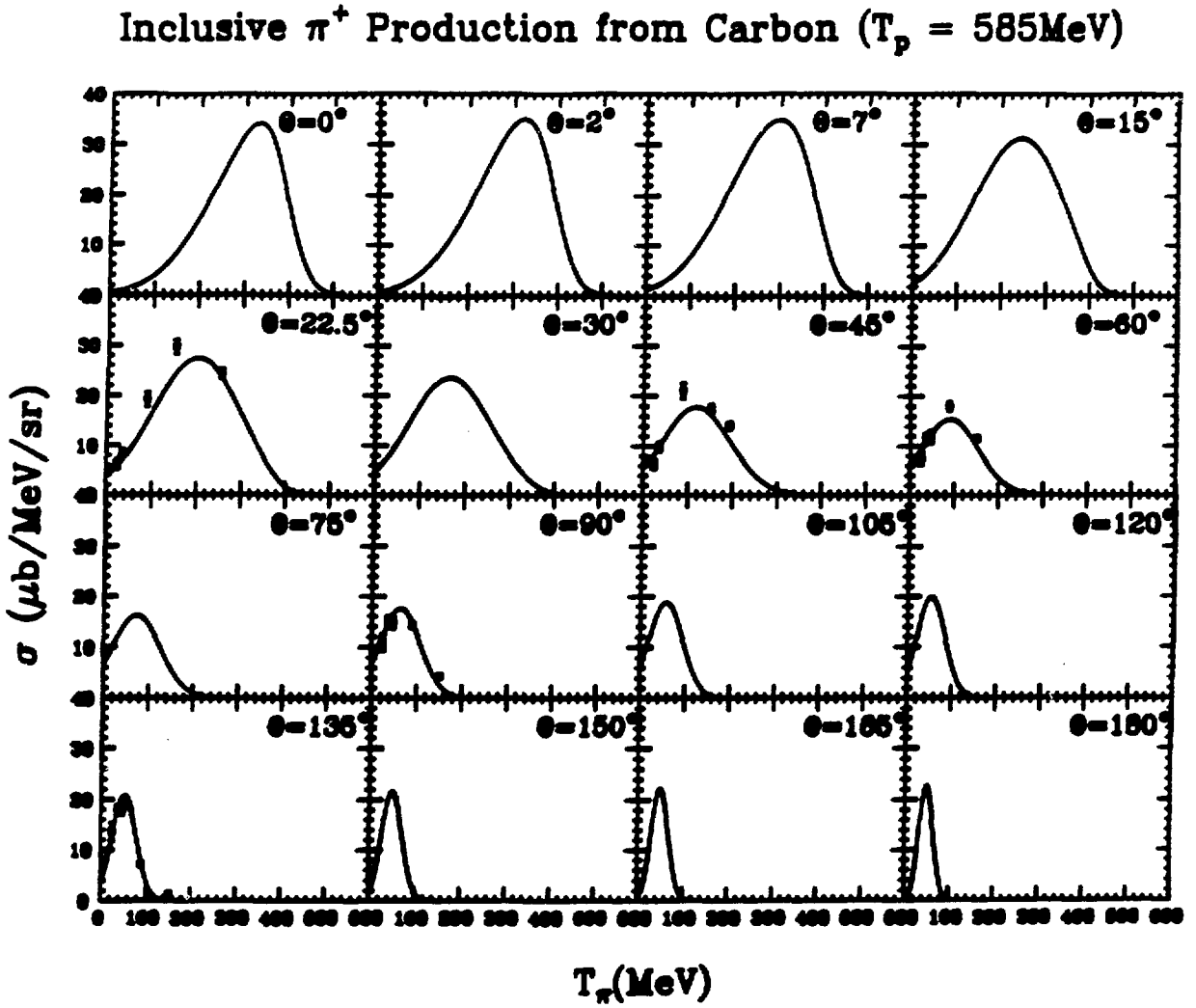

Figure 4: The parameterization for π^+ production from carbon at 585 MeV is compared with the data from reference [9].

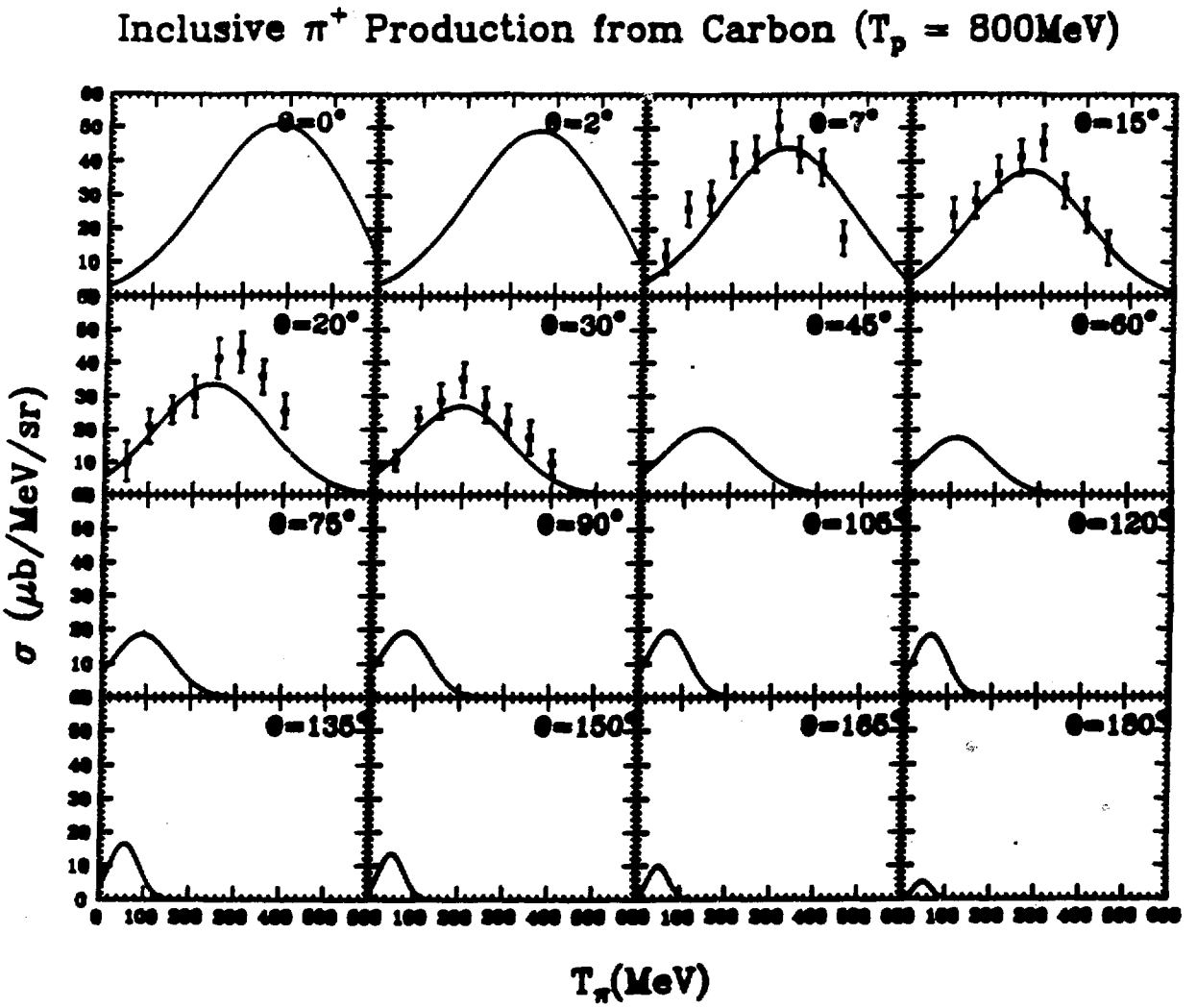

Figure 5: The parameterization for π^+ production from carbon at 800 MeV is compared with the data from reference [11]. These data are a test of the parameterization, as they were not used to fix any parameters.

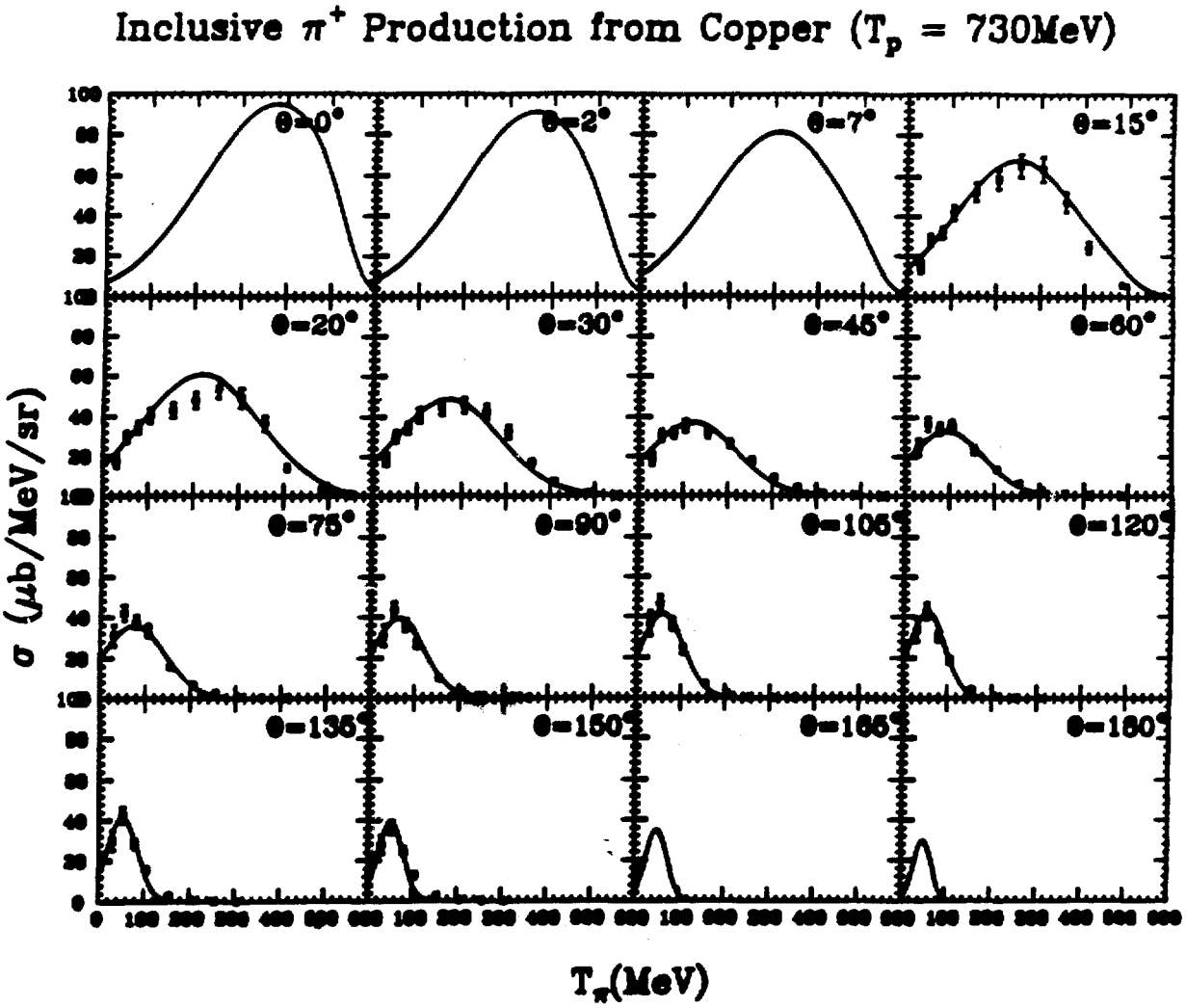

Figure 6: The parameterization for π^+ production from copper at 730 MeV is compared with the data from reference [10].

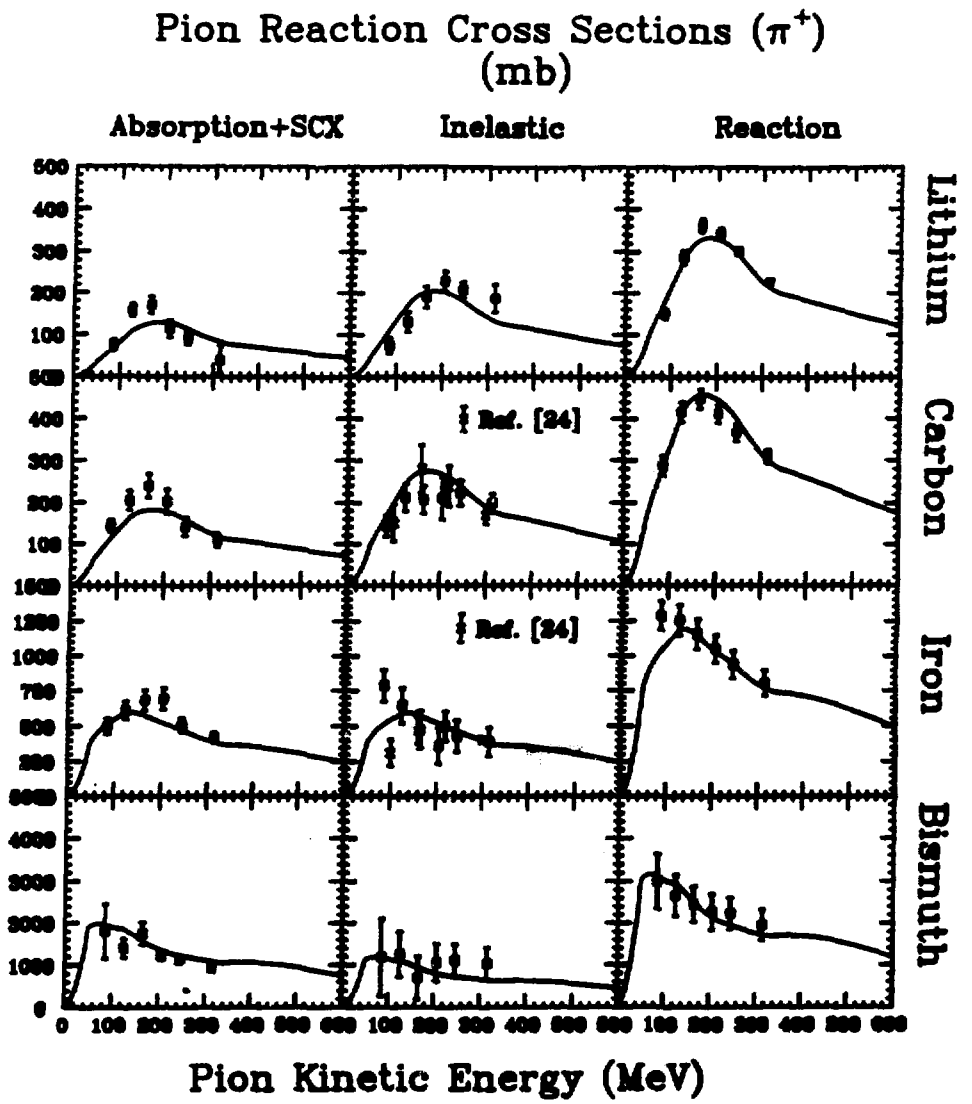

Figure 7: Comparison of the parameterization of σ_{reac} with the data from reference [21], except where noted.

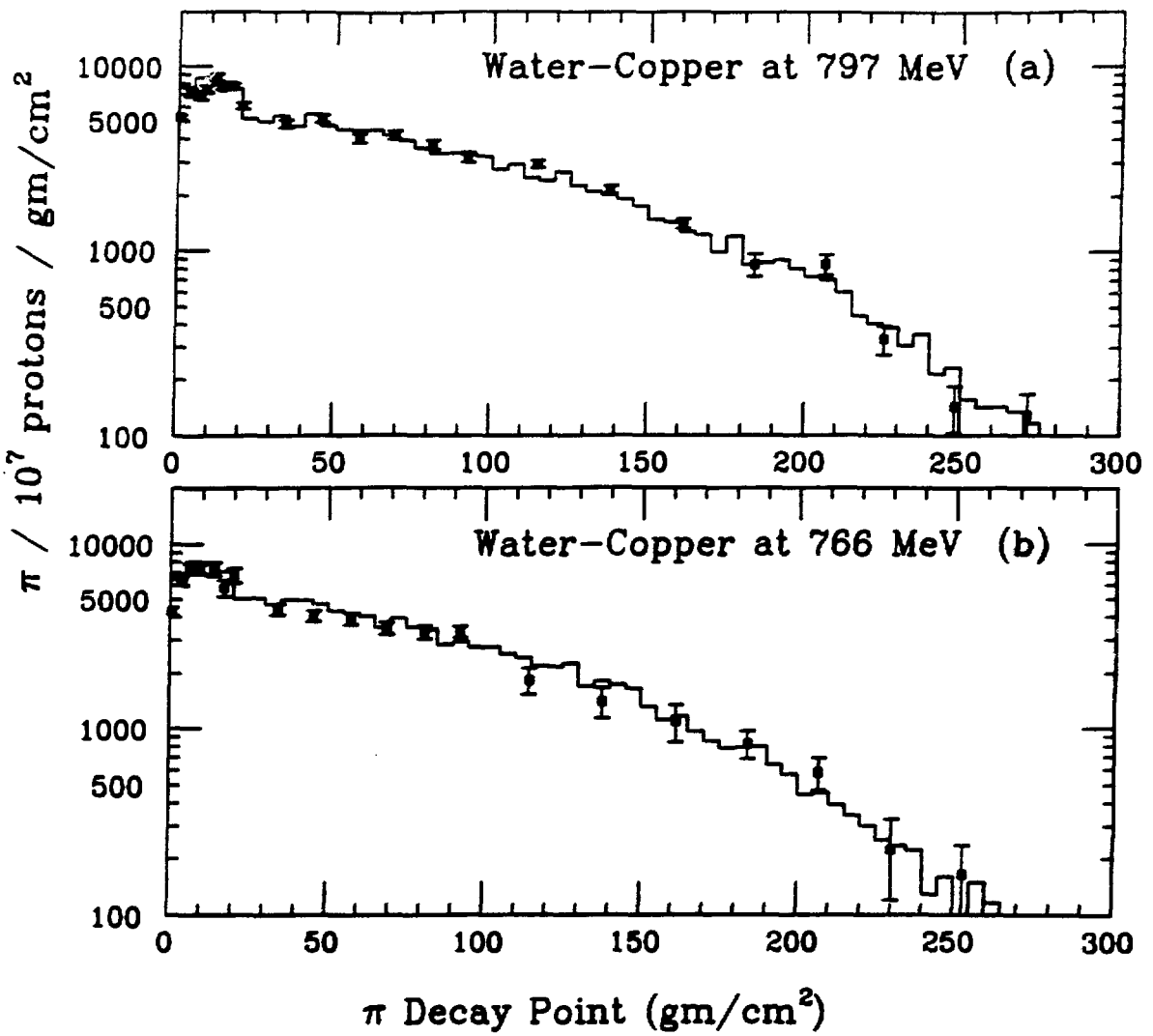

Figure 8: Distribution of stopped pion decays in the full (water plus copper) target at two energies: (a) 797 MeV, and (b) 766 MeV. The solid line is the Monte Carlo result normalised to all of of the data. The discontinuity at 20 g cm^{-2} shows the interface between the water and the copper.

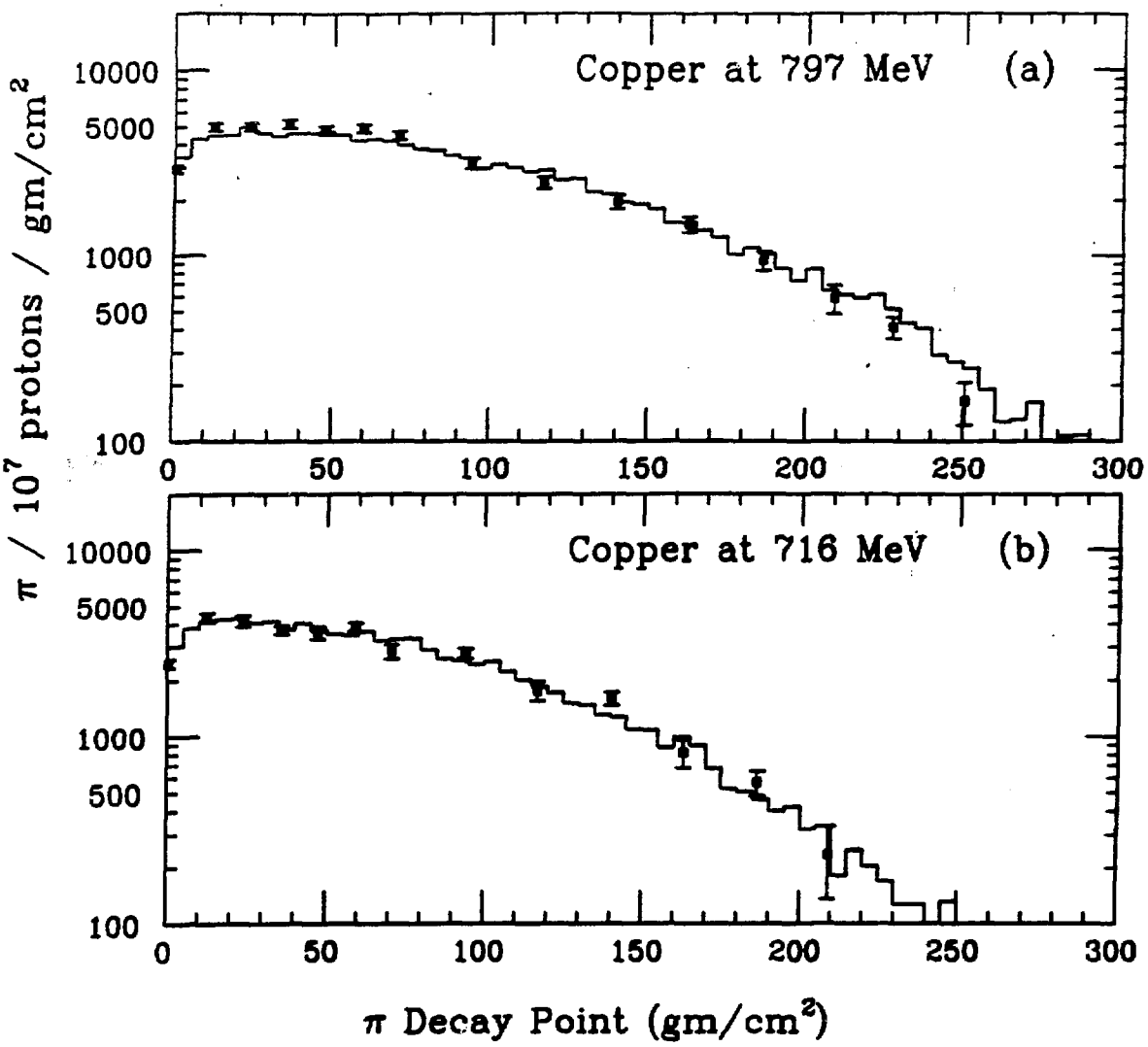

Figure 9: Distribution of stopped pion decays in the copper target at two energies: (a) 797 MeV, and (b) 716 MeV. The solid line is the Monte Carlo result normalized to all of of the data.

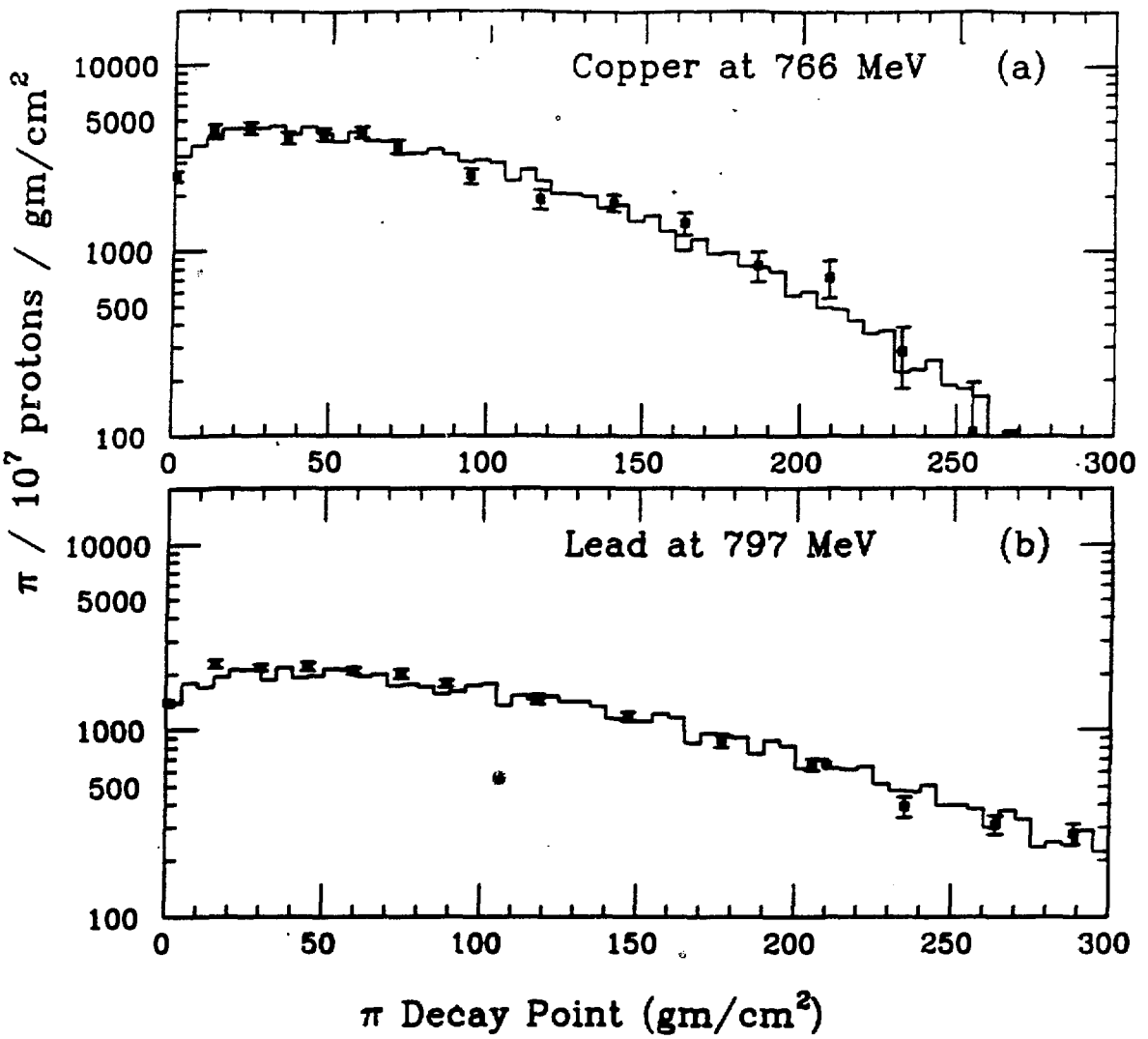

Figure 10: Distribution of stopped pion decays in (a) the copper target and (b) the lead target. The solid line is the Monte Carlo result normalized to all of of the data.

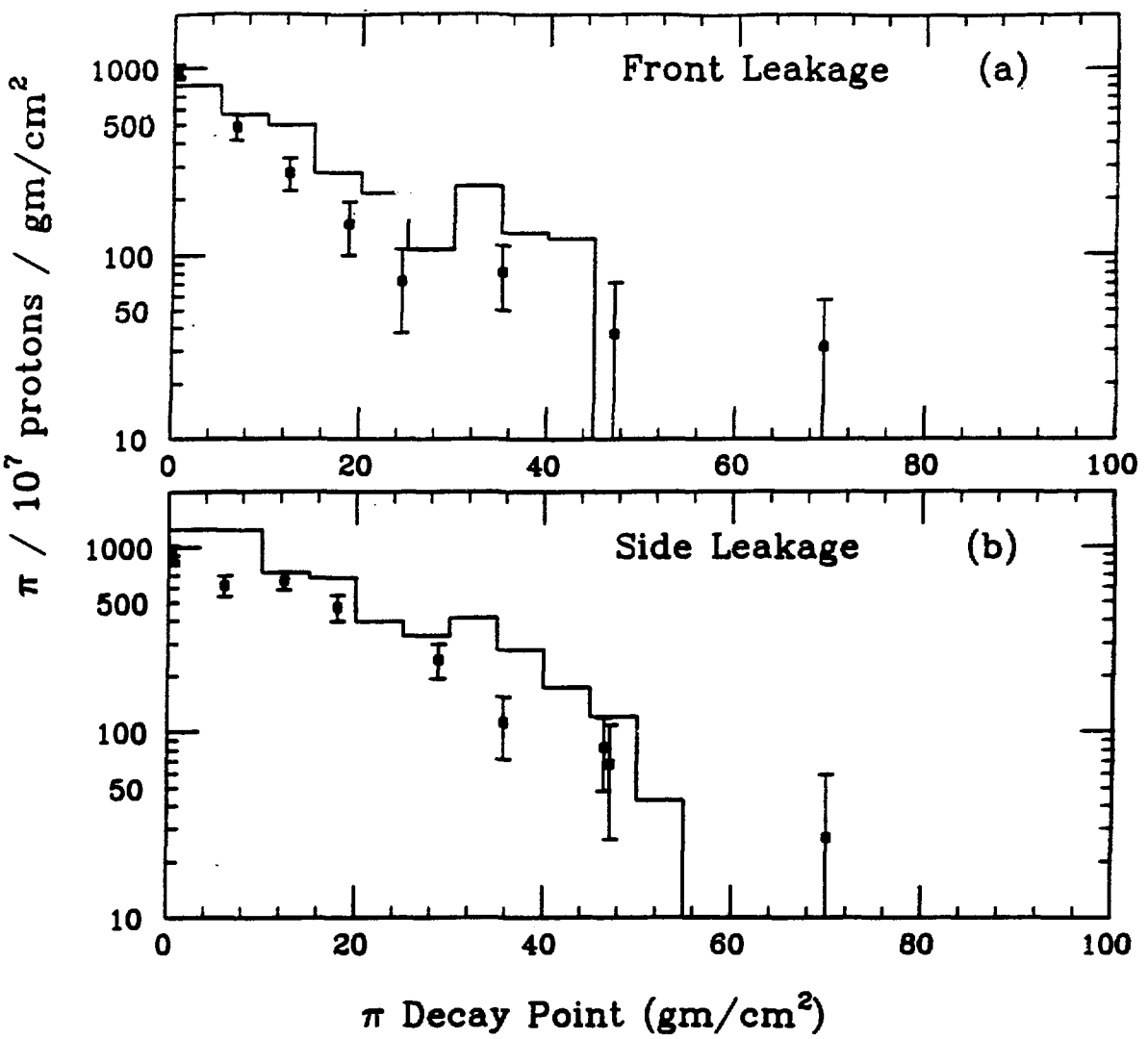

Figure 11: The leakage of stopped pions from (a) the front and (b) the side of the Full (water plus copper) target. The solid line is the Monte Carlo result normalized to all of of the data.

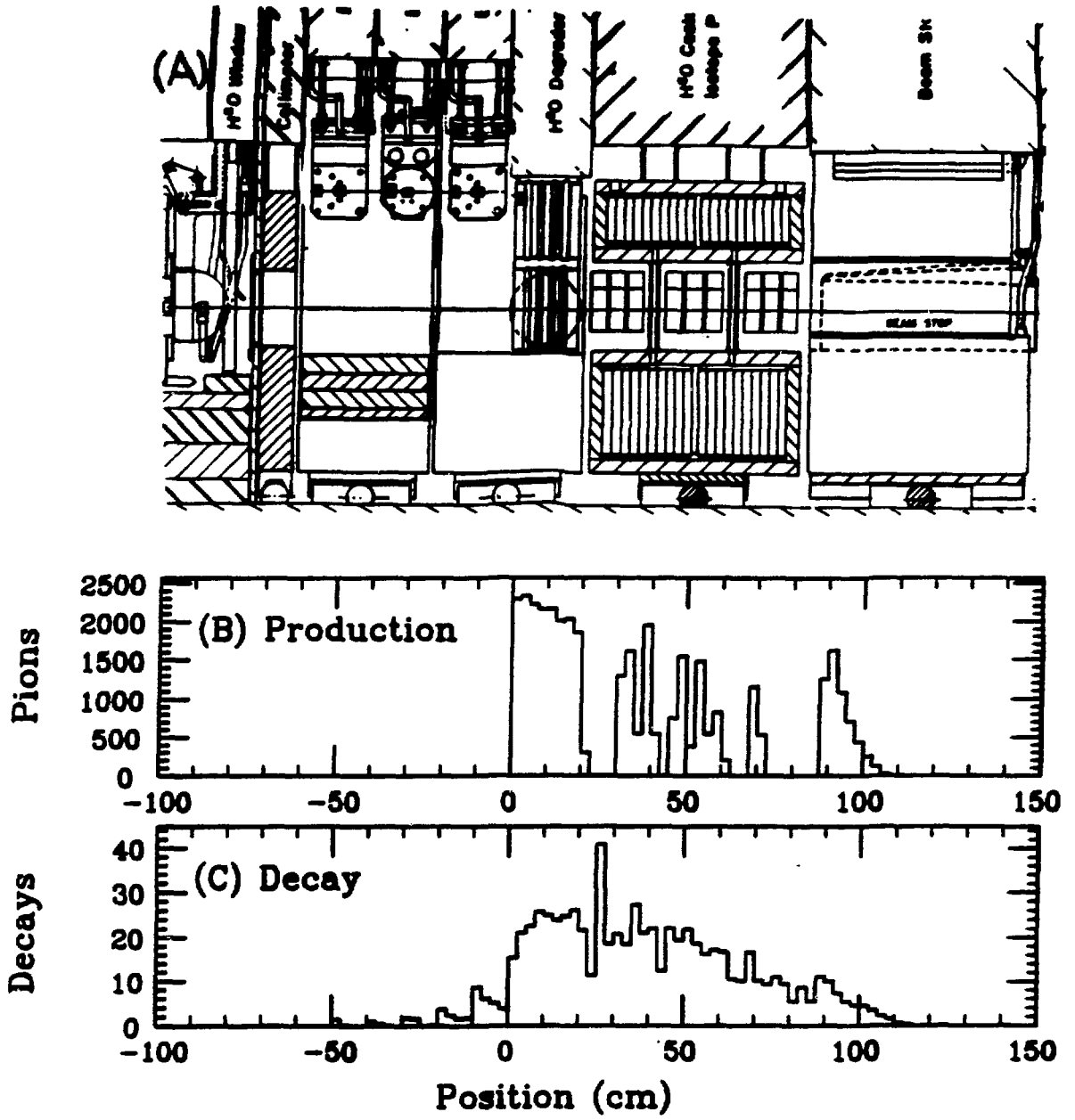

Figure 12: Pion decay at the LAMPF proton beam stop. Shown is (a) an elevation of the beam stop, and the distribution along the beam stop of (b) pion production, and (c) pion decay-in-flight.

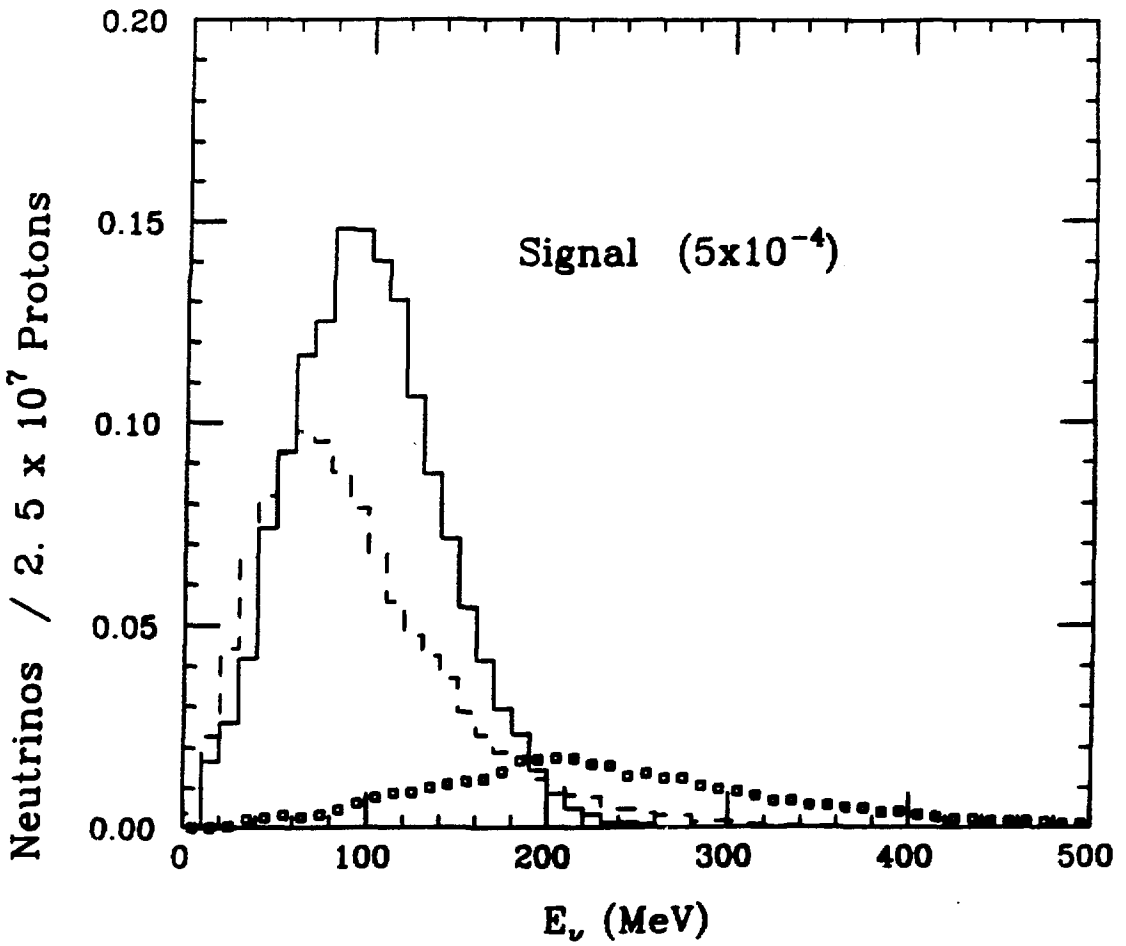

Figure 13: Neutrino fluxes from decay-in-flight for expected signal and backgrounds for a proposed $\nu_\mu \rightarrow \nu_e$ oscillation experiment at LAMPF [26]. The detector position is at 17° to the incident proton beam. The solid line is the ν_e signal; the dashes and boxes are the ν_e backgrounds from μ^+ decay and from π_{e2} decay, respectively.

APPENDIX I

REPORT ON THE PERFORMANCE AND OPERATING CHARACTERISTICS OF THE BURLE C83061E QUANTACON™ PHOTOMULTIPLIER TUBE

V. D. Sandberg and T. N. Thompson

Los Alamos National Laboratory, Los Alamos, New Mexico 87545

and

F. A. Helvy

Burle Industries, Inc., Lancaster, Pennsylvania, 17604

The Burle C83061E QUANTACON™ is a 10.4 inch diameter photomultiplier tube with improved photoelectron collection optics. We report here on the first tests of this newly developed tube. We find the single photoelectron charge resolution to be excellent, with a peak to (noise) valley ratio exceeding 3 and with a transit time spread of less than 2.3 ns (FWHM) for full photocathode illumination at the single photoelectron level. A design for a fast anode pulse base is also presented.

(To appear in "Proceedings of the Workshop on Physics and Experimental Techniques of High Energy Neutrinos and VHE and UHE Gamma-Ray Particle Astrophysics," Arkansas, 11-13 May 1989, to be published in Nuclear Physics B - Proceedings Supplements, Edited by G. B. Yodh and D. C. Wold.)

1. INTRODUCTION

This report describes our first tests of the performance and operating characteristics of the new Burle[1] C83061E QUANTACON™ high performance photomultiplier tube. The successful development of large imaging water Cherenkov detectors for use in nucleon decay searches and super nova neutrino detection[2,3] and their use in neutrino-electron scattering experiments for high precision tests of the standard model[4], searches for solar neutrinos[5], and in ultrahigh energy cosmic ray experiments[6] have provided substantial motivation for the development of large photocathode area photomultiplier tubes that have very good time resolution at light levels corresponding to a few photoelectrons. The C83061E was developed in response to a request from Los Alamos National Laboratory to Burle to develop a photomultiplier tube with characteristics suitable for such a detector. We report here on the first tests of timing and charge resolutions at single photoelectron levels for a sample of five prototype tubes.

Briefly, the C83061E is a developmental tube with a 10.4 inch diameter (9.25 inch diameter of photocathode material) end-window bialkali photocathode and a 12-stage multiplier consisting of a cessiated gallium-phosphide first dynode followed by eleven copper-beryllium dynodes. Its characteristics are highlighted by the following performance parameters: The high gain of the first dynode (with a secondary emission ratio of from 20 to 60 depending on electron kinetic energy) provides excellent single photoelectron resolution with peak to valley ratios greater than three and excellent resolution of multiple photoelectron signals. A gain of order 10^7 is achieved with a cathode-anode voltage of order 2000 V. A new electrostatic lens design (patented by Burle) isochronally images the full photocathode onto the first dynode and provides very good collection efficiency and excellent timing characteristics. Timing tests with full photocathode illumination at the single photoelectron level gave a measured time resolution of less than 2.3 ns full width at half maximum (FWHM). These tests and descriptions of the mechanical and electrical properties of the tubes are described in the following paragraphs.

2. MECHANICAL CHARACTERISTICS

A drawing of the C83061E illustrating the end-window photocathode, the equipotential surfaces and electron trajectories, and the positions of the focusing electrodes and dynode cage is shown in Fig. 1. The electrode assembly is supported by a metal fixture to allow high tolerance alignment of the electron collection optics and the photocathode. While the tube is quite rugged, the suspended structure is delicate and should be handled with reasonable care. Electrical connections to the grids, dynodes, and anode are made conventionally through a glass pinout at the base. The recommended socket (Burle types AJ2145A) requires care when installing or removing it to avoid unnecessary stress on the glass-metal seals.

The hemispherical electrodes are held at the appropriate electrical potentials to map in a

by a gain of 10 shaping amplifier (with a 50 ns time constant) and feed to the input of the ADC. Delay cables were used to compensate for time differences. The light of the LED was attenuated to a level such that there was one photoelectron produced in the photocathode for every five LED pulses. A representative charge spectrum is shown in Fig. 6.

In this spectrum the large number of pulses with no photoelectrons is indicated by the large peak at the pedestal. The single photoelectron peak stands out very clearly with a peak to valley ratio greater than 3. The two photoelectron signal is easily distinguished and a three photoelectron signal may be resolved. The relative proportions of these peaks (that is, the intensity of the light) are a characteristic of the light source, in this case the LED, not the photomultiplier tube. With a different light source the apportionment of the one, two, three, etc. peaks will be different. The single photoelectron resolving power of the photomultiplier tube is quantified by the peak to valley ratio between the single photoelectron peak and the valley adjacent to the pedestal. The time resolution of the C83061E under the conditions of full photocathode illumination at the single photoelectron level is measured by the arrangement shown in Fig. 7. The timing jitter and different colors of test light sources are well known causes of systematic errors in measurements of transit time variation.[10] To provide a fast light pulse with a Cherenkov light spectrum we use a prism made of lucite resin with a 1 μC ^{207}Bi source attached to one face. Relativistic electrons from the bismuth source produce Cherenkov photons in the lucite that are simultaneous in time and have a blue-green color. Two C83061E tubes are arranged to receive light uniformly over their photocathodes from the two faces of the prism. A coincidence gate then selects common events and timing is arranged so that one tube starts the TDC and the other tube stops the TDC. A time spectrum taken with this arrangement is shown in Fig. 8. The width of this histogram is 3.2 ns (FWHM) for two (assumed) identical tubes, so the time width per tube is $3.2 / \sqrt{(2)} = 2.3$ ns per tube. The actual time resolution is probably better than this since no pulse height walk correction has been made to compensate for the leading edge discriminators used in the test. This correction is not expected to be too large since the pulse height variations for single photoelectron events is small (that is, the anode pulses are very uniform for these tubes).

Tests are under way with an improved light source consisting of a laser diode driving a second harmonic generating crystal to produce short pulses of green light . Using this laser based system, timing results and the results of searches for afterpulsing and photocathode uniformity will be reported upon in a separate publication. Early tests of photocathode uniformity and collection efficiency indicate that these tubes have a variation across the photocathode of less than 10%.

The Burle C83061E QUANTACON™ photomultiplier tube has been tested under worst-case conditions at the single photoelectron level and found to have a time resolution of 2.3 ns (FWHM) and a single electron peak to valley

ratio of order 3. The large area of its photocathode makes it an attractive candidate for use in Cherenkov detectors for a wide variety of detector systems.

REFERENCES

1. Burle Industries, Inc., Lancaster, Pennsylvania 17604.

2. IMB Experiment for the Observation of Nucleon Decay, Irvine-Michigan-Brookhaven Collaboration (Proposal).

3. Kamioka Nucleon Decay Experiment, KAMIOKANDE Collaboration, Kamioka, Japan (Proposal).

4. Precision Test of the Standard Model by Neutrino-Electron Scattering, Large Cherenkov Detector Collaboration, Los Alamos (Proposal).

5. Solar Neutrino Observatory, SNO Collaboration, Sudbury, Ontario, Canada (Proposal).

6. Ultra-High Energy Gamma Ray Observatory,CYGNUS III Collaboration, Los Alamos (Proposal); and GRANDE, GRANDE Collaboration, Little Rock, Arkansas (Proposal).

7. H. R. Krall, F. A. Helvy, and D. E. Persyk, IEEE Trans. Nuclear Sci. NS-17, #3, 71 (June 1970).

8. Available from Burle Industries, Inc., Lancaster, Pennsylvania 17604.

9. The characteristic impedance of two parallel wires in open air is given by $Z_0 = 120\ \mathrm{Cosh}^{-1}(\mathrm{diameter/separation})$, which for the dimensions of the C83061E anode-stem electrodes evaluates to 95Ω.

10. M. Moszy´nski and J. Vacher, Nucl. Instr. and Meth. 141, 319 (1977); R. Bosshard et al., IEEE Trans. Nuclear Sci. NS-19, #3,107 (1972).

11. D. B. Scarl, IEEE Trans. Nuclear Sci. NS-19, #3, 7 (1972).

spherically symmetric way the equipotential surface at the photocathode onto the plane just above the first dynode. The photoelectron trajectories behave as though they were in a spherical tube with a radius of curvature of approximately 8 inches and with the consequent equal time trajectories. The trajectories end on the cessiated gallium-phosphide surface of the first dynode with a kinetic energy of order 800 eV to 1200 eV. Cessiated gallium-phosphide is a negative electron affinity material[7] that is much more linear with voltage than conventional dynode materials. Secondary electrons from cessiated gallium phosphide have greater escape depth and are more nearly thermalized. These properties give improved gain and allow better time resolution due to the lower emission velocity and smaller velocity spread. For primary electrons in the above range we expect ≈40 secondary electrons per incident photoelectron. The remaining eleven dynodes in the multiplier cage are copper-beryllium and provide a ratio of approximately 3.5 per stage. The multiplier cage is based on the Burle 8854 design.

The glass envelope is made from borosilicate glass (Schott 8250 or equivalent). This is a hard glass that shows good resistance to crazing in water and retains its transparency when immersed in water for long periods of time.

3. ELECTRICAL CHARACTERISTICS

The C83061E is a 12-stage tube with two additional focusing electrodes (the third focus electrode is internally connected to dynode 1). A positive high voltage base design to supply the voltages to these electrodes is shown in Fig. 2. The choice of a positive anode voltage requires capacitive coupling but allows operation of the tube with the cathode at ground potential. The base shares high voltage and signal lines and the anode signal may be picked off by the simple circuit shown in Fig. 2. The design is a conventional resistor divider with a few modifications to supply focus electrode voltages and to transport the fast anode pulse without ringing.

The base taper shown allocates 40% of the of the anode-cathode voltage to be between the cathode and dynode 1. This allocation represents a nominal compromise between exploiting the large secondary emission ratio of dynode 1 and keeping enough voltage on the dynode cage to provide high gain without producing large dark currents due to thermionic electron emission. Tapers of 33% and 50% for V_{DY1} have also been tested. The 33% taper gives poorer charge and time resolution due to the lower voltage and hence lower gain of dynode 1, which is consistent with the $1/\sqrt{(n_{DY1})}$ counting statistics expected from a high gain dynode. The 50% taper has slightly better timing statistics, but at a cost of a larger dark pulse rate and the necessity of operating the tube at a higher than desired voltage. The voltages for the focusing electrodes G1 and G2 are approximately $V_{G1\text{-}K} \approx 0.06 \times V_{DY1\text{-}K}$ and $V_{G2\text{-}K} \approx 0.13 \times V_{DY1\text{-}K}$, respectively. These should be trimmed for individual tubes, for example, by maximizing the dark current and hence the collection efficiency. (Detailed studies and techniques to set these

potentials for optimal performance for a given application are reported on in the Burle C83061E Bulletin.[8])

The fast-pulse performance of the anode signal is preserved by the anode stem arrangement, which consists of connecting dynode 12, the anode, and dynode 11 to a three element parallel transmission line. The three elements are metal strips approximately 3 mm wide and separated 4 mm apart, arranged with dynode 11 and dynode 12 connected to the outside strips and the anode connected to the inside strip. It is difficult to estimate the characteristic impedance of this arrangement, but we expect it to be on the the order of 100Ω.[9] To maintain pulse fidelity these lines must be terminated, for example, as shown in Fig. 2. Anode waveforms (recorded by a transient digitizer) for different values of the damping resistors are shown in Fig. 3. By tuning these resistors a pulse with a 3 ns 10% to 90% rise time and an exponential tail with a 9 ns time constant can be achieved. The exponential fall is very clean and may be clipped by conventional techniques (for example, with a short section of cable and a mismatched resistive termination) to produce a pulse of less than 10 ns total duration.

Operating the tube at a gain of $\approx 10^7$ gives a single photoelectron pulse height of ≈25 mV across 50Ω, which corresponds to an anode charge of 1 to 2 x 10^{-12} Coulombs. Charge spectrum histograms for tubes at these gains are shown in the next section.

4. SINGLE PHOTOELECTRON CHARACTERISTICS

Resolution of single electron initiated events, both from photoelectrons and thermal electrons, requires the tube under test to be stabilized in the dark with high voltage on for at least 24 hours. The relatively high-resistivity photocathode must be allowed to charge to operating voltage. The glass envelope on a tube exposed to light will phosphoresce for several hours producing a higher than normal dark current. These are particularly acute effects for photomultiplier tubes with large area photocathodes.

The dark count plateaus are shown in Fig. 4. The high voltage on the tube under test was varied from 1400 V to 2400 V, the tube was allowed to come to equilibrium at each voltage setting, and anode pulse rates above a 5mV threshold were measured. Plateau curves were taken for two different situations: no illumination (a true dark rate) and constant illumination by a green light emitting diode (LED) flooding the full photocathode. The LED light level was set to provide a counting rate approximately a factor of 10 above the dark rate. The sharp edge of the plateau curve in both cases is due, in part, to the single electron amplification by the cessiated gallium-phosphide first dynode.

The charge spectrum of the anode pulses is measured with the arrangement shown in Fig. 5. The pulse generator drives the green LED to produce light for 50 ns and supplies the gate (300 ns wide for these tests) to a 10-bit ADC. The anode signal from the tube under test is amplified

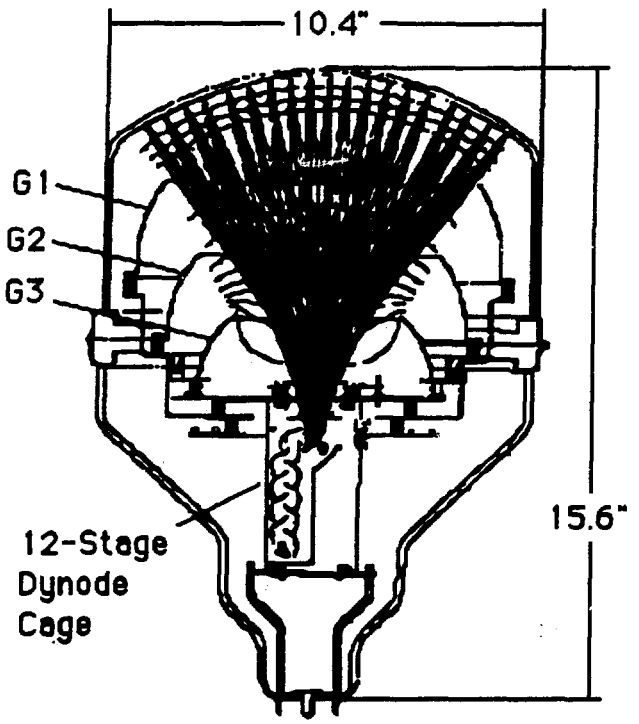

FIGURE 1
Cross sectional drawing of the Burle C83061E photomultiplier.

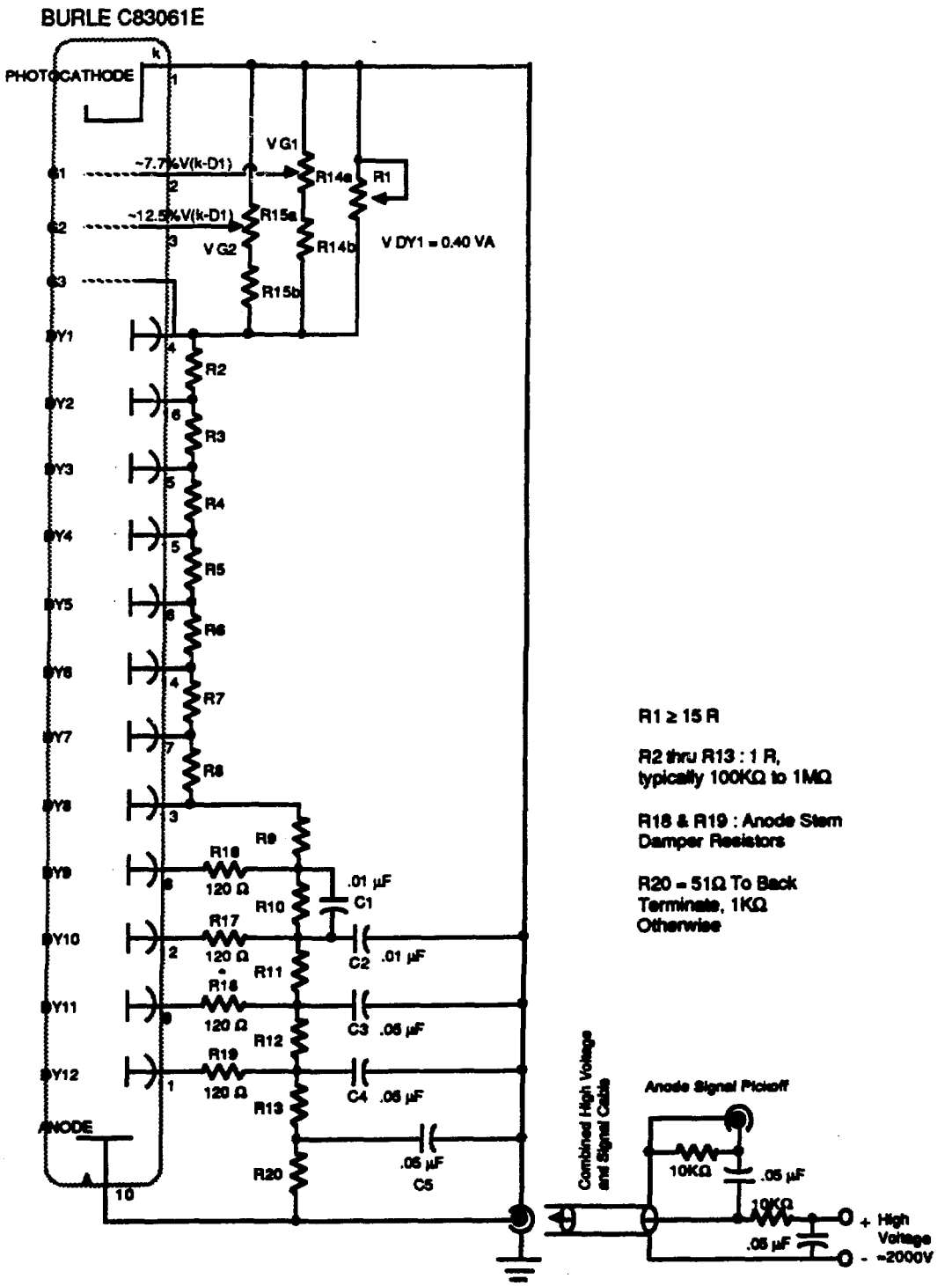

FIGURE 2
Positive high voltage fast anode pulse base for the Burle C83061E. Shown are the pmt base and anode signal pickoff circuits. This design uses a single coaxial cable for both high voltage and anode signal.

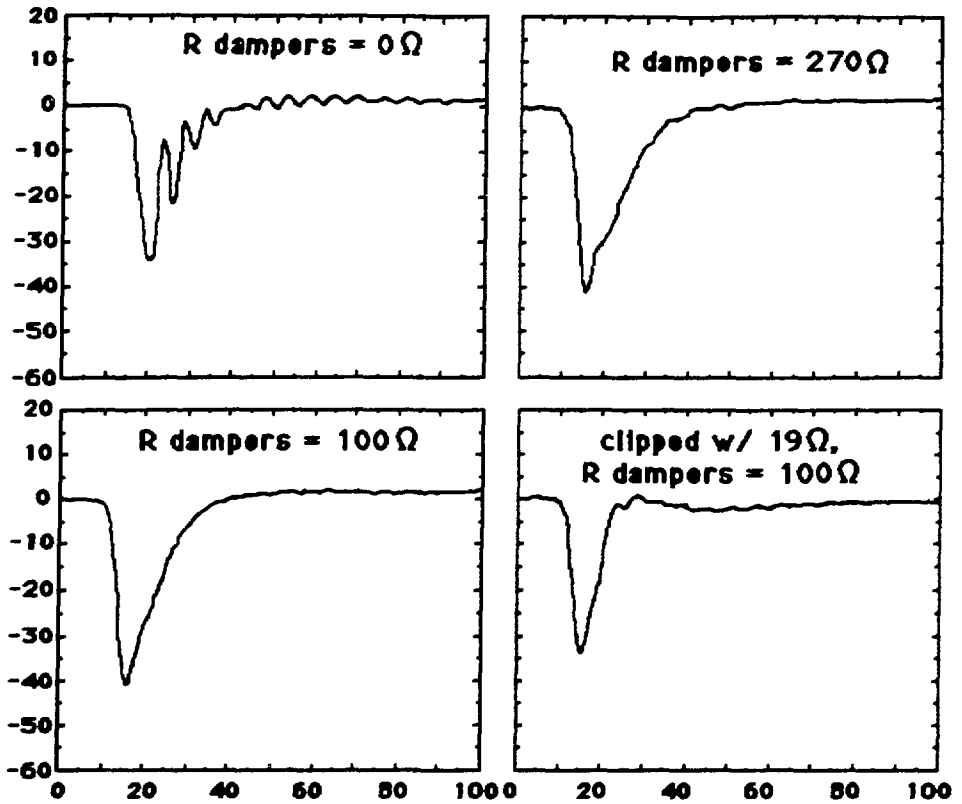

FIGURE 3
Transient digitizer records of anode waveforms from anode stem circuit designs for under damped, over damped, critically damped, and cable clipped pmt bases. Y-axis is in mV, x-axis is in nsec.

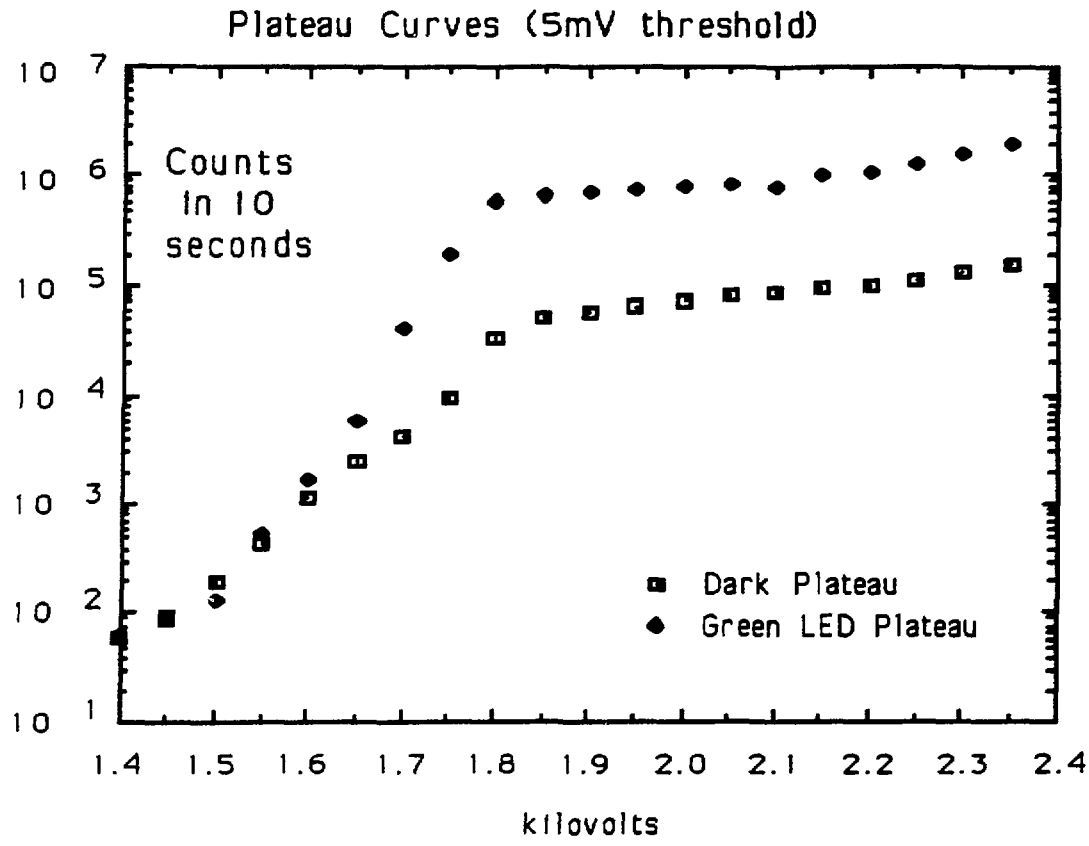

FIGURE 4

Dark pulse and green LED pulse plateau curves.

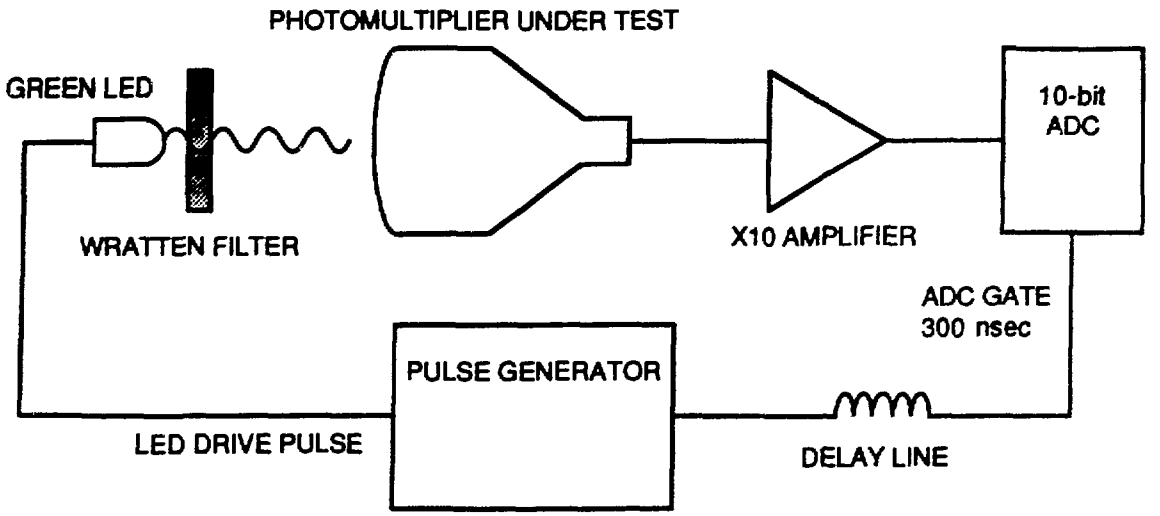

FIGURE 5

ADC charge resolution test setup.

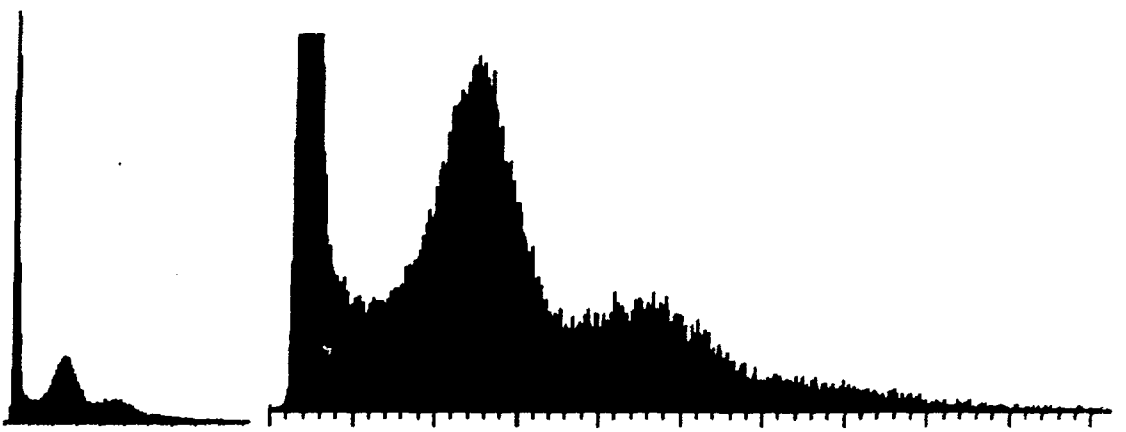

FIGURE 6

Charge spectrum for full photocathode illumination by a green light emitting diode. The histogram on the right is an expansion of the full histogram, shown on the left. The x-axis scale calibration is 1 pC per major division. Note the one, two , and three photoelectron peaks.

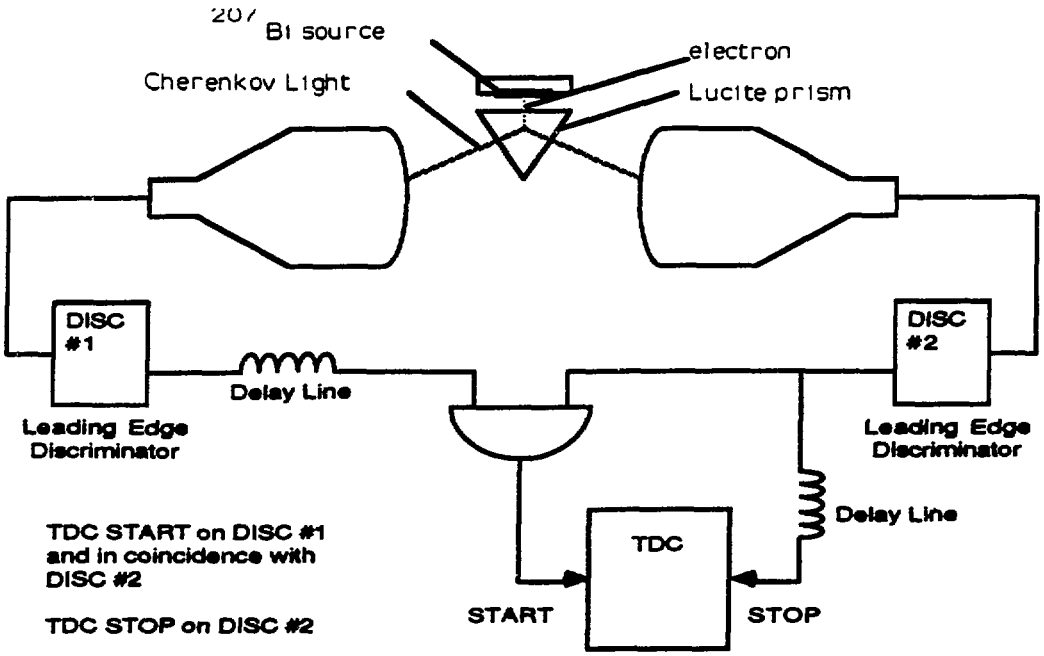

FIGURE 7

Cherenkov light source and TDC test setup.

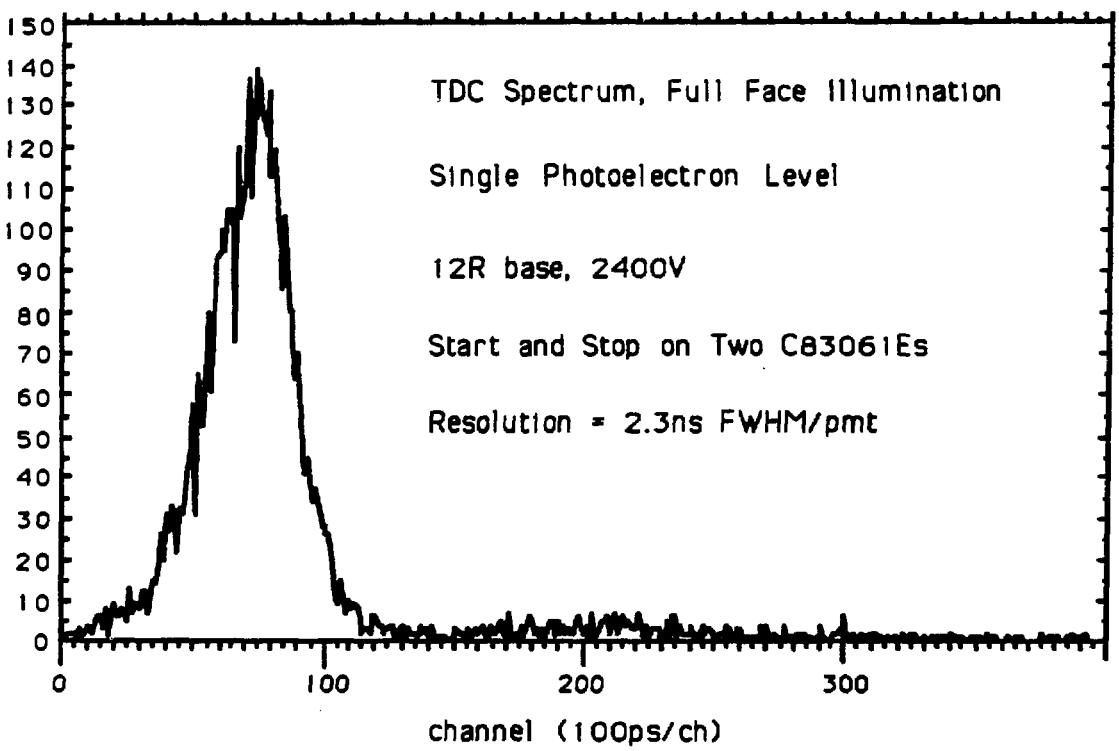

FIGURE 8

Time spectrum with start and stop signals provided by two C83061Es.

*U.S. GOVERNMENT PRINTING OFFICE: 1990-0-773-034/20065